Lecture Notes in Mechanical Engineering

Guy Pluvinage
Ljubica Milovic *Editors*

Fracture at all Scales

Springer

Lecture Notes in Mechanical Engineering

About this Series

Lecture Notes in Mechanical Engineering (LNME) publishes the latest developments in Mechanical Engineering—quickly, informally and with high quality. Original research reported in proceedings and post-proceedings represents the core of LNME. Also considered for publication are monographs, contributed volumes and lecture notes of exceptionally high quality and interest. Volumes published in LNME embrace all aspects, subfields and new challenges of mechanical engineering. Topics in the series include:

- Engineering Design
- Machinery and Machine Elements
- Mechanical Structures and Stress Analysis
- Automotive Engineering
- Engine Technology
- Aerospace Technology and Astronautics
- Nanotechnology and Microengineering
- Control, Robotics, Mechatronics
- MEMS
- Theoretical and Applied Mechanics
- Dynamical Systems, Control
- Fluid Mechanics
- Engineering Thermodynamics, Heat and Mass Transfer
- Manufacturing
- Precision Engineering, Instrumentation, Measurement
- Materials Engineering
- Tribology and Surface Technology

More information about this series at http://www.springer.com/series/11236

Guy Pluvinage · Ljubica Milovic
Editors

Fracture at all Scales

Springer

Editors
Guy Pluvinage
LABPS
ENIM
Metz
France

Ljubica Milovic
Faculty of Technology and Metallurgy
University of Beograd
Beograd
Serbia

ISSN 2195-4356 ISSN 2195-4364 (electronic)
Lecture Notes in Mechanical Engineering
ISBN 978-3-319-32633-7 ISBN 978-3-319-32634-4 (eBook)
DOI 10.1007/978-3-319-32634-4

Library of Congress Control Number: 2016946303

Printed on acid-free paper

This Springer imprint is published by Springer Nature
The registered company is Springer International Publishing AG Switzerland

Preface

The idea of establishing the NT2F conferences came in year 2000 from the scientists of the Laboratoire de Fiabilité Mécanique de l'Ecole Nationale d'Ingénieur de Metz in the form of the annual meeting of the "Without Walls European Institute on Fatigue and Fracture". Since then, 15 successful conferences were held: NT2F1-Metz (France) in 2001, NT2F2-Hammamet (Tunisia) and NT2F3-Ningbo (China) in 2003, NT2F4-Aleppo (Syria) in 2004, NT2F5-Bari (Italy) in 2005, NT2F6-Kranj (Slovenia) in 2006, NT2F7-Miskolc (Hungary) in 2007, NT2F8-Ankaran (Slovenia) in 2008, NT2F9-Belgrade (Serbia) in 2009. The tenth anniversary conference NT2F10 was held again in Metz in august 2010. After that, the series was continued by NT2F11-Polignano a Mare (Italy) in 2011, NT2F12-Brasov (Romania) in 2012, NT2F13-Moscow (Russia) in 2013, NT2F14-Belgrade (Serbia) in 2014 and NT2F15-Oran (Algeria) in 2015. These prestigious and long running conferences bring together delegates from around the world to discuss how to characterize, predict and analyze the fatigue and fracture of engineering materials.

The 14 New Trends in Fatigue and Fracture international conference "Fatigue and fracture at all scales" was held on 15–18 September 2014 in Belgrade, Serbia. NT2F14 was focused on all aspects of fracture and fatigue of wide range of materials, components and structures.

The New Trends in Fatigue and Fracture international meeting conference is the occasion at which NT2F awards are presented to recognize the achievements of researchers. At this fourteenth conference two awards were presented. Special award was given to the honorary chair of NT2F14 and to the founder and first president of Society for Structural Integrity and Life, Prof. Stojan Sedmak for his outstanding contribution of development and application of Fracture Mechanics in former Yugoslavia. To Prof. Guy Pluvinage special gratitude, for establishing the standing NT2F conference and for his outstanding efforts and contributions to the Conference, is given.

The proceedings have been divided into two parts. The first part is dedicated to the late Prof. Stojan Sedmak, the most prominent scientist in the field of fracture mechanics and structural integrity in Serbia and the second one consists of selected papers presented at the NT2F14 conference.

Metz, France — Guy Pluvinage
Beograd, Serbia — Ljubica Milovic

Contents

48 Years of Fracture Mechanics and Structural Integrity in South East Europe

Vencislav Grabulov

Abstract Development of fracture mechanics and structural integrity in South East Europe has been presented and analysed. As the starting point, the Magister thesis of Prof. Stojan Sedmak, 48 years ago (1968), has been taken, followed by his Doctoral thesis and some of the most important achievements afterwards, including International Fracture Mechanics Summer Schools and USA-ExYu project "Weldment Fracture Mechanics".

Keywords Fracture mechanics history · South-East Europe

1 Introduction—Magister Thesis

Development of Fracture Mechanics and Structural Integrity in the region was initiated by the Magister thesis of Prof. Stojan Sedmak, at least as far as we could found, [1]. Its title was "Some problems of stress concentration in two-dimensional elasticity theory", and the first version of the thesis has included only theory of linear elasticity, applied to solve stress concentration problems by using photo-elasticity. Nevertheless, upon request of the advisor, Acad. Nikola Hajdin, president of Serbian Academy of Sciences and Arts (2005–2014), Stojan Sedmak added Chap. 5 "Theory of brittle fracture" and presented the Bovie's problem, as an illustration of the linear elastic fracture mechanics, Fig. 1a. It is interesting to note that thesis has been defended at the Faculty of Mathematics and Natural Sciences, University of Belgrade, although Prof. Stojan Sedmak was a Mechanical Engineer, teaching at the Faculty of Technology and Metallurgy, whereas Prof. Nikola Hajdin was Civil Engineer, teaching at his own faculty. Namely, at that time, there was a strong group of Theoretic and Applied Mechanics at the Faculty of Mathematics and Natural Sciences, capable of getting together researchers in multidisciplinary topics like Fracture Mechanics.

V. Grabulov (✉)
Institute for Materials Testing, Bulevar vojvode Misica 43, Belgrade 11000, Serbia
e-mail: vencislav.grabulov@institutims.rs

G. Pluvinage and L. Milovic (eds.), *Fracture at all Scales*,
Lecture Notes in Mechanical Engineering, DOI 10.1007/978-3-319-32634-4_1

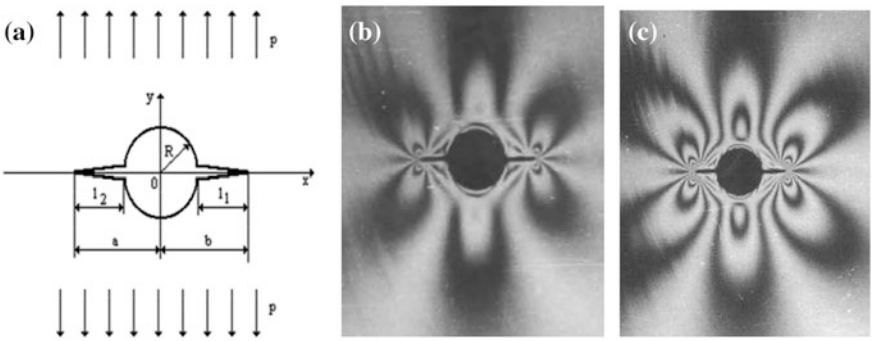

Fig. 1 **a** Bovie's problem; **b** Isohromes (No = 4); **c** Isochromes (No = 7)

Photo-elasticity was a standard method to solve stress concentration problems, but it was not so often applied to solve fracture mechanics problems back in Sixties. On the contrary, it was quite difficult to apply this method to solve the Bovie's problem, requiring long and tedious work, for more than a year. Actually, the first results (Fig. 1b, c) indicated value 3, as shown in Table 1, which was not correct for the notches emanating from the circular opening. By repeating experiments to get more readable photos, Fig. 2, Stojan was capable to get more realistic results, as shown in Table 2. Also, one should notice extrapolation technique, applied along the line shown in Fig. 2b, to get more precise number of isochromes.

Table 1 Results for the stress concentration factor (units given as originally)

Photo	Number of isochromes	Stress (kp/cm^2)	Remote stress (kp/cm^2)	Stress concentration factor
Figure 1b	4	104	35	≈3
Figure 1c	7	182	64	2.82

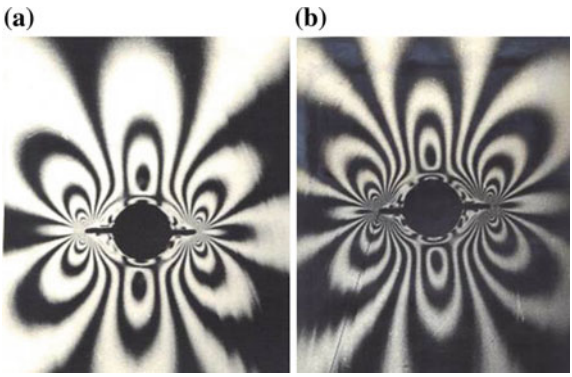

Fig. 2 **a** Isohromes (No = 10); **b** Isochromes (No = 14.7 after extrapolation)

Table 2 Results for the stress concentration factor (units given as originally)

Photo	Number of isochromes	Stress (kp/cm^2)	Remote stress (kp/cm^2)	Stress concentration factor
Figure 2a	10	260	81	3.22
Figure 2b	13 (14.7*)	338	98	3.45 (3.9*)

*Repeated with extrapolated number of isochromes

Anyhow, he was still not satisfied with the results, so he made another model to be tested under the same conditions, but with some technical improvements (different expositions to get sharper images, better magnifying glass). This has led to the final result for the stress concentration factor of 5.24. Based on the experience gathered during this experimental work, Stojan Sedmak also concluded that photo-elasticity is not suitable method to deal with crack problems.

2 Doctoral Thesis

Later on, in 1976, Prof. Stojan Sedmak has completed his doctoral thesis, "Effects of Notches and Cracks on Elastic and Plastic Fracture", under the supervision of Prof. Kosara Jojic, at the Faculty of Mechanical Engineering, University of Belgrade, [2]. The experimental part of thesis was performed in cooperation with Aleksandar Radovic and Vencislav Grabulov, Military-Technical Institute, Belgrade, and comprising determination of K_{Ic} for Al alloys (AZ) and two low-alloyed high strength steels (ČN and ČV), including dynamic effects assessed by different loading rates, drop weight testing and by Charpy impact testing on instrumented pendulum to separate energies for crack initiation and propagation.

One should also note that plasticity was taken into account by introducing CTOD measurement, as the standard method for fracture mechanics testing, and also by theoretical analysis, including Dugdale's model (just to mention, this model was briefly described even in the Magister thesis!) and J integral. In other words, material behaviour in presence of cracks was thoroughly analysed using three different alloys, all of them susceptible to brittle fracture, but also capable of plastic straining.

Couple of crucial results are presented in following figures, showing specimens used for experiments (Fig. 3), diagram force-displacement for K_{Ic} evaluation (Fig. 4), and diagram K_{Ic} vs. loading rate (Fig. 5), both for Al alloy AZ.

Finally, reading from instrumented Charpy pendulum are shown in Fig. 6 (Al alloy AZ). It was only the third such equipment in the world, used for the first time in South East Europe.

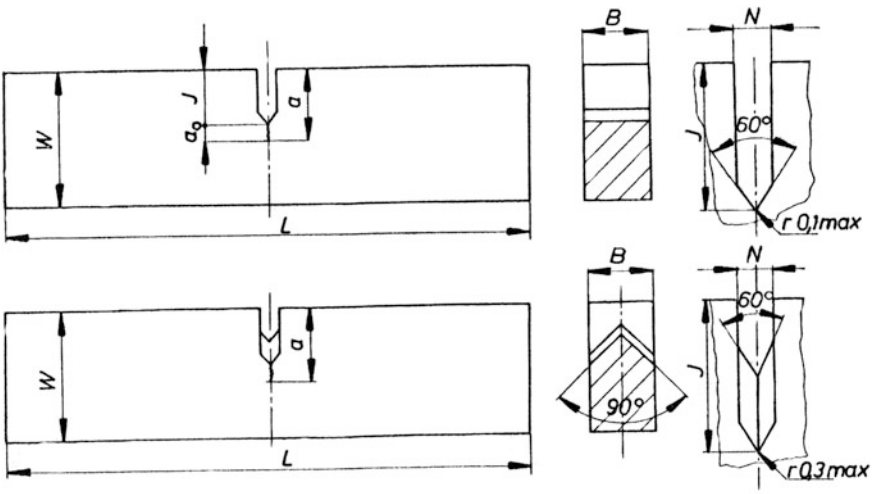

ČV: B=20	W=40	L=172	J=20	N=2.2	a0=1.3 mm
AZ: B=22	W=44	L=210	J=21	N=2.6	a0=1.3 mm
ČN: B=12	W=24	L=120	J=10	N=2.2	a0=1.3 mm

Fig. 3 Specimens used for experiments

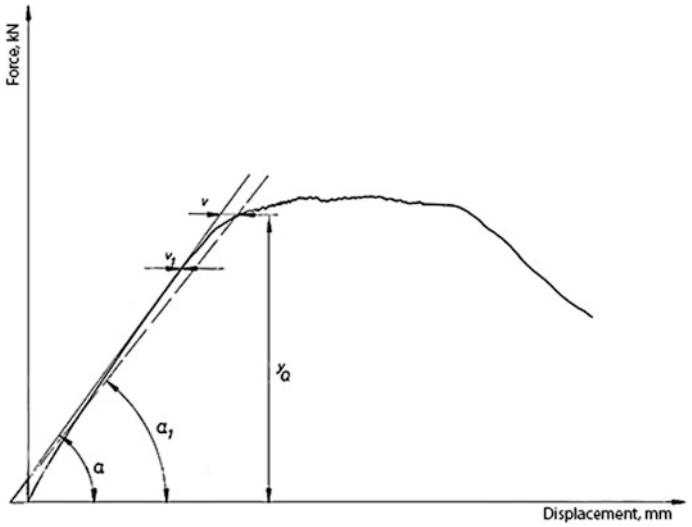

Fig. 4 Diagram force-displacement for K_{Ic} evaluation—Al alloy AZ

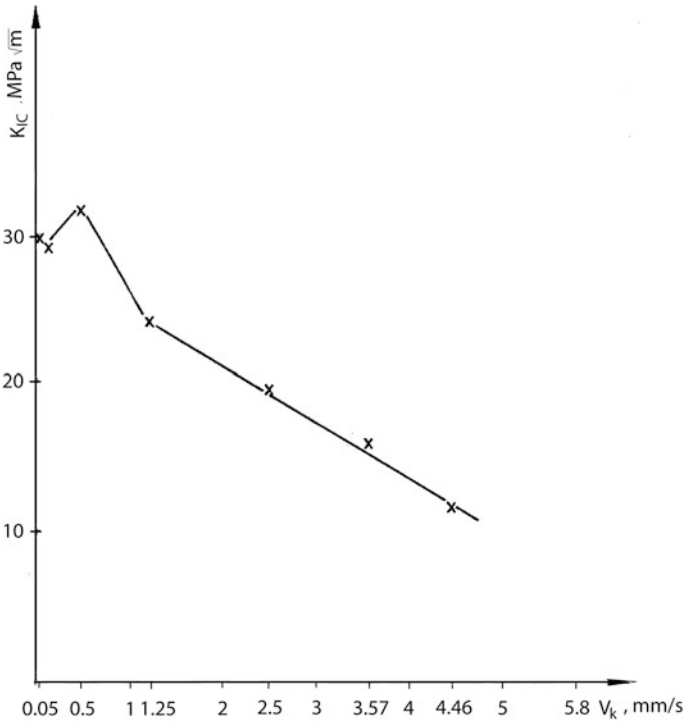

Fig. 5 Diagram K_{Ic} versus loading rate, V_k—Al alloy AZ

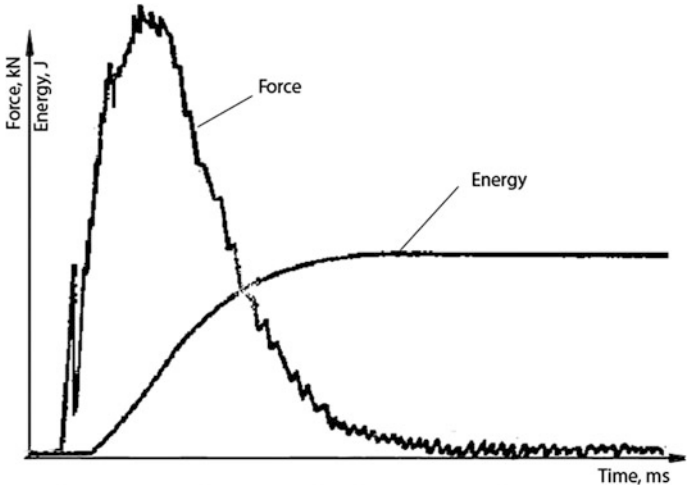

Fig. 6 Reading from instrumented Charpy pendulum—Al alloy AZ

3 Later Developments

As the typical example of later developments, leading to application of fracture mechanics principles to assessment of structural integrity, leakage problem in large spherical storage tanks is presented, mostly taken from the monograph [3].

Spherical storage vessel is preferred for storage of fluids under high pressure. An advantage of spherical storage vessels is that they have a smaller surface area per unit volume than any other shape of vessel. The uniform distribution of stresses, both internally and externally, generally means that there are no weak points in a sphere. The sphere, shown in Fig. 7, volume 2000 m^3, was introduced in service in Serbia in 1977 for storage of vinyl chloride monomer (VCM).

At the seventies of last century normalized fine-grained steel TTSt E-47, microalloyed by vanadium, of 460 MPa nominal yield strength, was developed as promising and world-wide applied for manufacturing of spherical storage tanks in process industry and oil refineries, [4]. The wall thickness of sphere could be reduced compared to cylindrical vessel to one half due to stress distribution, and also due to applied steel of yield strength (460 MPa) compared to mild steel of

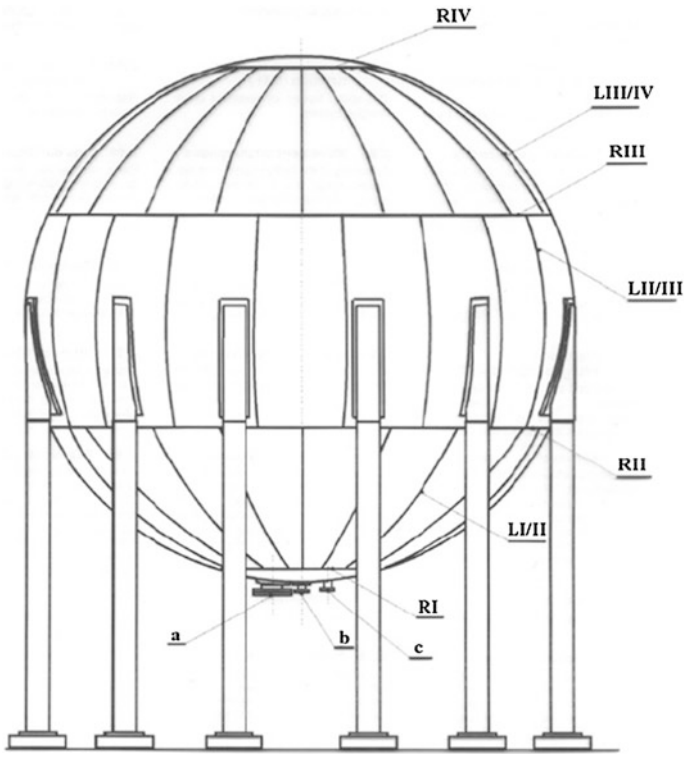

Fig. 7 Spherical storage tank

maximum 355 MPa. Between 1970 and 1987, most spherical storage tanks had been produced of TTSt E-47 microalloyed steels. The benefit was twofold: significantly reduced weight and cost of welding due to reduced volume of weld metal (less work, less consumable). The disadvantages were lack of experience with new type of steel with unpredictable problems in welding and steel properties in heat-affected-zone (HAZ), [4]. After several years of service, in the beginning of eighties, a large number of storage tanks leaked in succession, as reported. Faced with frequent failures of spherical storage tanks produced of TTSt E-47 some national inspection offices decided in late eighties of last century to prevent the production of new tanks applying this steel, like in Germany and former Yugoslavia. However, a large number of such tanks were already in service, and many of them failed.

3.1 Origin and Analysis of Leakage Problem

The most intensive reaction regarding leakage, including repairing, took place in Czechoslovakia, [3]. The analysis have shown that cracks propagated in metal-manual-arc (SMAW) welded joint through the fusion region between weld and parent metals, in underbead zone of high hardness, containing martensite (up to 90 %). Through-wall cracks were attributed to initiation of existing cold hydrogen induced crack (HIC). During regular inspection after 8 years the damage on spherical storage tanks for natural gas had been detected. This was through-wall crack, 50 mm long, which caused leakage, cooling and wall frozen. The crack developed along fusion line. It was attributed to initiation of existing cold hydrogen-induced crack and their growth by stress corrosion. After that, numerous cracks had been detected by ultrasound in other vessels. Number of defects ranged from 24 to 239, and their total length per vessel was 11 mm to 193.5 m. Further 16–183 cracks per vessel had been found by magnetic methods. In addition to macroscopic surface cracks, a lot of short cracks had been revealed in welded joints, on inner side. The length of individual cracks ranged from 10 mm to 2.4 m, and depth was from 1 to 27 mm (half of the wall thickness). During removal of cracks by grinding, new cracks, up to 2 mm long, were revealed by dye penetrant in the fusion regions, which were not found by other methods. The possibility to repair so many cracks was questioned, since by repair welding new cracks could be initiated, sized bellow the sensitivity of equipment for non-destructive-testing (NDT).

Many of cca 100 tanks failed in service in former Yugoslavia due to cracking. First one failed in 1982, by leakage due to a transversal crack, after regular in-service inspection and proof pressure test at 24 bar. Careful ultrasonic and magnetic particles testing revealed significant number of cracks on inner surface. Crack initiation and growth was attributed to following causes:

- the attack of H_2S—hydrogen-induced crack contained in stored medium;
- low cycle fatigue by variation in pressure and temperature;
- initiation of cracks from manufacturing defects;

- support of high pressure during required proof test;
- quality of applied steel and presence of brittle microstructure in its HAZ;
- other factors (residual stress, thermal stress, geometrical stress concentration).

Several spherical tanks are also in service in the company HIP-AZOTARA, Pančevo, for storage of under pressure liquefied gases. In regular in-service inspection, performed in 1993, many defects, mostly cracks, had been detected on the inner side of a sphere. The cracks mostly developed in radial welded joints (RIII, Fig. 9), in its upper part, at the border of liquid and gaseous phases. The occurrence of cracks was intensive in the HAZ of micro-alloyed steel NIOVAL 47 (class TTSt E-47), Steelworks Jesenice. The cracks were also detected in tanks of plane carbon steels, but after long-term service. Only cracks in HAZ of TTSt E-47 steels passed through the wall, due to low toughness in the fusion region. After grinding of small cracks it had been confirmed that they ended in the pore or inclusion, the locations of stress concentration, involved during manufacturing. In all tested vessels, only individual cracks initiated from defects.

3.1.1 Description of Cracks and Defects

It has turned out that fine-grain micro-alloyed steel TTSt E-47 is sensitive to cold cracks in HAZ. Some hostile stored media produced stress corrosion in existing initial cracks in SMAW welded joints, mostly through the fusion region, in underbead zone containing up to 90 % of martensite of high hardness. Careful ultrasonic and magnetic particles testing revealed significant number of cracks on inner surface. For macro- and micro-structure analysis, hardness measurement and chemical analysis, the samples, 10 mm wide, 70 mm long and 12 mm deep, encompassing the crack, were cut in the form of a small boat. Crack initiation region, shown in Fig. 8, contained intercrystalline surface crack which passed through underbead bainite-martensite.

Fig. 8 Crack initiation location in the underbead zone

Also small embedded cracks were found in welded joints, 10–30 mm long and 3–10 mm wide. After grinding numerous cracks of 0.5–2 mm were discovered. Similar cracks were observed on the surface with oxides, indicating that small cracks were present in welded joints even prior to annealing procedure.

Hydrogen content in consumables, mistakes in prescribed welding technology, including disrespect of welding technology specification (WPS), stress corrosion and damages in service caused the initiation of cold cracks induced by welding. Non-allowable defects had not been detected in the previous periodic inspections, confirming the data of existing incubation period for stress corrosion cracks nucleation and growth.

Adverse effect of specified proof test (cold-water test with pressure up to 50 % higher than operating pressure) was accentuated. The testing of the tanks before and after inspection (by not specified additional test) has clearly shown that proof test in service can cause new cracks in the positions of "old" (but not repaired) welded joints. For that reason the suggestions had been addressed to Boiler Inspection Office to reduce test pressure, especially in service. The experience has shown that the pressure vessel repaired by welding should not be subjected to pressure testing, but only periodical ultrasonic test of typical repaired positions from the outer side should be performed, e.g. immediately after repair ("initial" state) and after operating parameters are reached. If no crack has been detected, these tests should be repeated every 6–12 months, until the term of regular periodical proof test. Due to significant financial expenses (repeated cycles: testing, repair with testing, testing after repair, proof test, testing after proof test, periodical inspection), selective approach to testing and repair of vessels prevailed, so that only the overfills in critical locations (radial welded joints and crossings) should be ground and subjected to ultrasonic testing. If defects are detected in this locations, overfills grinding and ultrasonic testing should be increased up to 100 %. It should be noticed that there is no reason to perform ultrasonic test when a significant number of shallow cracks has been detected by magnetic particle testing, which is a frequent case. In this situation it is better to grind cracks first, and then to perform ultrasonic test. The through crack causing leakage is shown in Fig. 9.

3.1.2 Analysis of Crack Occurrence in One Spherical Storage Tanks

Many of spherical storage tanks are still in service, requiring inspection, maintenance and repair. Here is presented the situation with one vessel in Serbia, shown in Fig. 7. During regular inspection, a great number of cracks of different directions

Fig. 9 Macrostructure across welded joint with through crack on spherical tank

and sizes has been detected by non-destructive testing in 1986–1990 and in 1996 on the inner wall side, in welded joints regions.

The spheres are not insulated, the inner pressure depends on ambient temperature (e.g. at +10 °C pressure is 1.51 bar, at +35 °C it is 4.23 bar). Spherical storage tanks are produced of 24 assembled segments and two lids (bottom and top), with wall thickness 20 mm, and are supported by 12 legs, Fig. 7. The tanks are produced of NIOVAL 47 steel, 20 mm thick. The measured values of mechanical properties are: yield stress $R_{p0.2}$ = 470–506 MPa, tensile strength R_m = 639–660 MPa, elongation at fracture A_5 = 25–27 % and impact toughness 120–166 J/cm^2 at 0 °C.

Tanks are welded by longitudinal joints—L (total length 483 m), performed 50 % by submerged arc welding (SAW) and 50 % by SMAW, and radial joints—R (total length 120 m), performed by SMAW. Corresponding consumables were used for welding, e.g. electrodes EVB-60 (EN 499 classifications as E 50 2 Mo B 42) made by Steelworks Jesenice.

In spherical storage tank exploitation following events took place:

- November 1976—I proof test (12 bar)—no data.
- September 1977—Spherical storage tank put in service.
- September 1983—II proof test—no leakage recorded.
- April 1987—III proof test—no leakage recorded. UT, performed on the outer side of two radial welded joints (RI and RII) in service revealed no indication.
- October 1989—IV proof test (special inspection required by Boiler Inspection Office)—no leakage recorded. Following inspector's request, the overfill in the inner side was grinded for non-destructive inspection. A great number of cracks of different length and depth in the longitudinal and radial welds were revealed by magnetic and ultrasonic testing. After the repair by grinding and welding, no crack indication was found by magnetic and ultrasonic testing.
- March 1990—V proof test (special inspection)—no leakage recorded, again a great number of cracks of different lengths and depths in longitudinal and radial welds were detected by magnetic and ultrasonic testing. After the repair, no crack was found by magnetic and ultrasonic testing.
- In March 1991 cracks were found in 331 locations, by inspection and testing of longitudinal and radial welded joints on the inner storage tank side. Table 3

Table 3 Location and orientation of cracks on spherical storage tank

Number of crack before (after) proof pressure test			
Welded joint	Longitudinal	Transversal	Total
RI	2 (3)	9 (2)	11 (5)
RII	36 (2)	85 (–)	121 (2)
RIII	109 (35)	– (12)	109 (47)
RIV	6 (10)	5 (–)	6 (10)
LI/II	33 (106)	17 (8)	38 (106)
LII/III	29 (2)	– (–)	46 (10)
LIII/IV	– (–)	116 (22)	– (–)
Total	215 (158)	116 (22)	331 (180)

indicates location, number and directions of cracks in a tank, repaired by grinding, and also notches deeper than 5 mm repaired by welding, which were found before and after proof test in inspection performed in 1991.

Number of cracks repaired before (after) proof test by different procedures are shown in Table 4. It is clear that the pressure proof test before putting in service, if applied at the level of the first proof test, produces new cracks in welded joints exposed to service conditions, whereas in new welded joints (performed during repairing) there are no crack indications.

However, in the case of one spherical storage tanks and of one road trailer tanks it is definitely confirmed that the cracks initiated during exploitation, since in the previous periodic inspections non-allowable defects had not been detected. These data confirm the reference data on the existence of incubation period for stress corrosion cracks nucleation. Based on testing of several cylindrical tanks and tank wagons, with residual stress relieved after manufacturing, proof test had not caused the occurrence of new cracks.

It turned out that steels of TTSt E-47 are sensitive to cold cracking in HAZ. Cracks initiated in service under applied tensile stress, and in some stored media stress corrosion cracking contributed to faster growth of initiating cracks. The cracks propagated in SMAW joints (designated also as MMA), through the fusion region, in underbead zone of high hardness, containing up to 90 % of martensite.

The complexity of crack problem was confirmed by the fact that due to repair action additional stress was induced, which might initiated small cracks, of the size bellow the sensitivity level of applied equipment. They were opened during proof test, sometimes performed by pressure as high as steel yield stress level.

Anyhow, described repair was unexpectedly successful, since:

- Number of cracks detected in 1996 is negligible compared to 1989/90 (10 cracks against 1354).
- Typical for cracks detected in the year 1996 is that they are of significantly smaller depth and length compared to the average crack dimensions found in 1989/90.

Table 4 Number of cracks repaired before (after) proof test by different procedures

Welded joint	Applied repair procedure		
	Grinding only	One side welding	Both sides welding
RI	5 (3)	6 (–)	– (1)
RII	15 –(2)	87 (2)	19 (–)
RIII	36 (45)	58 (2)	15 (–)
RIV	– (–)	5 (1)	1 (–)
LI/II	12 (101)	25 (5)	1 (–)
LII/III	34 (10)	12 (–)	– (–)
LIII/IV	– (–)	– (−2)	– (–)
Total	102 (165)	193 (14)	36 (14)

- The experience from previous testing is confirmed by testing in 1996 regarding the location of crack occurrence (mostly radial welded joints in the middle tank part), crack direction (dominant longitudinal cracks) and, as most important, that proof test by cold water pressure induced new cracks.

This is confirmed by magnetic particles testing before and after the cold water proof test on joints R-I and R-III (Fig. 9) and adjacent vertical joints, where the new cracks were found in the old parts of joints, not repaired by welding. The cracks were detected in the longitudinal joint L-17 close to R-III joint, in the notch induced by cracks repair by grinding in 1991, as well as cracks in HAZ on joint L-12 close to R-I, not existing before proof test. On 6 of 10 detected locations, the crack is located inside the notch produced by repair grinding in the year 1991.

Anyhow, repair by welding is not the direct cause of crack occurrence, since:

- Cracks were revealed in 80 notches produced by grinding repair in 1991.
- Repair in 1991 was performed by proper rounding.
- Cracks emanating from notches in R-I and R-III were not found before the proof test.
- In the locations of repairing performed by grinding in the year 1996 after proof test no indications of crack-like defects was detected.

It can be stated that the cause of crack initiation is local overstressing induced by the effect of test pressure. Therefore, the revised repair technology for this tank includes hammering of welded joints as well, in order to reduce residual stress.

Efficiency of inspection and repair is at high level, since reduced number crack is incomparable (10 cracks in 1996, 1354 in 1989/90).

3.2 Structural Integrity Assessment

Upon the request of spherical storage tank owner, fracture mechanics analysis by J integral was applied for an atypical case of cracking. These cracks occurred in the weldments of temporary attachments (fixtures) on tank inner surface served solely for next operations of welding and assembling. Being temporary they had not been specified in design documentation, and after use they had to be removed. The cracks, up to 4 mm deep and 30–50 mm long had been initiated in the heat-affected-zone and arrested in the parent metal wall. Cracks occurred because specified SMAW welding technology was disrespected in situ. Based on experience with mild structural steels the welding of temporary attachments was considered as of low importance, and selection of locations and performance of their welding was left to the skill of welders. Neither the specified preheat was applied nor, probably, was the required procedure used for drying electrodes. High content of diffusible hydrogen enabled crack initiation. Thus, the crack nuclei were already present in the tank at the assembly stage and grew to macroscopic size in subsequent operations, e.g. proof pressure testing. It is to add that required inspection of welding

and welded joints had not been done in this location, since the attachments are not structural components and should be removed after assembling. These defects from manufacturing were remote from structural weldments, their inspection was not required and they were not detected. However, after occurrence of first cracks of that type, careful inspection revealed cracks up to 2.4 m long and 5 mm deep, in the HAZ of temporary fixture in the wall 25 mm thick,. This situation dictated extended non-destructive testing. In order to provide necessary sensitivity, the weld overfills on both inner and outer sides were ground flush.

Next extension of these crack was possible in virgin, non-affected parent metal, but, in both rolling and cross-rolling direction. It is also to mention that in this way induced cracks are prone to corrosion and stress corrosion in a hostile environment, what might contribute to their extension. Structural integrity assessment in presence of such cracks can be helpful, but these locations have to be repaired either by grinding of small cracks or by additional welding if crack size was significant. The aim of structural integrity assessment applying J integral was to document possible operation in short time, before the final decision regarding the repair. Pre-cracked specimens for J integral testing were taken in rolling and cross-rolling directions.

Spherical storage tank was of an outer diameter D_s = 12,500 mm and wall thickness h = 25 mm, designed for pressure p_d = 6 bar and proof test pressure p_0 = 10 bar at temperature t_0 = 15 °C. Considered tank was also produced of fine-grained steel, TTSt E-47 class, V micro-alloyed. Its properties, obtained by testing (Yield Stress 480 MPa and Ultimate Tensile Strength 680 MPa, Impact Energy at −20 °C ranged from 55 to 200 J/cm^2 and Hardness HV10 between 180 and 200) satisfied the specification.

Following assumptions had been involved:

- Plane stress is assumed, and membrane stress is dominant since wall thickness versus diameter ratio is small (25/12,500 = 0.002).
- Spherical shell is shallow and can be analyzed as plane plate.
- Maximum crack size is supposed to be 5 mm in depth and 100 mm in length.

3.2.1 Material Crack Resistance Curves and Structural Integrity of Damaged Tanks

J integral testing had been performed using standard C(T) specimen and unloading compliance method to evaluate J_{Ic}, a measure of fracture toughness, and to define J-R curve. Resistance curves are obtained for parent metal, with the cracks in rolling direction (CT1, CT2) and transversal to it (CT3, CT4).

The transfer of experimentally obtained results to a real construction requires many conditions to be fulfilled, primarily due to differences in stress state for quasi-static loading, applied to specimen and full-scale structure. Typical crack in spherical storage tanks occurred in HAZ of temporary fixtures, welded

disrespecting WPS. The cracks in this case can extend in PM only, and brittle fracture significance is evaluated using K_{Ic} value of PM. The lowest value of fracture toughness $K_{Ic} = 111\ \text{MPa}\sqrt{\text{m}}$ was found in specimen testing with the crack in rolling direction, and it is still two times higher than applied K_I value (63.7 $\text{MPa}\sqrt{\text{m}}$, indicating that the brittle fracture is not probable.

Stable crack growth behavior is evaluated comparing J-R curve of PM with crack driving force from King's model (Fig. 10). In it, surface crack is replaced by a through crack, and effect of residual ligament simulated by series of springs which close the crack. In this way three-dimensional problem is replaced by combination of two dimensional problems: when through crack is in plane stress field, or when the surface crack is in plane strain state spread across plate width. Equations for King's model are:

$$J_e = \frac{1-v^2}{E}K_I^2 \quad J_p = \frac{4\sigma_F}{E}(a+a_p)\sigma - a\sigma_{LY} - \frac{h-d}{h}a_p\sigma_Y \quad J = J_e + J_p$$

where v is Poisson's ratio, K_I stress intensity factor, σ_F flow stress (mean value of yield stress and tensile stress), a_p plastic extension of a crack, σ applied stress, σ_{LY} net section yielding stress, J_e elastic part of J integral and J_p its plastic part.

Set of CDFs was compared with typical J-R curves for parent metal in rolling (CT1) and cross-rolling (CT4) direction. The conclusion was that stable crack growth is not critical since required CDF for detected small cracks corresponded to pressure of 22 bar, and the pressure in proof test is 10 bar. Cracks were removed by grinding and their roots were rounded.

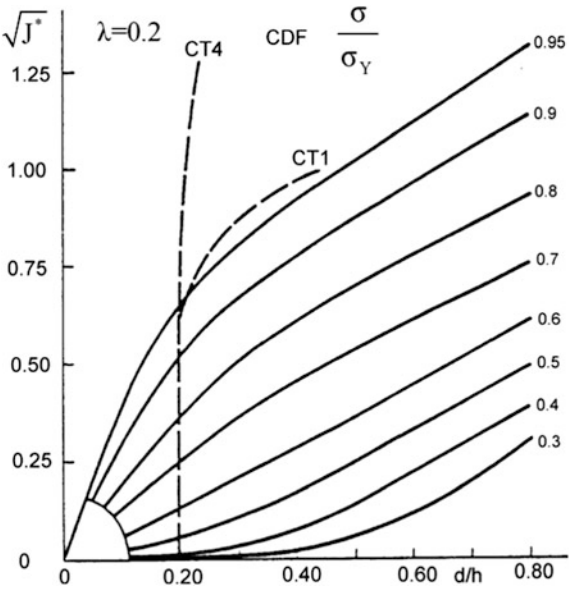

Fig. 10 Crack resistance J-R curves for parent metal and J crack driving force (CDF), calculated for King's model for ratio $d/h = 0.2$

3.2.2 Conclusion

Fracture Mechanics parameters have been applied to evaluate Structural Integrity of large spherical storage tanks, in order to contribute to the solution of complicated cracking problem. High-strength low-alloyed steel was used with little previous experience regarding its resistance to cracks, causing many problems, especially due to unjustified pressure proof testing.

Described experiment that included a comprehensive examination of all aspects of fracture mechanics in the function of structural integrity assessment and conclusions that were a result, at that time represented the pioneering work in this field, not only in South-East Europe.

4 International Fracture Mechanics Summer Schools

Starting 35 years ago, in 1980, International Fracture Mechanics Summer Schools (IFMASS) has been organized ten times, the last one in 2008. Monographs were published in Serbian after first seven Schools under the School title, whereas "The

Fig. 11 IFMASS 9 photo taken by Prof. L. Toth [6]

Application of Fracture Mechanics to Life Estimation of Power Plant Components" (IFMASS 5), was published also in English by EMAS. Starting from the IFMASS 8 monographs have been published in English. The number of participants was from 62 in the first School, up to 145 in IFMASS 5, and 107 in IFMASS 8 (Fig. 11).

The IFMASS lecturers staff included more than 70 well known world experts, e.g.: P. Agatonovic, R. Labens, P. Marcel, P. Albrecht, M. Burdekin, D. Francois, H. Hoffmeister, T. Hollstein, I. Hrivnak, V. Ivanova, J. Landes, J. Joyce, H. Mac Henry, A. Mazur, G. Pluvinage, J. Radon, M. Ratwani, R.P. Reed, D. Read, K.H. Schwalbe, T. Siewert, M. Skorupa, R. Stephens, V. Troshchenko, R. Fields, H. Weber, M. Wnuk, including many lecturers from former Yugoslavia, like B. Petrovski, Lj. Nedeljkovic, F. Vodopivec, M. Kojic, M. Berkovic, A. Radovic, V. Grabulov, Z. Burzic, A.Sedmak, S. Kuzmanovic, T. Adziev, D. Drobnjak, M. Marincek, I. Rak, V. Culafic, D. Drenic, D. Mitrakovic, V. Sijacki, A. Jovanovic, K. Geric, Dj. Dobi. One can say that ever since the 3rd IFMASS it was a kind of prestige to be the lecturer at the School [5].

5 USA-Yu Project Weldment Fracture Mechanics (1982–1990)

ExYugoslavia has been recognized in early eighties as one of the leading countries in the field of fracture mechanics and, thus, National Bureau of Standards (now NIST) from Boulder, USA, has chosen team led by Stojan, for the partners in the project Weldment fracture mechanics [7].

As the benefit of this project and IFMASS 1–6, new generation of experts and new research centers emerged, such as Maribor, Slavonski Brod, Sarajevo, Skopje, Podgorica, Novi Sad. More than 25 Doctoral theses were finished and defended in that University centres. Many of these doctors of science are becoming well-known professors who have significant achievements. Just to mention couple of names: B. Petrovski, J. Legat, Z. Lukacevic, S. Kuzmanovic, T. Adziev, V. Culafic, I. Glavardanov… followed by V. Grabulov, A. Sedmak, Z. Burzic, M. Zrilic, K. Geric, N. Gubeljak, D. Kozak, M. Arsic…and then followed by M. Rakin, Lj. Milovic, G. Adziev…and so on…to the youngest generation of D.Sc. students, including third Sedmak's generation, Simon Sedmak, civil engineer, now scheduled to work on his thesis, in a cooperation with ISIM and Polytechnical University of Timisoara.

6 Conclusions

The key points in 48 years of development of Fracture Mechanics and Structural Integrity in South East Europe are:

- The Magister and doctoral thesis, defended by prof. Stojan Sedmak in 1968 and 1977, respectively, including experimental work performed in the Military-Technical Institute Belgrade, Serbia.

- Ten International Fracture Mechanics Summer Schools, held from 1980 till 2008, including large number of world known lecturers and more than 1000 participants.
- The USA-YU project on Weldment Fracture Mechanics, leading also to practical applications in the scope of Structural Integrity.
- Large number of D.Sc. thesis, often done in the scope of regional cooperation.
- Highly developed regional and international cooperation, including active participation of regional national societies under the umbrella of the European Structural Integrity Society (ESIS), leading not only to already organized European Conferences on Fracture (ECF 9 in Varna, Bulgaria, in 1992, by Stojan Sedmak, from Belgrade, under sunctions!), but also to the ECF 22 to be held in Belgrade, Serbia, in 2018.
- Establishment of Serbian Society for Structural Integrity and Life (DIVK), in 2001, renamed in 2014 by adding "Prof. Stojan Sedmak", to honour his founder, and of its Journal, Structural Integrity and Life, also in 2001. Is there a better way to complete this story of development then to say that Stojan witnessed in July 2014 his own son, Aleksandar, the President of DIVK, becoming the vice-president of ESIS, at the same occasion when ECF22 organization was granted to Serbia. Both events on the behalf of the legacy of the father of Fracture Mechanics and Structural Integrity in South East Europe, Prof. Stojan Sedmak.

References

1. Sedmak S (1968) Some problems of stress concentration in two-dimensional theory of elasticity. Magister thesis, Faculty of Mathematics and Natural Sciences, University of Belgrade (in Serbian)
2. Sedmak S (1977) The effect of notches and cracks on fracture with elastic and plastic strain. D.Sc. thesis, Faculty of Mechanical Engineering, University of Belgrade (in Serbian)
3. Sedmak A, Sedmak S, Milović LJ (2010) Pressure equipment integrity assessment by elastic-plastic fracture mechanics methods. Monograph. Society for Structural Integrity and Life (DIVK)
4. Hrivnak I (1988) Breakdown and repair of large spherical containers for liquefied hydrocarbon gases. IIW Doc. IX-1516-88, Bratislava
5. Grabulov V (2015) Fracture mechanics and Structural Integrity in South East Europe—47 years of development. In: Proceedings, the 3rd Southeast Europe IIW Conference, pp 31–38, Timisoara
6. In memoriam, Structural integrity and life, vol 15, p 93, 2015
7. Sedmak A et al (2015) Weldment fracture mechanics. In: The 3rd Southeast Europe IIW Conference, Timisoara

Scientific Biography and Bibliography of Professor Stojan Sedmak

Aleksandar Sedmak and Simon Sedmak

Professor Stojan Sedmak was born in 1929 in Kratovo, then Kingdom of Yugoslavia. He finished high school—gymnasium in Belgrade in 1948, and graduated in 1954 from the Faculty of Mechanical Engineering, University of Belgrade. Afterwards, he completed his magisterium at the Faculty of Natural and Mathematical Sciences, 1970, and came back to the Faculty of Mechanical Engineering for his D.Sc. thesis, 1977, both University of Belgrade. His professional career started in Bugojno, ex-Yugoslavia, at the Factory "Slavko Rodić", 1954–1958, to be continued in Sarajevu up to 1961 (Factory "FAMOS") and in Belgrade up to 1966 (Military Technical Institute). His academic career started at the Faculty of Technology and Metallurgy, University of Belgrade, where he started working as the teaching assistant in 1966 to become assistant Professor in 1971, and full professor in 1981 godine. Officially he has retired in 1995, but he kept on working until he died in 2014.

In his young days, Stojan witnessed a lot of turmoil in his country, even before the Second World War. His family (father Anton, military officer, and mother Ratka, teacher, his older sister Milena and younger brother Tomislav) moved from Kratovo to Negotin (east Serbia nowadays) in 1936, and to Belgrade in 1940. Under strict command of his father and with loving support of his mother he was brilliant student both in so-called First Gymnasium and later on during his studies. His sister Milena married to Aleksandar Vesic and moved to USA, to become the well-known couple in academic circles in Atlanta (Georgia Tech) and Durham

A. Sedmak (✉)
Faculty of Technology and Metallurgy, University of Belgrade,
Kraljice Marije 16, 11120 Belgrade, Serbia
e-mail: asedmak@mas.bg.ac.rs

S. Sedmak
Innovation Center of the Faculty of Mechanical Engineering,
Kraljice Marije 16, 11120 Belgrade, Serbia
e-mail: simon.sedmak@yahoo.com

G. Pluvinage and L. Milovic (eds.), *Fracture at all Scales*,
Lecture Notes in Mechanical Engineering, DOI 10.1007/978-3-319-32634-4_2

(Duke University). The family name Sedmak is well preserved at Duke University through the Aleksandar Sedmak Vesic and Milena Sedmak Vesic Scholarship Fund, established by Stojan's own son, Aleksandar Sedmak, the executor of his aunt Milena's estate in 2007. His brother Tomislav is famous Serbian neuropsychiatrist. Stojan married in 1954 to Matilda Jovanovic. Their only child was born in 1955, nowadays well-known professor at the University of Belgrade, Aleksandar Sedmak, who has three children (Simon, Tamara and Tea) and one grandchild, Lara.

Stojan's magister thesis under the title "Some problems of stress concentration in twodimensional theory of plasticity", written in 1968 and defended after long period of reviewing in 1970, was the milestone for fracture mechanics development, not only at the Univeristy of Belgrade, but also in the region of South East Europe. It all started with Chap. 5 "Brittle Fracture Theory" which was added to the original version of the thesis upon request of the advisor, Prof. Nikola Hajdin (the president of Serbian Academy of Sciences and Arts 2005–2014). Later on, Stojan performed the first fracture mechanics experiments during his work on doctoral thesis, entitled "Effect of Cracks and Notches to Elastic and Plastic Fracture", together with Prof. Aleksandar Radović, in the Military Technical Institute in Belgrade. Completing and defending of his D.Sc. thesis, under guidance of his advisor, Prof. Kosara Jojic, was just the beginning of intensive research and development of fracture mechanics, and later on structural integrity, focused to the most complicated problems when dealing with metallic materials—welding. Afterwards, application of knowledge, gathered during a decade of intensive research, emerged only naturally through numerous projects, starting with the hydro power plant Bajina Basta. Namely, during its construction, fracture mechanics principles were used to design its crucial component—the pipeline, as well as to assess and prove its structural integrity. Couple of very important papers have resulted and been presented by Prof. Sedmak at the Conferences in Leoben (1984), Waterloo (1977) and Cambridge (1979). Some of these experimental results are still analysed, using modern numerical methods, as was presented recently in Leoben (once again!) by Stojan's grandson, Simon Sedmak, civil engineer, now working on his D.Sc. thesis. One can't escape noticing this fascinating three-generation tradition, which also includes his granddaughter, Tamara Golubovic, teaching assistant at the Faculty of Mechanical Engineering.

Profesor Sedmak is the founder and driving force of prestigious International Fracture Mechanics Summer Schools, dating back to the first on in 1980 godine (1st IFMASS, Smederevska Palanka, ex-Yugoslavia). It all started as the result of cooperation with Prof. Michael Wnuk, whose ad hoc idea turned into 10 success stories, with the last edition in 2007 (10th IFMASS, Zlatibor, Serbia). Large number of experts from all over the world have been lecturers, and many young researchers from the region have had the opportunity to learn about fracture mechanics principles and parameters, as well as structural integrity and its application to pressure vessels, pipelines and their weldments, large and other important constructions.

Another important development was USA-YU project "Weldment Fracture Mechanics", started in 1982 and ended, but not completed in 1990. Namely, large turmoil in the country was once again to be witnessed by Stojan starting in late Eighties. Anyhow, he was capable to make, as the project leader, excellent team of researchers from all six exYu republics, including tens of young researchers doing their D.Sc. many of them in NIST, Boulder, Colorado. The whole region still benefits from this project and Stojan's tireless efforts, since the cooperation between University in Belgrade and Novom Sadu (Serbia), Maribor (Slovenia), Osijek—Slavonski Brod (Croatia), Skopje (Macedonia), Podgorica (Montenegro), and Bosnia never stopped. On the contrary, it has spread in the whole region, including Timisoara (Romania), Miscolc (Hungary), Sofia (Bulgaria).

Prof. Sedmak's contribution to the activities of the Yugoslav Welding Association is also of great significance. He was the president until it was shut down in 2000 and during the Nineties he undertook editing of the Welder journal, later renamed to Welding and Welded Structures, the oldest welding related journal in the region. He was also the honorary member of Romanian Welding Society and a delegate in the tenth International Institute of Welding (IIW) committee which dealt with welded joint fracture mechanics. He was an acknowledged expert in IIW and took part in their annual Meetings a number of times.

In 2001, he founded the Serbian Society for Structural Integrity and Life, along with the journal "Structural Integrity and Life". He served as the president of the Society and editor-in-chief of the journal until 2007. Thanks to a very active role of the Society in the scope of European Structural Integrity Society (ESIS), the European Conference on Fracture (ECF 22) will be held in Belgrade, Serbia in 2018, coinciding with 50 years of fracture mechanics activities in the region. This is only the natural continuation of activities dating back to the ECF4 in Leoben in 1982, when Prof. Stojan Sedmak was the representative in European Group on Fracture (predecessor of ESIS) for the first time. The most important event in the meantime was the organisation of ECF9 in Varna in 1992, which was "mission impossible", but was carried out successfully by Stojan and his team, under the sanctions of UN.

As the professor, he taught multiple subjects in the field of chemical and graphical engineering, fracture mechanics, mechanics of materials and welding. He was the head of the Department for general technical sciences and the Department for graphical engineering at the Faculty of Technology and Metallurgy. From 1991 to 1996, he was the director of the programme "Material Reliability and Structure Safety Evaluation" by the European Centre for Peace and Development.

Stojan Sedmak wrote seven books and textbooks, was the editor of 9 monographs and the Proceedings of the Ninth European Conference on Fracture, organised in Varna (Bulgaria) in 1992. He published 216 scientific papers, a chapter titled "Of J integral and J integral testing (with special focus on welded structures)" in the monograph "Nonlinear fracture mechanics", issued by M. Wnuk, Springer, 1990 and the chapter titled "Welded pipelines, made of high strength steel, and the application of fracture mechanics parameters in structural integrity assessment" (co-author A. Sedmak) in the monograph "Safety, reliability and risk of water, oil

and gas pipelines", issued by G. Pluvinage, Springer, 2007. He was the leader of 9 scientific research projects related to the behaviour of materials and welded structures under exploitation, pipelines, and criteria for revitalisation. He cooperated on 4 additional projects, wrote 37 studies, 8 investment programmes and 7 expertises. He was the advisor for 17 doctoral dissertations and 14 master theses. He was a member of the National Accreditation Committee according to the International Welding Institute rules.

Stojan Sedmak held a number of invited lectures: NIST (Boulder, Colorado), Duke University (Durham, North Carolina), University of Wisconsin (Milwaukee), University of Iowa (Iowa City), the Nuclear Research Centre, Ispra, Italy, Hsinhua University in Beijing, China and Faculty of Civil Engineering, Tripoli, Libya. He participated at numerous local and international conferences and meetings (European Conference on Fracture, International conferences on mechanical behaviour of materials, International conferences on fracture, Meetings of the International Welding Institute, American Society for Testing and Materials conferences, International conferences on fatigue).

As of 1980, Stojan Sedmak was the editor of a number of monographs involving fracture mechanics and structural integrity. Of particular significance are "Assessment of life of power plants using fracture mechanics" in 1990, and "From fracture mechanics to structural integrity assessment" in 2004, "The Challenge of Materials and Weldments" in 2006, and "Fundamentals of Fracture Mechanics and Structural Integrity Assessment methods" in 2009.

Stojan Sedmak's scientific contribution to the analysis of behaviour and integrity assessment of welded structures is reflected in the conclusion that overmatching is suitable for higher strength and better crack resistance of welded joints, and that direct measuring of the J integral can be used to determine the crack driving force on a real structure as well. Thanks to Stojan Sedmak's efforts, fracture mechanics and structural integrity analysis were established in our country, which lead to considerable international cooperation in this scientific field. He introduced a comprehensive approach to metal material characterisation, which, in addition to classic properties, defines the material using fracture mechanics parameters and impact characteristics

IFMASS 9, 2005, with Donka Angelova and Michael Wnuk

IFMASS 9, 2005, with Ljubica Milović and Stefan Vodenicharov

IFMASS 8, 2003, with Nenad Gubeljak, Vencislav Grabulov, Franjo Matejček, Ljubica Milović and Dražan Kozak

At home 2012

Annual assembly DIVK 2005

Family photo, 2013, wife Matilda, son Aleksandar (being firmly supported to look to the future), grandson Simon and granddaughter Tea

Hydro powerplant Bajina Bašta, 1977, Stojan (forth from left) with associates

International Fracture Mechanics Summer School IFMASS (first from the left sitting)

1 Bibliography-Editors' Choice

1.1 Textbooks, Practicums, Handbooks, Workbooks, Collections of Tables

Vojnovic, M., Dimitrijevic, M., Jurjevac, D., **Sedmak, S.**, Petrovski, B. and Zivanovic, S.: "Development of manufacturing of nickel—cadmium bateries with lamelar electrodes", Investment technical documentation for company Krusik-Valjevo, (in Serbian), IHTM, 1974.

Sedmak, S. et al.: "The study of HSLA steels weldments brittle fracture" (in Serbian), (in Serbian), RZN Srbije, 1976–1980.

Sedmak, S. i Petrovski, B.: "Investment study for the construction of the Gosa factory—Tekalemit", Beograd, 1978.

Sedmak, S., Petrovski, B. i ostali: "Determining of the influence of heat introduced by welding on the changes in the HAZ of a complex alloyed high strength steel", work report for 1979 and 1980, (in Serbian), OZN for region Kraljevo-Cacak.

Sedmak, S. et al.: "Weldability investigation of MKS Steels", (in Serbian) OZN Podunavskog regiona, 1980.

Sedmak, S., et al.: "The effect of welding parameters on thick plates welded joints quality", (in Serbian), OZN Podunavskog regiona, 1979–1982.

Sedmak, S., Petrovski, B. et al.: "Effect of welding parameters on the quality of welded joints of low-alloyed steels with great thickness", work report for 1979 and 1980, (in Serbian), OZN for Subdanubia region Smederevo.

Sedmak, S., Petrovski, B. and Milojevic, B.: "Practicum for the design of machine and device elements", Collection of tables part II, (in Serbian), TMF, 1980.

Sedmak, S., Petrovski, B. and Milojevic, B.: "Collection of machine and device element problems", (in Serbian), TMF, 1980.

Sedmak, S. i Petrovski, B.: "Study of welding technology parameters and heat affected zone properties of high strength steel welded joints", work report for 1982, (in Serbian), OZN for Kraljevo-Cacak region.

Sedmak, S., Petrovski, B. et al.: "Fracture mechanics of welded joints", work report for 1982, 1983 and 1984, (in Serbian), RZNS.

Brekic, M., **Sedmak, S**., Petrovski, B. et al.: "Investment programme for construction of production facilities for manufacturing metal semi-products for light sources", Metalac-Dolovo, notebooka I, II and III, (in Serbian), Beograd, 1982.

Sedmak, S. and Petrovski, B.: "Fracture mechanics of welded joints", Joint Yugoslavian—USA research project 1982-1989.

S. Sedmak, N. Grujić, A. Sedmak et al.: "Criteria for determining of possibility and justifiability of extending the worklife for ZEP thermoblocks", a study, Material testing institute of Republic of Serbia, (in Serbian), TMF, Beograd, 1992.

S. Sedmak, A. Sedmak et al.: "Quality assurance and reliable exploitation of welded joints in ZEP powerplant pipelines", Study performed on behalf of Elektroprivrede Srbije, 159 pages, (in Serbian), Beograd, 1993.

M. Zrilić, **S. Sedmak**, A. Sedmak, M. Vrhovac: "Local approach: ESIS round robin in experimental and numerical research—final report", (in Serbian), TMF, Belgrade, 1994.

1.2 Monographs: Professor Stojan Sedmak as the Editor

Introduction to Fracture Mechanics and Fracture-Safe Design, monograph from The First International Fracture Mechanics Summer School IFMASS 1, editor **S. Sedmak**, Institut GOŠA-TMF, Beograd, 1980, 566 pages, in Serbian.
Savremeni aspekti projektovanja i izrade sudova i cevovoda pod pritiskom, monograph from The Second International Fracture Mechanics Summer School IFMASS 2, editor **S. Sedmak**, Institut GOŠA-TMF, Beograd, 1982, 325 pages, in Serbian.
Fracture Mechanics of Welded Joints, monograph from The Third International Fracture Mechanics Summer School IFMASS 3, editor **S. Sedmak**, Institut GOŠA-TMF, Beograd, 1985, 441 pages, in Serbian.
Perspektive razvoja i primene mehanike loma, monograph from The Fourth International Fracture Mechanics Summer School IFMASS 4, editor **S. Sedmak**, Institut GOŠA-TMF, Beograd, 1987, 394 pages, in Serbian.
A. Sedmak, M. Stojaković: "Residual life prediction of steam turbine rotors", u monografiji "The application of fracture mechanics to life estimation of power plant components", Editor **S. Sedmak**, published by EMAS, Cradley Heath Warley, UK, 1990.
S. Sedmak, A. Sedmak: "An analysis of surface crack growth in full-scale pressure vessel test" u monografiji "22nd National Symposium on Fracture Mechanics", STP 1131, ASTM, Philadelphia.
The Application of Fracture Mechanics to Life Estimation of Power Plant Components, Proceedings of the Fifth International Fracture Mechanics Summer School IFMASS 5, editor **S. Sedmak**, EMAS, U.K. and TMF, Belgrade, 1990, 415 pages.
Eksploatacijske prsline u posudama pod pritiskom i rezervoarima, monograph from The Sixth International Fracture Mechanics Summer School IFMASS 6, editors **S. Sedmak** and A. Sedmak, TMF-ECPDUN-Institut GOŠA, Beograd, 1994, 351 pages, in Serbian.
S. Sedmak, A. Sedmak (urednici) Eksploatacijske Prsline u Posudama pod Pritiskom i Rezervoarima, predavanja Šeste međunarodne letnje škole mehanike loma, TMF, ECPD, GOŠA, 1994.
S. Sedmak, A. Sedmak (urednici) Eksperimentalne i Numeričke Metode Mehanike Loma u Oceni Integriteta Konstrukcija, predavanja Sedme međunarodne letnje škole mehanike loma, TMF, JSZ, GOŠA, 1997.

Eksperimentalne i numeričke metode mehanike loma u oceni integriteta konstrukcija, monograph from The Seventh International Fracture Mechanics Summer School IFMASS 7, editors **S. Sedmak** and A. Sedmak, TMF-JSZ-Institut GOŠA, Beograd, 2000, 352 pages, in Serbian.
From Fracture Mechanics to Structural Integrity Assessment, monograph from The Eigth International Fracture Mechanics Summer School IFMASS 8, editors **S. Sedmak** and Z. Radaković, DIVK-TMF, Beograd, 2004, 385 pages.
The Challenge of Materials and Weldments, monograph from The Ninth International Fracture Mechanics Summer School IFMASS 9, editors **S. Sedmak**, Z. Radaković and J. Lozanović, MF-DIVK-TMF- Institut GOŠA, Beograd, 2008, 300 pages.
Fundamentals of Fracture Mechanics and Structural Integrity Assessment Methods, monograph from The Tenth International Fracture Mechanics Summer School IFMASS 10, editor **S. Sedmak**, MF-DIVK-TMF- IMS, Beograd, 2009, 346 pages.

1.3 Monograph: Professor Stojan Sedmak as the Author

S. Sedmak: "Prikaz karakterističnih lomova sudova i cevovoda pod pritiskom u eksploataciji", u monografiji "Savremeni aspekti projektovanja i izrade sudova i cevovoda pod pritiskom", TMF—"Goša", Beograd, 1983.
S. Sedmak: "Ocena osobina zavarenih spojeva ispitivanjem epruveta sa prslinama", u monografiji "Mehanika loma zavarenih spojeva", TMF—"Goša", Beograd, 1985.
M. Wnuk, **S. Sedmak**: "Final stretch model of ductile fracture" u "Fracture mechanics", STP 743, ASTM, Philadelphia, 1981.
S. Sedmak: "Application and development of fracture mechanics in Yugoslavia" u "Progress in Fracture Mechanics", Pergamon Press, Oxford, 1983.
T. Adžiev, **S. Sedmak**: "Influence of residual stress on cracking in an excavator wheel" u "Residual Stresses in Science and Technology", DGM Informations–gesellshaft Verlag, Oberursel, 1987.
S. Sedmak, B. Petrovski: "The application of direct measurement of J integral on a pressure vessel with axial notch" u "Fracture Mechanics, 18th Symposium", STP 945, ASTM, Philadelphia, 1988.
B. Božić, **S. Sedmak**, B. Petrovski, A. Sedmak: "Crack growth resistance of weldment constituents in a real structure", u Bulletin T. Cl de l'Academie serbe des Science et des Arts, Classe de Science technique, No 25, Beograd, 1989.
T. Adžiev, **S. Sedmak**, B. Petrovski: "Residual stresses and their effect on J integral behaviour in full-scale pressure vessel test" u International Conference on Residual Stresses ICRS2, Elsevier Applied Science, London, 1989.
S. Sedmak: "On J integral and J_{Ic} material testing (with special reference to welded structures)" u "Nonlinear Fracture Mechanics", Ed. M. Wnuk, Springer Verlag, Vienna, 1990.

M. Vrhovac, **S. Sedmak**: "Life-assessment of U tubes in the "Krško" nuclear power plant steam generator" u monografiji "The application of fracture mechanics to life estimation of power plant components", EMAS, Cradley Heath Warley, UK, 1990.
T. Adžiev, **S. Sedmak**, B. Petrovski: "The effect of residual stresses on the residual strength of the welded pressure vessel with an axial notch" u "Defect assessment in components", ESIS-EGF9, MEP, UK, 1991.
S. Sedmak, T. Adžiev: "Residual stress effect on crack behaviour of welded panel samples", The Third International Conference on Residual Stresses, ICRS 3, 23–26. Juli 1991, Tokushima, Elsevier Applied Science, London.
S. Sedmak, A. Sedmak: "An analysis of surface crack growth in full-scale pressure vessel test" u "22nd National Symposium on Fracture Mechanics", STP 1131, ASTM, Philadelphia, 1992.
S. Sedmak, A. Sedmak, D. Ružić (editors) Reliability and Structural Integrity of Advanced Materials, ECF9 Proceedings, 1992, EMAS, UK.
S. Sedmak, A. Sedmak: "Ocena veka oštećenog materijala parne turbine" u monografiji "Turbomašine, grejanje i klimatizacija", (uredili B. Todorović, V. Grković), Mašinski fakultet, Beograd, 1992, str. 135.
Gerić K., Glavardanov I., **Sedmak S.:** J integral and Final Stretch zone for a Crack in HSLA of Undermatched and Overmatched Weldments, 1993, EMAS Publication, Engineering Materials Advisory Serviced LTD, 996–1005. (R22).
С. Седмак, А. Седмак, Б. Вељановски, З. Радаковић: Досадашња искуства у примени директног мерења J интеграла, Монографија радова са научног скупа САНУ априла 1995 "Механика, материјали и конструкције"–Књига LXXXIII, Одељење техничких наука–Књига 2, 1996, ст р. 179–184. ISBN 86-7025-232-5.
Sedmak A., **Sedmak S**., Milović Lj.: Pressure equipment integrity assessment by elastic-plastic fracture mechanics methods, monograph, DIVK, 1–294, 2011. ISBN 978-86-905595-1-0.
Sedmak, S., Sedmak, A., Crack significance and structural integrity problems at nano scale, in special edition on the occasion of Bernd Michel's 60th birthday, Fraunhofer IZM, Berlin, 2009.

1.4 Papers Published in the International Journals

Sedmak, S., Petrovski, B.: "Stress and strain distribution on HSLA steel welded pressure vessel", The Proceedings of International Meeting of Chemical Engineering ACHEMA 82, Frankfurt am Main, FR Germany, June 6–10, 1982. pp. 1–4.
Mitraković, D., Grabec I., **Sedmak, S**.: "Simulation of AE signal analysis systems", Ultrasonics, Sept. 1985, pp. 227–233.
Bozic, B., **Sedmak, S**., Petrovski, B., Sedmak, A.: "Crack Growth Resistance of Weldment Constituents in a Real Structure", Extrait du BULLETIN T. CI de

l'Academie Serbe des Sciences et des Arts, Classe des Sciences techniques, No 25, Beograd, 1989. (Reported at 9th Meeting, June 23, 1987.), pp. 21–42.
Sedmak, S., Petrovski, B.: "Application of Direct Measurement of J-Integral on a Pressure Vessel with Axial Notch", Fracture Mechanics: Eighteenth Symposium, ASTM STP 945, D.T. Read and R.P. Reed, Eds., American Society for Testing and Materials, Philadelphia, 1987, pp. 730–740.
Sedmak, **S**., Adžiev T., Petrovski, B., Sedmak, A.: "J integral as a measure of CDF in full scale pressure vessel test", ICF7, Houston, 1989, pp. 447–454.
Legat, J., **Sedmak S**., Petrovski, B.: "Influence of initial plastic deformation in weld metal on fatigue crack growth", Third International Conference on Biaxial/Multiaxial Fatigue, Stutgart, 1989.
Sedmak, A., **Sedmak**, **S**., Jokanović, Z.: "Numerical analysis of crack behaviour in the full-scale pressure vessel test", 5th IC on NMFM, Freiburg, 1990, pp. 611–618.
Sedmak, A., **Sedmak**, **S**., Vukomanović, N.: "Theoretical, numerical and experimental analysis of cracked tensile panels", ECF8, Torino, 1990, pp. 1596–1600.
Adžiev, T., **Sedmak**, **S**., Gočev, J.: "Comparison of J integral behaviour for the tensile panel and pressure vessel", ECF8, Torino, pp. 1592–1595.
Petrovski, B., Koçak, M., **Sedmak, S**.: "Fracture Behaviour of Undermatched Weld Joint with Short Surface Crack", GKSS-Forschungszentrum Internal Publication GKSS 91/E/93, Geesthacht 1991, pp. 101–107.
Gerić, K., **Sedmak, S**.: Automation in Fracture Mechanics Test for J integral Direct Evalution, 3rd International DAAAM Symposium, Budapest, 1992, pp. 59–60.
Sedmak, S., Petrovski, B., Sedmak, A., "Resistance to crack growth of different regions of weldments in a realstructure", International Journal of Pressure Vessels and Piping, Vol. 52 No.3, 1992, pp. 313–335.
Gerić, K., **Sedmak, S**., Glavardanov, I.: Fracture mechanics parameters of heat affected zone of high strength microalloyed steel, Metallurgy and new materials researches, Vol. II, No. 1–2, 1994, pp. 114–125.
Sedmak, S., Sedmak, A,. Gerić, K., Milosavljević, A., Radaković, Z.: An analysis of directly measured J integral on pressure vessels, EUROMAT 94, 1994, 1246–1250.
Gerić K., **Sedmak S**., Glavardanov I.: Fracture mechanics parameters of heat affected zone of high strength microalloyed steel, Metallurgy and new materials researches, Vol. II, No. 1–2, 1994, pp. 114–125.
Sedmak S., Gerić K.: Evaluation of crack significance in welded joint by fracture mechanics approach, Kovine, Zlitine Tehnologije 1–2, 32,1998, pp. 21–27.
Gerić K., **Sedmak S**.: Comparison of fracture mechanic parameters for different microstructures in heat-affected zone, Achievements and Perspectives Concerning Welding and Material Testing, Timisoara, Romania, 1995, 110–117.
Glavardanov I., **Sedmak S**., Gerić K., Fišl J.: Direct Measurement of J Integral of Thin Walled Presure Vessel, Material Study and Heat Treatments, Timisoara, 1995, 298–306.

Z. Burzić, S. Sedmak, S. Maksimović, N. Grahovac, J. Čurović, M. Zrilić, "Fracture toughness and fatigue crack propagation behaviour of Al–Li 8090 alloy", Physicochemical Mechanics of Materials, 1995, Vol 34, No. 1, p. 46–58.
Sedmak, A., **Sedmak, S**., "Critical crack assessment procedure for high pressure steam turbine rotors", Fatigue and Fracture of Engineering Materials and Structures, 1995, Vol. 18 (9), pp. 923–934.
Sedmak, S., Sedmak, A., "Experimental investigation into the operational safety of a welded penstock by a fracture mechanics approach", Fatigue and Fracture of Engineering Materials and Structures, 1995, Vol. 18 (5), pp. 527–538.
Sedmak, S., Petrovski, B., Sedmak, A.: "Crack significance evaluation with special reference to welded structures", Fracture Mechanics, Strength and Integrity of Materials, Jubilee Book Devoted to V.V. Panasyak (Ed. O.M. Romaniv), Shevchenko Scientific Society, Lviv, Ukraine, 205–216, 1996.
Sedmak, S., Petrovski, B., Sedmak, A., "Crack significance evaluation with special reference to welded structures", Materials Science, 1996, Vol. 32 (2), pp. 231–243.
Sedmak, S., Gerić, K., Sedmak, A.: Properties and microstructure of heat affected zone of microalloyed high strength steel, Jubilee conference 60 years of scientific co-operation in welding, Timisoara, 1997, 109–118.
Gerić, K., **Sedmak, S**.: Final stretch zone size evaluated by scanning electron microscopy as a fracture parameter, Fortschritte in der Metallographie, Sonderbande der Praktischen Metallographie, 1995, pp. 483–486.
Burzić, M., **Sedmak**, **S**., Burzić, Z., Jaković, D., Momčilović, D.: The Effect of Reinforcement Content on Impact Toughness of Cast Al-SiC p Metal Matrix Composite—Scientific-Technical Review, 1998.
Sedmak, S., Gerić, K: Properties and crack resistance of heat affected zone of microalloyed high strength steels, Pipeline welding 98, Istambul, 1998, 108–116.
Gerić, K., **Sedmak, S**. Sabo, B.: Fracture properties and microstructure in heat affected zone microalloyed steels, Halkidiki, 1998, p. 43.
Gerić, K., **Sedmak, S.:** Krta područja u zoni uticaja toplote zavarenog spoja, DEMI, 1999, Banja Luka, 2001, pp. 87–92.
M. Rakin, A. Sedmak, P. Matejić, M. Zrilić, **S. Sedmak**: Numerical simulation of ductile fracture initiation by application of Rice-Tracey void growth model. Proceeding of The 13th European Conference on Fracture, San Sebastian, Published on CD by Elsevier Science Ltd (2000).
Rakin, M., Cvijovic, Z., Sedmak, A., **Sedmak, S**., "Analysis of the transferability of micromechanical parameters of damage of steel under the conditions of ductile-fracture initiation", Materials Science, 2002, Vol. 38 (1), pp. 104–113.
Burzić, M., Burzić, Z., **Sedmak, S**., "Fracture Mechanics Standard Testing" From Fracture Mechanics to Structural Integrity Assessment, Eight International Fracture Mechanics Summer School (IFMASS 8), Belgrade 2004, pp. 95–123.
S. Sedmak, A. Sedmak, Integrity of Penstock of Hydroelectric Powerplant, Structural Integrity and Life, Vol. 5, No 2, 2005, pp. 59–70.

Rakin, M., Sedmak, A., Cvijović, Z., Zrilić, M., **Sedmak, S.:** *Micromechanical coupled study of crack growth initiation criterion in pressure vessel steel*. Strength of Materials, 2004, Vol. 36, pp. 33–38.
Zrilić, M., Rakin, M., Cvijović, Z., Sedmak, A., **Sedmak, S**.: *Structural integrity assessment by local approach to fracture*. Proceedings of 16th European Conference of Fracture ECF 16: Failure Analysis of Nano and Engineering Materials and Structures, Alexandroupolis, published on CD by Springer, 2006.
Maneski, T., Sedmak, A., Milović, Lj., Fertilio, A.**, Sedmak**, **S.:** Fitness-for-Purpose Assessment of Repaired Feedwater Heater, Structural Integrity and Life, Vol.6, No3, 2006, pp. 111–120.
Milović, Lj., Sedmak, A., **Sedmak, S**., Putić, S., Zrilić, M.: Numerical and Analytical Modelling of Elastic-plastic Fracture Mechanics Parameters. Materials Science Forum 2007, *555*, 565–571.
Sedmak, S., Sedmak, A., Arsić, M., Tuma, J. V.: An Experimental Verification of Numerical Models for the Fracture and Fatigue of Welded Structures. Materials in technology, 2007, *41*, 4, pp. 173–178.
Burzić, Z., Grabulov, V., **Sedmak, S**., Sedmak, A.: "Fatigue properties of a high-strength-steel welded joint", Materials and technology, 2007, Vol. 41, No 4, pp. 163–166.
Zrilic, M., Grabulov, V., Burzic, Z., Arsic, M., **Sedmak, S**., "Static and impact crack properties of a high-strength steel welded joint", International Journal of Pressure Vessels and piping, 2007, Vol. 84, No. 3, pp. 139–150.
Zrilich, M., Vuherer, T., Milovich, Lj., **Sedmak, S**.: New design of closed loop servo hydraulic device for thermal fatigue testing. International Scientific&Technical Journal Reliability and Life of Machines and Structures, 2009, *32*, 35–40.
Sedmak, S., Gerić, K., Burzić, Z., Grabulov, V., Jovičić, R.: Welded joints behavior in service with special reference to pressure equipment, Security and Reliability of Damaged Structures and Defective Materials, 2009, Springer Science, 231–253.
Grabulov, V., Romhanji, E., **Sedmak**, **S**., Odanović, Z.: "Loading rate effects on fracture strength of HSLA steel welded joints/Efectual vitezei de solicitare asupra rezistentei la rupere a imbinarilor sudate din otel HSLA", Welding & Material Testing/Sudarea si Incercarea Materialelor, 2009, Vol. 18, No. 1, pp. 29–36.
Sedmak, S., Grabulov, V., Momčilović, D.: "Chronology of lost structural integrity initiated from manualturing defects in welded structures", Structural Integrity and Life, 2009, Vol. 9, No 1, pp. 39–50.
Sedmak, S., Sedmak, A., "Fracture mechanics and non-destructive testing for structural integrity assessment", *Key Engineering Materials*, 2009, Vol. 399, pp. 27–36.
Sedmak, T., Bakic, R., **Sedmak, S**., Milović, Lj., Kirin, S.: The applicability of strategy for risk based maintenance to a penstock, Structural Integrity and Life, 2012, Vol. 12, No. 3, pp. 191–196.

1.5 International Conference Papers

Glavardanov, I., **Sedmak, S**., Petrovski, B.: "Determination of Crack Resistance Properties of HSLA Steel Welded Joint using J Integral", The Proceedings of 8th Congress on Material Testing, Budapest, Hungary, 28 September–1 October, 1982. II. Volume pp. 486–490.

Radović, A., **Sedmak**, **S**., Nedeljković, Lj.: "Comparative study of crack resistance properties of three differently alloyed HSLA steels", ICM4, Stokholm, Sweden, 1983, pp. 919–926.

Šijački, V., Sedmak, A., **Sedmak, S.:** "Experimental investigation of notch sensitivity of TM treated Al alloy", ICF6, New Delhi, 1984, pp. 1507–1513.

Sedmak, S., Petrovski, B.: "Direct Evaluation of the J-Integral on HSLA Steel Weldments" The Proceedings of Conference "Cracks in Welded Joints", Bratislava, CSSR, 1985., Vol. 1, pp. 243–249.

Sedmak, S., Petrovski, B.: "Experimental Analysis of Penstock Safety using Heat - Affected-Zone J-R Curves", The Proceedings of Third International Conference "Welding and Performance of Pipelines", London, November 18–21, 1986., pp. P28.1–P28.10.

Sedmak, S., Petrovski, B.: "The Experimental Analysis for Differently Matched Weld Metals", Proceedings of "The International Conference Joining of Metals" JOM-3, Helsinger, Denmark, December 19–22, 1986, pp. 309–313.

Sedmak, **S**., Petrovski, B., Drenić, D.: "Experimental analysis of J integral in full-scale pressure vessel test", ECF6, Amsterdam, 1986, pp. 999–1014.

Sedmak, S., Petrovski, B., Terzic, P., Ogarevic, V.: "Post Yield Crack Growth Analysis in Full-Scale Pressure Vessel Test", Proceedings of the Fifth International Conference "Mechanical Behaviour of Materials-V", Beijing, China, June 3–6, 1987, pp. 469–476.

Adziev, T., Petrovski, B., **Sedmak, S**.: "The Effect of Residual Stresses on J Integral Behaviour in Full-Scale Pressure Vessel Test", Proceedings of the 7th European Conference on Fracture, Editor E. Czoboly, Budapest, September 1988, pp. 362–364.

Adzijev, T., **Sedmak, S**., Petrovski, B.: "Residual Stresses and their Effect on J Integral in Full-Scale Pressure Vessel Test," Third International Conference on Residual Stresses, Nancy, France, November 1988.

Sedmak, S., Petrovski, B., Sedmak, A., Lukaćevic, Z.: "The Study of Crack Significance in Spherical Storage Tanks by J Resistance Curve", The Proceedings of Internatioal Conference on Weld Failures, London, November 21–24, 1988, pp. P18.1–P18.10.

Sedmak, S., Adziev, T., Petrovski, B., Sedmak, A.: "J Integral as Measure of Crack Driving Force in Full-Scale Pressure Vessel Test", Proceedings of the Seventh International Conference on Fracture ICF 7, Editors K. Salama, K. Ravi-Chandar, D.M.R.Taplin, P. Rama Rao, Houston, Texas, March 20–24, 1989, Volume 1, pp. 447–454.

Legat, J., **Sedmak, S**., Petrovski, B.: "Influence of Initial Plastic Deformation in Weld Metal on Fatigue Crack Growth", The Proceedings of Third International Conference on Biaxial/Multiaxial Fatigue, Stutgart, FR Germany, April 3–6, 1989., pp. 68.1–68.18.

Burzić, Z., Zrilić, M., **Sedmak, S**., Mitraković, D.: Application of acoustic emission for monitoring fracture mechanics in composite materials, III International Symposium an Acoustic Emission from Composite Materials AECM-3, Paris, 1989, pp. 422–431.

Petrovski, B., **Sedmak, S.:** "Evaluation of Crack Driving Force for HAZ of Mismatched Weldments Using Direct J Integral Measurements in Tensile Panels", Proceedings of the International Conference Welding-90, Technology, Material, Fracture, GKSS-Research Center Geesthacht, Geesthacht (Hamburg), Germany, October 22–24, 1990, pp. 341–352.

Petrovski, B., and **Sedmak, S**.: "Evaluation of Crack Driving Force for HAZ of Mismatched Weldments Using Direct J Integral Measurements in Tensile Panels", Proceedings of the DVM -Arbeitskreis "Bruchvorgänge" 23. Vortragsveranstaltung, February 26–27, 1991, Bundesanstalt für Materialforschung und -prüfung, Berlin, Germany, pp. 59–71.

Petrovski, B., Koçak, M., **Sedmak, S**.: "Fracture Behaviour of Undermatched Weld Joint with Short Surface Crack", Proceedings of the 10th International Conference on OMAE 91—Offshore Mechanics and Arctic Engineering, June 23–28, 1991, Stavanger Forum, Stavanger, Norway, Volume III—Part A, pp. 101–107.

Petrovski, B., Koçak, M., **Sedmak, S**.: "Fracture Behaviour of Undermatched Weld Joint with Short Surface Crack", Presented on the 21st plenary meeting of the European Structural Integrity Society (ESIS), Technical Committee I, Elasto-Plastic Fracture Mechanics, November 4and 5, 1991, GKSS—Geesthacht (Hamburg), Germany.

Petrovski, B., Koçak, M., **Sedmak, S**.: "Fracture Behaviour of Undermatched Weld Joint with Short Surface Crack", European Structural Integrity Society (ESIS), Technical Committee I, Elasto-Plastic Fracture Mechanics, The 21st Plenary Meeting of the ESIS-TCI, Geesthacht, Germany.

Sedmak, **S**., Adžiev, T., Sedmak, A.: "Crack behaviour of HAZ in small specimens, welded panels and pressure vessels", ICM 6, Kyoto, 1991, Vol. 4, pp. 99–104.

Radović, A., **Sedmak, S**., Grabulov, V.: The Evaluation of Brittle Fracture Behaviour of High Strenght Steels Veldments, Preprints of Ninth European Conference of Fracture, Bulgaria—Varna, 1992, Reliability and structural integrity of advanced materials, EMAS, U.K., pp. 926–932.

Sedmak, **S**., Sedmak, A., Zrilić, M., Glavardanov, I.: Direct measurement of J integral on a full-scale pressure vessel, VII International Congress on Experimental Mechanics, Las Vegas, USA, 1992, pp. 568–575.

Veljanovski, B., **Sedmak**, **S**., Radović, A., Pavlović, M.: "Resistance to fracture of AlZnMgCu high strength alloys", ECF9, Reliability and structural integrity of advanced materials, EMAS, Warley, West Midlands, U.K, 1992, Vol. I, p. 133.

Zrilić, M., **Sedmak**, **S**., Sedmak, A.: "Results and analysis of local criteria experiments in the scope of ESIS round robin", ECF9, Reliability and structural integrity of advanced materials, EMAS, Warley, West Midlands, U.K, 1992, Vol. I, p. 653.
Radović, A., **Sedmak**, **S**., Grabulov, V., Veljanovski, B.: "The evaluation of brittle fracture behaviour of high strength steels weldments", ECF9, Reliability and structural integrity of advanced materials, EMAS, Warley, West Midlands, U.K, 1992, Vol. II, p. 926.
Adžiev, T., Gočev, J., Cvetkovski, J., **Sedmak, S**.: "Fracture resistance of cracked welded joint", ECF9, Reliability and structural integrity of advanced materials, EMAS, Warley, West Midlands, U.K, 1992, Vol.II, p. 985.
Zrilić, M., **Sedmak, S**., Sedmak, A.: *Results and analysis of local criteria experiments in the scope of ESIS round robin*, 9th European Conference on Fracture, EMAS, Warley, West Middlands, 1992, pp. 653–657.
Gerić, K., Glavardanov, I., **Sedmak, S**.: "J integral and final stretch zone for a crack in HAZ of undermatched and overmatched weldments", ECF9, Reliability and structural integrity of advanced materials, EMAS, Warley, West Midlands, U.K, 1992, Vol. II, p. 996.
Aberšek, B., **Sedmak**, **S**., Flašker, J.: "Determination of remain life of short and long fatigue cracks on gears", ECF9, Reliability and structural integrity of advanced materials, EMAS, Warley, West Midlands, U.K, 1992, Vol. II, p. 1063.
Gerić, K., **Sedmak, S**., Glavardanov, I.: Measuring of crack growth in integral test, 4th International DAAAM Symposium, Brno, 1993, pp. 79–80.
Gerić, K., **Sedmak, S**.: Micromechanism of fracture in pre-cracked welded specimens, Eight International Conference on Fracture, ICF-8, Ukraine 93, 1993, Kiev, p. 552.
Grabulov, V., **Sedmak, S**.: The effect of cold cracks susceptibility on high strenght steel welding technology, Interantional Welding Conference, Timisoara, Romania, 1995., p. 16–17.
Gerić, K., **Sedmak, S.:** Analysis of heat affected zone properties of microalloyed steels, 11th European Conference on Fracture, ECF11, France, 1996, pp. 2235–2240.
Burzić, Z., **Sedmak**, **S**., Grahovac, N., Čurović, J., Stefanović, V.: "Fracture toughness and fatigue crack propagation behaviour of 8090 alloy", 8th International Conference on MTCM, 1997, Sofia, Bulgaria, pp. 190–198.
Zrilić, M., Rakin, M., Sedmak, A., **Sedmak, S**.: *Experience in fracture mechanics local approach application*, 6th International Scientific Conference on Achievements in the Mechanical Materials Engineering—AMME`97, Miskolc, 1997, pp. 71–75.
Zrilić, M., Rakin, M., Sedmak, A., **Sedmak, S**.: Measurement Techniques in Local Approach to Fracture, Proceedings of Fourth International Symposium on Measurement Technology and Inteligent Instruments, Miskolc, Hungary, 1998, pp. 358–361.
Gerić, K., **Sedmak, S**.: Crack behaviour analysis in the heat affected zone of microalloyed steels, 12th European Conference on Fracture, ECF12, Fracture from defects, Sheffild, 1998, pp. 2138–2143.

Zrilić, M., Rakin, M., Sedmak, A., **Sedmak, S**.: Measurement techniques in local approach to fracture. Proceedings of Fourth International Symposium on Measurement Technology and Intelligent Instruments, Miskolc, Hungary, 1998 pp. 358–361.

Grujić, B., **Sedmak**, **S**., Burzić, Z., Sedmak, A. "Crack growth resistance of creep damaged material", Facta Universitatis, 1999, Vol. 2, No. 9, pp. 895–901.

Zrilić, M., Rakin, M., Sedmak, A., **Sedmak, S**.: Assessment of in—service degradation of steam pipeline steel by local approach method", Resurs 2000. "Life assessment and management for sructural components", Kiev, Ukraine, 2000, pp. 247–253.

Rakin, M., Sedmak, A., Matejić, P., Zrilić, M., **Sedmak**, S.: Numerical simulation of ductile fracture initiation by application of Rice—Tracey void growth model, ECF 13, The 13th European Conference on Fracture, Fracture Mechanics: Applications and Challenges, San Sebastian, Spain, Published on CD by Elsevier, 2000.

Burzić, M., Burzić, Z., **Sedmak**, **S**., Zrilić, M., Jaković, D., Momčilović, D. "The effect of fiber orientation on impact toughness and fracture properties of carbon fiber-epoxy composite", International Charpy centenary conference, Pioters-France, 2001, pp. 621–628.

Burzić, Z., Burzić, M., Čurović, J., **Sedmak, S**., Jaković, D., Momčilović, D.: "The effect of reinforcement content on impact toughness of cast Al-SiCp metal matrix composites", International Charpy centenary conference, Pioters-France, 2001, pp. 629–636.

Rakin, M., Sedmak, A., **Sedmak**, **S**., Zrilić, M., Putić, S.: "Ductile fracture analysis of structural steel using micromechanical modelling", Proceeding of The 10th International Conference on Fracture, Honolulu, Published on CD by Elsevier Science Ltd., 2001.

Rakin, M., Sedmak, A., Matejić, P., Zrilić, M., **Sedmak**, **S**.: Numerical simulation of ductile fracture initiation by application of Rice-Tracey void growth model. Proceeding of The 13th European Conference on Fracture, San Sebastian, Published on CD by Elsevier Science Ltd, 2000.

Grabulov, V., Blačić, I., Mac Gilivray, H.J., **Sedmak, S**.: Dynamic J-R curve evaluation applying pre-cracked Charpy specimen, Proceedings, International Charpy centenary conference, Pioters-France, 2001, pp. 313–320.

Burzic, M., Burzic, Z., Čurovic, J., **Sedmak, S**., Jakovic, D., Momčilovic, D., "The effect of reinforcement content on impact toughness of cast Al-SiCp metal matrix composite", International Charpy centenary conference, Pioters-France, 2001, pp. 337–344.

Burzic, M., Burzic, Z., **Sedmak, S**., Zrilic, M., Jakovic, D., Momčilovic, D.: "The effect of fiber orientation on impact toughness and fracture properties of carbon fiber-epoxy composite", International Charpy centenary conference, Pioters-France, 2001, pp. 345–352.

Arsić, M., **Sedmak, S**., Aleksić, V.: Experimental and Numerical Analysis of Fatigue Strength of Welded Strukture. *International Conference Welded Joints Resistance*, Timisoara, Romania, 2002.

Rakin, M., Sedmak, A., Cvijović, Z., Zrilić, M., **Sedmak S.:** Micromechanical approach—transferability of ductile fracture parameters, Proceeding of The 14th European Conference on Fracture—Vol III, Krakow, 2002, pp. 27–34.
Arsić, M., **Sedmak, S**., Grabulov, V., Aleksić, V.: Experimental and numerical analysis of fatigue strength of welded structure, International conference Welded joints resistance, Timisoara-Romania, 2002, p.6.
Sedmak, S., Sedmak, A., Grabulov, V., Burzić, Z., Arsić, M.: Crack problem in welded joint for different types of loading. *International Conference Examination methods for welded structure components*, Timisoara, Romania, 2003.
Arsić, M., **Sedmak, S**., Aleksić, V.: Experimental and Numerical Evaluation of Cumulative Fatigue Damage of Welded Structure. *Proceedings of the Conference Fatigue Damage,* Seville, Spain, 2003, pp. 143–147.
Sedmak, S., Sedmak, A., Grabulov, V., Burzic, Z., Arsic, M.: "Crack problem in welded joint for different types of loading", ISIM International Conference Examination methods for welded structure components, Timosoara, Romania, 2003, pp. 27–42.
Hosin, M.M., **Sedmak**, **S**., Grabulov, V., Burzic Z., Sedmak, A.: "Fatigue of high strength steel weldment in pressure vessels application", International Conference Methods for welded structure components, Tripoly, Lybia, 2003, pp. 157–170.
Sedmak, S., Sedmak, A., Grabulov, V.: Strength, toughnees and structural integrity of storage tanks in urban environment" ASR International conference, Bucarest-2003, proceedings, pp. 59–72.
Sedmak, S., Sedmak, A., Grabulov, V., Arsić, M.: Crack problem in welded joint for different types of loading, International conference—Welded joint resistance, Timisuara 2003. pp. 7–8.
Mousbah, S.S., **Sedmak, S**., Grabulov, V.: Testing of fracture properties of welded joints by notched and precracked specimen, *International Conference- Modern welding ttechniques and its effects on industrial products quality improvement*, Book of abstracts, Tripoli, Libya, 2003. pp. 17–18.
Burzić, Z., **Sedmak**, **S**., Grabulov, V., Pašić, S., Sedmak, A.: "Application of fracture mechanics in integrity assessment of welded joint on microalloyed stell", Proceedings, International Conference "Welding in Maritime Engineering" Hvar, Croatia, 2004, pp. 463–472.
Burzic, Z., **Sedmak**, **S**., Sedmak, A., Grabulov, V.: "Characterisation of different crack parameters in high strength steel welded joint", IIW International Congress on Welding and Allied Processes, Vol. 1, A6, Cairo, Egypt.
Burzic, Z., Sedmak, S., Sedmak, A., Grabulov, V., Agroub, M.O.: "Structural integrity assessment of pressure vessels with defect in welded joints", IIW International Congress on Welding and Allied Processes, Vol. 2, B2, Cairo, Egypt.
Blačić, I., Vračarić, D., Zrilić, M., **Sedmak, S.:** Failure analzsis of blade of first rotor stage of jet engine Wiper 632/633 compressor, Second International Conference Problems of Dynamics and Strength in Gas-Turbine Construction, Kyiv, Ukraine, 2004, pp. 209–210.

Sedmak, A., Maneski, T., Milović, Lj., **Sedmak, S**.: Fitness-for-purpose assessment of repaired inlet water heater, International Conference WELDS 2005 «Design, Testing, Assessment and Safety of High Temperature Welded Structures», GKSS-Geesthacht, Hamburg, Germany, 2005.

Sedmak, **S**., Geric, K., Burzic, Z., Grabulov, V. Sedmak A.: "Static and dynamic fracture mechanics parameters of material in the heat-affected-zone", 11th International Conference on Fracture, Turin, Italy, 2005.

Sedmak, S., Gerić, K., Grabulov, V., Burzić Z., Sedmak A.: Static and dynamic fracture mechanics parameters of material in the heat-affected-zone, ICF 11, Torino, Italija, 2005.

Sedmak, A., **Sedmak, S**., Gerić, K., Milović, Lj.: "Evaluation of Crack Resistance of the Heat-Affected-Zone Applying J Integral", Sect. 2: Structural Integrity. *The First South-East European Welding Congress «Welding and Joining Technologies for a Sustainable Development and Environment»*, Timisoara, Romania, 2006.

Milović, Lj., **Sedmak, S**.: Structural Integrity at Elevated Temperatures- Residual Service Life Evaluation. *16th European Conference of Fracture*, Alexandroupolis, Greece, 2006. Published on CD.

Milović, Lj., Sedmak, A., **Sedmak, S**., Putić, S., Zrilić, M.: "Numerical and analytical modelling of elastic-plastic fracture mechanics parameters", «*Research Trends in Contemporary Materials Science*», book of abstracts of the eight YUCOMAT 2006., p. 115.

Zrilić, M., Rakin, M., Cvijović, Z., Sedmak, A., **Sedmak**, **S**.: *Structural integrity assessment by local approach to fracture*, 16th European Conference of Fracture, Alexandroupolis, Greece, 2006. Published on CD.

Gerić, K, **Sedmak, S.:** Crack initiation and growth in HAZ of microalloyed steel Proceeding of the 16th European Conference of fracture, Alexandroupolis, Greece, 2006, p 1053.

Grabulov, V., Blačić, I., Radović, A., **Sedmak, S.:** "Loading rate effect on HSLA steel welded joints fracture resistance", Proceedings, 16th European Conference of Fracture—ECF 16,, Alexsandroupolis, Greece, 2006, pp. 234–241.

Radović, N., Radaković, Z., Đurović, A., **Sedmak**, **S**., Jandrlić, A., Zrilić, M., Prokić-Cvetković, R., Milović, Lj., Rakin, M., Engh, E.: Welders passport-program structure and application. Proceedings of the 1st South-East European Welding Congress "Welding and joining technologies for a sustainable development and environment", Timisoara, 2006, pp. 260–263.

Jovičić, R., Sedmak, A., **Sedmak**, **S**., Grabulov, V.: "An analysis of the influence of weldment heterogenity on ferrite—austenite welded structure", 5th Int. Conf. Structural integrity of Welded Structures, Timisoara 2007, Romania, pp. 180–191.

Milović, Lj., Zrilić, M., **Sedmak, S**., Sedmak, A., Burzić, M.: Experimental Determination of J-integral at Elevated Temperatures. *Proceedings of the 17th European Conference of Fracture*, Brno, Czech Republic, 2008.

Sedmak, S., Grabulov, V., Momčilović, D., Sedmak, A., Milović, Lj, Burzić, Z., Büyükyildirim, G.: Behavior of cracks existing in welded joints in different failure modes. *The 6th International Conference Structural integrity of welded structures*, Timişoara, Romania, 2008.

Sedmak, S., Grabulov V., Momčilović, D.: "Chronology of lost structural integrity initiated from manufacturing defect in welded structures", Proceedings, Eight Meeting" New Trend in Fatigue and Fracture" (NT2F8), Ankaran, Slovenia, 2008.

Popović, O., Prokić-Cvetković, R.M., Sedmak, A., Jovičić, R., **Sedmak**, **S**., Grabulov, V.: "Investigation of crack resistance parameters in rail surface welded layer" International Symposium "Surface engineering", organized in the frame of Excellency Research Project (CEEX) no. 266/2006–2008, ISIM, Timisoara, 2008.

Milović, Lj., **Sedmak, S**., Zrilić, M., Vuherer, T., Momčilović, D., Trišović, N., Putić, S.: "Toughness of region IV of the Heat Affected Zone of 9 % Chromium Steel for Elevated Temperature Application". *Book of the selected papers of 4th International Conference Fracture Mechanics of Materials and Structural Integrity*, Lviv, Ukraine, 2009, pp. 637–642.

Milović, Lj., **Sedmak, S**.: "Mechanical properties and J-integral characterization for type IV region of HAZ simulated specimens", *Tenth International Conference New Trends in Fatigue and Fracture «Materials and structures design against fatigue and fracture»*, Metz, France, 2010.

Milović, Lj., Vuherer, T., **Sedmak, S**., Sedmak, A., Zrilić, M., Manjgo, M., Janković M., Dondur, N.: "Some aspects of operating life assessment of pressurized components in power plants". *6. Međunarodno znanstveno-stručno savjetovanje SB 2011 "Suvremene tehnologije i postupci pri izradi tlačne opreme, zavarenih metalnih konstrukcija i proizvoda"*, Slavonski Brod, Croatia, 2011, pp. 115–130.

Milović, Lj., Bulatović, S., Radaković, Z., Aleksić, V., **Sedmak, S**.: "Assessment of the behaviour of fatigue loaded hsla welded steel joint by applying fracture mechanics parameters. *Twelfth International Conference New Trends in Fatigue and Fracture NT2F12*, 2012, Brasov, Romania.

Sedmak, T., **Sedmak, S**., Milović, Lj.: "The applicability of strategy for risk based maintenance to a penstock", *Twelfth International Conference New Trends in Fatigue and Fracture NT2F12*, 2012, Brasov, Romania.

Sedmak, T., **Sedmak**, **S**., Stamenkovic; A.: The applicability of risk- based maintenance and inspection to a penstock; SIE 2012, Belgrade, pp. 297–301.

Sedmak, S.A., Tatić, U., Mahdi, A., Sedmak, A., Petrovski, B., **Sedmak, S**.: "Mismatching Behaviour Of Hsla Steel Weldments In The Full-Scale Pressure Vessel Testing", International Conference of Technologies Technologies and Exhibition (ICWET'14), 2014, Manisa, Turkey.

Sedmak, S.A., Tatić, U., Jovičić, R., Sedmak, A., Milošević, M., Bakić, R., **Sedmak**, **S**.,: "Numerical modeling of austenite-ferrite weldment tensile test", 20th European Conference on Fracture (ECF 20), Trondheim, Norway, 2014.

Materials as the Simplest Self-Organised Systems, and the Consequences of This

L. Tóth

Abstract The mechanical testing of a material is a simple procedure that records the response of a specimen to an external effect. The recorded result reflects some kind of damage process that takes place in the material for given external conditions. This damage process can be considered to be the response of a self-organised system. If a single damage process takes place during the testing (or one process predominates), then the simplest testing evaluation procedure would be based on a power law relationship with two parameters, i.e. the response of the material is proportional to the external effect. This approach raises two questions. Why does a single (unknown) damage process require two parameters to characterise it? If the same external conditions are applied for a group of materials and the responses of those materials (the damage process) are also the same, is there a correlation of the power relationship parameters between the materials in the group? These questions will be discussed in this paper.

Keywords Mechanical testing · Fatigue crack propagation resistance · LCF properties · Testing versus material response · Self-organised system

1 Introduction

Two basic questions underpin the consideration of the mechanical testing of materials: how to define "materials", and how to explain the testing and evaluating procedures. It is difficult to find an exact definition for "materials". Entering the expression "definition of materials" into the Google search engine returns over 600 million results. Reading the definitions provided by the first 20 web addresses listed is not enlightening, bringing to mind Enrico Fermi's comment: "Before listening to your presentation I was confused about this topic; after finishing it I am still

L. Tóth (✉)
Bay Zoltán Nonprofit Ltd. for Applied Research, Engineering Division, Iglói Str. 2, Miskolc 3519, Hungary
e-mail: laszlo.toth@bayzoltan.hu

G. Pluvinage and L. Milovic (eds.), *Fracture at all Scales*,
Lecture Notes in Mechanical Engineering, DOI 10.1007/978-3-319-32634-4_3

confused, but on a higher level!" Unfortunately, there appears to be no universal definition of materials that can be accepted as a model. Yet the natural sciences are based on models, i.e. ways of thinking that provide a description of natural processes. Understanding the working of these natural processes depends on having a defined model and then applying mathematical procedures to this. It therefore follows that the first step for understanding the mechanical testing of materials should be a "generalised model", or the definition of materials; however, as yet this is missing, or it is not exact.

2 How Can a Generalised Model of Materials Be Defined?

Defining materials in a general way is difficult and complex. The definition needs to summarise concisely all the substantial features of materials used for their characterisation, including behaviours, properties, structures, etc. A possible preliminary suggestion (for further discussion) is shown in Fig. 1.

As a general case, a "material", represented by its mass (or energy), can be defined as a region of space with an elementary volume V_e and an elementary surface S_e, with at least one parameter differentiating the region within the material from the space outside it. This model can be regarded as the "elementary cell of materials" (analogous to an elementary lattice cell). **Bulk materials**, representing a set of **bulk properties** in volume **V**, can be built up from these elementary cells, with **internal** and **external borders**. Regarding to the internal surfaces (borders) they could be the grain- or sub grain borders the twin-interfaces or the borders of different phases. The surface **S** of the bulk material, which represents the material's **surface properties**, is formed from the sum of the external sections of the material cell surfaces. In this model, the **bulk material behaviour** can be influenced by the elementary bulk properties, the elementary internal surface behaviours, the properties of the phases and their volume ratios, etc. In this approach, SIZE and

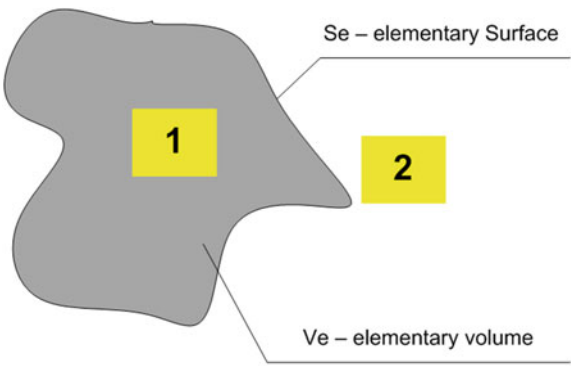

Fig. 1 A possible elementary model of a "material"

GEOMETRIC effects are included directly because both of these can be considered to be factors that influence the LOCAL modification of the GLOBAL EXTERNAL conditions (loading or loading rate, temperature, environmental conditions, etc.).

3 The Role of the Ratio of Surface and Bulk Behaviours in Size Effects

The relative weights of the bulk and surface behaviours of an elementary cell are constants. But for a real structural element the relative weights of these behaviours depend on the size of the structures. This can easily be illustrated with a sphere of material that has a radius R, a volume V with bulk behaviour properties B_p and a surface S with surface properties S_p. The ratio of surface properties to bulk behaviour is then as follows:

$$S_p/B_p = Surface/Volume = 4R^2\pi/(4R^3\pi/3) = C/R \quad (1)$$

where C is a constant. From this, it directly follows that when a material's geometry or volume is

- Larger, then bulk behaviour dominates,
- Smaller, then the surface properties dominate.

This last conclusion underpins the importance of nanotechnology or the "operating circumstances" of nature, because of many of the processes take place through the surfaces.

4 Mechanical Testing of Materials

Engineering structures are designed on the basis of loading, external operating conditions, and certain material properties. These material properties can change during a long period of operation; this is an ageing process which needs to be monitored. Mechanical testing, such as for monitoring an ageing process, is performed in a material during specific operating conditions (e.g., for a pipeline, Fig. 2). In principle there are two possibilities: monitoring the ageing process directly on the structures, or testing the properties of sample specimens.

If using specimens for testing, these need to be taken from the operating structure, prepared, and used to measure the properties that are most important for the safety of the structure. A basic problem with this approach is TRANSFERABILITY: how well do the properties measured in the specimen represent the actual properties of the real engineering component? This question requires consideration of the SIZE EFFECT and/or the GEOMETRICAL PROBLEM.

Fig. 2 Ageing monitoring is necessary for engineering structures and components, such as this pipeline

A pure, straightforward *size effect* could be the dominant problem in, for example, a fracture process of a statistical nature (such as high cycle fatigue or creep) or during procedures for testing small specimens. The GEOMETRICAL PROBLEM may be dominant in the determination of crack growth resistance properties. This problem follows directly from the stress and strain distributions in the vicinity of cracks in different types and sizes of specimens, whereas there is always a state of plane strain in the middle plane of the specimens and a state of plane stress on the free surface of the specimen. This problem is considered in depth in the theories of various kinds of fracture mechanics [1–10].

Whether or not there is a size effect or geometrical problem, use of a sample specimen allows completely free determination of the external testing conditions. These are the following:

- The loading condition with all its parameters, i.e. uniaxial, biaxial, complex, load history, loading rate of each components,
- Temperature (or time dependence of temperature field),
- Environmental conditions (or time dependence of environmental conditions).

During the mechanical testing, the MATERIAL (specimen) is subjected to these freely selected external conditions (in Fig. 1 indicated with a simple expression of "LOADING" and the RESPONSE(s) measured). These responses are the material's behaviours and properties. The RESPONSES are always answers (reactions) of the given (tested) material. Because non-living materials are the simplest self-organised systems, their responses to a given set of external conditions have only a statistical nature.

The RESPONSE(s) can be evaluated at different levels. The simplest way is to consider the response of the system to be proportional (linear or non-linear) to the external condition. In this case the simplest relationship is a power law with two parameters, i.e.

$$\mathbf{y} = \mathbf{C}\mathbf{x}^{\mathbf{n}} = \mathbf{B}(\mathbf{x}/\mathbf{x_0})^{\mathbf{n}} \tag{2}$$

where **y** is the parameter describing the material's RESPONSE, **x** is the LOADING (EXTERNAL) parameter, and **C** and **n**—or, in the x_0 normalised form, **B** and **n**—are the **independent material characteristics**. In such an evaluation procedure, the physical nature and parameters of any DAMAGE process or processes are not taken into consideration.

The response of the MATERIAL to a given external condition can also be evaluated at the microscopic level. In this case, the description of the damage process includes not only the MATERIAL parameters but also the external LOADING parameters (Fig. 3).

An obvious example of this is the process of thermoactivated damage, which can be described by the following relationship:

$$t_t = t_0 \cdot \exp \cdot [U(\sigma)/kT] \tag{3}$$

where $\mathbf{t_t}$ is the time the given damage process takes effect (residual time), $\mathbf{U(\sigma)}$ is the activation energy, which deepens on the external loading conditions, **T** is temperature, **k** is the Boltzman constant, and $\mathbf{t_0}$ is a constant that is independent of the temperature, the material and other circumstances ($t_0 = 10^{-12}$–10^{-13} s). Equation (3) contains the parameters of the selected external LOADING conditions, i.e. U(σ) and T. From this relationship it directly follows that the thermoactivated damage processes in different materials differ only in the function U(σ). This means that a given thermoactivated damage process (or residual life time) in different materials differs only in a single U(σ) parameter. From this, the following question and consequences arise:

- If the damage process is the same in different materials for the same external LOADING conditions, why does Eq. (2) need to be characterised by two parameters (**C** and **n**)?
- If the microstructure or damage process changes (for instance, for different type of cast iron, or for aluminium alloys with different microstructures), then the possible relationship between **C** and **n** in the equation has to change.
- If the external LOADING conditions are the same and only the testing temperature changes, the lifetime is then proportional to ln (1/T).

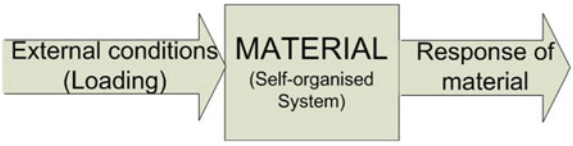

Fig. 3 Mechanical testing as the RESPONSE of a self-organised system to the freely selected external conditions

Regarding Eq. (2), much discussion can be found in the literature about the obvious correlation between the material parameters **C** and **n** in the form of $\mathbf{\ln C = B + n \ln x}$, where **C** and **B** are the independent material constants. This argument is based on the following. Each power law relationship based on Eq. (2) can be expressed in the following form: $\mathbf{\ln y = \ln C + n \ln x}$, or in the normalised form, $\mathbf{\ln y} = \ln B + n(\ln x - \ln x_0) = \mathbf{\ln B + n \ln x - n \ln x_0}$.

From this it follows that $\mathbf{\ln C = \ln B - n \ln x_0}$, and thus that C and B are independent constants if $x_0 \equiv 1$.

5 Correlation of Fatigue Crack Growth Resistance Parameters in the Paris Region

Around 40 years ago, in the mid-1970s, correlations between the two parameters of the Paris–Erdogan law [$da/dN = C(\Delta K)^n$] were published for the first time. The authors of the first papers were Gurney, Kobayashi, Kanazawa and their co-workers. They found correlations between the two parameters in the following forms:

GURNEY	$C = 1.31510^{-4}/895^n$	$1.8 < n < 4.0$
KOBAYASHI	$C = 2.72010^{-4}/1129^n$	$3.0 < n < 6.5$
KANAZAWA	$C = 2.4810^{-5}/577.8^n$	$2.0 < n < 5.5$

where ΔK is in units of $N/mm^{3/2}$ and da/dN in units of mm/cycle (Fig. 4).

These correlations initiated a systematic data collection for different materials. The results are summarized in Table 1.

Many other expressions for describing the connections between the two parameters of the Paris region can be found in the literature, but these do not differ significantly from each other [14, 17–21].

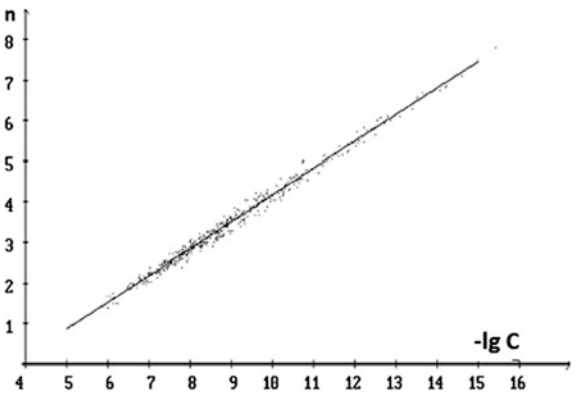

Fig. 4 Correlation between the parameters n and lg C in the Paris region of STEELS. There were 352 data points; ΔK is in units of $MPam^{0.5}$ and da/dN in units of mm/cycle

Table 1 Correlations between the parameters **n** and **lg C** in the Paris regions of different materials

Material	Number of data points	C (mm/cycle)	X_0 ($MPam^{0.5}$)	Correlation coefficient (%)	Range of validity
Steels	352	1.03×10^{-4}	27.20	98.9	$1.05 < n < 11.00$
Al alloys **non-tempered**	47	5.15×10^{-4}	5.09	96.5	$2.00 < n < 5.69$
Al alloys **tempered**	23	4.58×10^{-5}	39.79	99.7	$1.87 < n < 14.43$
Ti alloys	43	2.25×10^{-4}	17.72	98.3	$2.04 < n < 8.25$
Cast iron	45	4.62×10^{-5}	18.14	98.8	$3.00 < n < 8.25$

From the above, it can be concluded that the crack growth resistance of material in the Paris region depends only a single factor, i.e. the damage process in the second, in the stationary fatigue crack growth range consists of only one parameter, but this depends on the type of material. This is manifested exactly in the case of aluminium alloys with different microstructures, i.e. tempered and non-tempered.

6 Correlation of the Manson–Coffin Parameters in the Low Cycle Fatigue Range

The relationship between plastic strain amplitude and lifetime is commonly described by the power law proposed by Manson in 1954. One of the most generally used versions is the following:

$$N_f = C\varepsilon_{ap}^{n} \tag{4}$$

where $\boldsymbol{\varepsilon_{ap}}$ is a measure of the plastic strain amplitude (i.e. the component of the external effect that is directly connected with the damage process taking place in the material), $\mathbf{N_f}$ is the lifetime (i.e. the "response" of the material, the number of cycles to failure), and **C** and **n** are material constants.

It is obvious that the damage processes would be different in completely different types of materials, but they are quite similar within a given material at different temperatures. The parameters of Eq. (4) for different materials have been collected from the handbooks and evaluated [22–25]. The results are summarised in Table 2. From the evaluation of almost 300 data items in the table, it can be seen that

- Unambiguous correlations exist between **ln C** and **n** from Eq. (4)
- The correlations always depend on the type of steel (unalloyed, low alloyed or high alloyed) and also the temperature
- The coefficients of the correlations are over 90 % (except for a single case out of the 10)

Table 2 Correlations between the parameters n and ln C [from Eq. (4)] for different materials and temperatures

Material	Temperature (°C)	Number of data items	Correlation equation	Cc (%)	Range of validity
Unalloyed steels	23	69	ln C = 6.600n + 10.00	96.8	−3.70 < n < −1.33
	350	14	ln C = 7.067n + 9.615	96.0	−2.33 < n < −1.21
	500	6	ln C = 5.491n + 7.535	93.9	−1.59 < n < −1.22
Low alloyed steel	23	36	ln C = 5.609n + 7.813	86.0	−2.44 < n < −1.33
	400	10	ln C = 5.458n + 7.042	94.9	−2.27 < n < −1.33
	600	12	ln C = 4.934n + 5.988	90.8	−1.54 < n < −1.15
High alloyed steel	23	45	ln C = 6.541n + 10.204	73.0	−4.00 < n < −1.54
	600	35	ln C = 5.976n + 8.000	90.6	−4.00 < n < −1.43
	700	23	ln C = 5.733n + 7.407	91.8	−2.56 < n < −1.54
	800	6	ln C = 5.000n + 5.848	88.9	−2.22 < n < −1.39
Ti and Al alloys	23	40	ln C = 6.479n + 7.042	91.2	−3.13 < n < −1.00

Cc correlation coefficient

- As the temperature increases, the correlation coefficient for the **n** values decreases.

From the evaluated data series it can also be concluded that the low cycle fatigue (LCF) resistances of materials characterised by Manson–Coffin laws depend only on a single parameter, but that these correlations depend on the types of material and the temperature. Considering that the Manson–Coffin relationship provides an empirically good description of the stationary range of low cycle fatigue, it can be concluded that the damage process that takes place in this region is determined by a single material characteristic. This is the same as for fatigue crack propagation, as described earlier. In both of these cases the damage process (**d**) took place over its whole range, i.e. $0 < d < 1$.

7 Correlation of the Wöhler Line (Basquin Relationship) Parameters in the Lifetime Fatigue Rang

For high cycle loading conditions in the lifetime range, the following relationship, proposed by Basquin in 1910, is widely used:

$$N_f = C(\Delta\sigma)^n \tag{5}$$

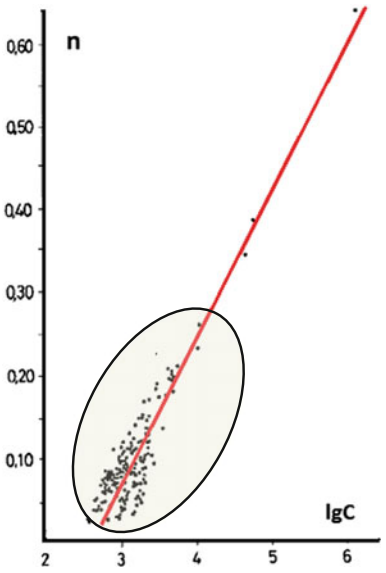

Fig. 5 Correlation between the parameters **n** and **lg C** in the Basquin relationship for **STEELS lg C = 2.61–5.71 n**

In this relationship, used for more than a century, the external effect is characterised by the value of the stress amplitude (if the asymmetry factor is given and is constant) and the response of the material by parameters **C** and **n**. Using data from handbooks and catalogues [20, 26], **C** and **n** values have been calculated for Wöhler lines for more than 100 types of steel and approximately 50 titanium alloys. These results are summarised in Figs. 5 and 6.

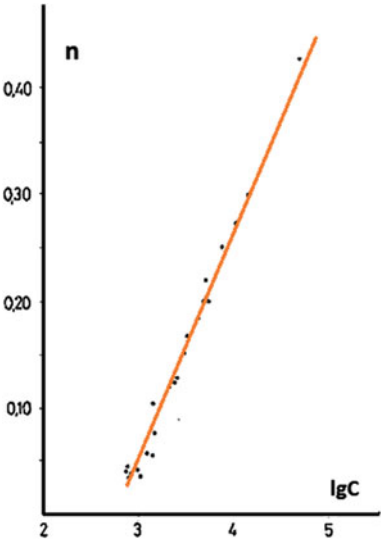

Fig. 6 Correlation between the parameters **n** and **lg C** in the Basquin relationship for **titanium alloys lg C = 2.70–4.4 n**

Comparing these two graphs, the following conclusions can be drawn:

- Clear correlations can be seen for both types of metals but the expressions are slightly different, even though the values of the constant are almost the same (**2.61** for steels and **2.70** for titanium alloys)
- The scatter band of the parameters calculated from the Wöhler lines for steels is much greater for the steels in the lowest part of the slope, i.e. for $0.05 < n < 0.20$.

As with fatigue crack growth and LCF data evolution described earlier, here again the damage process (**d**) in each analysed case took place over its whole range, i.e. $0 < d \leq 1$.

8 Correlation of Material Parameters in Power Law Relationships Used to Describe Creep Processes

The following empirical relationships are widely used to characterise material behaviour at a given temperature in conditions where there is creep:

$$\dot{\varepsilon} = C_1 \sigma^n \tag{6}$$

$$t_f = C_2 \sigma^m \tag{7}$$

$$\dot{\varepsilon} = C_3 (t_f)^i \tag{8}$$

where **σ** is the loading stress, i.e. the **external condition**, and the **response of the material** can be characterised by the time to fracture (lifetime) $\mathbf{t_f}$, the stationary

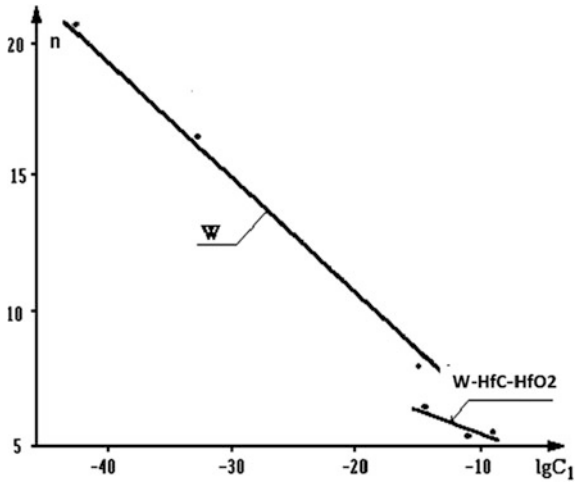

Fig. 7 Correlation between the material parameters **lg C_1** and **n** [from Eq. (6)] for **tungsten** and **tungsten alloys** at 1500 and 2000 °C ($T_{melting}$ = 3422 °C)

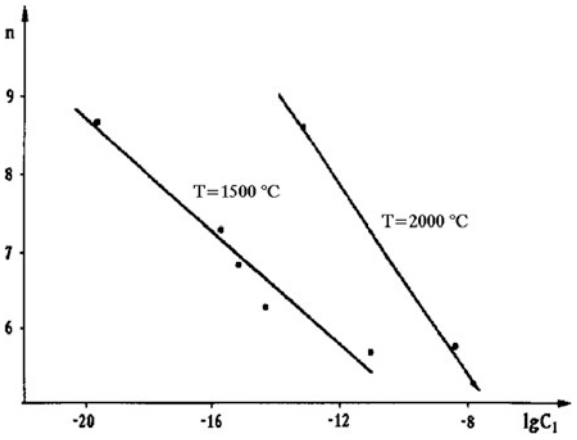

Fig. 8 Correlation between material parameters **lg C_1** and **n** [from Eq. (6)] for **molybdenum alloys** at 1500 and 2000 °C ($T_{melting}$ = 2623 °C)

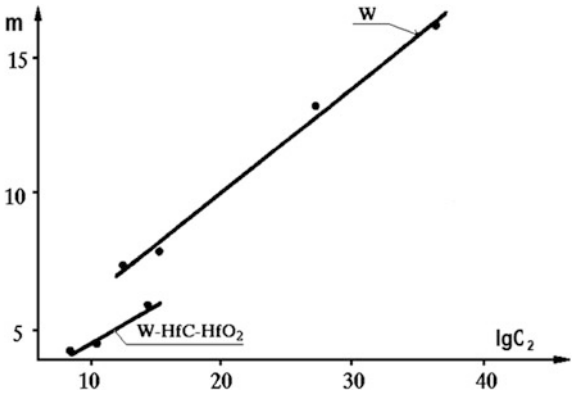

Fig. 9 Correlation between the material parameters **lg C_2** and **m** [from Eq. (7)] for **tungsten** and **tungsten alloys** at 1500 and 2000 °C ($T_{melting}$ = 3422 °C)

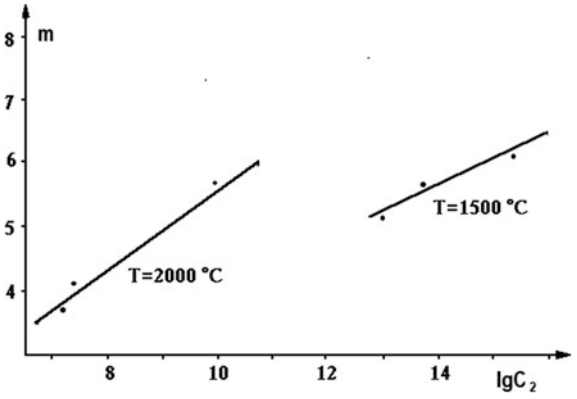

Fig. 10 Correlation between the material parameters **lg C_2** and **m** [from Eq. (7)] for **molybdenum alloys** at 1500 and 2000 °C ($T_{melting}$ = 2623 °C)

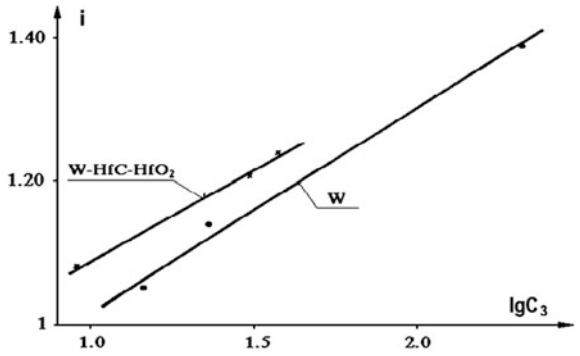

Fig. 11 Correlation between the material parameters **lg C_3** and **i** [from Eq. (8)] for **tungsten** and **tungsten alloys** at 1500 and 2000 °C ($T_{melting}$ = 3422 °C)

creep rate $\dot{\varepsilon}$, and two parameters of the material, i.e. $\mathbf{C_1}$ and **n**, or $\mathbf{C_2}$ and **m**, or $\mathbf{C_3}$ and **i**, from Eqs. (6), (7) or (8), respectively. All the material parameters are functions of the external conditions, i.e. the temperature and environment (Fig. 7, 8, 9, 10).

The situation is the same if the correlation of the material properties is evaluated in relationship (7). The results for tungsten and tungsten alloys at 1500 and 2000 °C can be seen in Fig. 11; the damage processes in the given material are the same at both temperatures. For molybdenum alloys at the same temperatures, there is a correlation between the two material characteristics from Eq. (8).

For creep in materials where the damage process (d) extends over the entire range, i.e. to $0 < d \leq 1$ (as was the case for fatigue crack propagation, LCF and the lifetime range of the Wöhler line), there exist clear correlations between the two parameters in the widely used power law relationships.

Unfortunately, similar data has not been collected for steels and steel groups used in and around power stations. This could be carried out using the material data sheets that have been collected in many countries and by many organisations, such as the European Creep Collaborative Committee formed in 1991.

The possible thermomechanical background of the correlations has also been analysed for creep [27–31] and for low cycle fatigue behaviours [34].

9 Power Law Relationships in the Evaluation of Other Mechanical Testing Results

Power law relationships are widely used in the evaluation of other mechanical testing procedures. One well-known relationship used in hardness testing is Meyer's law, which expresses the relationship between indentation depths (as the RESPONSE of materials) and load values (as the EXTERNAL conditions). The most important difference from the cases considered earlier is that during hardness testing some kind of damage process takes place (as the RESPONSE of materials)

but this does not extend to the unit, to d = 1. The following two series of hardness testing have been performed for more than 20 selected materials:

Brinell testing with 2.5 mm diameter ball and different load levels
Vickers harness testing with various loads.

The material characteristics have been determined in the following relationships:

$$F = ad^n \tag{9}$$

$$F = a_1 d_1^m \tag{10}$$

where the RESPONSE of materials is characterised by the diameters of the indentations **d** in the Brinell testing, and by the diagonals of the indentations $\mathbf{d_1}$ in the Vickers testing. The material parameters in these two power law relationships are **a** and **n** or $\mathbf{a_1}$ and **m**, respectively (Figs. 12, 13).

The results of tensile testing performed on smooth and notched specimens can be used to characterise the "notch sensitivity" sensitivity of materials in quasistatic loading conditions. The absorbed energy until fracture can be measured for both smooth (W_0) and notched specimens (W_m) as the area under true stress ($\boldsymbol{\sigma'}$) true strain ($\boldsymbol{\varphi}$) diagrams. True stress is defined as the ratio of the actual load to the actual cross-sectional area, and the true strain for cylindrical specimens is $\boldsymbol{\varphi = 2\ \ln\ (d_0/d)}$, where $\mathbf{d_0}$ is the initial diameter and **d** is the actual measured diameter at the given load. The notch of the specimen is characterised by the stress concentration factor K_t, i.e. by the ratio of the notch tip stress to the nominal stress. The value of K_t characterises the external geometrical effect (i.e. localisation of the damage process) on material behaviour. In this case, the notch sensitivity of materials can be characterised by measuring the reduction in the absorbed energy until fracture caused by a notch for any value of K_t. This can be expressed in the following form:

$$W_m = W_0 K_t^{-b} \tag{11}$$

where $\mathbf{W_0}$ is the absorbed specific energy measured for a smooth specimen, $\mathbf{W_m}$ is measured on a notched specimen with stress concentration factor $\mathbf{K_t}$, and **b** is the notch sensitivity factor expressed as the tendency of the fracture energy to decrease with the stress concentration factor. The material RESPONSE has been determined experimentally for 11 different materials, as summarised in Fig. 14.

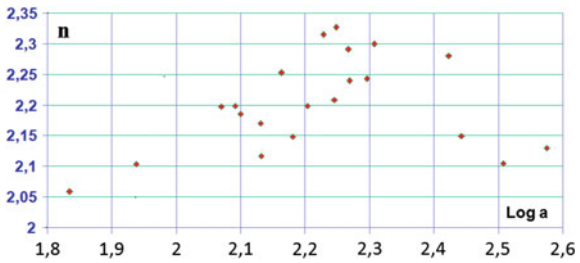

Fig. 12 Correlation between the material parameters **a** and **n** [from Eq. (9)] when measuring the Brinell hardness of more than 20 types of steel. (*Ball* diameter D = 2.5 mm)

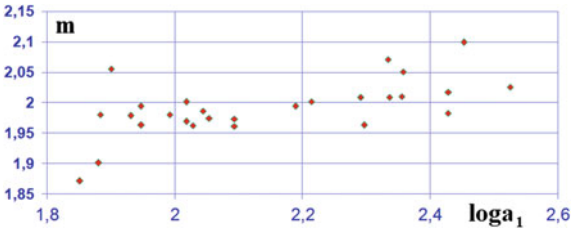

Fig. 13 Correlation between the material parameters $\mathbf{a_1}$ and **m** [from Eq. (10)] when measuring the Vickers hardness of more than 20 types of steel

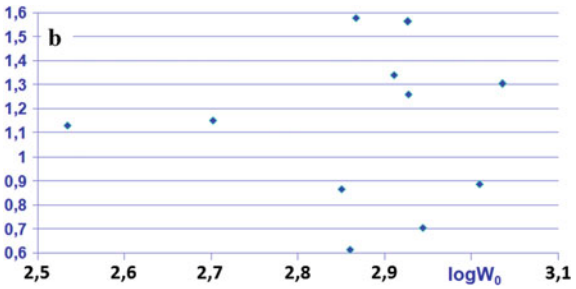

Fig. 14 Correlation between the material parameters $\mathbf{W_0}$ and **b** [from Eq. (11)] when measuring the Vickers hardness of more than 20 different types of steel

It can clearly be seen from this that there is no relationship between the parameters for the steels investigated.

As no correlation was found either in the material parameters of Meyer's law used in hardness testing, nor in the characterisation of the notch sensitivity of materials, the following conclusion can be drawn. In the absence of correlations between the two material parameters are expressed not the bulk behaviour (as the response of a material—the result of a damage process), but the relocalisation of the damage process, as the geometrical effect on the bulk behaviour.

10 Summary

The following points summarise the topics and detailed results discussed in this paper:

1. A generalised definition for materials with bulk and surface properties has been proposed.
2. The size and geometry effects in specimens used for the determination of mechanical (bulk) properties were distinguished.
3. It was suggested that the bulk properties of materials can be explained as the response of a self-organised system.
4. In practice, power law relationships with two material parameters are widely used to describe a self-organised system, i.e. the relationship between the external effect and the response.

5. Close correlations have been found between such material parameters for groups of materials if the external conditions are the same and the types of damage processes (taking place at the given external loading conditions from zero-to-unit) are similar. These have been demonstrated for fatigue crack growth, for Wöhler lines and for creep conditions.
6. No correlation was found between the two material characteristics for other power law relationships used to describe the **relocalisation of the damage process** (such as Meyer's law in hardness testing, or the notch sensitivity of the materials).
7. The possible physical backgrounds for the observed correlations between the empirical material constants for LCF and creep circumstances have been analysed in the publications cited in this paper.

Acknowledgments The paper is dedicated to the memory of Prof. Stojan Sedmak, a perfect mechanical engineer who performed reliability assessment of engineering components and structures under different operating conditions. From the various items discussed in this paper it directly follows that a reliability assessment of structures operating under the circumstances can be performed through only a single empirical material property. Given the statistical nature of the material parameters, the reliability of lifetime estimates can be directly evaluated from the distribution functions of the single material parameters.

References

1. Pluvinage G, Dhiab A (2002) Notch sensitivity analysis on fracture toughness. Transferability of fracture mechanical characteristics. Ed Y Dlouhy 78:303–320
2. Akourri O, Elayachi I, Pluvinage G (2007) Stress triaxiality as fracture toughness transferability parameter for notched specimens. Int Rev Mech Eng 1(6)
3. Akourri O, Elayachi I, Pluvinage G (2007) Stress triaxiality as fracture toughness transferability for notched specimens. Model Optim Mach Build Field 4
4. Hadj Meliani M, Azari Z, Pluvinage G, Capelle J (2010) Gouge assessment for pipes and associated transferability problem. Eng Fail Anal 17(5):1117–1126
5. Pluvinage G, Capelle J, Hadj Méliani M (2014) A review of fracture toughness transferability with constraint and stress gradient. Fatigue Fract Eng Mater Struct 37(11):1165–1185
6. Elazzizi A, Hadj Meliani M, Khelil A, Pluvinage G, Matvienko YG (2015) The master failure curve of pipe steels and crack paths in connection with hydrogen embrittlement. Int J Hydrog Energy 40(5):2295–2302
7. Hadj Meliani M, Azari Z, Al-Qadhi M, Merah N, Pluvinage G (2015) A two-parameter approach to assessing notch fracture behaviour in clay/epoxy nanocomposites. Compos B Eng 80:126–133
8. Pluvinage G, Ben Amara M, Capelle J, Azari Z (2014) Role of constraint on ductile brittle transition temperature of pipe steel X65. Proc Mater Sci 3:1560–1565
9. Pluvinage G, Ben Amara M, Capelle J, Azari Z (2014) Role of constraint on the shift of brittle–ductile transition temperature of subsize Charpy specimens. J Fatigue Fract Eng Mater Struct 37(12):1291–1385
10. Coseru A, Capelle J, Pluvinage G (2014) On the use of Charpy transition temperature as reference temperature for the choice of a pipe steel. Eng Failure Anal 37:110–119

11. Romvári P, Tóth L, Nagy G (1980) Adalékok a fáradt repedésterjedési sebességét leíró összefüggésekhez. Gép 9(32):325–333 (in Hungarian)
12. Romvári P, Tóth L, Nagy G (1980) Analiz zakonomernoszti raszprosztranenija usztalosztnüh trescsin v metallah. Problemü Procsnoszti 12:18–28 (in Russian)
13. Iost A, Cavallini M, Tóth L (1998) Relations entre les coefficients m et C de l'équation de Paris en fatigue-fissuration. La Revue de Métallurgie-CIT/Science et Génie des Matériaux. Février, pp 229–242
14. Blumenauer H, Pusch G (1993) Tecnische Bruchmechanik. Deutsche Verlag für Grundstoffindustrie, Leipzig
15. Tóth L, Lukács J (1997) Reproducibility of the fatigue crack growth resistance of materials and its consequences. In: Romaniv OM, Yarema S, Shevchenko Y (eds) Fracture mechanics, strength and integrity of materials (Jubilee Book Devoted to V.V. Panasyuk). Scientific Society, Ukraine, pp 143–147
16. Romvári P, Tóth L. (1981) K voproszu povrezsdaemoszti pri raszprosztranenii usztalosztnüh trescsin. Mehanicseszkaja usztaloszt' metallov, Kiev. Naukova Dumka, pp 64–65, 142–143, 214–215 **(in Russian)**
17. Brecht K, Pusch G, Liesenberg O (2002) Bruchmechanische Kennwerte von Temperguβ. Teil 1: Schwarzer Temeperguβ. Konstruiren and Gieβen 27(2)
18. Hübner PV, Pusch G, Liesenberg O (2002) Bruchmechanische Kennwerte von Temperguβ. Teil 2: Weiβer Temeperguβ. Konstruiren and Gieβen. 28(3)
19. Tóth L. (1992) On relationships having two parameters used to evaluate the fatigue test results. In: Proceedings of the XIth international colloquium on mechanical fatigue of metals. Kiev, vol 1, pp 91–98
20. Troshenko VT, Szosznovszkij LA (1987) Szoprotivleni usztaloszti metallaov is szplavov. Csaszt.1. Handbbok
21. Romvári P, Tóth L, Dehne G, Blumenauer H, Kempe M (1988) Bruchmechanische Untersuchungen zum Erdmüdungsverhalten von Einsatz-stählen. Wissenschaftliche Zeitschrift der Technischen Universität "Otto von Guericke". Magdeburg Heft 4(32):59–64
22. Boller C, Seger T (eds) (1987) Materials data for cyclic loading. Materials science monographs, 42A, Unalloyed steels. Elsevier Science Publishers B.V., Amsterdam
23. Boller C, Seger T (eds) (1987) Materials data for cyclic loading. Materials science monographs, 42B, Low-alloy steels. Elsevier Science Publishers B.V., Amsterdam
24. Boller C, Seger T (eds) (1987) Materials data for cyclic loading. Materials science monographs, 42C, high-alloy steels. Elsevier Science Publishers B.V, Amsterdam
25. Boller C, Seger T (eds) (1987) Materials data for cyclic loading. Materials science monographs, 42D, aluminium and titanium alloys. Elsevier Science Publishers B.V., Amsterdam
26. Troshenko VT, Szosznovszkij LA (1987) Szoprotivleni usztaloszti metallaov is szplavov. Csaszt.2. Handbbok
27. Tóth L, Krasowsky AJ (1993) A kér parameter korrelációjának Fizikai tartalma az anyagvizsgálati eredmények feldolgozásakor használt kétparaméteres összefüggásekben. Kohászati Lapok 126(10–11):359–363 (in Hungarian)
28. Krasowsky AJ, Tóth L (1993) Physical background of the empirical relationships of the material strength and fracture properties on time. In: International conference on fracture, ICF 8, Kiev, 1993. június 8–13. Part I, pp 36
29. Krasowsky AJ, Tóth L (1994) Fiticheskaja priroda empiricheszkij zaviszimoszti kharakterisztik prochnoszti I razrushenija materialov ot vremeni. Problemü Prochnosti 6: 3–9 (in Russian)
30. Tóth L, Krasowsky AJ (1994) Material testing results in mechanical engineering and their physical background. In: Proceedings of the IIIrd international scientific conference

"Achievements in the mechanical and material engineering", Gliwice, 1994, pp 371–381. Poland, May 17–21, 1995. "Extended Abstract" volume, pp 469–472
31. Tóth L, Krasowsky AJ (1995) Fracture as the result of self-organised damage process. In: Proceedings of the 14th international scientific conference advanced materials and technologies, Gliwice-Zakopane
32. Krasowsky AJ, Tóth L (1996) Termodinamicheskaja priroda stepennykh ehmpirichjeskikh zavisimostej kharakteristik prochnosti I razrushenija materialov ot vremeni. Soobschenie 1. Polzuchest I dlitelnaja prochnost. Problemy Prochnosti 2:5–24
33. Krasowsky AJ, Tóth L (1997) A thermodynamic analysis of the empirical power relationships for creep rate and rupture time. Metall Mater Trans A 28:1831–1843
34. Krasowsky AJ, Tóth L (1997) Material characterisation required for the reliability assessment of the cyclically loaded engineering structure. Part 1. In Fatigue and failure of materials. NATO ASI series, vol 39. Kluwer Academic Publishers, pp 165–223

The CTOA as a Parameter of Resistance to Crack Extension in Pipes Under Internal Pressure

M. Ben Amara, Guy Pluvinage, J. Capelle and Z. Azari

Abstract Different methods of CTOA measurements are described: Optical microscopy coupled with digital image correlation, analytical analysis of experimental load-displacement curves or simulation by Finite Element method. Using a Modified Compact Tension (MCT) specimen at room temperature, tests are performed to measure the value of the CTOA of API 5L X65 pipe steel. The influence of thickness on CTOA has been studied and explained through a "triaxial stress constraint". Crack extension is modelled by the finite element method using the CTOA criterion coupled with the node release technique. Crack velocity, arrest pressure and crack extension at arrest have been determined. Values of the CTOA are not intrinsic to materials. Like other measures of fracture toughness, it is sensitive to geometry and loading mode. This sensitivity can be described by a constraint parameter. For the thickness effect, the constraint parameter T_z is very appropriate.

Keywords CTOA · Pipe · Steel · Crack extension · Crack arrest

1 Introduction

In fracture mechanics, the resistance crack to crack extension is generally expressed by the experimental crack growth resistance curve (i.e. the R-Curve). The crack driving force is expressed in terms of the stress intensity factor (SIF), J integral (J) or crack-tip opening displacement (CTOD) interconnected parameters based on the crack extension da. The crack-tip opening angle (CTOA), defined as the angle between two element sides representing the crack tip, is one of the latest ways to describe fracture resistance to crack extension.

M. Ben Amara · J. Capelle · Z. Azari
LaBPS—ENIM, 1 route d'Ars Laquenexy, CS 65820, 57078 Metz, France

G. Pluvinage (✉)
FM.C, 57530 Silly Sur-Nied, France
e-mail: pluvinage@cegetel.net

G. Pluvinage and L. Milovic (eds.), *Fracture at all Scales*,
Lecture Notes in Mechanical Engineering, DOI 10.1007/978-3-319-32634-4_4

Conditions of stable crack growth require that the rate of change of the crack driving force with increasing crack length Δa be smaller than the increase of crack growth resistance expressed in terms of crack opening displacement δ:

$$\frac{d\delta}{da} \leq \frac{d\delta_R}{da} \tag{1}$$

It can be seen on the R curve $\delta_R = f(a)$ that the left term in (1) is precisely the CTOA that is constant in the linear part of the R curve (Fig. 1).

$$\frac{d\delta_R}{da} = CTOA \tag{2}$$

The concept of Crack Tip Opening Angle (CTOA) was probably introduced by Andersson [2] to simulate stable crack growth by the Finite Element method (FEM). In this method, crack growth is obtained by successive relaxation of the nodal forces at the node representing the crack tip. The ψ angle as CTOA between two element sides representing the crack tip is chosen as the criterion for the crack extension. However, crack-growth dependence of this angle was expected, and a constant value was used for all of the stages of growth. The value at the first increment of crack growth is called ψ_0. Anderson assumed that after large crack growth, steady state conditions prevail and ψ stabilises to the ψ_c value with $\psi_c < \psi_0$. ψ_c is called the critical crack tip opening angle ($CTOA_c$).

Several authors [5, 23, 29, 35, 36] using two dimensional analyses, showed that CTOA at initiation is always larger than the value at stable crack growth (Fig. 2).

Since the 1990s, the use of this criterion has been extended to numerical simulations by FEM of the crack extension.

Nowadays, $CTOA_c$ is used to predict crack length and pressure at arrest of a ductile running crack and particularly in gas pipes [13].

Gas pipeline fracture initiation is usually followed by extended running crack propagation. This occurs when driving force energy, caused by internal pipe pressure, overcomes the crack propagation resistance. Such disasters lead to significant financial loss, and should be avoided as much as possible or confined to a

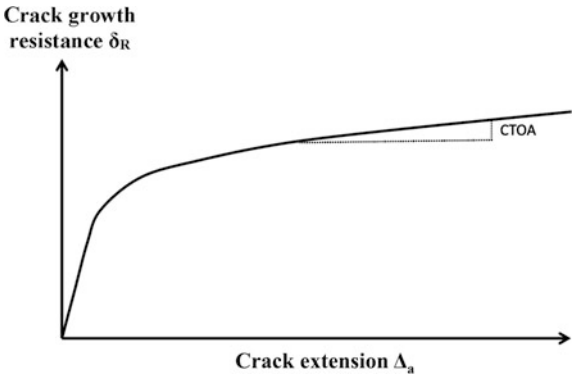

Fig. 1 Definition of CTOA on R curve $\delta_R = f(a)$

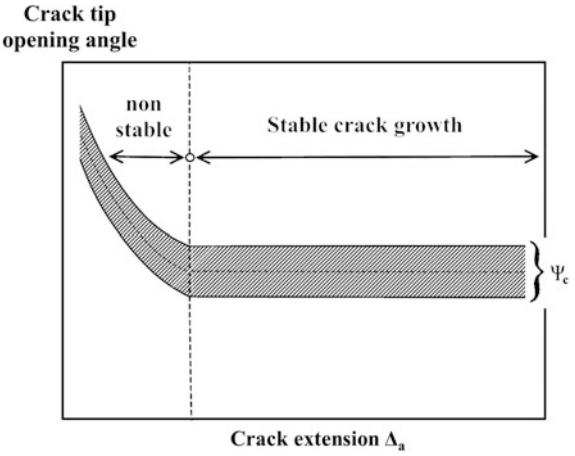

Fig. 2 Evolution of CTOA during crack extension

short portion of the pipe. Therefore, an important question is whether and when the fracture will self-arrest.

Conditions for crack propagation or arrest are given by a coupled fluid-structure problem. Depressurisation due to crack opening will cause fluid egress from the pipe. This induces a depressurisation wave propagating in the opposite direction to the tips of the opening crack. Crack propagation speed is controlled by pressure distribution of the opening pipe. If the decompression wave is faster than the propagating crack fracture, the pressure at the crack tip will decrease, and the crack arrests.

In terms of a limit state design, the arrest pressure can be predicted by solving Eq. (3) between the fracture resistance and component stress, which depend on the pipeline dimensions, internal pressure and material strength. This material resistance is balanced with a component stressing that is determined involving specific pipe dimensions, pressure p and material strength. In terms of a limit state design, the arrest pressure can be predicted by solving the equation between the stress state at crack tip:

$$\langle \sigma_{ij}(p) \rangle = \langle \sigma_{ij,c}(p_{ar}) \rangle \tag{3}$$

where p_{ar} is the pressure at arrest. Condition of arrest can be transformed by the new following condition:

$$\mathrm{CTOA(p)} = \mathrm{CTOA_c(p_{ar})} \tag{4}$$

where CTOA is the crack tip opening angle induced by the current pressure and $\mathrm{CTOA_c}$ the fracture resistance.

In the standard codes for gas transmission pipelines, the toughness requirement for crack arrest is based on models that express the fracture resistance and driving force in terms of the fracture and gas decompression wave velocities. This approach

involves the superposition of two curves: the gas decompression wave speed and the ductile fracture propagation speed characteristic, each as a function of the local gas pressure. For this reason, it is called Two Curves Method (TCM).

In the present work, the crack arrest criterion, given by Eqs. (4, 5), is extended to the two-curves method through an FEM simulation model in conjunction with the node release technique. This method is used for the prediction of crack velocity, pressure at arrest and crack length after arrest by numerical simulation on pipe steel API 5L X65. A comparison has been made with the TCM codes for crack arrest [33, 34].

2 Experimental Determination of CTOA on API 5L X65 Pipe Steel

2.1 Definition

The CTOA is defined as the angle between the crack faces of a growing crack. A practical realisation of this definition is not possible because the crack faces are not straight but curved with a curvature that depends on the specimen and loading type. A definition based on crack tip opening displacement δ at a distance d of the order of 1 mm is consistent for both experimental and numerical determination (Fig. 3).

$$\Psi = \operatorname{arctg}\left(\frac{\delta}{2d}\right) \tag{5}$$

In order to overcome the zigzag pattern of real crack faces or the influence of mesh size, it is more convenient to determine CTOAs at several distinct complementary positions on the upper and lower crack surfaces, ψ_i, and to average over these values afterwards (Fig. 4). The points used to determine the ψ_i values should be chosen in the range of 0.5–1.5 mm behind the crack tip.

$$\Psi = \frac{1}{N_i}\sum_{1}^{N_i}\Psi_i \tag{6}$$

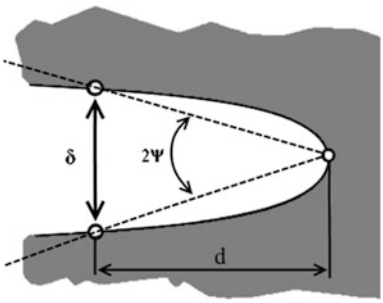

Fig. 3 Definition of CTOA on the curved crack profile

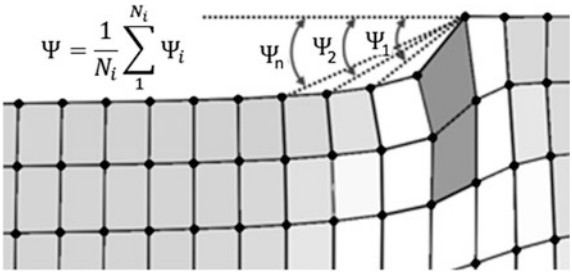

Fig. 4 Definition of CTOA according to the meshing crack

2.2 Choice of Specimen to Determine CTOA

Different specimen types can be used for experimental determination of CTOA. Specimens loaded by bending are generally chosen because the specimens are smaller and need less material and less testing capacity. The choice of aspecimen loaded by bending leads to the risk of crack bifurcation, which is not compatible with a CTOA measurement over a large crack extension.

Cotterel [8] pointed out the role of T stress in crack bifurcation. The T stress is a stress that acts parallel to the crack direction. Therefore, this stress combined with the opening stress induces a mixed mode of loading with a biaxiality ratio Θ:

$$\Theta = \frac{T\sqrt{\pi \cdot a}}{K_I} \tag{7}$$

The maximum stress along the $\sigma_{\theta\theta}$ distribution is not always null for $\theta = 0$ and angular deviation can occur only for positive values of T stress. When the T stress is negative, the maximum $\sigma_{\theta\theta}$ is always along the direction of propagation $\theta = 0$.

If T stress is positive, the crack curves according to the criterion of maximum tangential stress introduced by Erdogan and Sih [14]. By applying this criterion, the opening stress is given by:

$$\sigma_{\theta\theta} = \frac{K_I}{\sqrt{2\pi r}}\left[\frac{3}{4}\cos\frac{\theta}{2} + \frac{1}{4}\cos\frac{3\theta}{2}\right] + T\sin^2(\theta) \tag{8}$$

$$\frac{\sqrt{2\pi r}\cdot\sigma_{\theta\theta}}{K_I} = \left[\frac{3}{4}\cos\frac{\theta}{2} + \frac{1}{4}\cos\frac{3\theta}{2}\right] + \frac{T\sqrt{2\pi r}}{K_I}\sin^2(\theta) \tag{9}$$

The evolution of the ratio $\frac{\sqrt{2\pi r}\cdot\sigma_{\theta\theta}}{K_I}$ with the direction of propagation θ is plotted in Fig. 5 for positive or negative values of T. The maximum opening stress is indicated by a black spot only for positive T stress. For negative T stress, this maximum occurs for negative values of opening stress and bifurcation cannot occur because the crack surfaces cannot overlap [6]. The bifurcation angle θ^* is given when the

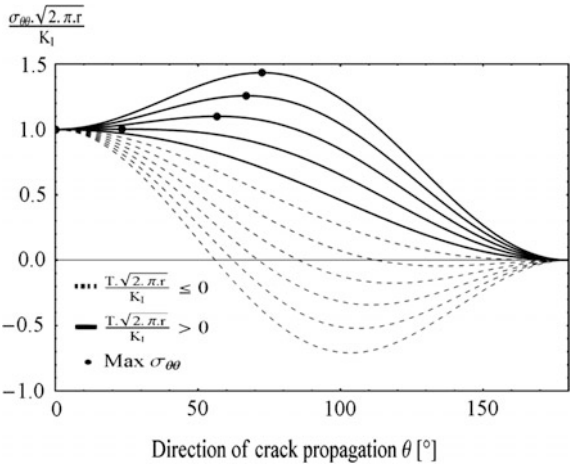

Fig. 5 Evolution of the ratio $\frac{\sqrt{2\pi r}\cdot\sigma_{\theta\theta}}{K_I}$ with crack propagation direction θ in the presence of T stress

first derivative of Eq. (10) is equal to zero and the second derivative must be negative.

$$\theta^* = \cos^{-1}\left[\frac{1+\sqrt{1+\frac{1024\pi}{9}\cdot X_{ef}\cdot\left(\frac{T_c}{K_{Ic}}\right)^2}}{\frac{512\,\pi}{9}\cdot X_{ef}\cdot\left(\frac{T_c}{K_{Ic}}\right)^2}\right] \tag{10}$$

Introducing a local fracture criterion in this analysis for which at fracture $K_I = K_c$, $T = T_c$ and $\sigma_{\theta\theta} = \sigma_c$ for $x = X_{ef}$ allows us to compute the bifurcation angle θ^*. X_{ef} is the size of the fracture process volume or effective distance. The condition on the second derivative implies that for crack curving:

$$\frac{T_c}{K_c} > \frac{3}{8}\frac{1}{\sqrt{2\pi X_{ef}}} \tag{11}$$

We now compare the potentiality of crack curving of two specimens: the first is a classical compact tension (CT) specimen with 10 mm thickness; the second a modified CT specimen (MCT) with the same thickness.

The geometry of the MCT specimen is given in Fig. 6 and is similar to the geometry of the specimen used by Darcis et al. [10]. T stress has been computed by FEM versus non dimensional crack size a/W assuming a linear behaviour. Results are reported in Fig. 7.

For negative T stress, after initiation, the crack propagates first in an unstable manner and secondly, after several millimetres, in a stable manner.

During crack propagation in a stable manner, the crack tip opening angle CTOA remains constant and its constant value is considered a characteristic of the fracture resistance of the material to crack extension. It can be noted that during the stable

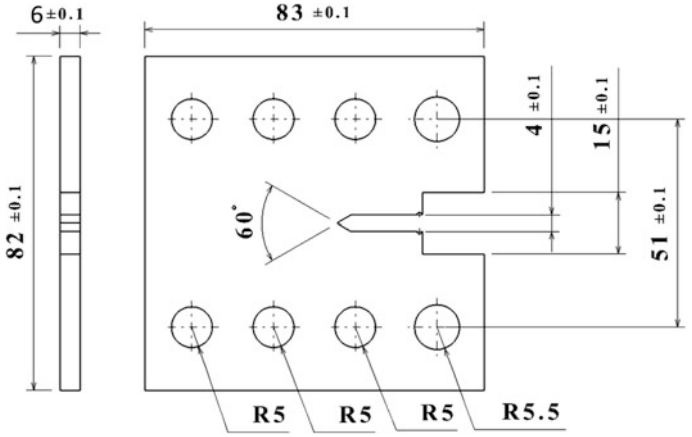

Fig. 6 Geometry and design dimensions of modified CT (MCT) specimen

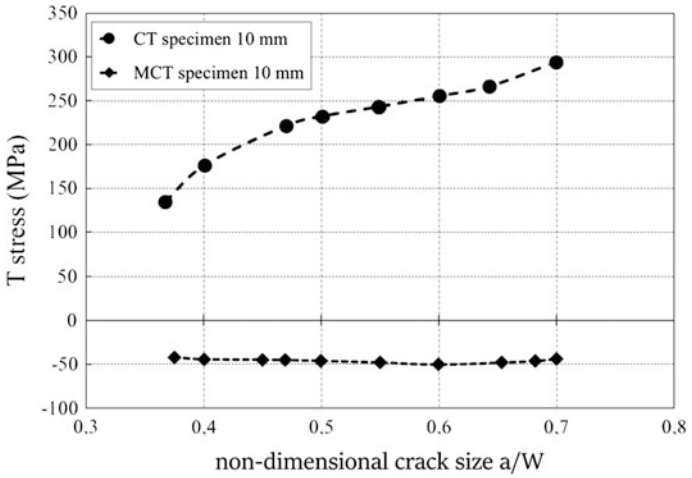

Fig. 7 Evolution of T stress with non-dimensional crack size for a CT and an MCT specimen

crack propagation both CTOA and T stress are constant [33, 34]. T stress is negative for the MCT specimen and practically constant with an average value $T_{CT} = -45$ MPa. For the CT specimen, T stress increases with a/W ratio and its value for a/W = 0.5 is $T_{MCT} = 220$ MPa. The positive value of T stress explains the crack bifurcation that can be seen on Fig. 8. Therefore the MCT specimen with a negative T stress is more appropriate to determine CTOA.

Fig. 8 Crack bifurcation in CT specimen with positive with positive T-stress-induced crack curving T/K = +2.05

2.3 Different Methods of Measurements of CTOA

Various methods are used for experimental determination of the CTOA. They can be divided into two categories: direct and indirect methods. Direct methods comprise micro-topography [24], optical microscopy coupled with image correlation method [11, 20]. Indirect methods are based on the analysis of the load displacement diagram, either numerically [4] or analytically [40, 41].

2.3.1 Direct Methods

In micro-topography [24] the fracture surfaces are topographically analysed *post-mortem.* This method is based on the assumption that the CTOA is preserved in the plastic deformations of the fracture surface. After both surfaces have been scanned, they are recombined in the computer. The reconstructed crack contours at fracture allow the determination of the CTOA. This method is of interest because it allows the CTOA to be identified in positions of different thicknesses, but it is time consuming.

Optical microscopy is one of the most common methods of measuring CTOA [28]. The crack contour close to the crack tip is investigated at the polished surface using a light microscope. A special case of optical measurement is the digital image correlation (DIC) method. For our measurements, a commercial DIC camera (Gom FASTCAM SA.1 Photron) and a software analysis package with integrated length and angle measurement tools (ARAMIS V6.3) have been used to measure CTOA and crack extension Δa. The recording time was automatically available from the videotapes, where a digital stopwatch was used to synchronise the still images.

All of this allowed test parameters such as load, displacement, and crack length Δa to be correlated with CTOA. One example of such a digital image and the corresponding CTOA values is given in Fig. 9.

Two methods are used to determine the CTOA value:

The first method (Method 1) requires the use of an algorithm to locate the crack front, on the studied image and for selecting the pairs of points along the crack profile with imposed distances (Fig. 10). The pairs of points allow us to obtain series values $CTOA_i$ using the following formula:

$$CTOA_i = \left.\frac{\delta_i}{L_i}\right|_{\Delta a} [\text{rad}] \tag{12}$$

where δ_i is the distance between two points of coordinates i and L_i the distance between the crack tip and point with coordinate i. $CTOA_i$ are averaged to obtain $\overline{CTOA}_{\Delta a}$ value for a given crack extension Δa.

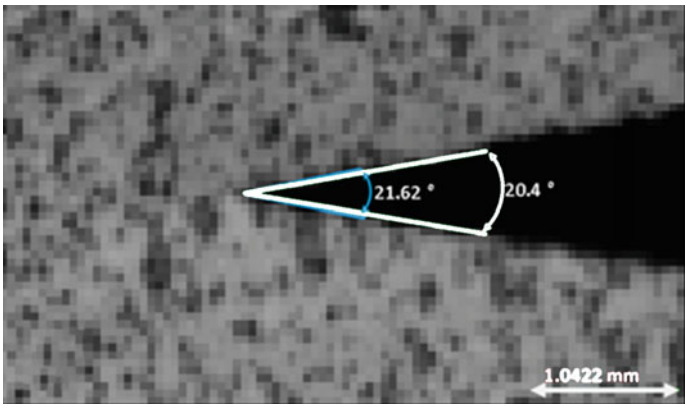

Fig. 9 Digital image of a crack and corresponding CTOA values

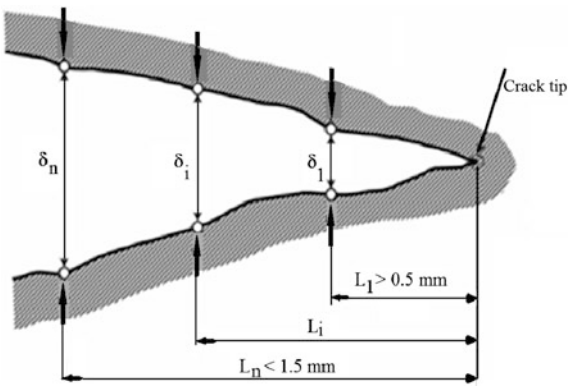

Fig. 10 Methods for determining $\overline{CTOA}_{\Delta a}$ using crack tip location

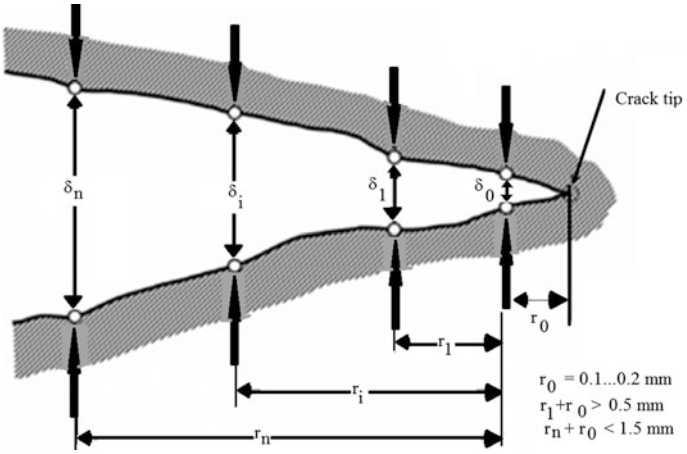

Fig. 11 Methods for determining $\overline{CTOA}_{\Delta a}$ without using crack tip location

The second method (Method 2) requires also the use of an algorithm and the selection of pairs of points along the crack profile as the first method, (Fig. 10). In this method, the position of crack tip that is often difficult to localise is not necessary, and the point of coordinates i=0 is used. Series values $CTOA_i$ are obtained using the following formula:

$$CTOA_i = \left.\frac{\delta_i - \delta_0}{r_i}\right|_{\Delta a} [rad] \tag{13}$$

r_i is the distance between the crack tip and points with coordinates i and δ_0 is the distance between two points of coordinates i = 0. As previously, the average value gives the $\overline{CTOA}_{\Delta a}$.

This method is preferred since it does not need crack tip localisation and leads to less scatter. The two methods have been compared with a series of 4 tests named (a, b, c and d) on CT specimen made from pipe steel X65. The two methods give similar values of CTOA. However the standard deviation is higher for method 2. Therefore, method 1 has been used in the next for CTOA measures on MCT specimens (Fig. 11; Table 1).

Table 1 Mean and standard deviation for CTOA measurement on CT specimens made in pipe steel X65

	Method 1		Method 2	
Specimen test	a (°)	b (°)	c (°)	d (°)
Mean	18.3	17.5	20.5	18.1
Standard deviation	2.9	1.3	4.7	3.2

Comparison of methods 1 and 2

2.3.2 Indirect Methods

These methods are based on the simulation by Finite Element Analysis or analytically of the load displacement diagram. Analytical analysis of experimental load-displacement curves in order to determine the CTOA can be carried out using different assumptions. The first one considers that the material has the stress-strain behaviour of an elastic perfectly plastic material. The second assumption considers that the material is strain hardening and the stress strain curve is described by a key curve. The third introduces the real stress strain curve in a finite element code.

Xu et al. [41] developed a method derived from the plastic hinge ductile fracture model [25] called the "simplified single-specimen method" (SSM). This model employs a regression algorithm of logarithmic load against displacement, avoiding the determination of crack extension and removing the requirements of material-based parameters. It is assumed that the ligament is fully yielded and the specimen rotates around a fixed centre of rotation at a distance of $r^*(W - a) = r^*b$ from the crack tip (Fig. 12), where r^* is the rotation constant, b the ligament size, a the crack length and W the specimen width. Neglecting the small change in position of the centre of rotation for a small increment of crack length, the half crack-tip opening displacement can be related to a small increment of rotation angle (dα) by:

$$\frac{\delta}{2} = r^*(W - a)d\alpha \tag{14}$$

From these relations, CTOA can be written as

$$tang\,\Psi/2 = \mathrm{r} * \mathrm{b}\frac{d\alpha}{dy} \tag{15}$$

Assuming that the material has a perfectly plastic behaviour, the limit moment M_L of a 3 PB specimen is given by:

$$M_L = \frac{P_L S}{4} \tag{16}$$

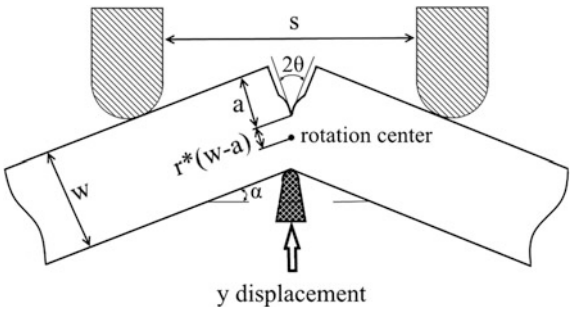

Fig. 12 Mechanisms of plastic deformation of a 3 PB specimen assuming the existence of a rotation centre

where P_L is the limit load and S the span. The limit load is given by:

$$P_L = \frac{4AR_cBb^2}{S} \tag{17}$$

where A is a geometrical constant that depends on the stress state, R_c the flow stress, b the ligament size and B the thickness. During the crack extension increment Δa, the limit load decreases by ΔP_L, the specimen arms rotate by dα and the deflection y increases by dy. The derivative of the limit load is given by:

$$dP_L = \frac{8AR_cBb}{S}db = \frac{8AR_cBb}{S}.\left(-\frac{r*b}{tang\Psi/2}d\alpha\right) = \frac{8AR_cBb}{S}.\left(-\frac{r*b}{tang\Psi/2}\frac{2dy}{S}\right) \tag{18}$$

with db = −da and $d\alpha = \frac{2dy}{S}$. By substituting dα into (13), one obtains:

$$dP_L = -\frac{4r*P_L}{Stang\Psi/2}dy \tag{19}$$

By rearrangement:

$$\frac{dLnP_L}{dy} = -\frac{4r*}{Stang\Psi/2} \tag{20}$$

The LnP_L versus $(y - y_{max}/S)$ curve may be used to evaluate Ψ, requiring values only for r^*. Constancy of the slope implies constancy of the CTOA.

$$\psi(^\circ) = 2.180/\pi \arctang((-4r^*)/((dLn(P))/dy)) \tag{21}$$

An example of such an evaluation of CTOA from a Charpy test of X65 pipe steel is given in Fig. 13.

Moreover, this method is strongly dependent on the reliability of the limit bending load hypothesis. In addition, strain hardening is not taken into account. For this reason, Fang et al. [22] evaluated the crack extension according to the procedure of the key-curve method, where load and displacement are related according to:

$$\frac{PW}{b_0^2} = m\left(\frac{y}{W}\right)^n \tag{22}$$

where W is the width, b_0 the initial ligament size, and m and n are constants. The key curve is analytically established by fitting the original relationship between the load P and the displacement y on the pre-peak part of the instrumented test curve.

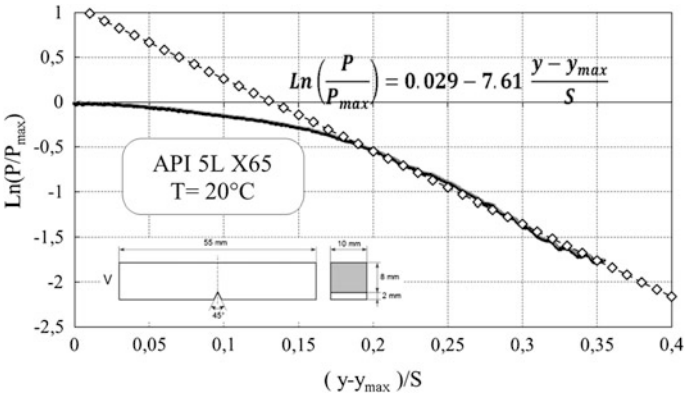

Fig. 13 Example of simplified single-specimen method (SSM) applied to a Charpy specimen made of X65 pipe steel

After obtaining the parameters m and n, the amount of crack extension is estimated at any displacement on the post-peak part of the force-displacement curve, as:

$$\Delta a = W - \left[\sqrt{\left(\frac{PW^{n+1}}{my^n}\right) + a_0}\right] \tag{23}$$

Combining (22) and (23),

$$\frac{tang\Psi}{2} = \frac{-2r*}{S}\frac{dy}{dLn(W-a)} \tag{24}$$

The $\Delta Ln(W-a)$ versus ($y - y_{max}/S$) curve may be used to evaluate Ψ, requiring values only for r^*.

$$\frac{tang\Psi}{2} = -2r* \frac{d[(y - y_{max})/s]}{\Delta Ln(W - a_0 - \Delta a)} \tag{25}$$

These two methods have been compared with a series of 3 tests named A, AA and AAA on Charpy V specimens made in pipe steel X65. Results are presented in Table 2. The load-displacement is simulated with the Abaqus software through a

Table 2 CTOA measurement on Charpy V specimens made in pipe steel X65 from load-displacement curve

Charpy test	A (°)	AA (°)	AAA (°)
CTOA Eq. (21)	22.0	24.0	24.0
CTOA Eq. (26)	21.7	23.8	23.7

Comparison of Eqs. (21) and (25)

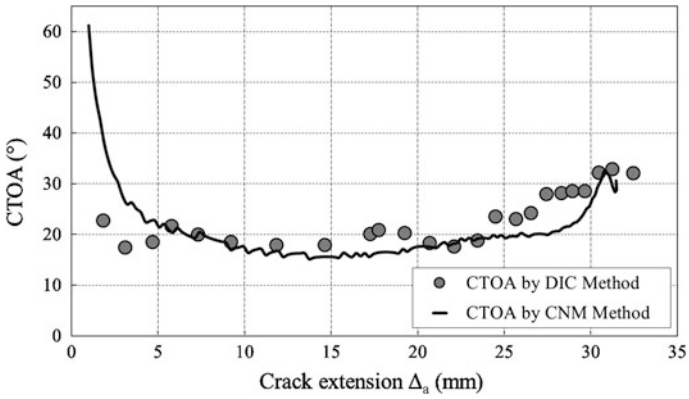

Fig. 14 Comparison of CTOA versus crack extension curve obtained by CNM and the DIC method for a modified CT specimen made of X65 pipe steel

subprogram called "routine". Once this curve is published in code, an algorithm will compare the numerical and experimental responses. The following condition is introduced: the numerically calculated load cannot exceed the experimental load level. A node release action is taken as soon as this condition is met. This node release simulates the crack extension and reduces the load level.

In the second step, the R curve is obtained from crack driving force (SIF or COD) deduced from simulated load versus crack extension deduced from node release technique. This curve is fitted by a power relationship and CTOA deduced from Eq. (2). This method is called the "Combining Numerical Method" (CNM).

With intent to validate this tool, we compared the numerical measures of CTOA to those provided by the direct method, Fig. 14. Unlike DIC, it does not allow the identification of the zone of instability that preceded the stable crack extension with high values of CTOA. CNM detects the rapid decrease of CTOA reported in the literature. However the difference in the zone of unstable crack extension, the two methods are in good agreement in the range of the studied crack extension. The second method provides more advantages in accuracy, and in its easer implementation.

2.4 CTOA Value at Stable Crack Growth for an X65 Pipe Steel

The investigated material is an API 5L X65 grade pipeline steel supplied as a seamless tube with a wall thickness equal to 19 mm and external diameter of 355 mm. The mechanical properties, measured at room temperature on three tensile test specimens in the circumferential direction, are given in Table 3.

Table 3 Mechanical properties of pipeline steel API 5L X65 at 20 °C

Yield stress σ_y (MPa)	Ultimate strength σ_{ul} (MPa)	Elongation at failure A (%)	Charpy energy K_{CV} (J)	Fracture toughness K_{Jc} (MP$\sqrt{a}$m)
465.5	558.6	10.94	285.2	280

Using a Modified Compact Tension (MCT) specimen at room temperature, tests are performed to measure the value of the CTOA during crack extension. The geometry and dimensions of the test specimen are shown in Fig. 6. The study specimens were pre-cracked to provide an initial ratio of crack length to specimen width of a/W = 0.4 using a fatigue stress ratio R = 0.1. The sinusoidal loading oscillates at a frequency of 15 Hz and the maximum load is kept below 7.2 kN. According to ASTM (E 2472) [3] requirements, the CTOA measurements were made at a distance behind the crack tip ranging between 0.5 and 1.5 mm. CTOA was determined using optical microscopy and also by finite element fitting of the experimental load. In addition, CTOA was also determined on a Charpy specimen using the simplified single-specimen method. Values obtained with the different methods are given in Table 4.

For all experimental tests, the CTOA versus crack extension behaviour consisted of an initially high CTOA region that quickly transitioned into a clearly constant CTOA region. The stable value of CTOA is called $CTOA_C$. Values of $CTOA_C$ of API 5L X65 pipe steel obtained with three different methods are reported in Table 4.

A lower bound of $CTOA_C$ is set as 20°. This value is compared to other values of $CTOA_C$ found in the literature (see Table 4).

We note that the values obtained are higher than other values found in the literature (Table 5).

Table 4 Values of $CTOA_C$ of API 5L X65 pipe steel obtained with three different methods

Method	DIC (MCT)	CNM (MCT)	SSM (Charpy)
Ψc (°)	20.66	24.68	21.8

Table 5 Values of $CTOA_C$ found in the literature and in the present study for API 5L X65 steel

References	Yield stress (MPa)	$CTOA_c$ (°)	Specimen
O'Donoghue et al. [31]	447	8.1	DWTT
O'Donoghue et al. [31]	529	14.2	DWTT
Darcis et al. [10]	543	11.61	MDCB
Amaro et al. [1]	460	11.0	MDCB
Amaro et al. [1]	522	8.6	MDCB
Current study	465	20	M(CT)

2.5 *Influence of Thickness on CTOA*

It is now well known that fracture resistance decreases when the thickness increases However CTOA seems less affected by thickness (Fig. 15). The fracture resistance is maximum for plane stress conditions and trends asymptotically to a minimum called K_{Ic} or J_{Ic} if the plane strain conditions are satisfied. The effect of thickness B on fracture toughness is introduced through a "triaxial stress constraint" T_z. This parameter is defined as:

$$T_Z = \frac{\sigma_{zz}}{\sigma_{yy} + \sigma_{xx}} \tag{26}$$

For a straight through-thickness crack, which is a typical case of 3D cracks, y is the direction normal to the crack plane xoz. In an isotropic linear elastic cracked body, T_z ranges from 0 to N, $T_z = 0$ for the plane stress state, and $T_z = N$ for the plane strain state. N is the strain hardening exponent of the Ramberg-Osgood strain-stress relationship. Values of T_z for different pipe thicknesses and for the same pipe diameter of 355 mm are reported in Table 6 and compared to plane stress or plane

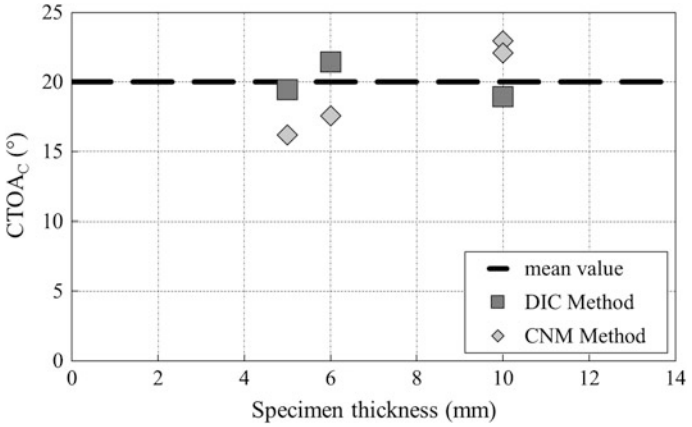

Fig. 15 Influence of thickness on critical CTOA. API5L X65 pipe steel

Table 6 Triaxial stress constraint T_z values with pipe thickness for a pipe diameter of 355 mm

Wall thickness (mm)	T_z
Plane stress	0
6 (this study)	0.204
10	0.2629
15	0.3109
19	0.335
Plane strain	9.52

strain stress states. We note the low value of T_z for the MCT specimen used in this study. A combined effect of constraint and thickness can explain the lower values of CTOA found in the literature.

3 Node Release Technique for Crack Extension

The modelling of crack propagation using CTOA has been the subject of several studies [17, 18, 42]. Crack extension is modelled by the finite element method using the CTOA criterion coupled with the node release technique. The node release technique algorithm has been presented in an earlier study [6]. It is based on the assumption that cracks grow step by step, and each step has the length of one mesh element.

This approach needs implementation in FE code without any particular problems. In this work, this has been made on Abaqus 6.11 code with the node debonding option called "Debond". Implementation of the CTOA approach is made using the subroutine "User Subroutine" associated with the finite element solver Abaqus. This programming task is divided into two major steps:

The first step is to develop a routine that allows the identification of the crack tip and evaluating CTOA during the calculation. To accomplish this step, the Abaqus solver is associated with the subprogram "URDFIL".

The second step is to modify the crack surfaces during each resolution step. This can be done by releasing representative node of the crack tip. This node release task is performed via the subroutine "MPC" (Multipoint Constraint Subroutine).

In addition, it is necessary to identify the crack tip and all necessary nodes for evaluation CTOA of each computing increment. Evaluation of CTOA during the progression of calculations is made by a subroutine "URDFIL". To simplify this task of identification, the mesh used in the simulation is adapted. In order to do that, the representative nodes of the crack path are incremented starting from the crack tip with respect to the direction of crack extension.

The subprogram "URDFIL" imports data from a results file at the end of each computing increment calculation. This allows us to know the coordinates of each node and to evaluate CTOA through a vectorial computing program, according to Eq. (27).

$$\mathrm{CTOA} = \sum_{j=1}^{m} \left(\sum_{i=1}^{n} ACos \left[\frac{\left(X_1^j - X_i^j\right)^2 + \left(Y_1^j - Y_i^j\right) * \left(Y_1^j + Y_i^j\right) + \left(Z_1^j - Z_i^j\right)^2}{\sqrt{\left(X_1^j - X_i^j\right)^2 + \left(Y_1^j - Y_i^j\right)^2 + \left(Z_1^j - Z_i^j\right)^2}} \right] / n \right) / m \tag{27}$$

The MPC (Multi-Point Constraints) method with ABAQUS (version 11.6), made possible the implementation of the node release technique in a three-dimensional simulation. The MPC method involves a special mesh. Unlike a conventional mesh

that uses a node at each corner of element, four nodes are located at identical coordinates. The nodes a, b, c and d of the four elements A, B, C, and D are coupled together. This means that their movements are forced to be the same. To create a new crack surface, it is necessary that these nodes be able to separate Fig. 16. This separation process needs the debonding of one or two nodes at the same time. According to the chosen node, crack extension has three possible directions. This operation can be represented by the following equation

$$\begin{pmatrix} k_1^1 & k_2^1 & k_3^1 & k_4^1 \\ 0 & k_1^2 & k_2^2 & k_3^2 \\ 0 & 0 & k_1^3 & k_2^3 \end{pmatrix} \begin{pmatrix} u_a \\ u_b \\ u_c \\ u_d \end{pmatrix} = \begin{pmatrix} 0 \\ 0 \\ 0 \end{pmatrix} \tag{28}$$

where u_a, u_b, u_c and u_d are displacements of nodes a, b, c and d. k_i^j are scalars with values 0, 1 or −1, according to crack extension direction.

Two increment strategies are available in the ABAQUS code: automatic and fixed. Computing has been made according to both strategies. The ratio accuracy/computing time has been used as the criterion of choice of the most appropriate strategy. Results are reported in Table 7. It is obvious that the strategy of a fixed increment reduces the computing CTOA, but this involves a considerable calculation time. To overcome this difficulty, a hybrid strategy has been used. The solver ABAQUS automatically manages the computing step size until a CTOA amplitude reaches a value equal to than 80% of CTOAc. Then the subprogram "URDFIL" takes over to reduce the increment size gradually to the critical value of CTOA.

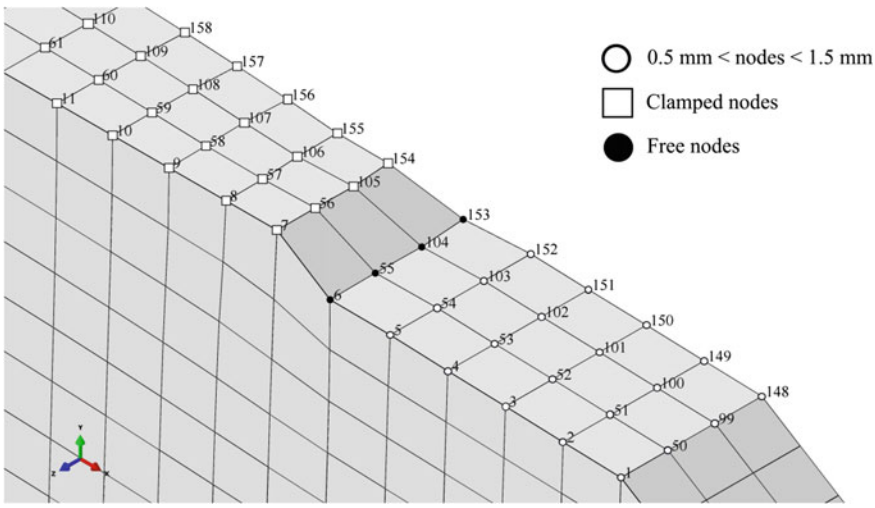

Fig. 16 The node release technique configuration of debonded and fixed nodes

Table 7 Computing time and error according to increment strategies automatic or fixed

Incrementation strategy	Error (°)	Error (%)	Number of increments	Computing time (h)
Automatic	0.365	1.85	2178	2 h 27
Fixed	0.076	0.38	6325	7 h 33

Table 8 Influence of mesh type on error and computing time

Mesh	Mesh type	Nodes number	Error (%)	Computing time (h)
1	C3D8R	22,008	5.95	2 h 26
2	C3D8R	33,612	5.8	4 h 17
3	C3D8R	55,513	3.74	7 h 23

Mesh dependence was checked with three different 3D meshes. The results presented in Table 8 indicate that a good convergence can be obtained by observing a minimum level of mesh refinement. This level may be related to the definition of the CTOA and the maximum size of an element cannot exceed 1.5 mm.

4 Finite Element Modelling of Crack Extension

4.1 Meshing

The modelling task begins with the three-dimensional mesh of the geometry of the pipeline. Owing to symmetry, only ¼ geometry is analysed to reduce the computation time further. Two zones of meshes were generated: a first fine mesh zone along the crack plane with an element size equal to 1.4 mm, and a second coarse mesh with an average size of 15 mm; see Fig. 17.

The connection between the two mesh regions is performed under ABAQUS which allows the connection of the solid type of surface. The final step of meshing

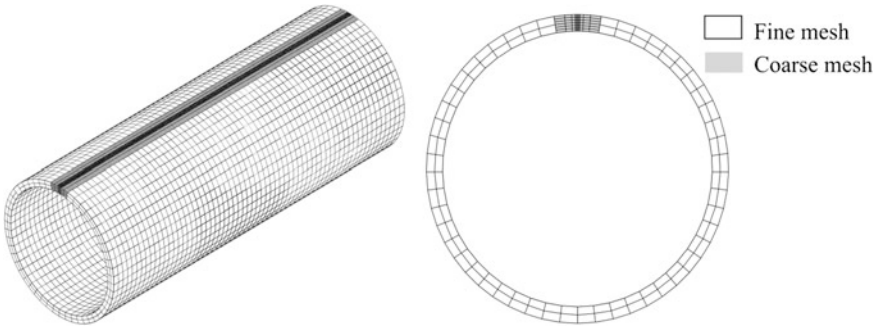

Fig. 17 Mixed mesh for a pipe and a running crack

is to name the crack plane nodes by the procedure described previously allowing the identification of the crack tip and calculation CTOA in its vicinity. A total of 50,976 eight node, hexahedral elements were generated along the crack path and combined with 6000 shell elements.

4.2 Boundaries Conditions

Conditions of crack symmetry in the $\vec{x}$ direction allow the removal of two rotations along the $\vec{y}, \vec{z}$ axes and the displacement in the $\vec{x}$ direction. By analysing only ¼ of the pipeline, a symmetry condition in the $\vec{y}$ direction is imposed to the central plane of the pipeline. The end of the pipeline is assumed to be clamped.

4.3 Loading

Computing is made by applying a gradual pressure on the inner surface of the pipeline. During the computing progress, the CTOA value increases until it reaches its critical value $CTOA_c$. Then, the node releasing subroutine applies the release action of crack tip nodes, which leads to crack extension.

To fulfil the conditions of energy balance, the node release action is associated with a decrease of the loading level. A third sub-program type "DLOAD" reduces by 2% the pressure on the inner wall of the pipeline following each node release action. Under this same routine and as close as possible to the actual conditions of a burst test. According to the assumption of Maxey [26], only the portion of the pipeline downstream of the crack tip is constantly charged by the gas pressure. Using this same routine, the internal pressure is imposed to a certain distance ahead of the crack tip. This distance is estimated from a model based on the cohesive zone model of Dugdale-Barenblatt [32]. In this model, the distance over which the internal pressure is applied is based on the dimensions of the pipeline:

$$2b = 3\sqrt{R.t} \tag{29}$$

where R and t are the outer radius and thickness of the pipeline, respectively.

In order to check Maxey's assumption, we have studied the influence of the extent of the applied pressure zone on the rate of crack propagation. Five simulations at an internal pressure of 40 MPa and for different lengths $2b = h\sqrt{Rt}$ where h is a factor that takes values [2, 2.5, 3, 4 and 5], have been performed. The crack propagation velocity versus $h\sqrt{Re}$ is reported in Table 9 and Fig. 18. We justify the choice of the length 2b according to Eq. (29).

Table 9 Influence of h parameter on crack extension velocity

h	2	2.5	3	4	5
V_c(m/s)	180	240	266	263	262

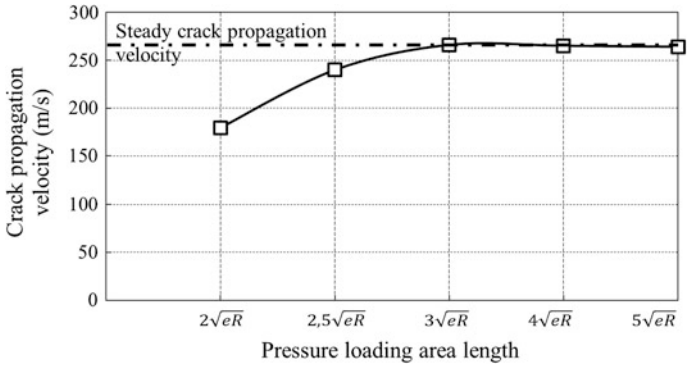

Fig. 18 Influence of distance ahead of the crack tip where internal pressure is imposed

4.4 Strain Rate Effect

The crack propagation following the burst of the pipeline is a dynamic phenomenon. A strain rate that amounts to more than 1500 s^{-1} was measured in the vicinity of the crack tip according to the results reported by Oikonomidis et al. [30]. Thus, the influence of the strain rate is necessary taking into account in the numerical model through the dynamic behaviour law of Johnson Cook:

$$\sigma_{eq} = \left(A + B\varepsilon_{eq}^{n}\right)\left(1 + Cln\left(\frac{\dot{\varepsilon}_{eq}}{\dot{\varepsilon}_0}\right)\right) \tag{30}$$

where σ_{eq} is the equivalent von Mises stress, ε_{eq} the equivalent strain, $\dot{\varepsilon}_{eq}$ equivalent deformation rate and $\dot{\varepsilon}_0$ the reference strain rate. A, B, C and n are the Johnson Cook parameters. These parameters for API 5L X65 pipeline steel, have been reported by Jakobsen [16]: Table 10.

Numerical results obtained with and without the strain rate dependence indicates a small influence on crack speed in pipes made of API 5L X65 steel with a variation of the crack growth rate of less than 5%. This is explained by the low strain rate sensitivity of the API 5L X65 steel [34]. However despite the minor influence of the crack velocity, the influence of strain rate is taken into consideration in order to build a more accurate model.

Table 10 Johnson Cook parameters for API 5l X65 pipe steel [34]

Material parameters	A (MPa)	B (MPa)	n	C	$\dot{\varepsilon}_0$ (s^{-1})
	465.5	410.83	0.4793	0.0104	0.000806

At the time of the occurrence of a through crack in the pipeline, the gas escapes through the created opening and provokes a sudden decompression that consists of two decompression waves running along the pipeline at a speed of the order 300 m/s. These opposed waves play an important role in the dynamics of failure.

Indeed, if the propagation rate of the decompression wave is lower than the crack speed, the crack tip will be continuously loaded at the initial pressure. An infinite stationary crack propagation occurs. On the contrary, the crack is gradually discharged until arrest. In order to predict the velocity of the decompression wave of the gas, numerous models have been developed based on the Finite Difference Method, the Characteristics Method, or an experimental method such as the shock tube test. These methods generally assume a one-dimensional flow (along the axis of the pipe) and isentropic gas behaviour. According to Civallero et al. [7] and in the case of a pure gas phase, the pressure in the vicinity of the crack follows the following relationship:

$$\begin{aligned} V_c > V_d p_l &= p_0 \\ V_c < V_d p_l &= p_0 \left[\left(\frac{2}{\gamma+1} \right) + \left(\frac{\gamma-1}{\gamma+1} \right) . \frac{v_c}{v_d} \right]^{(2\gamma/\gamma-1)} \end{aligned} \tag{31}$$

where V_c and V_d are, respectively, the crack and decompression wave speed, p_0 and p_l, initial and leak pressures, γ ratio of specific heats of the gas (iso-pressure and isochore).

Cen [9] studied the decompression of supercritical CO_2 through shock tube tests and numerical simulations with the calculation code GASDECOM [15]. A simplified gas depressurisation model similar to Cheng et al.'s solution is used in this work and assumes that the gas decompression pressure depends only on time and distance from the crack tip and that the crack propagation cannot outrun the decompression wave. The expansion of the ideal gas is isentropic, and the pipe is considered as a large pressure vessel with constant volume. The pressure drop ahead of the running crack tip is given by the following equation:

$$p(t) = p_0 . \exp(kt) \tag{32}$$

where k is a constant k = −7.5 s^{-1} [37] that can be related to the gas parameters and initial conditions of pressure and temperature.

5 Results

Crack extension modelled by the Finite Element method using CTOA criterion coupled with the node release technique allows us to predict the crack velocity, the arrest pressure and crack length. It has been applied for a pipe with wall thickness equal to t = 19 mm and external diameter OD = 355 mm made in API 5L X65 pipe steel.

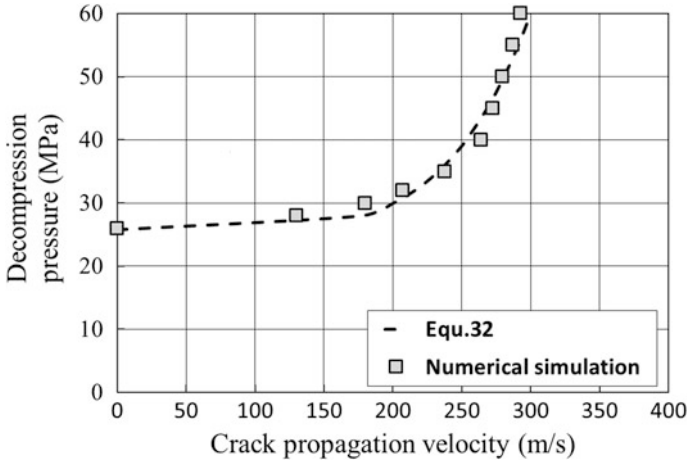

Fig. 19 Decompression wave versus crack velocity; pipe made of API5L X65, diameter 355 mm and thickness 19 mm

5.1 Crack Velocity

Crack extension from an initial crack like defect is computed using the described model. Running crack propagation along the tube consists of two stages: a boost phase where the crack reaches its full velocity in a few milliseconds, followed by a steady stage at constant speed. The absence of a deceleration phase is explained by the lack of gas decompression law in the model. One notes that the crack velocity increases with the initial pressure. Ten simulations were performed at different levels of pressure in the range 25–60 MPa. Results reported in Fig. 19 indicate that the stationary crack velocity V_c (m/s) increases with decompression pressure p_d in MPa according to:

$$V_c = 284.2 * \left(\frac{P_d}{25.8} - 1\right)^{0.193} \tag{33}$$

5.2 Arrest Pressure

The arrest pressure is defined relative to crack propagation and not arrest. Therefore it is considered as the minimum pressure level to ensure the steady crack propagation. Above this pressure p_{ar}, the crack propagates in an unstable manner and along a long distance. Under this value, the crack propagation will auto-arrest or propagate along a short distance. The arrest pressure is obtained using the CTOA Abaqus user subroutine within a static analysis.

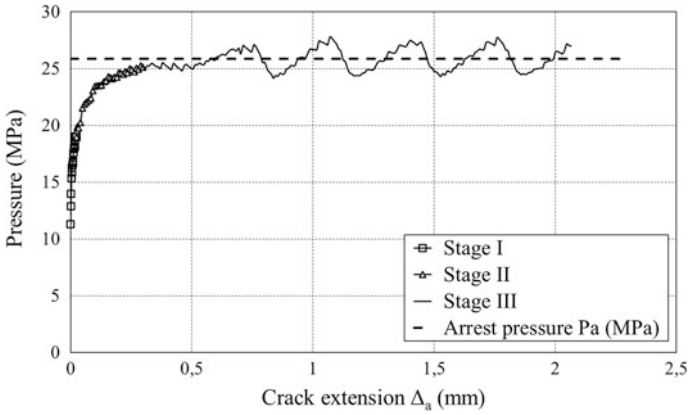

Fig. 20 Determination of arrest pressure by static analysis using CTOA Abaqus User Subroutine

Evolution of the crack tip pressure travel is characterized by three stages (Fig. 20): first, the crack tip pressure experienced a sharp rise to a crack extension equivalent to the wall thickness of the pipeline, followed by a second and more gradual increase. Finally, the pressure converges to a relatively stable value during a third stage and is defined as the arrest pressure. The increase of the crack tip pressure is linked to increasing fracture toughness with crack extension, as described by the R curve concept. James and Newman [21] assume that the increase of fracture toughness is related to the tunnel effect, and find that a crack propagates in an unstable manner along a distance equivalent to the thickness. Experimental tests on modified CT specimens in our experimental study of CTOA confirm this assumption.

During the second stage, the wall deformation of the pipe modifies the loading mode. Scheider et al. [37] indicate that during this transitional stage, crack propagation extension is about the same as the diameter of the pipeline.

The third stage is characterised by the stability of the crack tip pressure and no variation in the stress distribution near the crack tip. Although the crack propagation is stationary, we see waves in the pipe opening geometry at crack tip pressure near the arrest one. This is due to the local buckling phenomenon in bursting tests on pipelines made of X70 steeland analysed by Tran [39]. Tran links these ripples to the level of ductility of the material and nonlinear geometrical effects associated with modification of the load surface at the crack tip.

To define the arrest pressure, these waves are neglected and the mean value is considered. In the case presented in Fig. 17, the arrest pressure p_a = 25.8 MPa is obtained.

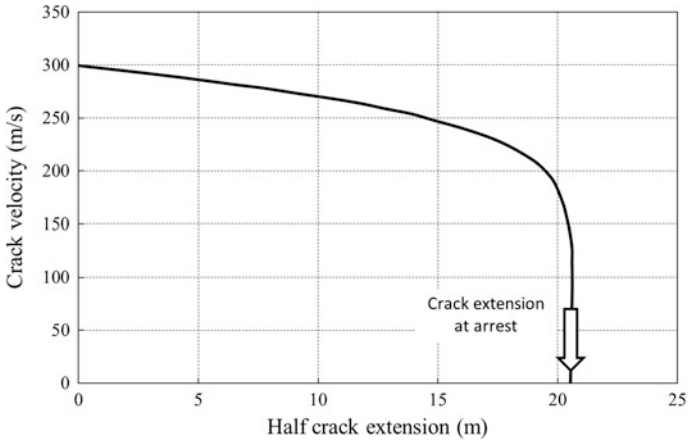

Fig. 21 Graph crack velocity half of the crack extension, determination of crack extension at arrest X65 pipe steel, initial pressure p_0 = 45 MPa

5.3 Crack Extension at Arrest

Crack extension at arrest is obtained from the graph crack velocity half of the crack extension to take into account the symmetry of the problem (Fig. 21). For the aforementioned conditions of geometry, material and initial pressure, the numerical simulation gives a crack extension of 42 m, which is of the same order of magnitude to those obtained experimentally.

6 Discussion

The use of CTOA for prediction of dynamic ductile fracture arrest in pipelines began in the late 1980s with a model that calculates the crack driving force in terms of CTOA as a function of crack speed.

The CTOA fracture criterion has now become one of the most promising fracture criteria used for characterising stable tearing in thin metallic materials. Initially, fracture resistance to crack extension was given by the Charpy energy, as in the Batelle Two-Curves method (BTCM) [27]. The Charpy test is related to crack initiation, bending of the specimen, and plastic deformation at the load points. It is necessary that tests performed to characterise the propagation resistance be able to isolate and quantify the propagation energy with respect to incremental crack advance. For this reason and due to the development of higher-strength steels with increased toughness and lower transition temperatures using controlled rolling techniques, the Charpy energy was replaced by drop-weight tear test (DWTT) energy in the HLP [38] and HLP Sumitomo [19] two-curves methods. DWTT tests

are also related to crack initiation, bending of the specimen, and plastic deformation. However, notched DWTT specimens are larger than Charpy ones, and therefore relatively less of the total fracture energy is related to initiation. The statically pre-cracked DWTT showed the best compromise between isolating the propagation energy and ease of specimen preparation. Another step was the development of a test methodology to measure CTOA indirectly, derived on the basis of the difference in energy between two modified DWTT specimens with different initial crack lengths [12].

CTOA is defined from the crack growth resistance curve (R-curve) and particularly from the δ_R–Δa curve slope. This does not integrate fracture resistance to initiation, but only fracture resistance to crack extension. However, based on the CTOA, δ_R–Δa curve slope cannot be assumed as a material constant. For a better agreement between the experimental and predicted curves, a bilinear form of CTOA should be used instead of the constant CTOA criterion (Fig. 22). Therefore the non-stable ductile crack extension can also be modelled. Non-stable crack extension affects few millimetres, while the stable one sometimes affects several metres.

The critical CTOA is sensitive to geometrical parameters such as thickness or ligament size and loading mode through constraints, but this is a general problem for all fracture criteria.

The influence of geometrical parameters of pipes on CTOA has been proposed [7] and is given by the general form:

$$CTOA_c = C\left(\left(\frac{\sigma_h}{E}\right)^m \left(\frac{\sigma_h}{\sigma_0}\right)^n \left(\frac{D}{t}\right)^q\right) \tag{34}$$

where m, n, and q are dimensionless constants and C is expressed in degrees; σ_h is the hoop stress (MPa), σ_0 is the flow stress (MPa), D is the diameter (mm), and t is thickness (mm). The following values can be used for methane: C = 106, m = 0.753, n = 0.778 and q = 0.65. Therefore in a model based on $CTOA_c$, leads to an influence of pipe diameter and thickness on crack velocity V_c and arrest

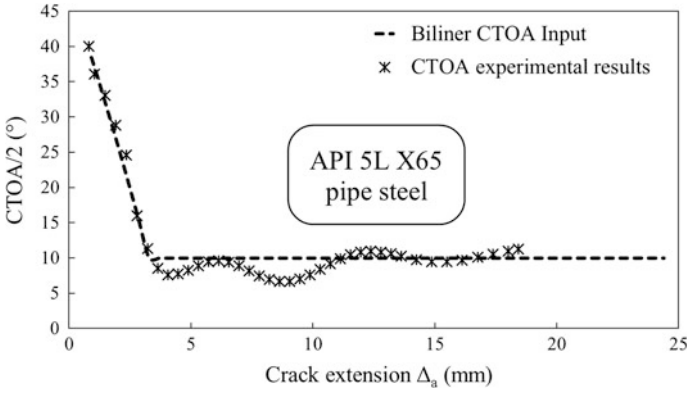

Fig. 22 Bilinear description of critical CTOA versus crack extension

Table 11 33 values of parameters α, β and γ of Eq. (35), thickness 19 mm

Pipe diameter	α	α	γ
355 mm	0.193	25.8	284.2
393 mm	0.14	24	290

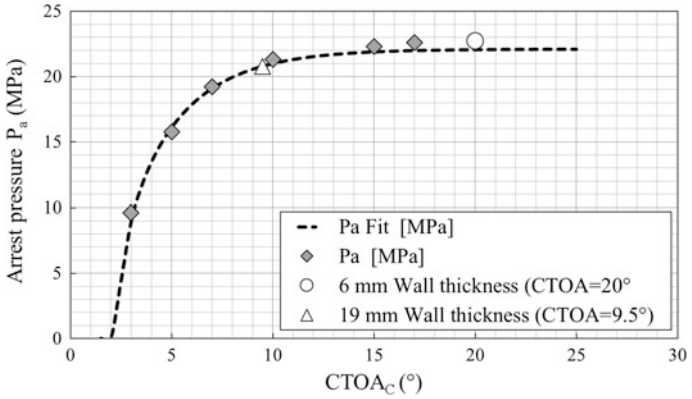

Fig. 23 Influence of CTOA$_c$ on arrest pressure API 5L X100 pipe steel

Table 12 Influence of thickness on predictions of arrest pressure

Thickness (mm)	CTOA$_c$ (°)	Pa (MPa)
6	20	23.1
19	9.5	20.5

Pipe with outer diameter D 393 mm made in API 5L X65 steel

pressure P_a. The crack velocity is expressed versus decompression wave pressure by Eq. (35), where the parameters α, β and g depend on pipe diameter (Table 11).

$$V_c = \alpha \cdot \frac{\sigma_0}{\sqrt{R_f}} \cdot \left(\frac{p_d}{p_a} - 1\right)^{\beta} \tag{35}$$

CTOA$_c$ has been determined on 6 mm thick test specimen and the thickness of the pipe is 19 mm. The influence of CTOA$_c$ on arrest pressure has been determined and results are presented in Fig. 23. The influence of thickness on arrest pressure for API 5L X65 pipe steel (pipe diameter) is small and about 12 % in the range 6–19 mm: Table 12.

7 Conclusions

CTOA is a measure of fracture toughness. More precisely, it expresses the fracture resistance to ductile crack extension in radians or degrees. These units come naturally from the definition of the CTOA as the angle between the crack faces of a

growing crack or as the slope of the R curve $\delta_R = f(a)$. However simple a definition, it exhibits some difficulty due to the irregular shape of the crack profile. The most appropriate methods follow the ASTM E2472-06e1 Standard [3] using an MDCB specimen and optical microscopy. An alternative method is to use the finite element method to fit experimental load-displacement diagrams mainly when the test temperature is low (it becomes difficult to carry out an optical examination of the specimen surface) or when the specimen is thick (due to the tunnelling effect).

Values of the CTOA are not intrinsic to materials. Like other measures of fracture toughness, it is sensitive to geometry and loading mode. This sensitivity can be described by a constraint parameter. For the thickness effect, the constraint parameter T_z is very appropriate.

CTOA is a good candidate to describe the fracture resistance of a ductile running crack. It represents only this resistance to crack extension and not a mixture of crack propagation and crack initiation energies. The use of this criterion requires a single parameter that can be obtained easily with a fracture test. Using the node release technique associated with the CTOA as a criterion for crack extension, numerical modelling is able to predict crack length and pressure at arrest.

References

1. Amaro RL, Sowards JW, Drexler ES, McColskey JD, MacCowan C (2013) CTOA testing of pipe line steels using MDCB specimens. J Pipe Eng 3:199–216
2. Andersson H (1973) A finite element representation of stable crack growth. J Mech Phys Solids 21:337–356
3. ASTM E2472-06e1 (2002) Standard test method for determination of resistance to stable crack extension under low-constraint conditions
4. Ben Amara M, Capelle J, Azari Z, Pluvinage G (2015) Prediction of arrest pressure in pipe based on CTOA. J Pipe Eng 14
5. Brocks W, Yuan H (1991) Numerical studies on stable crack growth. In: Defect assessment in components fundamentals and applications, vol 9. ESIS Publication, Oxford, UK, pp 19–33
6. Capelle J, Ben Amara M, Pluvinage G, Azari Z (2014) Role of constraint on the shift of ductile–brittle transition temperature of subsize Charpy specimens. Fatigue Fract Eng Mater Struct 37:1291–1385
7. Civallero M, Mirabile M, Sih GC (1981) Fracture mechanics in pipeline technology. In: Sih GC, Mirabile M (eds) Analytical and experimental fracture mechanics. Kluwer Academic Publishers, Dordrecht, Netherlands, pp 157–174
8. Cotterell B (1980) Slightly curved or kinked cracks. Int J Fract 16(2):155–169
9. Cen C (2013) Characterization and calculation of fracture toughness for high grade pipes. PhD thesis, University of Alberta
10. Darcis PhP, McCowan CN, Windhoff H, McColskey JD, Siewert TA (2008) Crack tip opening angle optical measurement methods in five pipeline steels. Eng Fract Mech 75:2453–2468
11. Dawicke D, Sutton M (1994) CTOA and crack-tunneling measurements in thin sheet 2024-T3 aluminum alloy. Exp Mech 34(4):357–368
12. Demofonti G, Buzzichelli G, Venzi S, Kanninen M (1995) Step by step procedure for the two specimen CTOA test. In: Denys R (ed) Pipeline technology, vol II. Elsevier, Amsterdam

13. Demofonti G, Mannucci G, Hillenbrand HG, Harris D (2004) Evaluation of X100 steel pipes for high pressure gas transportation pipelines by full scale tests. In: International pipeline conference, Calgary, Canada
14. Erdogan F, Sih GC (1963) On the crack extension in plates under loading and transverse shear. Trans ASMEJ Basic Eng 85:519–527
15. Eiber R, Bubenik T, Maxey W (1993) GASDECOM, computer code for the calculation of gas decompression speed that is included in fracture control technology for natural gas pipelines. NG-18 Report 208, American Gas Association Catalog
16. Jakobsen E (2013) Deformation of pressurized pipelines. Master thesis, Norwegian University of Science and Technology
17. Gullerud AS, Dodds RH, Hampton RW, Dawicke DS (1999) Three-dimensional modeling of ductile crack growth in thin sheet metals: computational aspects and validation. Eng Fract Mech 63(4):347–374
18. Hampton RW, Nelson D (2003) Stable crack growth and instability prediction in thin plates and cylinders. Eng Fract Mech 70(3–4):469–491
19. Higuchi R, Makino H, Takeuchi I (2009) New concept and test method on running ductile fracture arrest for high pressure gas pipeline. In: 24th world gas conference, WGC 2009, vol 4. International Gas Union, Buenos Aires, Argentina, pp 2730–2737
20. Heerens J, Schödel M (2003) On the determination of crack tip opening angle CTOA using light microscopy and δ5 measurement technique. Eng Fract Mech 70(3–4):417–426
21. James MA, Newman JC (2003) The effect of crack tunnelling on crack growth: experiments and CTOA analyses. Eng Fract Mech 70(3):457–468
22. Fang J, Zhang J, Wang L (2014) Evaluation of cracking behavior and critical CTOA values of pipeline steel from DWTT specimens. Eng Fract Mech 124(125):18–29
23. Kanninen MF, Rybicki EF, Stonesifer RB, Broek D, Rosenfield AR, Nalin GT (1979) Elastic–plastic fracture mechanics for two dimensional stable crack growth and instability problems. ASTM STP 668:121–150
24. Lloyd W, McClintock F (2003) Microtopography for ductile fracture process characterization part 2: application for CTOA analysis. Eng Fract Mech 70(3–4):403–415
25. Martinelli A, Venzi S (1996) Tearing modulus, J-integral, CTOA and crack profile shape obtained from the load–displacement curve only. Eng Fract Mech 53:263–277
26. Maxey WA (1981) Dynamic crack propagation in line pipe. In: Sih GC, Mirabile M (eds) Analytical and experimental, fracture mechanics. Kluwer Academic Publishers, Dordrecht, Netherlands, pp 109–123
27. Maxey WA (1974) 5th symposium on line pipe research, PRCI Catalog No. L30174, Paper J, p 16
28. Newman JC, James MA, Zerbst U (2003) A review of the CTOA/CTOD fracture criterion. Eng Fract Mech 70:371–385
29. Newman JC Jr (1984) An elastic–plastic finite element analysis of crack initiation, stable crack growth, and instability. ASTM STP 833:93–117
30. Oikonomidis F, Shterenlikht A, Truman CE (2013) Prediction of crack propagation and arrest in x100 natural gas transmission pipelines with the strain rate dependent damage model, part 1: a novel specimen for the measurement of high strain rate fracture properties and validation of the SRDD model parameters. Int J Press Vessels Pip 105:60–68
31. O'Donoghue PE, Kanninen MF, Leung CP, Demofonti GetVenzi S (1997) The development and validation of a dynamic fracture propagation model for gas transmission pipelines. Int J Press Vessels Pip 70:11–25
32. Pirondi A, Fersini D (2009) Simulation of ductile crack growth in thin panels using the crack tip opening angle. Eng Fract Mech 76(1):88–100
33. Pluvinage G, Ben Amara M, Capelle J, Azari Z (2015) Crack tip opening angle as a fracture resistance parameter to describe ductile crack extension and arrest in steel pipes under service pressure. Phys Mesomech 18(4):355–369

34. Pluvinage G, Capelle J, Hadj Méliani M (2015) A review of fracture toughness transferability with constraint. In: Boukharouba T, Pluvinage G, Azouaoui K (eds) Applied mechanics, behavior of materials, and engineering systems—selected papers from 5th Algerian Congress of Mechanics, CAM2015, 25–29 October, El-Oued, Algeria
35. Rice JR, Sorensen EP (1978) Continuing crack tip deformation and fracture for plane-strain crack growth in elastic–plastic solids. J Mech Phys Solids 26:163–186
36. Shih CF, de Lorenzi HG, Andrews WR (1979) Studies on crack initiation and stable crack growth. ASTM STP 668:65–120
37. Scheider I, Schödel M, Brocks W, Schönfeld W (2006) "Crack propagation analyses with CTOA and cohesive model": comparison and experimental validation. Eng Fract Mech 73 (2):252–263
38. Sugie E, Matsuoka M, Akiyama H, Mimura T, Kawaguchi Y (1982) A study of shear crack-propagation in gas-pressurized pipelines. J Press Vessel Technol ASME 104(4):338–343
39. Tran DC (2013) Interaction rupture-flambage, le cas du «splitting» de tube métallique Approche expérimentale et numérique. PhD thesis, INSA de Lyon
40. Xu S, Petri N, Tyson WR (2009) Evaluation of CTOA from load vs. load-line displacement for C(T) specimen. Eng Fract Mech 76(13):2126–2134
41. Xu S, Bouchard R, Tyson WR (2007) Simplified single-specimen method for evaluating CTOA. Eng Fract Mech 74(15):2459–2464
42. Zerbst U, Heinimann M, Donne D, Steglich C (2007) Fracture and damage mechanics modelling of thin-walled structures—an overview. Eng Fract Mech. doi:10.1016/j.engfracmech.2007.10.005

Is Substituting P91 for P22 Justified?

Ljubica Milovic

Abstract While refurbishing fossil fuel power plants, it is of great importance for safety precaution to replace the aged components which exceeded their designed service life with new ones. The most important parameter for thick-walled components is thickness value and the most important procedure is its reduction. Reduction of wall-thickness is achieved by changing the material of thick-walled components. In present paper some examples of wall-thickness reduction are shown in case of substituting a ferritic/martensitic micro-alloyed steel P91 for P22.

Keywords Service life · Power plants · Micro-alloyed steel

1 Introduction

Thermal efficiency of fossil power plants depends on steam parameters (pressure and temperature) and could be increased if those parameters are increased. In the same time, the necessity to reduce CO_2 emission has yielded additional motive for increasing thermal efficiency of power stations. Nowadays usual power plants steam temperatures ranges are around 600 °C and pressures around 30 MPa. It is expected that steam temperatures will rise another 50–100 °C in the next 30 years [1, 2].

Steels for supercritical operating conditions which comprise steam temperature of 650 °C and pressure of 35 MPa have been progressively overtook by advanced materials for ultrasupercritical (USC) steam conditions (steam temperatures 700 °C). Nickel-based alloys, advanced steels and stainless steels are able to withstand such high efficiency cycles [3].

Older generations of conventional steam turbine fossil power plants and other plant components in Serbia were conservatively designed for 10^5 service hours

L. Milovic (✉)
Faculty of Technology and Metallurgy, University of Belgrade, Karnegijeva 4, 11120 Belgrade, Serbia
e-mail: acibulj@tmf.bg.ac.rs

G. Pluvinage and L. Milovic (eds.), *Fracture at all Scales*,
Lecture Notes in Mechanical Engineering, DOI 10.1007/978-3-319-32634-4_5

under fresh steam pressure of 13–15 MPa and 540 °C. It is not unusual to find plants operating in the creep regime for periods well in excess of 10^5 h. Along with thick-walled components like pipelines of fresh- and reheated steam, they are made of low alloyed low-carbon steels and exposed to very complex operating conditions, i.e. to gradual degradation in the performance ability and reliability [4–7]. In the beginning of the 21st century, the replacing of used material by new one, began.

In present paper, behavior of two materials under creep conditions will be compared in order to gain insight in environmental and economic impact of using each steel grade. Those are ASTM A335 Grade P22 (2.25Cr-1Mo) steel and EN 10 216-2 Grade X10CrMoVNb9-1 (9Cr-1Mo) steel.

2 Development of Materials for Elevated Temperature Application

Increases in fossil fuel prices and growing concern about global warming destructive impact, brought back to consciousness the necessity of reducing the emissions of greenhouse gases. It is well known how difficult is to minimize the CO_2 emission since coal possesses a high carbon content. Experts agree that increasing of the efficiency of the power plants by increasing the operating temperature and pressure which leads to reduced fuel consumption, is the cost-effective method and first step in the fight against air pollution.

Since mid 1960s, when the first high chromium ferritic steels appeared in Europe, a great progress in developing advanced materials for elevated temperature application has been achieved. In early sixties EM12 steel has been developed in France and Belgium and X20CrMoV12-1 in Germany, both with increased creep rupture strength, see Table 1 [8]. Since the late seventies, the research efforts in Japan, USA and Europe on promoting development of ferritic-martensitic 9–12 % Cr steels were carried out through research programs. In Japan such programs were initiated and supported by Electrical Power Development Company (EPDC), in USA it was the Electric Power Research Institute (EPRI) basic studies and project 1403 and in Europe the Co-operation in the field of Science and Technology

Table 1 Steels for elevated temperature application in Europe, USA and Japan

Year	Europe	USA	Japan
Before 1960s	10CrMo9-10 14MoV6-3 (0.5 % Cr, 0.5 % Mo, 0.25 % V)	T/P22	STBA24-STPA24
In 1960s	X20CrMoV12-1 (12 % Cr, 1 % Mo, 0.25 % V)	T/P22	STBA24-STPA24
Mid 1960s	EM12 (9 % Cr, 2 % Mo, V, Nb)	T/P22	STBA24-STPA24
Since mid 1980s	X10CrMoVNb9-1 (9 % Cr, 1 % Mo, 0.25 % V, Nb)	T/P91	STBA28-STPA28

(COST) 501 and 522 programs [2]. Further developments in Europe and Japan since the late eighties has led to steel grades 7CrMoVTiB10-10 (T24), E911 (T/P911), T23, T/P92 and T/P122 [8]. Steels P92 and P122 were approved by ASME code for use in thick section components for temperatures up to 620 °C [8].

To achieve steam temperatures around 700 °C with good creep strength and corrosion resistance, nickel-based alloys were developed. Most of them evolved from Ni20 %Cr alloy by adding Mo, W and Co for strengthening solid solution. Additions of Ti and Al are limited to very small amounts because of weldability and reducing the possible occurrence of cracking in the heat-affected zone (HAZ). Dispersion strengthening of solid solutions is achieved by adding Nb. For better flue gas corrosion resistance it is necessary to increase level of Cr in the solution. In order to reduce the high price of nickel-based alloys production, significant amounts of Fe are added in the solution [2].

Nowadays, countries with the highest CO_2 emission are China, USA and India. In China, the installed capacity of fossil fuel power has reached 69.5 % by the end of 2012 and it is still growing. In 2013 the CO_2 emission in China was 11×10^9 tons, in the USA 5.8×10^9 tons and in India 2.6×10^9 tons [9].

The struggle against pollution continues, in the European Union project NextGenPower [10] (2010–2014) has been established to develop new alloys and coatings for application in USC power plants by combining biomass and carbon combustion at steam temperatures ≤750 °C. This combined combustion at elevated temperatures creates more aggressive environments which thus require the use of coatings like NiCr, FeCrAl, NiCrAlY, NiCrWMoCu, NiCrMoWFe, CrNiC and NiCrMo (Nb + Ta). The goal of USA Program on Materials Technology for Ultrasupercritical Coal-Fired Boilers is to develop higher alloy materials for steam temperatures of 760 °C. China also initiated advanced USC technology projects for temperatures up to 750 °C, testing advanced austenitic heat-resisting alloys like TP347H, Super304H and HR3C and Ni-base super alloy NiCrCoMoNbTiAl type [3].

3 Uniaxial Creep

Phenomena of progressive time-dependent inelastic deformation under constant load and temperature named cause of many problems in critical components of power plants. Creep is accompanied by different slow microstructural rearrangements like dislocation movement, ageing of microstructure and grain-boundary cavitation [11, 12].

Figure 1 demonstrates strain versus time curve which describes typical creep response of a material subjected to constant load.

It can be seen that the deformation is divided into four regimes. In the very beginning of applying load, material behaves elastic which is expressed as instantaneous strain ε_0. The first stage called primary or reduced creep occurs after a short time of applying the load and is characterized by minimum creep rate (strain rate decreases as the material strain hardens). The secondary stage called

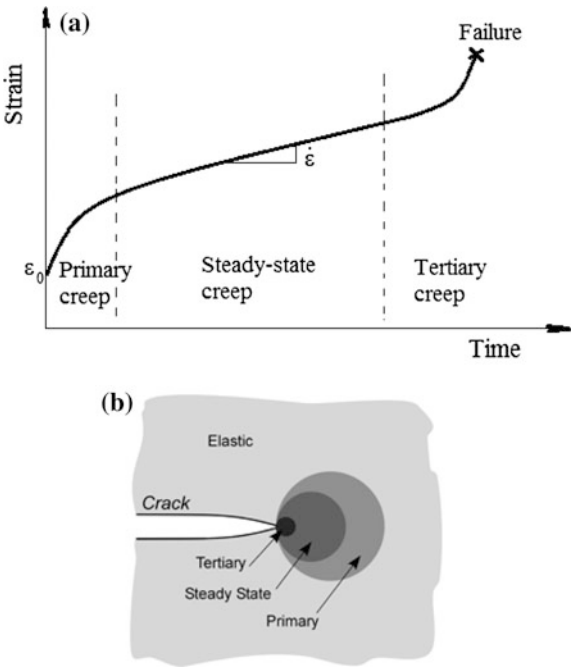

Fig. 1 **a** Creep curve under constant load and temperature and **b** creep response zones at a crack tip [13]

steady-state creep is characterized by almost constant creep rate; the deformation reaches the steady state because the strain hardening and softening are in balance. In the third stage called tertiary creep the strain rate rapidly increases leading to rupture of the specimen.

Creep crack behavior of creep-ductile CrMoV, CrMo and stainless steels is characterized by C^* integral in the secondary stage where the extensive creep regime occurs and is primarily defined for stationary cracks. Let us remind that C^* integral is suitable for characterizing creep crack growth behavior only in creep-ductile materials in which the strain rates associated with crack growth are small in comparison with the strain rates associated with creep deformation throughout the body except in a very small region near the crack tip [14].

C^* integral is defined as contour path independent integral and defines the amplitude of stress field around the crack tip:

$$C^* = \int_{\Gamma} \left(\dot{w} \cdot dy - \sigma_{ij} \cdot n_j \cdot \frac{\partial \dot{u}_i}{\partial x} ds \right) \tag{1}$$

where Γ presents path of the integral containing the crack tip, ds the increment in the contour path and $\dot{u}$ displacement rate vector at ds.

In the Eq. (1) $\sigma_{ij} \cdot n_j \cdot \frac{\partial \dot{u}_i}{\partial x}$ denotes the rate of the stress-power input into the area enclosed by Γ across the elementary length ds and $\dot{w}$ denotes the strain energy density rate defined as

$$\dot{w} = \int_0^{\dot{\varepsilon}_{kl}} \sigma_{ij} d\dot{\varepsilon}_{ij} \tag{2}$$

Experimental measurements of C^* take advantage of analogies with the J integral and it is defined in terms of a power release rate as:

$$C^* = -\frac{1}{B} \cdot \left(\frac{\partial}{\partial a} \int_0^{\Delta} P d\dot{\Delta} \right)_{\dot{\Delta}} \tag{3}$$

In Eq. (3) P is applied load, Δ is the load-line displacement and $\dot{\Delta}$ is load-line displacement rate.

4 Experimental Procedures

The aim of present paper is to demonstrate what could be obtained from replacements of aged power plant components made of P22 with new parts made of P91 steel.

The most important parameter for thick-walled components is thickness value and the most important procedure is its reduction. There is lot of technical and economical reasons for that. For instance, the time required for cooling of the component with the thinner wall is shorter so the thermal gradient through the wall thickness will be lower and lower will be thermal fatigue risk. Thinner wall is also more flexible and less residual stresses will appear during start-up and shutdown periods so the low-cycle fatigue risk will be lower.

Some advantages of grade 91 over the grade 22 are: much better elevated temperature strength and creep behavior, increased corrosion-oxidation resistance and improved resistance to thermal fatigue. Because of that the weight of boiler and piping components could be significantly reduced [15–17]. Grade 91 also posses' high thermal conductivity and low thermal expansion coefficient compared to austenitic steels.

Welding specifics of grade 91 will not be discussed here as well as the heat-affected zone properties [18, 19]. The effects of preheating and post-weld heat treatment on the economic benefits of material replacement are negligible comparing to the reduction of weld manufacturing work in whole.

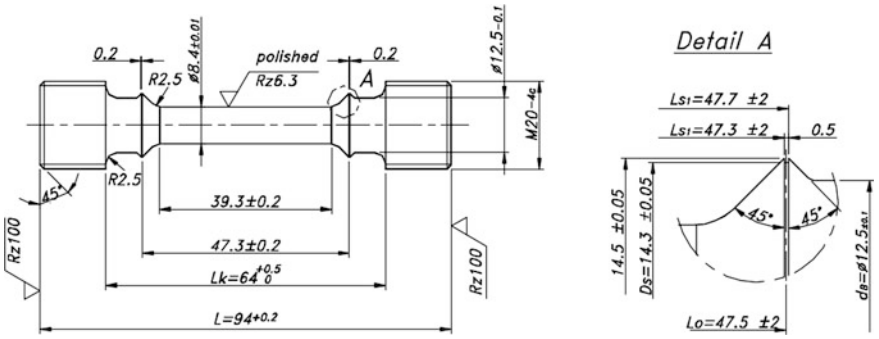

Fig. 2 Standard tensile and creep test specimen

Standard specimen used for tensile and creep testing at elevated temperatures is shown in Fig. 2. They were machined from the parent metal plate, welded plates and thermally simulated HAZ specimens [20, 21] (middle HAZ and Type IV cracking HAZ region). Tensile and uniaxial creep testing were carried out at operating temperatures which were 550 °C in case of P22 and 600 °C for P91 steel.

For creep crack growth testing standard Compact Specimens (CT) were machined according to ASTM E 1457 standard specifications [22]. CT specimens were taken from the welded plates where notches were positioned, using electrical discharge method (EDM), in the middle of the weld metal (WM) and in the HAZ (both in the centre of HAZ and the Type IV region), see Fig. 3. All CT specimens were side grooved 20 % after EDM nitching to $\frac{a_0}{W} = 0.5$ with the notch tip radius of 0.05 mm for sharp starter crack [22–25].

Typical extensometer used for tensile and uniaxial creep testings in a high temperature chamber is shown in Fig. 4.

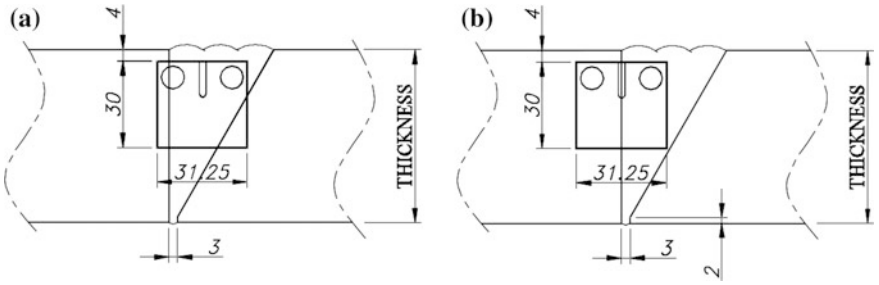

Fig. 3 Schematic drawings of CT specimens machined from the welded plates made of P22 and P91 with **a** notch in the WM and **b** notch in HAZ

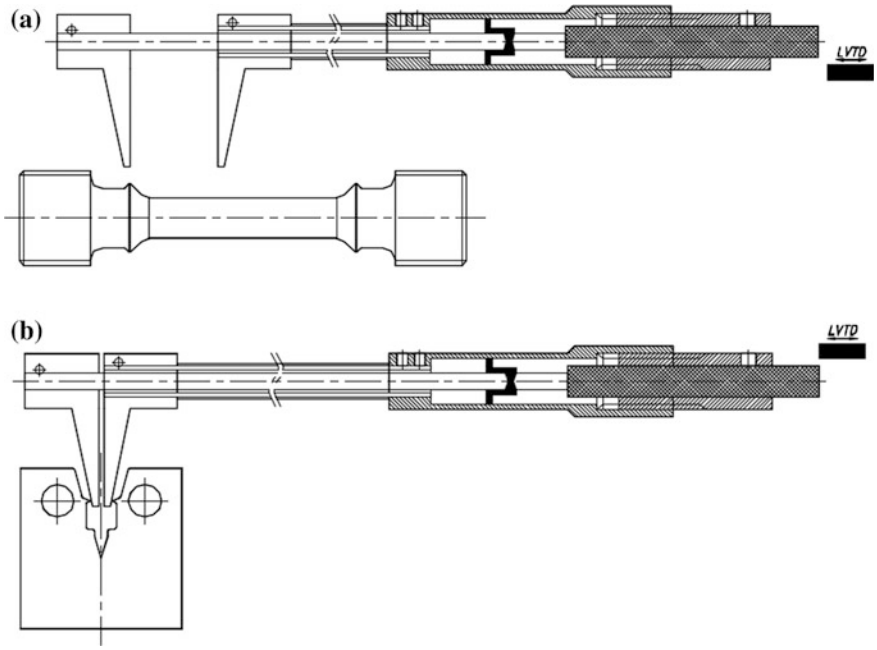

Fig. 4 Extensometer for high temperature **a** tensile and **b** uniaxial creep testings

5 Results and Discussions

In Fig. 5 tensile properties of all P22 specimens obtained at operating temperatures of 550 °C, are shown. From obtained stress-strain curves it can be seen that the welded joints were slightly undermatched because tensile properties of WM are lower than those of PM but the toughness is bigger. Type IV simulated HAZ region showed surprisingly high elongation meaning that the microstructure of this constituent is softened.

The reason why the elongation was so pronounced is that the simulation parameters were probably not properly selected. The yield strength of WM is higher than those of both HAZ constituents, but the ultimate strength values for the middle HAZ region were higher than for WM. Both yield and ultimate stresses in case of Type IV HAZ region are of lower values. In Fig. 6 the tensile properties of all P91 specimens obtained at operating temperatures of 600 °C, are shown. The welds in the case of new material were also undermatched. The values of both ultimate and yield stresses are decreasing from PM, WM, Type IV HAZ region and are lower in the middle HAZ region.

The dependence of rupture stress versus rupture time for P22 steel is shown in Fig. 7. After the long in-service period, degradation of PM expressed by lower values of rupture stresses can be seen. In Fig. 8 creep curves for rupture stress level of 120 MPa obtained at operating temperature for all types of tested specimens

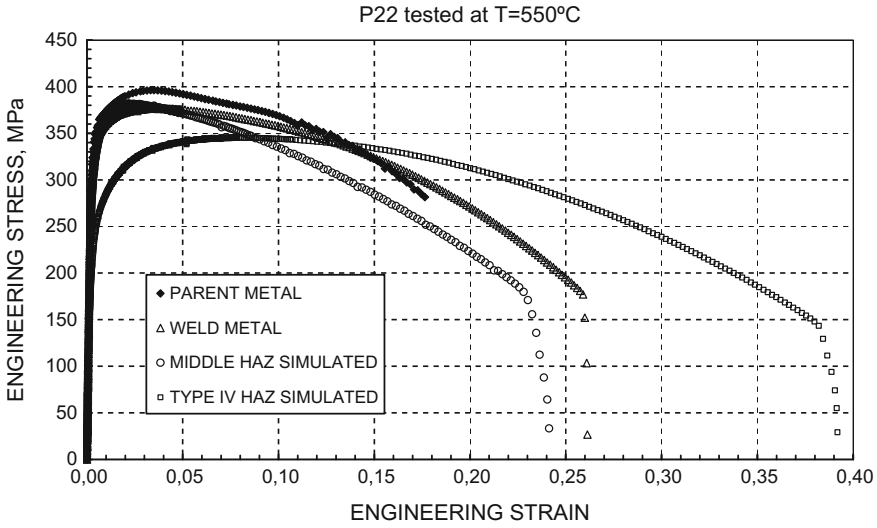

Fig. 5 Engineering stress versus engineering strain curves for P22 steel at 550 °C

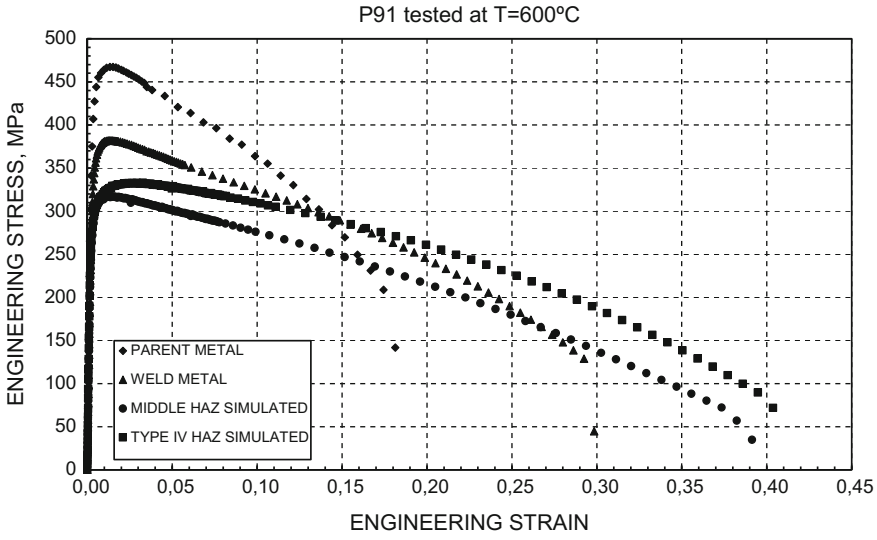

Fig. 6 Engineering stress versus engineering strain curves for P91 steel at 600 °C

made of P22 steel are shown. It can be seen that PM exhibits much lower creep strain than weld constituents. HAZ constituents have the highest strain rate and WM lies in between. The strain rate of Type IV HAZ region has the highest strain rate meaning, which was expected, because this particular region is the weakest HAZ constituent where the most of fractures occur.

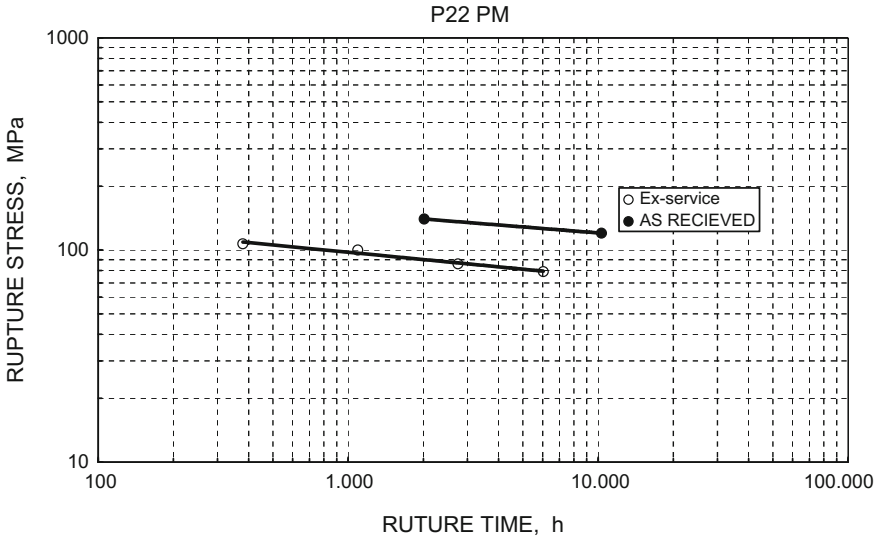

Fig. 7 Rupture stress versus rupture time correlation for P22 steel

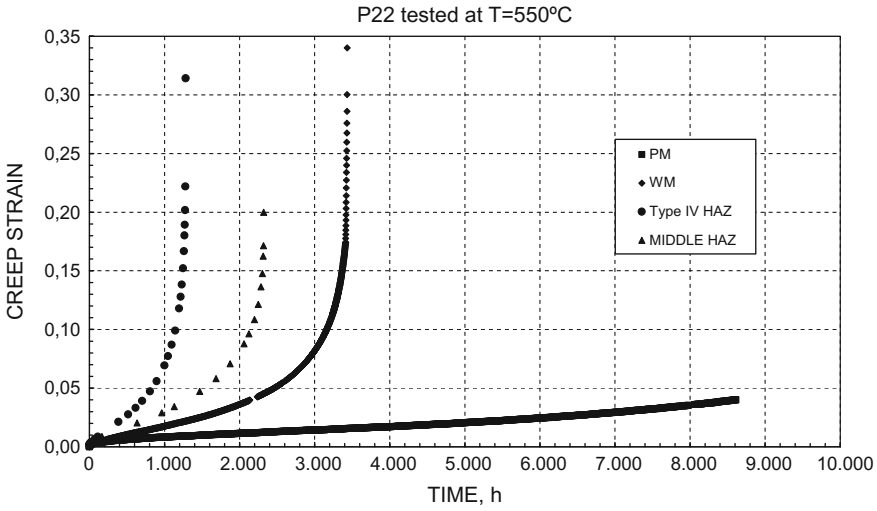

Fig. 8 Creep strain versus time curves under constant stress level of 120 MPa and constant temperature of 550 °C for tested material P22

Creep crack growth (CCG) is the slow extension of a macroscopic crack, which usually but not necessarily occurs along grain boundaries by the formation of creep cavities ahead of the crack tip [26, 27].

CCG tests were performed on standard CT specimens 25 mm thick which were first fatigue pre-cracked at room temperature. Then the fatigue tests were performed according to standard [22] at temperatures of 550 and 600 °C for steels P22 and P91, respectively.

In Fig. 9 the CCG rate $\frac{da}{dt}$ as a function of C^* integral is shown. Good correlation of CCG rates of P22 WM data with C^* is due to the fact that the notches were positioned in the center of WM and that cracks continued to propagate entirely through the WM.

Figure 10 shows the CCG correlation of P22 HAZ. It can be seen that the scatter is large particularly at lower crack growth rates. The explanation can be found in the fact that the HAZ microstructure heterogeneity makes that crack during propagation turns into WM or into PM. The crack path is unpredictable and precise positioning of the notch into the Type IV HAZ region is very difficult [28]. Besides that, a lot of secondary cracks appearing in HAZ are as well the reason of data scattering.

In Fig. 11 creep curves for rupture stress level of 145 MPa obtained at operating temperature for all types of tested specimens made of P91 steel are shown. From results shown in Figs. 8 and 11 it can be seen that the new material P91 is able to stand much higher stress level than P 22 steel. Unlike creep behavior of P22, in case of P91 steel higher creep strain rates are obtained for middle HAZ than for Type IV HAZ regions, and the PM slope is steeper than in case of P22. The reason for that could be improper selection of simulation parameters, most probably the cooling time $\Delta t_{8/5}$.

Figures 12 and 13 show the CCG correlation of steel P91WM and HAZ. Again data scattering is higher in the case of P91 HAZ.

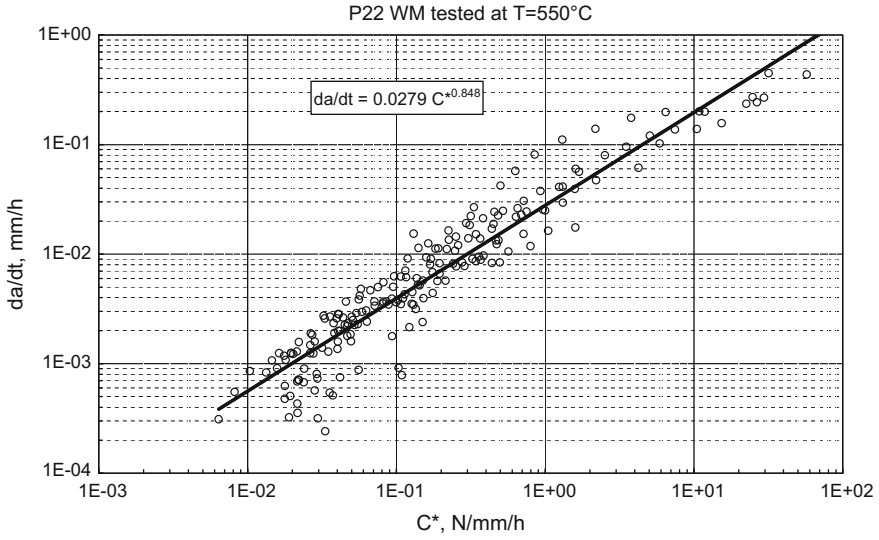

Fig. 9 Creep crack growth rate versus C^* integral for P22 WM at 550 °C

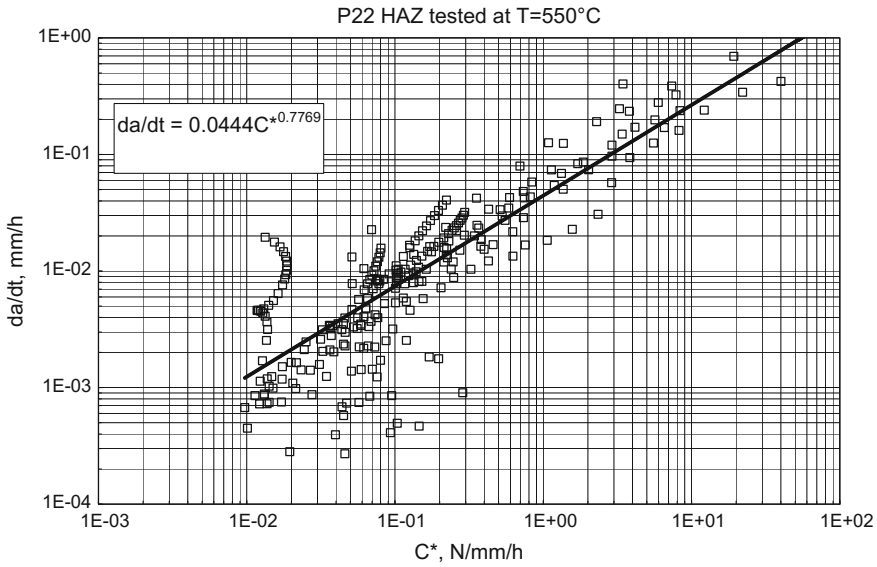

Fig. 10 Creep crack growth rate versus C^* integral for P22 HAZ at 550 °C

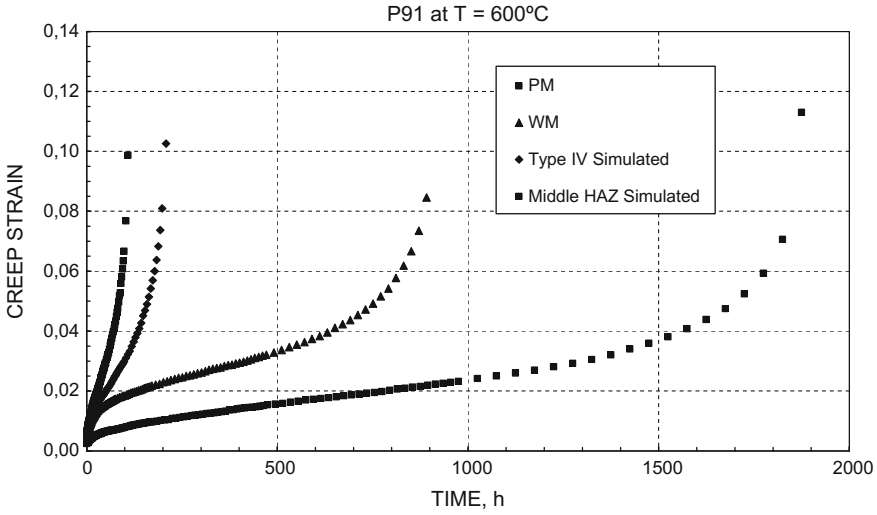

Fig. 11 Creep strain versus time curves under constant stress level of 145 MPa and constant temperature of 600 °C for tested material P91

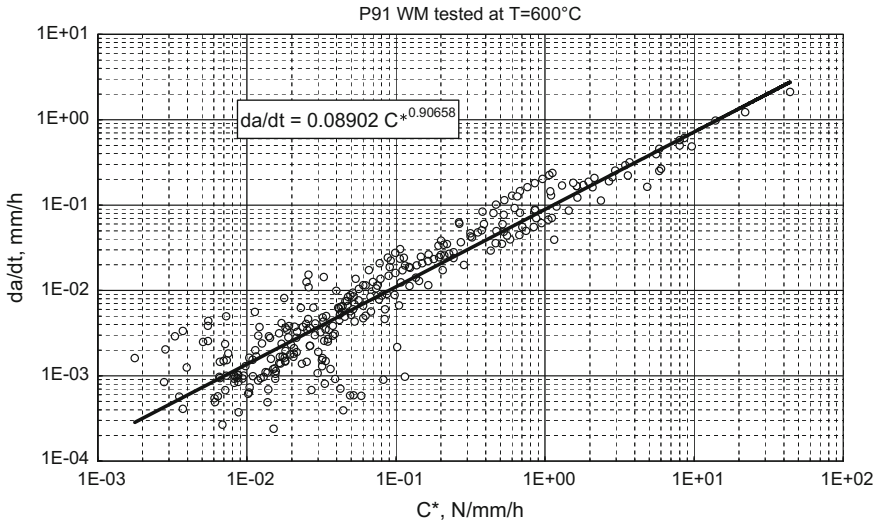

Fig. 12 Creep crack growth rate versus C^* integral for P91 WM at 600 °C

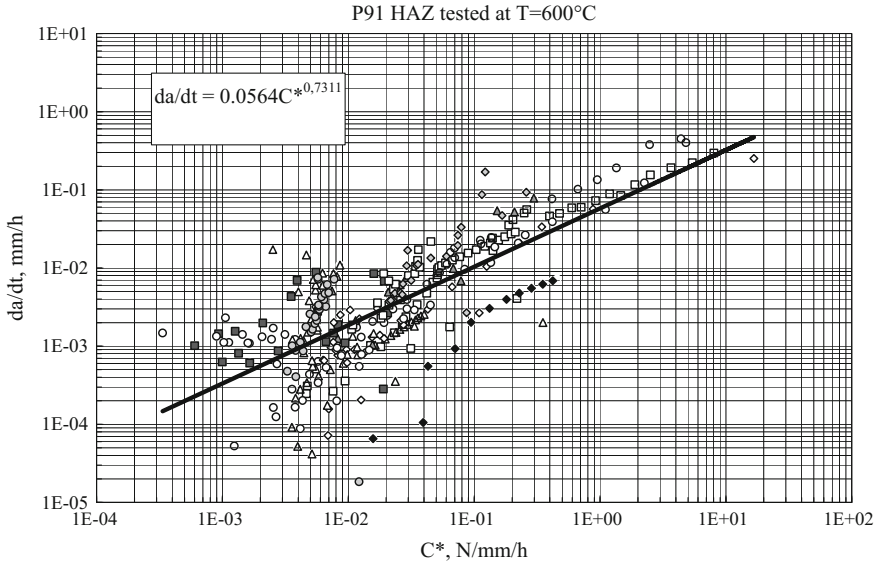

Fig. 13 Creep crack growth rate versus C^* integral for P91 HAZ at 600 °C

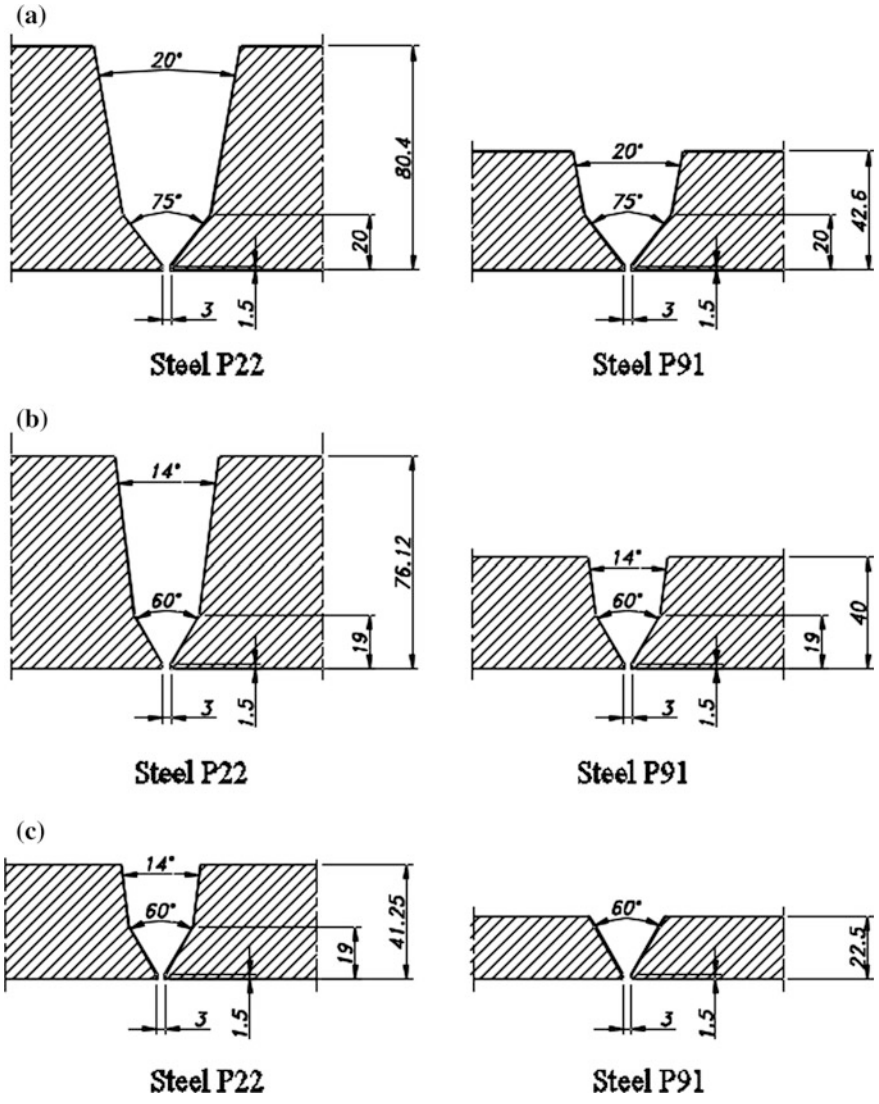

Fig. 14 Comparison of wall thicknesses in case of P22 and P91 steels: **a**, **b** superheater outlet headers and **c** reheater outlet header

6 Reduction of Thickness

Integrity and operational safety of power plant in whole depends largely on loaded welded components. Safety of welded structure is dependent of the properties of welded joint [29, 30]. So the calculation of minimum wall thickness should not neglect the type of joints and the shape of the weld grooves. As mentioned above,

replacement of aged power plants components with new ones made of advanced steels brings several benefits. The most important among benefits is the reduction of thickness of thick-walled components which results directly in weight reduction and reduction of weld material which leads indirectly to increase of reliability and safety of power plants components.

The replacement of P22 steel with P91 will be presented on three components: two final superheater outlet headers with wall thicknesses 80.4 and 76.12 mm and reheater outlet header with wall thickness 41.25 mm. The example of thickness reduction is shown in Fig. 14. It can be seen that thickness reduction in cases (a) and (b) was 47 % and in case (c) 45 %.

7 Summary

Steel P22 can be met in a large number of thermal power plants as the main material for manufacturing of critical power plant components like steam headers, pipelines or boilers. Throughout the modernizations of aged power plants P22 steel is commonly replaced with P91 steel. Critical power plant components are those whose failures cause prolonged outages and lead times and thus provoke high repair or replacement costs. Obviously, critical components of thermal power plants should be of the highest priority for inspection, maintenance and overhauls.

Acknowledgments Author acknowledges the financial support of the Serbian Ministry of Education, Science and Technological Development, project TR 35011. Author expresses gratitude to Professor Blagoj Petrovski from the University of Belgrade for valuable suggestions in writing this paper and to Jovan Savić, B.Sc. in Mechanical Engineering from Hydromech, Brazil for technical drawings of Figs. 2, 3, 4 and 14.

References

1. Milović L (2008) Significance of cracks in the heat-affected-zone of steels for elevated temperature application. Struct Integr Life 8(1):55–64
2. Viswanathan R, Bakker WT, Parker JD (eds) (2001) Advances in materials technology for fossil power plants. The Institute of Materials, London
3. Gandy D, Shingledecker J (eds) (2014) Advances in materials technology for fossil power plants. ASM International, Materials Park, OH
4. Bakić G, Sijački Žeravčić V, Đukić M et al (2011) Thermal history and stress state of a fresh steam-pipeline influencing its remaining service life. Thermal Sci 15(3):691–704
5. Bakić G, Sijački Žeravčić V, Đukić M et al (2013) Remaining life assessment of a high pressure turbine casing in creep and low cycle service regime. Thermal Sci 17(1):S127–S138
6. Bakić G, Šijački-Žeravčić V (2003) Estimation of long-term strength by microstructural parameters of low-alloyed steel exposed to creep-first part. Struct Integr Life 3(1):23–30
7. Bakić G, Šijački-Žeravčić V (2003) Estimation of long-term strength by microstructural parameters of low-alloyed steel exposed to creep-second part: determination of time-to-fracture. Struct Integr Life 3(2):85–92

8. The T91/P91 Book (2002): Vallourec and Mannesmann Tubes
9. http://www.globalcarbonproject.org
10. http://www.nextgenpower.eu
11. Naumenko K, Altenbach H (2007) Modeling of creep for structural analysis. Springer, Berlin
12. Webster GA, Ainsworth RA (1994) High temperature component life assessment. Chapman and Hall, London
13. Anderson TL (2005) Fracture mechanics-fundamentals and applications, 3rd edn. Taylor and Francis Group, Boca Raton, UK
14. Saxena A, Dogan B, Schwalbe K-H (1994) Evaluation of the relationship between C*, $\dot{\delta}_5$, and $\dot{\delta} t$ during creep crack growth. In: Landes JD, McCabe DE, Boulet JAM (eds) Fracture mechanics: twenty-fourth volume. ASTM STP 1207, pp 510–526
15. Milović L, Vuherer T, Blačić I, Vrhovac M, Stanković M (2013) Microstructures and mechanical properties of creep resistant steel for application at elevated temperatures. Mater Des 46:660–667
16. Milović L, Vuherer T, Zrilić M, Sedmak A, Putić S (2008) Study of the simulated heat affected zone of creep resistant 9–12 % advanced chromium steel. Mater Manuf Processes 23 (6):597–602
17. Zrilić M, Rakin M, Milović L, Burzić Z, Grabulov V (2007) Experimental and numerical evaluation of a steamline behaviour using local approach. Metalurgija 46(2):87–92
18. Milović L (2009) Steels for elevated temperature application: heat-affected zone specifics. In: Fundamentals of fracture mechanics and structural integrity assessment methods. MF-TMF-DIVK-IMS, Belgrade, pp 297–308
19. Vuherer T, Milović L, Gliha V (2011) Behaviour of small cracks during their propagation from Vickers indentations in coarse-grain steel: an experimental investigation. Int J Fatigue 33 (12):1505–1513
20. Milović L (2010) Microstructural investigations of the simulated heat affected zone of the creep resistant steel P91. Mater High Temp 27(3):233–242
21. Vuherer T, Dunđer M, L Milović, Zrilić M, Samardžić I (2013) Microstructural investigation of the heat-affected zone of simulated welded joint of P91 steel. Metalurgija 52(3):317–320
22. ASTM E 1457: 2015 standard test method for measurement of creep crack growth times in metals
23. Dogan B, Petrovski B (2001) Creep crack growth of high temperature weldments. Int J Press Vessels Pip 78:795–805
24. Damnjanović S, Sedmak A, Anyiam HA, Trišović N, Milović L (2002) C* Integral evaluation by using EPRI procedure, in Serb. Struct Integr Life 2(1–2):51–54
25. Sedmak A, Milović L, Pavišić M, Konjatić P (2014) Finite element modeling of creep process —steady state stresses and strains. Thermal Sci 18(1):179–188
26. Riedel H (1987) Fracture at high temperatures. Springer, Berlin
27. Riedel H (1989) Recent advances in modelling creep crack growth. In: Proceedings of the 7th international conference on fracture (ICF7). Houston, Texas, pp 1495–1523
28. Manjgo M, Međo B, Milović L, Rakin M, Burzić Z, Sedmak A (2010) Analysis of welded tensile plates with a surface notch in the weld metal and heat affected zone. Eng Fract Mech 77 (15):2958–2970
29. Vuherer T, Zrilić M, Milović L, Samardžić I, Gliha V (2014) Suitability of heat treatment for crack resistance of material in the connection part of heavy transporter for liquid slag. Metalurgija 53(2):243–246
30. Milović L, Vuherer T, Zrilić M, Momčilović D, Jaković D (2011) Structural integrity assessment of welded pressure vessel produced of HSLA steel. J Iron Steel Res Int 18 (1–2):888–892

The Two-Parameter Approach for Fracture Mechanics: Some Industrial Applications

M. Hadj Meliani, O. Bouledroua, M. Ould-M'beirick, K. El-miloudi, Dj. Neggaz, T. Nateche, A. El-azzizi, H. Bokort, F. Houari and Guy Pluvinage

Abstract The importance of the two-parameter approach in linear elastic fracture mechanics analysis is increasingly being recognized for fracture assessments in engineering applications. The consideration of the second parameter, namely, the elastic T-stress, allows estimating the level of constraint at a crack or notch tip. It is important to provide T-stress solutions for practical geometries to employ the constraint-based fracture mechanics methodology. In the present, the two-parameter approach solutions are provided for some industrial applications to (i) Assess a gouge defect in a pipe submitted to internal pressure, (ii) A V-shaped notch in the case of surface defects in a pressurised pipeline, (iii) The crack paths and a particular attention are given in the case of hydrogen embrittlement, (iv) To extend the analysis of constraint effect in the influences of notch radius on the Material Failure Master Curve (MFMC) and (v) To investigate the effects of non-singular stress (T-stress) on the mixed mode (I + II) of fracture near notch-tip fields elastic compression-sensitive under plane stress and small scale yielding conditions.

Keywords Material failure curve · Notch stress intensity factor · Two parameter fracture · Mixed mode

M. Hadj Meliani (✉) · O. Bouledroua · M. Ould-M'beirick · K. El-miloudi · Dj.Neggaz · T. Nateche · A. El-azzizi · H. Bokort · F. Houari
LPTPM, Hassiba Benbouali University of Chlef, Salem City, PO. Box 151, 02000 Chlef, Algeria
e-mail: hadjmeliani@yahoo.fr; hadjmeliani@univ-metz.fr

M. Hadj Meliani · G. Pluvinage
LaBPS-ENIM, Université Paul Verlaine de Metz, 57045 Île de Saulcy, France

G. Pluvinage and L. Milovic (eds.), *Fracture at all Scales*,
Lecture Notes in Mechanical Engineering, DOI 10.1007/978-3-319-32634-4_6

1 Introduction and Background on the Master Material Failure Curve

The volumetric method (VM) [1] is a local fracture criterion which assumes that the fracture process requires a certain cylindrical volume with the effective distance as its diameter. The fracture process volume is the "high stress region" where the necessary fracture energy release rate is stored. The difficulty is in finding the limit of this high stress region. This limit is a priori not a material constant, but depends on the loading mode, structure geometry and load level. The size of the fracture process reduced to the effective distance X_{ef} according to the abovementioned assumptions is obtained by examination of the stress distribution. The bi-logarithmic elastic-plastic opening stress σ_{yy} distribution (Fig. 1) along the ligament exhibits three distinct zones. The elastic-plastic stress primarily increases and then attains a peak value (zone I), then it gradually drops to the elastic-plastic regime (zone II). Zone III represents linear behaviour in the bi-logarithmic diagram. It has been shown by examination of fracture initiation sites that the effective distance corresponds to the beginning of zone III which is, in fact, an inflexion point on this bi-logarithmic stress distribution. A graphical method based on the relative stress gradient $\chi(r)$ associates the effective distance to the minimum of χ. The relative stress gradient is given by:

$$\chi(r) = \frac{1}{\sigma_{yy}(r)} \frac{\partial \sigma_{yy}(r)}{\partial r} \tag{1}$$

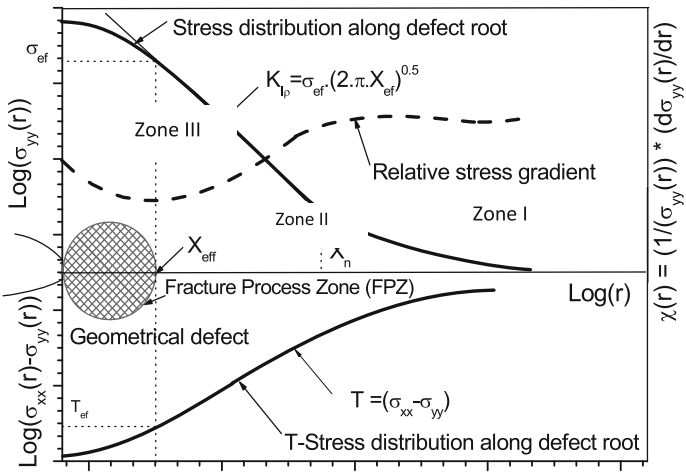

Fig. 1 Determination of the notch stress intensity factor and the effective T-stress at the notch tip (the stress distribution is computed for elastic behaviour)

where $\chi(r)$ and $\sigma_{yy}(r)$ are the relative stress gradient and maximum principal stress or opening stress, respectively. The effective stress for fracture σ_{ef} is then considered to be the average value of the stress distribution over the effective distance. However, stresses are multiplied by a weight function in order to take into account the stress gradient due to geometry, the loading mode and the acting distance r. The effective stress can then be obtained from:

$$\sigma_{ef} = \frac{1}{X_{ef}} \int_0^{X_{ef}} \sigma_{yy}(r) \times (1 - r) \times \chi(r)\, dr \tag{2}$$

Therefore, the notch stress intensity factor is defined as a function of effective distance and effective stress:

$$K_\rho = \sigma_{ef} (2\pi X_{ef})^\alpha \tag{3}$$

where K_ρ, σ_{ef} and X_{ef} are the notch stress intensity factor, effective stress and effective distance, respectively, and α is the slope of the stress distribution in zone III. The exponent α depends on the notch angle and is equal to 0.5 if the sides of the notch are parallel. A description of this kind of stress distribution at the notch tip and the procedure using the relative stress gradient are given in Fig. 1.

For fractures emanating from a notch-like defect where notch fracture mechanics can be applied, the transferability from fracture toughness obtained for a given geometry and loading mode to another is treated with the concept of the stress constraint, which emanates from the defect tip distribution. If we compare the stress distribution obtained in a reference situation (generally small scale yielding) with another general one, the stress distribution is modified in two ways: there is a shift in the stress distribution and a small rotation. The shift in the stress distribution is introduced into the plastic constraint. In the literature, we can note the following constraint parameters: the plastic constraint factor [2], the stress triaxiality [3], the Q parameter [4], T stress [5] and A_2 [6]. For a crack, Larsson et al. [7] have suggested describing the elastic stress field at the crack tip by three terms and introduced for the first time the T term as the second one of the series:

$$\sigma_{ij} = \frac{K_{ij}}{\sqrt{2\pi r}} f_{ij}(\theta) + T\delta_{1i}\delta_{1j} + A_2(\sqrt{r}) \tag{4}$$

Therefore, T stress is ideally a constant stress which acts along the crack direction and shifts the opening stress distribution according to the sign of this stress. For a stress distribution emanating from a blunt crack or notch, T stress is not constant along the ligament. This leads us to consider a conventional value defined as the effective T stress.

Several methods have been proposed in the literature to determine T-stress for cracked specimens. The stress difference method has been proposed by Yang and Ravichandar [8]. Chao et al. [9] computed by the finite element method σ_{xx} in the

direction $\theta = 180°$ and defined the T stress as the value of σ_{xx} in the region where its value is constant. Ayatollahi et al. [10] determined T stress by using the displacement method in the finite element and obtained a stabilised T stress distribution along the ligament. T was then computed by the sum of two contributions, one to the crack pressure distribution and the second to the difference $(\sigma_{xx} - \sigma_{yy})$ at a distance equal to the crack length. Eisele et al. [11] pointed out that the fracture toughness K_c or J_c increases with the loss of constraint T stress, A2 or Q. Hadj Meliani et al. [5] have also pointed out this effect on the notch fracture toughness K_ρ,c with the critical constraint $T_{ef,c}$ described by the critical value of the $T_{ef,Xef}$ parameter. The authors found a linear relationship between the two parameters

$$K_{\rho,c} = a\, T_{ef,c} + K^0_{\rho,c} \tag{5}$$

where $K^0_{\rho,c}$ is the fracture toughness corresponding to $T_{ef,c} = 0$, which is considered a reference. For example, $a = -0.069$ and $K^0_{\rho,c} = 77.2\,\text{MPa}\sqrt{\text{m}}$ for API X52 pipe steel. The curve K_ρ,c = f($T_{ef,c}$) is called the material failure master curve. This curve is used for the transferability of the value of fracture toughness obtained from a test to the real fracture resistance of the structure with a different constraint than that of the test specimen.

The ASTM E-399 testing procedure recommends certain types of specimen geometries and K_{Ic} can be considered as the plane-strain fracture toughness. All specimen geometries recommended by ASTM E-399 have high constraint. Using the recommendation specimen geometry for testing creates an "ASTM Window" since their corresponding T or A_3 values are within a certain range ($0.45 < a/W < 0.55$). A K_{IC} value is believed to represent a lower limiting value of fracture toughness and the ASTM E-399 may not be generally valid. Increasing the size of a specimen shifts the stress distribution closer to the K-stress. Consequently, larger specimens tend to possess better K-dominance. This may explain why a large specimen is better suited for ASTM fracture toughness K_{Ic} testing in addition to the reason for the plastic zone size. This phenomenon limiting the recommendation of ASTM and can be explained using the analytical K-T or K-A_3 relation for common the effects of specimen geometries.

In this paper, the fracture resistance of some type of steel was determined using notched specimens. The critical notch stress intensity factor ($K_{\rho,c}$) and the critical effective T stress ($T_{ef,c}$) as constraint parameters were determined and reported in a Material Failure Master Curve (MFMC), $K_{\rho,c}$ = f($T_{ef,c}$) and reported for some industrial applications.

2 Some Industrial Applications of the Two Fracture Mechanics Approach

2.1 *Assess a Gouge Defect in a Pipe Submitted to Internal Pressure*

According to the Williams [12], the importance of the global approach with two parameters (K-T) or (K-A_3) in the analysis of the linear elastic fracture mechanics in the field of structures is presented. Under internal pressure and in mode I loading, the (K-T) approach is applied for the API X52 steel, containing U-shaped longitudinal defects in the surface. The objective is to propose a numerical study, defining the stress intensity factor K and the transversal T-stress, by applying the finite element method, in 2D, using the software ANSYS 12.1. We propose the method of line, inspired from the volumetric approach developed by Pluvinage [1], this method is based on the determination of the effective stress T_{ef} over an effective distance X_{ef} ahead of the notch tip. We studied, in this part the stress distribution at the tip of the notches on a pipe transporting gas submitted to internal pressure. To cover a practical range, four different values of the internal ratio of the cylinder to the thickness, R_i/t ranging from 5 to 40; moreover, four different values of the notch depth to the thickness, a/t, extending from 0.1 to 0.75 and five different values of pressure extending from 40 to 75 bars, have been selected. The notch acuity radius has been fixed for all geometry at 0.25 mm. In an isotopic linear elastic body containing a two-dimensional notch submitted to symmetrical charging, the stress field distribution can be written by a development of the series of Williams [12]; near the crack bottom, where the high-order terms of the development of the series are insignificant, the stress for the mode I is written as follows:

$$\begin{aligned}
&\sigma_{XX} = \frac{K_I}{\sqrt{\pi r}}\cos\frac{\theta}{2}\left(1 - \sin\frac{\theta}{2}\sin\frac{3\theta}{2}\right) + T \quad \sigma_{YY} = \frac{K_I}{\sqrt{\pi r}}\cos\frac{\theta}{2}\left(1 + \sin\frac{\theta}{2}\sin\frac{3\theta}{2}\right)\\
&\sigma_{ZZ} = \frac{K_I}{\sqrt{\pi r}}2\upsilon\cos\frac{\theta}{2} + E\varepsilon_{ZZ} + \upsilon T \quad \sigma_{Xy} = \frac{K_I}{\sqrt{\pi r}}\sin\frac{\theta}{2}\cos\frac{\theta}{2}cos\frac{3\theta}{2}\\
&\sigma_{Xz} = \sigma_{yz} = 0
\end{aligned} \tag{6}$$

The low indexes *x*, *y* and *z* suggest a Cartesian coordinate local system constituted by normal stress and tangential stress at notch tip; *r* and θ are the local polar coordinates, K_I the stress intensity factor in a mode I, *E* the modulus of Young and υ is the coefficient of Poisson. The method known as the stress difference is first proposed by Yang and Ravichandar [8]. This method implements directly the simple analysis by finite elements. Its objective is to calculate approximately the T-stress by the evaluation of the stress difference (σ_{xx}–σ_{yy}) at a point ahead of the crack-tip. The fundamental idea is to describe the evolution of errors, in numerical values, obtained at the crack-tip over the distance r, c.-à-d. the crack-tip distance.

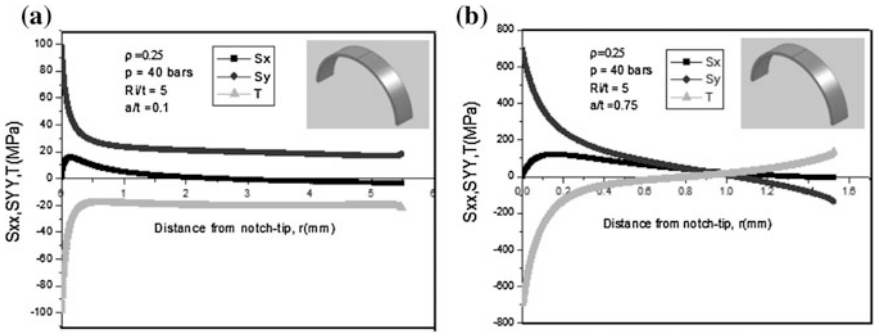

Fig. 2 Evolution of stress difference along ligament for **a** a/t = 0.1 and **b** a/t = 0.75

In the same way this difference should eliminate the effective errors. An example of the defect depth effect, over T-stress, is given in Fig. 2a and b for a/t = 0.1 and a/t = 0.75 for an under-pressure pipe containing a surface defect. The results are influenced by errors provided by the finite elements analysis.

We have noted according to Fig. 2, that there is a change in the sign of T-stress, from negative values to positive values, maybe due to the importance of the local moment opening the crack edges, which grows with the depth increase. The negative values indicate high constraint at the notch tip [5]. T-stress becomes more positive when getting closer, more quickly (acceleration), of the free surface of the pipeline.

Figure 2 shows the evolution of stress σ_{xx}, σ_{yy} along the ligament for a longitudinal surface defect with an acuteness radius ρ = 0.25 in a U shape. T-stress represents the difference of stress σ_{xx} and σ_{yy} calculated by Yang et al. [8]. This method doesn't give a constant value at certain distance of the notch tip contrary to the literature [13–16]. For the short notches (a/t = 0.1), T-stress always assumes negative values, when the ratio of the notch long was under 30 % (a/t < 0.3), on the other hand for long notches (a/t = 0.75) T-stress assumes negative values, as from 50 % of the ligament, T values will assume a positive sign, this change of the sign may be due to the importance of the local moment opening the crack edges, which grows with the depth increase. Figure 3a, b shows the evolution of T-stress, for a surface longitudinal notch under pressure of 40 bars, for different instances of the ratio (R_i/t = 5 and 20). We have noticed that T-stress grows with the notch depth. T-stress evolution, for a surface longitudinal notch under pressure of 40 bars, of a notch depth a/t = 0.1, 0.75 for different values R_i/t (R_i/t = 5, 10, 20, 40) is represented in Fig. 4.

We have noticed that T-stress grows with the increase of the ratio R_i/t. T-stress evaluation for short notches and long notch Fig. 5. We note that, for any notch depth value, the transition of T-stress from a negative value (tension) to a positive value (compression), is very quick when we increase the pressure. The crack will deflect swiftly from the main direction and the resultant path of the crack will be unstable (zig-zag). Near the notch tip, the results are influenced by numerical errors,

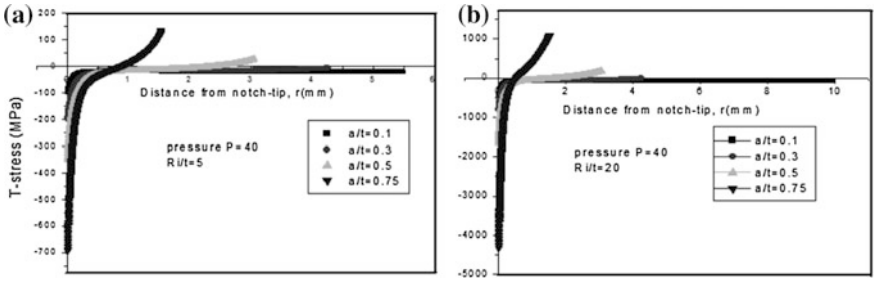

Fig. 3 Evolution of T-stress for a longitudinal surface notch under pressure of 40 bars, for the instances: **a** $R_i/t = 5$ and **b** $R_i/t = 20$

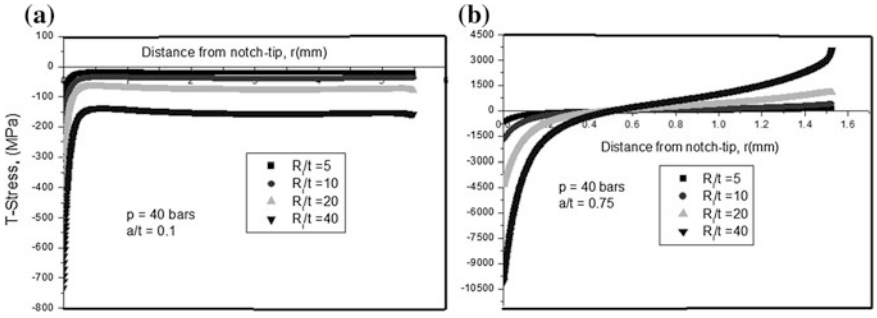

Fig. 4 Evolution of T-stress, for a surface longitudinal notch under pressure of 40 bars, with a notch thickness of a/t = 0.1, 0.75 for different values R_i/t **a** for short notches and **b** for long notches

obviously provided by the finite elements calculation, in the form of a highly conspicuous area. The effects of the superior terms, in the development of the series of Williams, are significant along the ligament.

Figure 6a, b show the variations of the constraint parameters for a pipe with a 219.1 mm of diameter to the notch-tip represented by the effective stress T_{ef}, for different pressures of 40 and 75 bars respectively, and the ratios $R_i/t = 5-40$ with the presence of depth notch a/t = 0.1–0.75. As noted, the effective T-stress is determined by the volumetric method, as the effective stress near the notch-tip at an effective distance. We note that according to the two (Figs. 6 and 7), values of the effective stress T_{ef} decrease with the increasing of the relative size of the notch tip (area 2); for the depths $a/t \leq 0.3$ (area 1), the effective stress T_{ef} keep nearly constant for any pressure and relative diameter (R/t). We distinguished that the values of the effective stress T_{ef} become the smallest with the increasing of any parameters values: the internal ratio of the cylinder to the thickness (R_i/t) and the pressure P. Another method used just a single parameter (the Notch Stress Intensity Factor, $K_{I\rho}$) was adopted by [17], calculate the toughness of the X52 steel, on curved Roman Tiles noted by RT, for two pipe diameters 219 and 610 mm as $K_{I\rho} = 57.21$ MPa $m^{0.5}$ and $K_{I\rho} = 69.25$ MPa $m^{0.5}$, respectively. They confirm that

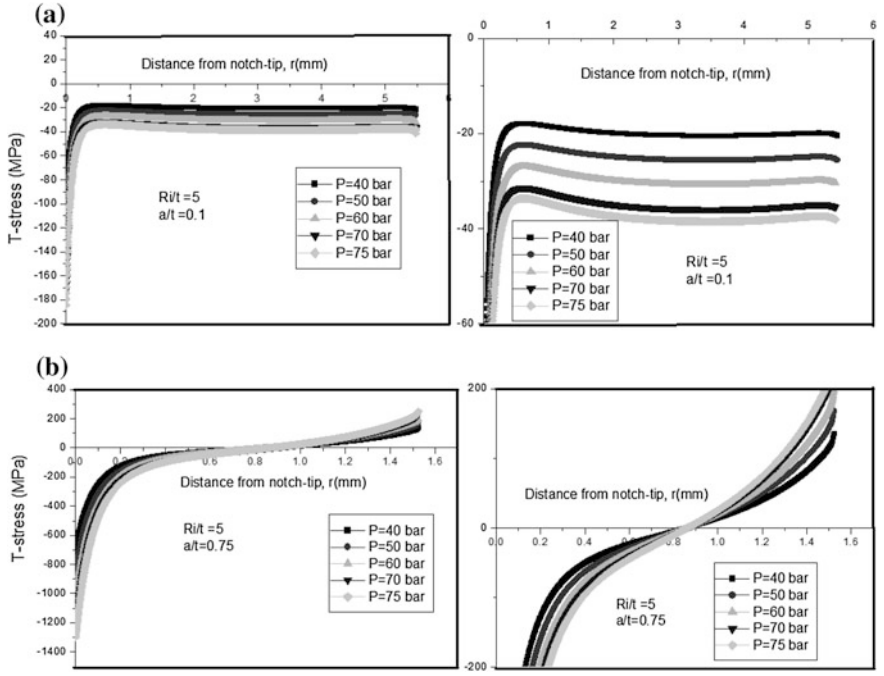

Fig. 5 Evolution of T-stress values, for a surface notch under pressure of P = 40, 50, 60, 70 and 75 bars) for **a** short notches and **b** long notches with ($R_i/t = 5$)

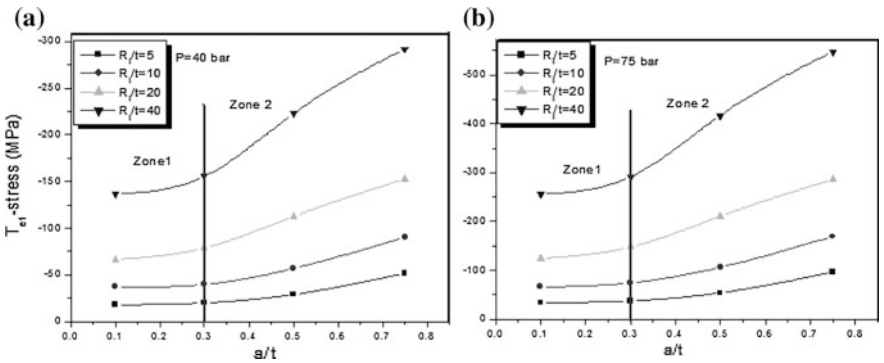

Fig. 6 Development of constraint parameter at notch tip represented by effective stress, for different situations of pressure **a** 40 bars and **b** 75 bars, for pipeline 219.1 mm in the diameter

the toughness value change with the geometrical parameters of the material. The difference between the two results is in the order of 17 %, this is accounted by the fact that their chemical compositions and their mechanical properties are not identical [18].

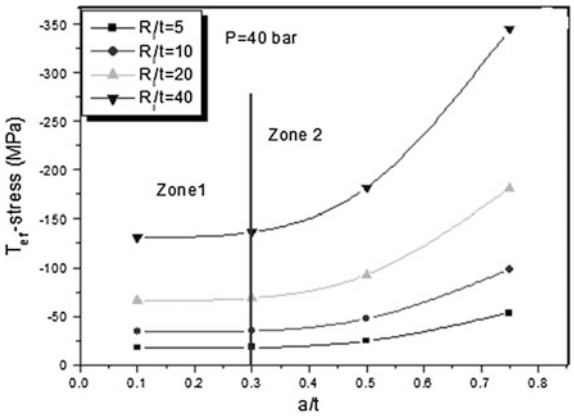

Fig. 7 Example of the constraint parameter development at the notch tip represented by an effective stress for a pressure of 40 bars and pipeline diameter of 610 mm

The same toughness has been resumed by [17] on CT specimens test. The fracture initiation point has been captured by acoustic emission and the results have given as critical Stress Intensity Factor K_{Ic} = 95.54 MPa $m^{0.5}$. This explains the difference between the two type of specimens by the fact that, the notch direction is different and the structure and the mechanical properties differ somewhat, according to specimen direction. Mangin [19] found an average value of the toughness, K_{Ic} = 95.5 MPa $m^{0.5}$, for CT specimen. We note that the explanation is simple, the both scale effect and the transferability between laboratory test specimens and the real structure play a very important role to predict the material toughness. According to our observation on Fig. 8a, b, we have mentioned that the effective stress intensity factor grows with the increase of the notch depth and the internal

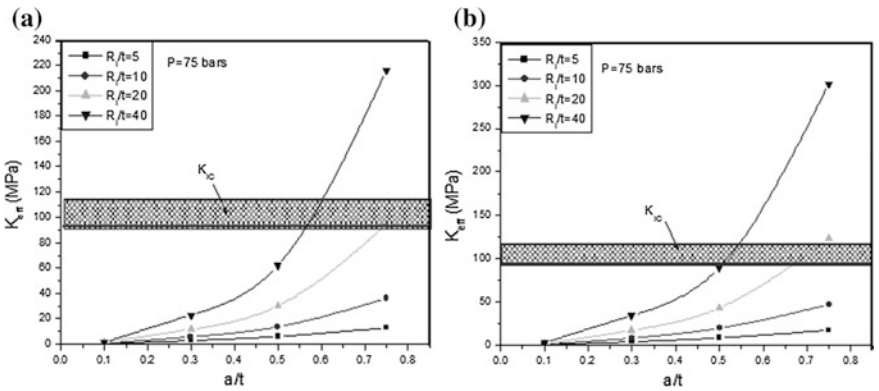

Fig. 8 Evolution of the effective stress intensity factor for a pressure of 75 bars on the **a** pipeline with 219.1 mm in diameter and **b** 610 mm

radius of the pipeline. It is also interesting to note that the bigger pipe with the smaller diameter for the same service pressure, the NSIF grows with the increase of the aspect ratio of the defect a/t. This means that the transverse notch exerts a more dangerous effect on big diameters pipelines than on those of small diameters, in the same conditions of loading.

2.2 The Crack Paths and Hydrogen Embrittlement

The materials used in this study are X52 steel meeting requirements of API 5L standard. API X52 steel was the most common gas pipeline material for transmission of oil and gas during 1950–1960. Chemical composition of the steels is given in Table 1. The mechanical properties of the steel have been also presented in Table 2. Here, E, σ_Y, σ_u, A%, n, k and K_{Ic} are the Young's modulus, yield stress, ultimate stress, elongation at fracture, strain hardening exponent and hardening coefficient in the Ramberg-Osgood law, the fracture toughness, respectively.

Specimens of three geometries, namely, CT (width of W = 63.80 mm, height of 61 mm), DCB (height of W = 45.70 mm) and SENT (width of W = 58.40 mm) were extracted from a steel pipe of diameter 610 mm. Thickness of all specimens was equal to 5.8 mm. The specimens have a notch with a notch angle $\varphi = 0$ and a notch radius $\rho = 0.25$ mm.

To measure the notch fracture toughness of the pipe steels in radial direction, non-standard curved notched specimens, so called "Roman tile" (RT) specimens, were also used since it is not possible to get flat specimens from small diameter pipes for measurement of through thickness mechanical characteristics. Therefore, the special device and specimens have been developed. The specimen shape is a circle arc. The specimen was loaded by three-point bending. The details of test set-up of three-point bend test for RT specimens and testing machine with the bend-test fixture are given in [20–22]. Test specimen sets include specimens with the initial notch aspect ratio a/W varied from 0.1 to 0.7. The specimens are immersed into the cell with solution NS4 (Table 3) and exposed under constant potential of polarization, which is slightly negative than free corrosion potential for given steel. The hydrogen charging process is controlled by registration of the

Table 1 Chemical composition of steel X52 (weight %)

C	Mn	P	Si	Cr	Ni	Mo	S	Cu	Ti	Nb	Al
0.22	1.220	–	0.240	0.16	0.14	0.06	0.036	0.19	0.04	<0.05	0.032

Table 2 Mechanical properties of steel X52

	E (GPa)	σ_Y (MPa)	σ_u (MPa)	A (%)	n	k	K_{Ic} MPa$\sqrt{m}$
X52	210	410	528	32	0.164	876	116.6

Table 3 Chemical composition of solution NS4

Chemical composition	Formula	Composition (mg/L)
Potassium chloride	KCl	122
Hydrogenocarbonate of sodium	$NaHCO_3$	483
Calcium chloride dihydrate	$CaCl_2{\cdot}2H_2O$	181
Sulfate of magnesium heptahydrate	$MgSO_4{\cdot}7H_2O$	131

cathodic polarisation current. The pH of solution is automatically controlled between 6.6 and 6.8. These values correspond to the pH of the ground, which surrounds the pipelines (approximately 6.7). The cell of loading out of electrolytic hydrogen, its various components and details of hydrogen charging are presented in [20]. The four specimens of each configuration were tested, two for reference test in air at room temperature, and two for the test after hydrogen charging. The tests were carried out at room temperature. Displacement rate was 0.02 mm/s.

The test procedure allowed measuring the load corresponding to crack initiation and fracture. For experimental determination of the notch stress intensity factor $K_{\rho,c}$ and the T -stress a strain gauge measurement technique has been employed [22]. Specimens were equipped with strain gauges. These gauges were glued at distance of 3 mm from the notch tip in particular direction. To minimize the strain averaging effects, the smallest available gauges with gauge length 0.8 mm and gauge factor 2.11 were used in the experiments. Acoustic emission technique has been employed for this purpose. Comparison of dependences of the load versus time and duration of acoustic emission versus time indicates crack initiation and fracture.

For this event, acoustic salves with the highest duration and the most important number of acoustic hits are detectable. An example of determination of strain at initiation and fracture is given in Fig. 9 for RT specimen with the notch aspect ratio a/W = 0.6.

Thus, fracture initiation and critical load were detected by acoustic emission and used for numerical calculation of the notch fracture toughness and the T-stress ahead of the notch tip by Finite Element method. The T-stress is evaluated using finite element method (Castem2000) and computing the difference of principal stresses along ligament for crack initiation and fracture. Time of exposition under hydrogenating conditions has been suggested as it was recommended in [23]. The effect of hydrogen charging on the critical notch stress intensity factor for the API 5L X52 steel in the case of CT specimen with a/t = 0.5 is presented in Table 4. It can be seen a saturation of the hydrogen embrittlement after 40 days under electrolytic hydrogen charging (Fig. 10). The critical notch stress intensity facture for crack initiation decreases by 15.7 %.

To analyze the effect of hydrogen charging on crack initiation and fracture, two fracture toughness parameters, namely, the critical notch stress intensity factor and the effective T-stress of X52 steel are determined for four specimens (SENT, CT, RT and DCB) with a/t = 0.5 and for constant electrolytic hydrogen charging

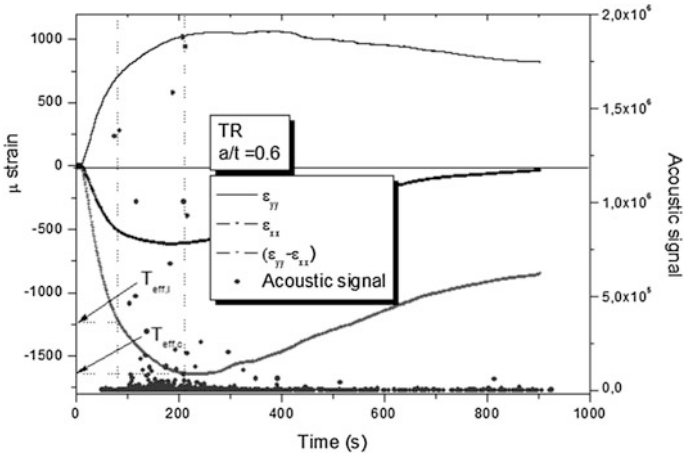

Fig. 9 Determination of initiation and fracture strain by acoustic emission

Table 4 Evolution of APL X52 test with and without hydrogen (in days)

Time of charging	0 days [14]	10 days		20 days		30 days		40 days
Specimen (CT, a/t = 0.5)	CT0	CT1	CT2	CT3	CT4	CT5	CT6	CT7
Critical load (kN)	12.57	12.40	12.32	11.89	11.93	11.02	10.92	10.90
$T^{i}_{\rho,3mm}$	−229.18	−220.80	−215.75	−214.45	−212.28	−208.79	−202.44	−203.16
$K^{i}_{\rho,3mm}$	74.88	71.70	70.21	67.10	66.88	64.43	63.12	63.25
$T^{c}_{\rho,3mm}$	−333.87	−327.66	−320.55	−318.29	−314.87	−309.02	−300.55	−298.26
$K^{c}_{\rho,3mm}$	98.04	94.39	92.68	88.26	87.65	86.36	82.54	81.66

holding time of 30 days (Table 5). To predict failure of the specimens after hydrogen charging, the following criterion of local failure should be considered [24]

$$C_{H\max}K^{m} = const. \tag{7}$$

Here, is maximum local hydrogen concentration ahead of the crack tip, $K_{\max}$ is the maximum value of the applied stress intensity factor.

Equation (7) gives the physical criterion for local failure in the fracture process zone, i.e. in the vicinity of the notch tip, and reflects changes in the hydrogen peak which resulted from the hydrogen redistribution due to the increase of the maximum stress intensity factor as the crack length increases under static loading. This conclusion is in agreement with the observed experimental results for different values of the maximum stress intensity factor [24].

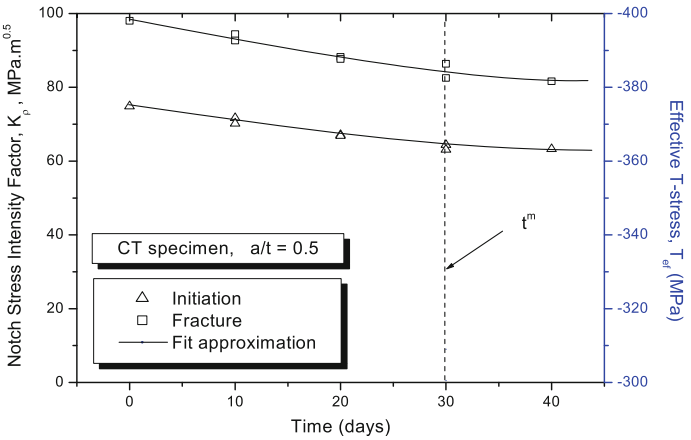

Fig. 10 Effect of electrolytic hydrogen charging on the critical notch stress intensity factor for the CT specimen (a/t = 0.5) of APL X52 steel

Table 5 Example of the two fracture parameters in hydrogen environment for X52 steel (a/t = 0.5)

Specimen a/t = 0.5	With hydrogen		Without hydrogen	
	$T^{exp}_{\rho,3mm}$	$K^{exp}_{\rho,3mm}$	$T^{exp}_{\rho,3mm}$	$K^{exp}_{\rho,3mm}$
CT	−210,632	87,856	−333.876	98.045
SENT	−326,865	99,263	−343.564	105.365
RT	−71,125	80,652	−79.343	89.985
DCB	75,785	63,854	82,430	67,933

For a solid with a notch the failure criterion (8) could be assumed to be the same replacing $K_{\max}$ on the notch fracture toughness $K_{\rho,c}$. It should be also noted, that the hydrogen peak $C_{H\max}$ corresponds to the effective distance. The value of $C_{H\max}$ is reduced and moves away from the crack tip as the maximum stress intensity factor $K_{\max}$ increases [24]. This fact allows concluding that $C_{H\max} \sim 1/X_{ef}$. In this case, the following dependence should be assumed $C_{H\max} \sim T_{ef,c}$ taking into account Eq. (6).

So, the physical criterion of local failure in the fracture process zone X_{ef} can be rewritten by introducing in the criterion (8) the time t of exposition under hydrogenating conditions

$$T_{ef,c} K^m_{\rho,c} t^h = M_H, \tag{8}$$

where M_H is constant for given conditions of hydrogen charging. To calculate M_H, h and m from Eq. (7), it is enough to use the information about 3 time of exposition, for example, 10, 20 and 30 days (Table 4). The estimation for the CT specimens leads to the following result: M_H = 21.742, n = 0.2475, m = 0.0561.

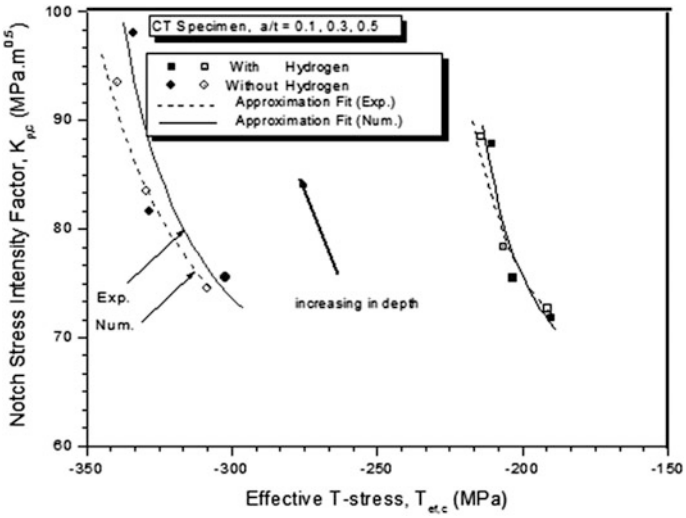

Fig. 11 Effect of degradation on the critical notch stress intensity factor and the effective T-stress for CT specimens in the saturation

It should be noted that specific feature of presented study is considering of hydrogenating conditions, which are very similar to real operating pipelines, therefore received data are very realistic for prediction of hydrogen embrittlement phenomenon than recorded in literature studies that were conducted with using of cathodic charging of hydrogen under high density of polarisation current (e.g., [20, 21]). In this case, we have criterion to predict failure taking into account time of exposition under realistic hydrogenating conditions. Thus, the failure criterion (8) allows predicting the critical notch stress intensity factor. To get different assessment points ($K_{\rho,c}, T_{ef,c}$), four specimen geometries (CT, SENT, RT and DCB) with several notch aspect ratio were tested. An example of the results of $K_{\rho,c} - T_{ef,c}$ estimations is given in Fig. 11 for the CT specimens with the notch aspect ratio a/t = 0.1; 0.3; 0.5 with and without the presence of hydrogen. Hydrogen charging leads to the shift of the curve in the region of more high constraint characterized by the value of $T_{ef,c}$ (Fig. 11).

The material failure curve (MFC) based on the critical notch stress intensity factor $K_{\rho,c}$ and the constraint parameter $T_{ef,c}$ has been successfully used to quantify the constraints of notch tip fields for various proposed geometry and loading configurations. We suggest extending the curve of $K_{\rho,c} = f\left(T_{ef,c}\right)$ for different steels charging by hydrogen. The results of test for the different specimens geometries with the notch aspect ratio a/t = 0.5 are presented for the case of electrolytic hydrogen charging during 30 days and compared with the results of initial state of the steels. The experimental assessment points ($K_{\rho,c}, T_{ef,c}$) for four specimen geometries (CT, SENT, RT and DCB) of APL X52 steel are summarized in Fig. 12. These experimental assessment points allow constructing a material

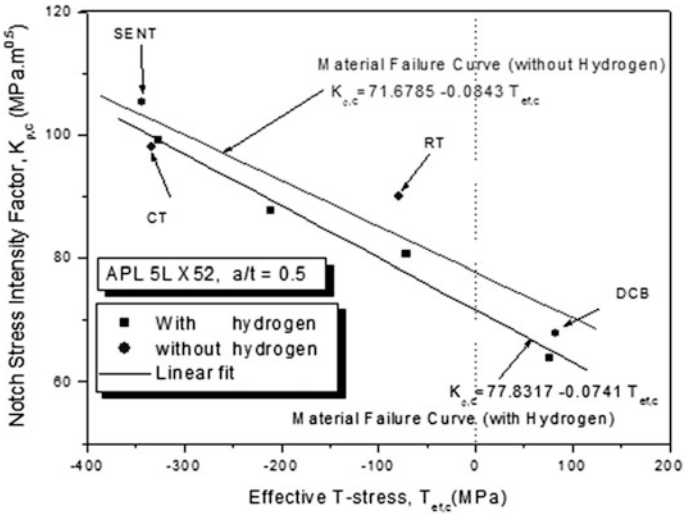

Fig. 12 The effect of specimen geometry on the material failure curve $K_{\rho,c} = f\left(T_{ef,c}\right)$ for APL X52 pipe steel with and without hydrogen charging

failure curve called also a material master curve which is approximated by the following expression

$$K_{\rho,c} = a\,T_{ef,c} + b \tag{9}$$

where a = −0.0843 and b = 71.6785 for the X52 pipe steel without hydrogen and a = −0.0741 and b = 77.8317 with the presence of hydrogen. The decrease of the critical notch stress intensity factor with the presence of hydrogen is in the range 5.8–9.8 % for the different specimens.

The shift between initial value of $K_{\rho,c}$ for the SENT specimen and the hydrogenated specimen is small; however, a real difference is noted in DCB specimen (about 10 %). At the same time, hydrogen charging leads to more high constraint. Such behavior of the critical notch stress intensity factor versus the critical value of $T_{ef,c}$ could be interpreted as constraint effect due to specimen geometry, type of loading and hydrogen charging.

Thus, hydrogen charging (or time of exposition under hydrogenating conditions) can be considered as an additional factor of the loss of notch tip constraint. Similar conclusion has been made for the loss of crack tip constraint for creep conditions of loading.

The effect of hydrogen on the material failure curves of APL 5L gas pipe steels was analysed from viewpoint of the notch fracture mechanics. The material failure curves based on two-parameter fracture criterion have been determined for API 5L X52 steel. The notch fracture toughness $K_{\rho,c}$ and the effective T-stress were employed to describe the material failure curve $K_{\rho,c} = f\left(T_{ef,c}\right)$. The key parameters

of the material failure curve, namely, $K_{\rho,c}$ and X_{ef} were derived from the volumetric method of notch fracture mechanics. The effective T-stress, T_{ef}, has been estimated as the average value of the T-stress in the vicinity of the notch tip at the effective distance X_{ef}. The above-mentioned parameters have been established by means of finite element analysis based on the results of the notched specimen tests under static loading. It was shown that the notch fracture toughness is a linear function of the $T_{ef,c}$-stress. Tests were carried out on electrolytic ally hydrogen charged SENT, CT, RT (Roman Tile) and DCB specimens with a notch. Fracture initiation was detected by acoustic emission. A numerical/experimental comparison of material failure curves for hydrogen charged steels and steels without hydrogen were made. It was shown that there is critical hydrogen concentration which causes significant reduction of local fracture resistance of pipe steels. This value could be applied as an important engineering parameter for structural integrity assessment of pipelines during long-term operation.

2.3 *Analysis of Constraint Effect in the Influences of Notch Radius on the Material Failure Master Curve (MFMC)*

It is well known that fracture resistance increases with defect tip radius and evolution can be considered using local fracture criterion particularly through the characteristic length. The characteristic length was firstly associated with notch radius in Creager and Paris [25] analysis of the stress distribution at notch tip. For rounded V-notches, analytical expression of notch tip stress distribution for elastic material was developed by Filippi et al. [26]. They introduces in this analytical expression the distance between the origin of the polar coordinates system and the notch tip r_0. This distance r_0 depends on notch radius and notch angle. For the particular case of a zero notch angle, one finds:

$$r_0 = \frac{\rho}{2} \tag{10}$$

This value is the same which was introduced by Creager and Paris [25] for a U notch with parallel sides. Then the mode I notch stress intensity factor is given by:

$$K_{\rho,I} = \frac{1}{2}\sigma_{\theta\theta}\sqrt{\pi\rho}\,(\frac{\rho}{2}, 0) \tag{11}$$

This leads to the following value of the characteristic length called here effective distance

$$X_{ef} = \frac{\rho}{2} \tag{12}$$

According to Eq. (12), the notch fracture toughness is a linear function of the square root of the notch radius and confirm by numerous experimental results [27].

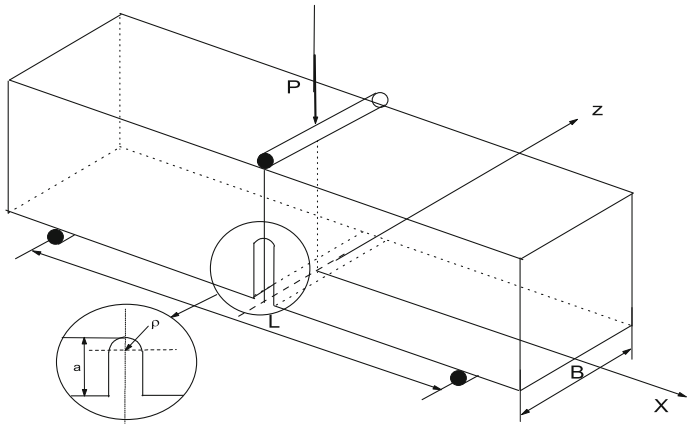

Fig. 13 Geometry and loading of the three-point bend plate

Increase of fracture toughness with notch radius may be assumed due a low of constraint, the stress field at notch tip is strongly modified by increasing the notch radius. In order to check this assumption, we have analysis experimental results obtained by Akourri et al. [27] on SENB specimens having different notch radius and made in XC38 steel. Stress distribution at notch tip has been determined by Finite Element analysis. The constraint was measured by the value of the effective T stress, T_{ef}. Procedure of determination of this parameter and the build-up of a material master curve ($K_\rho - T_{ef}$) are described in [21]. Notch fracture toughness has been determined on steel specimens. The material is a ductile steel (French name XC38) with the following mechanical properties: yield stress R_e = 304 MPa, ultimate strength R_m = 430 MPa [27].

Specimens used for experiments are of SENB type. The geometry is described in Fig. 13. Dimensions are listed in the following: thickness, B = 25 mm, width, w = 25 mm, length, h = 70 mm, ligament size, b = 5, 10, 15, 17.5 and 20 mm, notch opening $\alpha = 0°$ and the notch radius, 0.15, 0.25, 0.5, 1, 1.5, 2 and 4 mm. Specimens are loaded until fracture and the critical load P_c is registered.

The CASTEM^{TM} code was used for this purpose. SENB specimen exhibits a symmetry axis. In order to reduce the number of elements and saving time computing, only half the specimen has been represented by a mesh work. Loading conditions are represented by non-displacement along *y* axis in the ligament section. A typical, mesh type near notch-tip is presented in Fig. 14. The critical load for each specimen is plotted versus the non-dimensional notch length and presented in Table 6. Stress distribution at notch-tip has been computed using Finite Element Method. Figure 15 show distributions of the notch-opening stress σ_{yy} along the ligament obtained from the FEA (as denoted by symbols) for the SENB specimens with a shallow notch $a/W = 0.2$ and a deep notch of $a/W = 0.7$, respectively.

The opening stress distribution is presented in Fig. 16 for a notch with a notch depth a/W = 0.5 and notch radius 2 mm. The notch stress intensity factor is

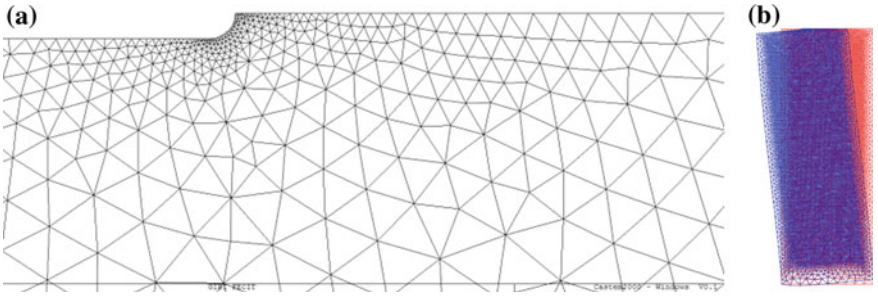

Fig. 14 **a** Mesh near notch-tip for SENB specimen and **b** specimen after deformation

Table 6 Recapitulation of different results for the SENB specimen

Ratio rapport	Notch radius (mm)	Max.P_c (kN) [27]	σ_{max} (MPa)	X_{ef} (mm)	σ_{ef} (MPa)	K_ρ (MPa $m^{0.5}$)
a/w = 0.7	0.150	8,584	471,670	0.029	336,205	4.561
	0.250	9,056	400,300	0.045	282,865	4.755
	0.500	8,898	274,095	0.104	183,320	4.685
	1.000	10,359	227,760	0.141	160,215	4.768
	1.500	11,011	196,915	0.182	142,520	4.818
	2.000	12,157	195,250	0.365	137,850	6.600
a/w = 0.5	0.150	24,988	2712,300	0.010	2423,200	19.203
	0.250	26,606	2179,650	0.022	1970,550	23.162
	0.500	27,752	1651,400	0.078	1270,000	28.108
	1.000	28,404	1215,600	0.162	905,000	28.866
	1.500	29,865	1050,550	0.261	755,815	30.617
	2.000	33,281	1037,500	0.570	630,000	37.693
a/w = 0.2	0.150	59,932	5819,500	0.020	4968,395	55.682
	0.250	61,55	5170,000	0.040	3855,000	61.099
	0.500	63,505	3579,250	0.080	2865,850	64.236
	1.000	66,269	2752,950	0.130	2364,450	67.559
	1.500	67,415	2567,600	0.150	2240,550	68.767
	2.000	70,000	2185,350	0.270	1852,175	76.268

calculated from Eq. (3). Table 6 reports the different results of notch stress intensity factor along principal direction (xx).

Numerical assessment points ($K_{\rho,c}, T_{ef,c}$) for SENB specimen geometry with notch aspect ratio (a/W = 0.2, 0.5 and 0.7) are summarized in Fig. 9. These points allow constructing a material failure curve called also a material master curve for different notch radius. The increasing of the notch stress intensity factor with the presence of constraint is in the range 27–49 % with the increasing of the notch tip for ρ = 0.15 to ρ = 2 mm. One notes that the material failure curve for the X38 steel is very sensitive to notch tip.

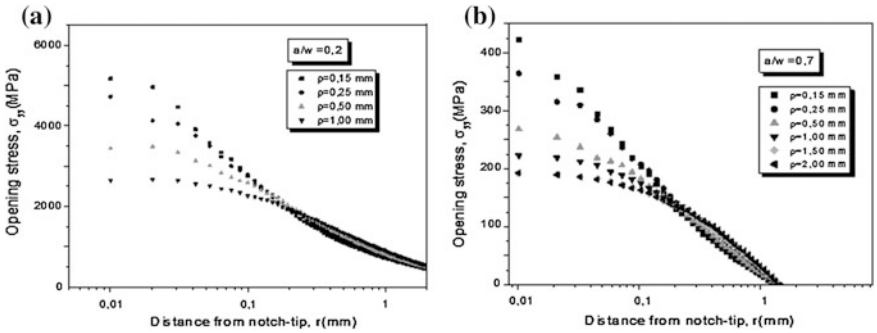

Fig. 15 **a** Distribution of notch-opening stress along the uncracked ligament from the notch tip for SENB specimen with short notch a/W = 0.2 and **b** for long notch a/W = 0.7 for different notch radius

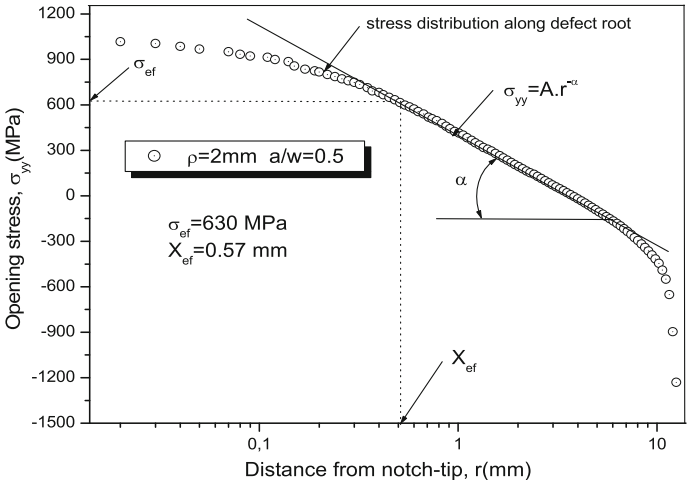

Fig. 16 Stress distribution versus notch tip radius in a bilogarithmic plot (a/W = 0.5, ρ = 2 mm)

Dependence of notch fracture toughness with notch radius has been obtained using the Material Failure Curve's relationship. Effect of notch root radius through constraint on fracture resistance consists of three phases: in the first one, increasing of the NSIF for very short notch ($\rho < 0.2$ mm), in second phase, it remains constant until a critical value of the notch radius; in the third phase $K_{\rho,c}$ increases linearly with ρ. The difference between results given in Akourri et al. [27] reference and the above mentioned numerical results are explain by the effect of constraint (not taken into account in [27]. The material failure curve is a tool introduce in Notch Failure Assessment Diagram (NFAD) as an extension of the FAD generally used for crack-like defect. It is less conservative because it takes into account the real defect acuity (Fig. 17).

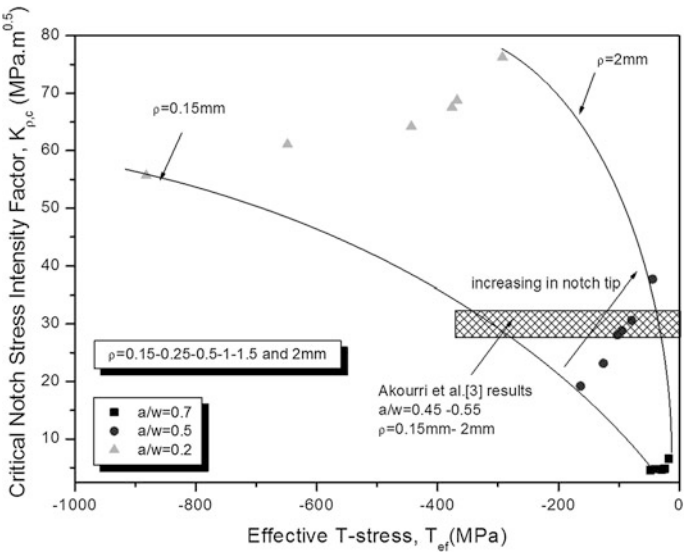

Fig. 17 Material failure curve for the SENB specimen with a/W = 0.2, 0.5 and 0.7

2.4 The Two Fracture Mechanics Approach for Mixed Mode (I + II) Loading

The evaluation of stress intensity factor K in mixed-mode of fracture (I/II), taking into consideration the effect of constraint parameters T-stress and A_3 is study in this part. Using the finite element techniques, the study is conducted on a standard test Compact Tension Shear, CTS, for different notch lengths, notch deeps and load orientation angles, in order to determine the stress intensity factor and the two constraint parameters (T-stress and A_3). The CTS specimen is a plate with a U-shaped notch, the purpose is to provide a numerical study, defining the notch stress intensity factor K_ρ and the T-stress with finite element method, based on the extension of the global approach and to determine the (K-T-A_3). In two dimensions (2D), the study is based on a steel plate API X52 subject to various loads angles, in order to obtain the status of a mixed mode of fracture while changing the radius and depth of notch. Several studies in the field of fracture mechanics mainly carried on evaluation of stress intensity factors (NSIFs) that characterize the stress singularity in the vicinity of the bottom of notch. However, it has long been recognized that the K_ρ is sensitive to the non-singular T-stress acting parallel to the vicinity of the notch tip. In practical case the T-stress play an important role in the stability of the path of the crack propagation.

For a two dimensional crack subjected to a symmetric loading, the stress can be written as Williams's development. We will use the Stress Difference Method (SDM), i.e. a numerical approach, to determine T-stress effectively and accurately,

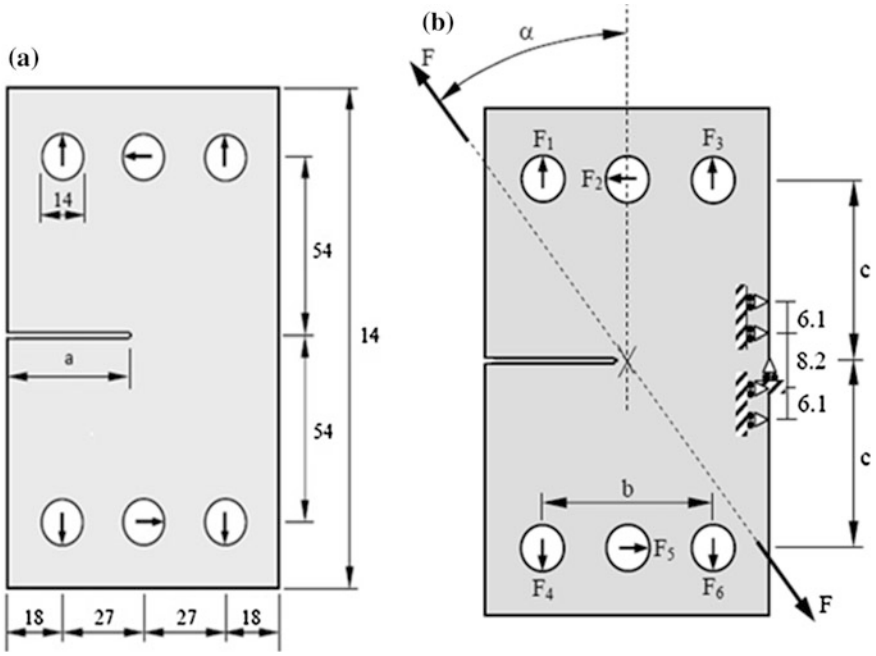

Fig. 18 **a** The geometry of CTS and **b** the loading and boundary conditions

focusing on a point just in front of notch tip by evaluating ($\sigma_{xx} - \sigma_{yy}$). This difference should be as small as possible in order to eliminate in an effective way the errors, which may occur along the notch tip with a parameter denoted as r. T-stress is evaluated using finite element method and computing the difference of principal stresses along ligament for direction $\theta = 0$. However, T-stress can be evaluated in any direction and given by simple relationships in some given θ directions. This research was conducted using the API 5L X52 carbon micro alloyed steel. Different research to calculate the notch stress intensity factor were evaluated for the CTS specimen [28, 29] shown on Fig. 18a. The CTS specimen is loaded with a static load of 1 kN. In computational analysis this load is replaced with three equivalent nodal forces in x-y direction as it is shown in Fig. 18b. Different load cases for load angles between 0° and 90°, with a step of 15°, were used to simulate different fracture mode conditions. Pure mode I condition was simulated with load angle of 0°, while the pure mode II was simulated with the load angle of 90°. The mixed mode conditions are simulated using load angles between 15° and 75°. Mixed-mode (I + II) were conducted on Compact Tension Shear (CTS) specimens with a thickness of 5.85 mm. The notch depth varied from $0.1 < a/W < 0.7$. The overall uniaxial load F shown in Fig. 18b is linked with point charges in the following expressions:

$$
\begin{aligned}
F_1 = F_6 &= F\left(\frac{1}{2}\cos\alpha + \frac{c}{b}\sin\alpha\right) \\
F_2 = F_5 &= F\sin\alpha \\
F_3 = F_4 &= F\left(\frac{1}{2}\cos\alpha - \frac{c}{b}\sin\alpha\right)
\end{aligned}
\tag{13}
$$

Before starting the calculation of the model we have completed the following steps sizing and mesh optimization. In order to have a calibration and optimum distribution of the mesh we divided the specimen into three parts while taking into consideration the tip of the notch and ligament.

Figure 19 shows the distribution of the main constraints in the CTS specimen for loading angle ($\alpha = 0°$). It is noted that the stress field is obtained a tensile stress field. Also there is the existence of three zones: a first zone where the stresses are very high near the notch tip, a transition zone with constraint and a final area where the stresses are almost null. Scale effects and geometry on the mechanical properties and fracture of the material are very important topic in engineering design. We study the evolution of the distribution of principal stresses along the ligament with the relative depth. The load angle ($\alpha = 0°$), the radius ($\rho = 0.25$ mm) are kept constant and the relative notch depth a/W varies in the range [0.1–0.7] where a is the notch depth, W is the width of the specimen and B the length specimen. There are several ways how stress intensity factors can be determined from finite element analysis results.

$$
\begin{aligned}
\mathrm{K}_{\rho I} &= \sigma_{ef}\sqrt{2X_{ef}} \\
\mathrm{K}_{\rho II} &= \tau_{ef}\sqrt{2X_{ef}}
\end{aligned}
\tag{14}
$$

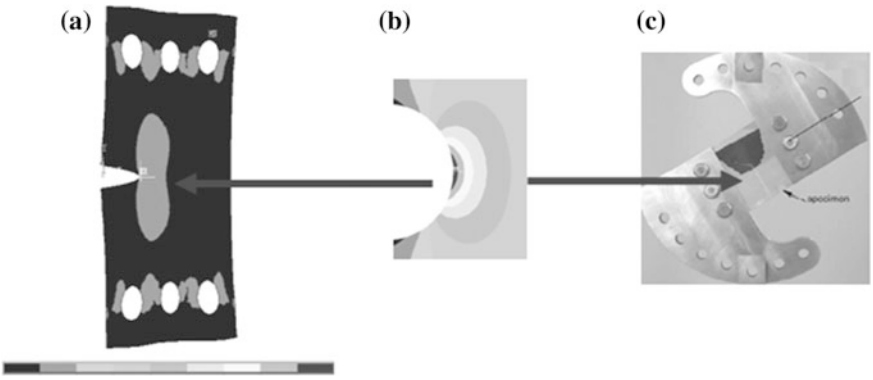

Fig. 19 **a** Distribution of σ_{yy} stress and **b** zoom notch tip and **c** CTS specimen with device loading

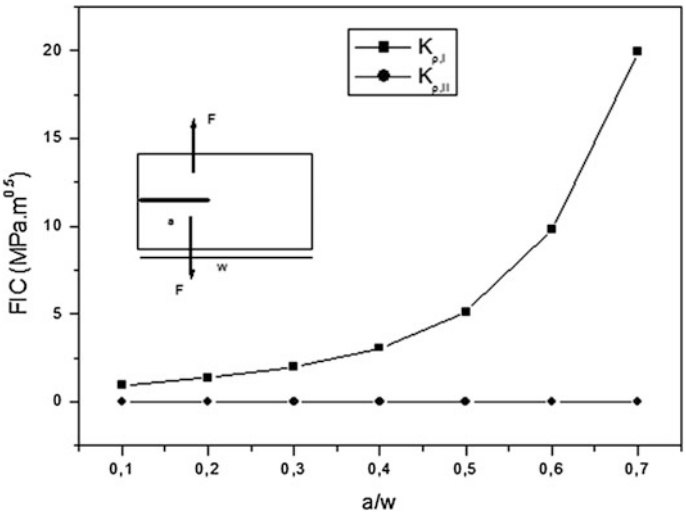

Fig. 20 Evolution of the notch stress intensity factors, $K_{\rho,I}$ and $K_{\rho,II}$ for different depths of notch (angle $\alpha = 0°$)

To evaluate the geometric parameters influence on the stress intensity factors, a depth ratio a/W vary between 0.1 and 0.7. Example of the finite element analysis is represented on Fig. 20.

The value of the notch stress intensity factor $K_{\rho,I}$ increases proportional with the relative notch deep, and the notch stress intensity factor $K_{\rho,II}$ take a zero value under mode I loading. To evaluate the equivalent notch stress intensity factor $K_{\rho,eq}$ under mixed mode loading, many models are available, Table 7 list some of the expressions of equivalent notch stress intensity factor $K_{\rho,eq}$ in mixed mode.

By a simple finite element method, the results should be noted that the equivalent notch stress intensity factor, $K_{\rho,eq}$ is virtually identical with the application of the formula used in the Table 7. Table 8 show numerical results of notch stress intensity factor $K_{\rho,eq}$ with and without the constraint parameters (T and A_3) depending on the loading angle $\rho = 0.25$ mm. In order to define the impact of the T-stress and the A_3 parameter on the notch tip, we have used finite element analysis. The influence of the T-stress of the notch stress intensity factor is significant for both the opening mode and the mixed mode in particular in the area close to the notch-tip.

The results of the finite elements show that for specimen with average notch $0.4 < a/W < 0.6$, the effect of the second and third terms of the Williams's equation T and A_3 parameters in the estimation of equivalent notch stress intensity factor of the specimen is rather minimal for long and short notch.

Table 7 Computing the equivalent notch stress intensity factor $K_{\rho,eq}$

Expression	Equation
$K_{eq} = \left[K_I^2 + 2K_{II}^2\right]^{\frac{1}{2}}$	(15)
$K_{eq} = \left[K_I^4 + 4K_{II}^4\right]^{\frac{1}{4}}$	(16)
$K_{eq} = \left[K_I^4 + 8K_{II}^4\right]^{\frac{1}{4}}$	(17)
$K_{eq} = \left[\left(K_I^2 + 3K_{II}^2\right)^3\left(K_I^2 + K_{II}^2\right)\right]^{\frac{1}{8}}$	(18)
$K_{eq} = \left[K_I^2(\theta_0) + 2K_{II}^2(\theta_0)\right]^{\frac{1}{2}}$, *où* $K_I(\theta_0) = \left(\frac{4}{3+cos^2\theta_0}\right)\left(\frac{1-\frac{\theta_0}{\pi}}{1+\frac{\theta_0}{\pi}}\right)^{\frac{\theta_0}{2}}\left(K_I cos\theta_0 + \frac{3}{2}K_{II} sin\theta_0\right)$ $K_{II}(\theta_0) = \left(\frac{4}{3+\cos^2\theta_0}\right)\left(\frac{1-\frac{\theta_0}{\pi}}{1+\frac{\theta_0}{\pi}}\right)^{\frac{\theta_0}{2}}\left(-\frac{1}{2}K_I \sin\theta_0 + K_{II}\cos\theta_0\right)$ θ_0 is the angle of loading	(19)
$K_{eq} = \left[K_I^2 + K_{II}^2\right]^{\frac{1}{2}}$	(20)

Table 8 Recapitulation of the results

a/W	Loading angle α (deg °)	Kρ,eq (MPa $m^{0.5}$)	Kρ,eq (MPa $m^{0.5}$) + A3	Kρ,eq (MPa $m^{0.5}$) + T-stress
0.1	0	0.806	0.806	0.946
	15	0.771	0.771	0.897
	30	0.712	0.712	0.828
	45	0.667	0.667	0.763
	60	0.640	0.640	0.702
	75	0.665	0.665	0.695
	90	0.806	0.806	0.946
0.4	0	2.985	2.985	3.076
	15	2.904	2.904	2.992
	30	2.672	2.672	2.751
	45	2.313	2.313	2.383
	60	1.893	1.893	1.949
	75	1.521	1.521	1.562
	90	1.3706	1.3706	1.394
0.7	0	18.499	18.499	19.949
	15	17.879	17.879	19.27
	30	15.991	15.991	17.381
	45	13.218	13.218	14.245
	60	9.542	9.542	10.270
	75	5.464	5.464	5.842
	90	2.744	2.744	2.746

2.5 Sandblating Test with the Presence of the Constraint

Different parameters affect the Material Master Failure curve in pipeline, as example the internal corrosion by hydrogen embrittlment [30], the quality of roughness, type of internal and/or external sandblasting [31], the heat treatment…. The degradations by sandblasting are taken account in this part of study, coupled with the constraint parameter (T stress is used as constraint parameter) on Master Material Failure Curve (MMFC). For the influence of sandblasting, the surfaces notched pipeline with API 5L X52 steel were studied in static test with flat specimens [30], dynamic test with Charpy specimens [31] and fatigue test [32]. This sandblasting technique for different times are reproduced for laboratory specimens SENT, CT, RT (Roman Tile) and DCB with U-notches. Except the RT specimens, the two faces of another's specimens are trated. The effects of sandblasting on mechanics properties in the two faces and in both directions of pipeline (longitudinal (L) and transverse (T)) are involved. The fracture toughness of sandblasted material for the different specimens are different in both L and T directions.

The observation of damage mode and distribution of residual stress under the notch tip show that the material hardening, the notch radius and the compressive stress play an important role in stabilizing the mechanical properties of the material. Tests have been made on X52 gas pipe with a diameter of 610 mm and a wall thickness of 11 mm. Chemical compositions of the pipe steel is given in [21] and its mechanical properties are detailed in Table 9 (measured on full thickness in the longitudinal and transvere direction). The different mechanical properties are reported and compared in Table 9 for different references [21, 30–32]. We note also that the capacity of strain hardening is less for small diameter X52 pipe steel. The fracture toughness of the pipe has been extracted using three types of specimens, Roman tile (RT) specimen, flat specimen and Compact Tensile (CT) specimen. We extracted flat test specimens according to the French standard (NF IN 100002-1) from the cylindrical volume of the tube. The flat specimens dimensions have dimensions of 20 mm width, 4 mm thickness, the notch depth was 6 mm and the crack length was 10 mm. Difficulties are met to manufacture these test specimens, we noticed that they are deformed enormously. Indeed, this explains by the existence of the internal stresses introduced into tubes after their elaboration. For these reasons, we chose to use test tubes with small dimensions. The results are presented

Table 9 Tensile properties of API X52 steel

Diam. (mm)	Direc.	Re (MPa)	Rm (MPa)	A%	n	k	K
610	C [30]	437	616	15	0.10	780	116
	C [31]	410	638	19	–	–	–
	C [21]	410	528	32	0.16	876	116
	L [30]	320	549	15	–		
	L [21]	493	623	30	–	–	–

C circonferential direction, *L* longitudinal direction

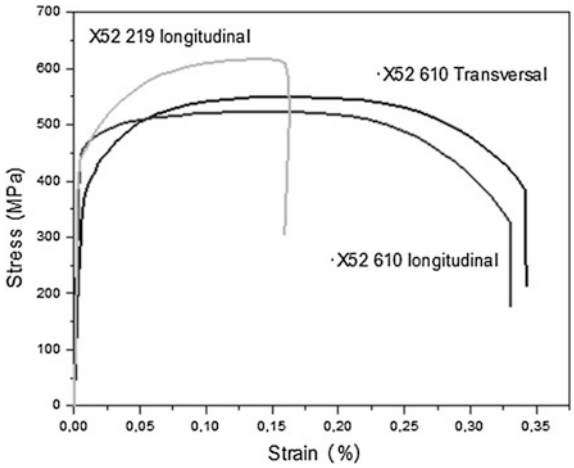

Fig. 21 Stress–strain curves of X52 steel tensile specimens extracted from pipes of diameter 219 and 610 mm

and compared to [30] results and [21]. Results of the stress- strain curves for the flat specimen, in the longitudinal and transversal direction, are presented in Fig. 21 and compared to the longitudinal direction for the same grade of pipe (X52) with a 219 mm diameter.

Mechanical tests were realized on specimens made in API 5L X52 steels taken from a pipe with two directions, longitudinal (L) and transverse (T). External diameter of 610 mm and a thickness of 11 mm are the dimension of the pipe traditionally used in the European natural gas transport network. The specimens are flat with a rectangular section, its dimensions fit with the European standard NF EN 10002-1, Fig. 22. We used a Blaster 2700 sandblasting machine, equipped with a

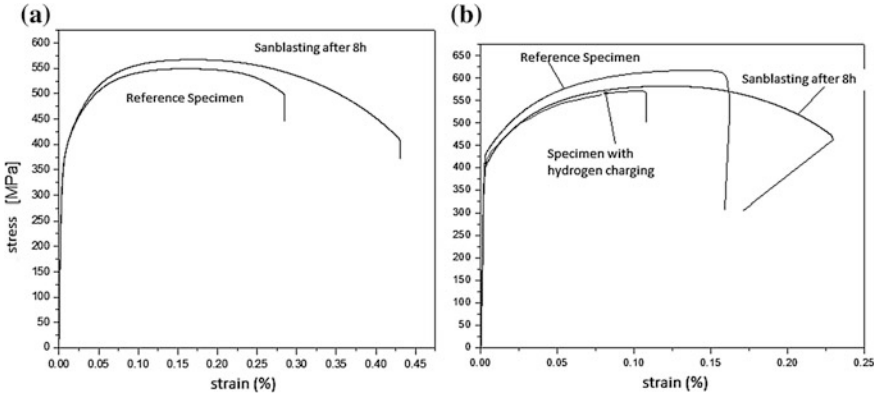

Fig. 22 Stress–strain curve of pipeline steel API 5L X52 in both L (**a**) and T directions (**b**)

pressure gauge, enabling it to adjust the desired power. Sand supply (Al_2O_3) is ensured by the venturi effect, with a constant sand feed throughout sandblasting operation. The air flow velocity (32 m s^{-1}) was measured by means of a wind gauge using an anemometer. The sand particles velocity was not determined because of the complexity related to the variations in the nature, size and shape of sand. The sand particles have an angular shape and their average size is between 300 and 400 µm, for more details see [32].

The same sandblasting procedure is taken for 4 types specimens, namely, CT, DCB, SENT and RT (roman tile) which were extracted from a steel pipe of diameter 610 mm. Geometries of these specimens are given in [21]. The specimens have a notch with a notch opening angle $\varphi = 0$ and a notch radius $\rho = 0.25$ mm. Except the RT specimens, the two faces of the other specimens are trated. Sandblasting on the two faces and in both directions of pipeline [longitudinal (L) and transverse (T)] affects the MMFC for the API X52 steel. The $K_\rho - T_{ef}$ curve is built in order to create a material characteristic taking into account specimen geometries (CT, SENT, RT and DCB), with ligament size given by the ratio a/W = 0.5. The performed tests are static with imposed displacement at room temperature. Displacement rate was monitored for a constant value of 0.02 mm/s. The test procedure allowed measuring the critical load corresponding to crack initiation. In the present case, acoustic emission technique has been employed for this purpose. Comparison of load versus time and acoustic emission pulse duration versus time indicates crack initiation. For this event, acoustic salves with the highest duration and the most important number of acoustic hits are easily detectable. Thus, the load for crack initiation was used to compute the notch stress intensity factor and the T-stress ahead of the notch tip by Finite Element method. Specimens were equipped with strain gauges in order to determine the notch stress intensity factor and the T-stress. These gauges were glued at distance of 3 mm from the notch tip.

The $K_\rho - T_{ef}$ curve is built in order to create a material characteristic taking into account specimen geometries, ligament size, type of steel, loading and environmental conditions. To get different assessment points (K_ρ, T_{ef}), four specimen geometries (CT, SENT, RT and DCB) with several notch aspect ratio were tested after sandblasting on one face and two face, except RT specimens and with or without the presence of hydrogen. The *K–T* crack approach was derived from a rigorous asymptotic solution which has been developed for a notch two-parameter fracture approach in order to determine the Material Master Failure Curve (MFC). With $K_{\rho c}$ as the driving force and $T_{ef,c}$ a constraint parameter, this approach has been successfully used to quantify the constraints of notch-tip fields for various proposed geometry and loading configurations. We suggest to extend the $K_{\rho c} - T_{ef,c}$ to different steels with the presence of various environment. The different specimens geometries are used with a relative notch depth of 0.5 (a/t = 0.5) after hydrogen diffusion during for 30 days. results are compared with these of [21]. The experimental assessment points $(K_{\rho,c}, T_{ef,c})$ for four specimen geometries (CT, SENT, RT and DCB) with notch aspect ratio (a/t = 0.5) are summarized in Fig. 23.

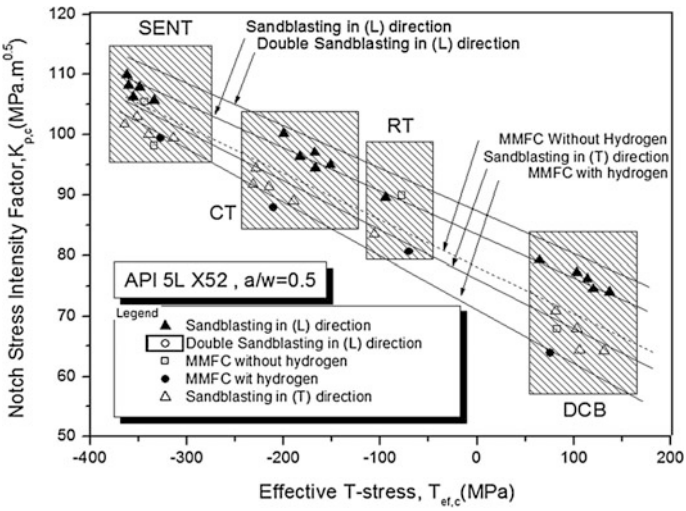

Fig. 23 MMFC with the different situation for API 5L X52 pipe, a/w = 0.5

The degradation of the notch stress intensity factor with constraint is in the range 5.8–9.8 % for the different specimens. The shift between the virgin SENT specimen and the hydrogenated is small, however a notifiable difference is noted for DCB specimen (about 10 %). The effect of the microstructure in (L) and (T) direction are noticeable as the difference between the MMFC relative to the two situations. Tone notes important difference between specimens loaded in tension or in bending. The decreasing of the fracture toughness for the different specimens is explained by constraint. which increases by increasing yield stress. Figure 23 presents the effect of the second terms of Williams' solutions, i.e. effective *T*-stress on the critical notch stress intensity factor for the different specimen's type with sandblasting in the two direction (L) and (T), the double sandblasting and hydrogen charging.

3 Conclusion

The Williams's type solution has been employed to analyse the stress distribution ahead of notch tip. It was shown that the T-stress is not constant along ligament ahead of the notch tip for pressurised pipes and Roman tile specimens. It was also found that the non-singular terms are not negligible for a notch as the distance from the notch tip increases. To avoid this difficulty, it has been proposed to use the effective T-stress. The effective T-stress is suggested to be the average T-stress inside the effective distance ahead of the notch tip. Thus, the concept of the T-stress in the case of the crack stress distribution has been extended to the notch stress distribution.

The use of two parameters fracture mechanics criterion as a tool for structural design and analysis has presented in this study. We have study the elastic solution for the stress distribution at notch tip for two geometries and constraint as T-stress, under various loading conditions. Using notch fracture mechanics and particularly the Volumetric Method approach, we study the stress distribution at the tip of a notch in pipes submitted to internal pressure. The critical Notch Stress Intensity Factor K_ρ and the effective T-stress are combined into a two-parameter fracture criterion ($K_{I\rho}-T_{ef}$). This approach is then used to quantify the constraint of notch-tip fields for various industrial applications with different geometry and loading conditions.

References

1. Pluvinage G (2001) Notch effects in fatigue and fracture. Kluwer, Dordrecht
2. Mouwakeh M, Pluvinage G, Masri S (2011) Failure of water pipes containing surface cracks using limit analysis notions. Res J Aleppo Univ Eng Sci Ser 63
3. Henry BS, Luxmore AR (1997) The stress triaxiality constraint and the Q-value as a ductile fracture parameter. Eng Fract Mech 57:375–390
4. Ruggieri C, Gao X, Dodds RH (2000) Transferability of elastic–plastic fracture toughness using the Weibull stress approach: Significance of parameter calibration. Eng Fract Mech 67:101–117
5. Hadj Meliani M, Matvienko YG, Pluvinage G (2011) Two-parameter fracture criterion (Kρ, χ-Tef, c) based on notch fracture mechanics. Int J Fract 167:173–182
6. Nikishkov GP (1995) An algorithm and computer program for the three-term asymptotic expansion of elastic–plastic crack tip stress and displacement field. Eng Fract Mech 50:65–83
7. Larsson SG, Carlsson AJ (1973) Influence of non-singular stress terms and specimen geometry on small-scale yielding at crack tips in elastic–plastic materials. J MechPhys Solids 1(21):263–277
8. Yang B, Ravichandar K (2001) Evaluation of T stress by stress difference method. Eng Fract Mech 64:589–605
9. Chao YJ, Liu S, Broviak BJ (2001) Brittle fracture: variation of fracture toughness with constraint and crack curving under mode I conditions. ExpMech 41:232–241
10. Ayatollahi MR, Pavier MJ, Smith DJ (2002) Mode I cracks subjected to large T stress. Int J Fract 117:159–174
11. Eisele U, Roos E (1990) Evaluation of different fracture-mechanical J-integral initiation values with regard to their usability in the safety assessment of components. Nucl Eng Des 130:237–247
12. Williams JG, Ewing PD (1972) Fracture under complex stress the angled crack problems. Int J Fract 8(4):416–441
13. Kim Y, Chao YJ (2007) Effect of loading rate on dynamic fracture initiation toughness of brittle materials. Int J Fract 145:195–204
14. Nguyen BN, Onck PR, van der Giessen E (1999). Study of higher order crack tip in intergranular creep fracture. In: Proceedings of the conference on modelling of microstructural evolution in creep resistant materials. The Institute of Materials, London
15. Liu C, Knauss WG, Rosakis AJ (1998) Loading rates and the dynamic initiation toughness in brittle solids. Int J Fract 90:103–118
16. Chao YJ, Zhang X (1996) Constraint effect in brittle fracture. In: Piasik RS, Newman JC Jr., Dowling NE (eds) Fatigue and fracture mechanics: 27th volume, ASTM STP 1296. American Society for Testing and Materials, Philadelphia

17. Adib H (2003) Theorical and numerical aspects of the volumetric approach for fatigue life prediction in notched components. Int J Fatigue 25:67–76
18. Capelle J (2008) Etude de la nocivité d'un défaut de type éraflure sur une conduite destinée au transport de gaz naturel soumise à une pression d'hydrogène. Thèse de doctorat, Laboratoire de Fiabilité Mécanique, LFM, Ecole d'Ingénieur de Metz –ENIM-, Novembre, Université de Metz, France
19. Mangain F, Internal Rapport of DESS (2006) Laboratoire de Fiabilité Mécanique, LFM-ENIM, Metz
20. Capelle J, Gilgert J, Dmytrakh I, Pluvinage G (2008) Sensitivity of pipelines with steel API X52 to hydrogen embrittlement. Int J Hydrog Energy 33(24):7630–7641
21. Hadj Meliani M, Pluvinage G, Matvienko YG (2011) Two parameter fracture criterion (K_ρ-T_{ef}) derived from notch fracture mechanics. Int J Fract 167(2011):173–182
22. Hadj Meliani M, Pluvinage G, Matvienko YG (2011) Corrosion defect assessment on pipes using limit analysis and notch fracture mechanics. Eng Fail Anal 18:271–283
23. El-azzizi A, Hadj Meliani M, Khelil A, Pluvinage G, Matvienko YG (2014) The master failure curve of pipe steels and crack paths in connection with hydrogen embrittlement. Int J Hydrog Energy 40(5):2295–2302 (9 February 2015)
24. Matvienko YG (2011). A damage evolution approach in fracture mechanics of pipelines. In: Bolzon G, Boukharouba T, Gabetta G, Elboujdaini M, Mellas M (eds) Integrity of pipelines transporting hydrocarbons, NATO science for peace and security series C: environmental security. Springer, Dordrecht, pp 227–244
25. Creager M, Paris PC (1967) Elastic field equations for blunt cracks with reference to stress corrosion cracking. Int J Fract 3:247–252
26. Filippi S, Lazzarin P, Tovo R (2002) A unified approach to problems of stress concentration near V-shaped notches with sharp and rounded tip. Int J Solid Struct 39:4543–4565
27. Akourri O, Elayachi I, Pluvinage G (2007) Plastic zone and volumetric approach-mixed mode fracture I+II emanating from notches. IREME, Vol. 1, No 6 November
28. Richard HA, Benitz K (1983) A loading device for the creation of mixed mode in fracture mechanics. Int J Fract 22:R55–R58
29. Schillig R (1990) Ein Beitrag zur Ermüdungsrissausbreitung bei gleichphasiger Mixed-Mode Belastung. Fortschr.-Ber. VDI Reihe 18 Nr. 86, VDI Verlag, Düsseldorf
30. Wang X (2003) Elastic stress solutions for semi-elliptical surface cracks in infinite thickness plates. Eng Fract Mech 70:731–756
31. Hadj Meliani M, Moustabchir H, Azari Z (2007) T-stress by stress difference method (SDM): numerical analysis on mode (I) loading. Particle and continuum aspect of mesomechanics. Mesomechanics 2007, Lille, France, pp 253–260, edited by ISTE Publishing Knowledge
32. Alhussein A, Capelle J, Gilgert J, Tidu A, Hariri S, Azari Z (2013) Static, dynamic and fatigue characteristics of the pipeline API 5L X52 steel after sandblasting. Eng Fail Anal 27:1–15

Determination of Mechanical Properties of Operating Components Using Instrumented Hardness Testing, Small Punch and Small Size Tensile Testing Techniques

Szabolcs Szávai, Péter Rózsahegyi, Judit Dudra, Róbert Beleznai, Zoltán Bézi and Szabolcs Jónás

Abstract To have reliable information about the actual mechanical properties of an operating structure is a key issue for the fitness for service assessment. In many cases either there is no any data available about an ageing structural material or the reliability and validity of the available data is questionable. In most cases, it is not allowed to cut off larger pieces from an operating structure to perform destructive laboratory tests, because it may have significant impact on its integrity. Thus other non-destructive or semi non-destructive techniques are needed. If a small piece of material can be excavated form the component, it is possible to determine the yield stress and ultimate tensile strength of steels using small size specimen test techniques. The Small Punch Test (SPT) is a useful technique in residual life assessment owing to the lower tests evaluation cost compared to destructive methods and has higher life evaluation accuracy than the NDT techniques. In several cases the hardness measurement is the only accepted non-destructive test method, whose results can be used to assess the actual mechanical properties such as yield or tensile stress. Since scattering of the properties calculated directly from the pure hardness value is usually too large, methods have been developed for the evaluation of the mechanical properties from the load-indentation curve using instrumented hardness (IH) testing. The uniaxial small size tensile (SST) test is the most commonly used material testing method. Ideally the results of the tensile test are independent of the size of the specimen, but in practice the size of the grains and the test speed are relevant if it is not possible to sample standard sized specimens from in situ components. Validation of these methods is done using experimental tests and finite element simulations.

Keywords Small punch · Instrumented hardness test · Small size specimen · Small size tensile · Material testing · Finite element

S. Szávai (✉) · P. Rózsahegyi · J. Dudra · R. Beleznai · Z. Bézi · S. Jónás
Engineering Division, Bay Zoltán Nonprofit Ltd., Iglói Str. 2, Miskolc 3519, Hungary
e-mail: szabolcs.szavai@bayzoltan.hu

G. Pluvinage and L. Milovic (eds.), *Fracture at all Scales*,
Lecture Notes in Mechanical Engineering, DOI 10.1007/978-3-319-32634-4_7

1 Introduction

The pressure vessels in particular the RPVs are very hazardous equipment, so the monitoring of the material properties is especially important. The influences of the operational conditions such as the fluctuating loads, thermal effects or the effects of the radiation are causing degradation in the micro-structure and the material properties. These and the remaining life assessment are the reasons why the pressure vessels should be inspected. In most cases, the required amount of material is not available or the applied material testing method is not sufficient. Ageing monitoring of certain components requires up-to-date information. During the operation the mechanical properties of the structural materials can change due to several factors. It is essential for the fitness for service assessment to have reliable information on actual mechanical properties of an operating structure.

In most cases standard size specimens are non-applicable for analysing the ageing processes of NPPs because of their impact on the further safety operation. There are some methods to determine the actual values of mechanical properties using small size specimen technique. The determination of the necessary data is possible with non-destructive or semi-destructive techniques. The Fig. 1 shows the summarization of the possible test methods.

In the frame of a research programme, the small specimen test techniques were studied to understand the size effect between the different sized specimens and to

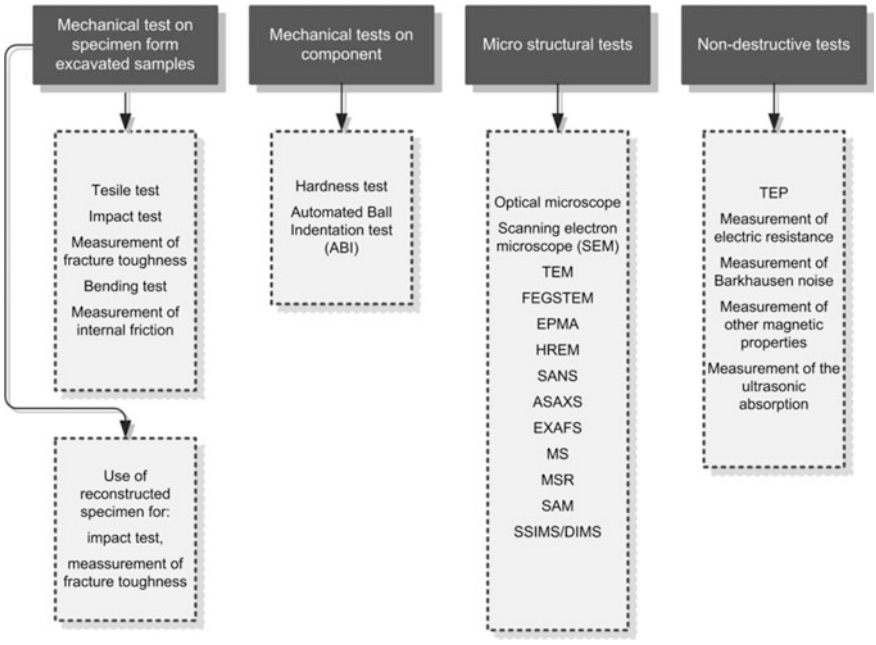

Fig. 1 Possible test methods concerning non-destructive and semi-destructive techniques

find an up-to-date measurement technique to evaluate the nuclear pressure vessels aging problems. The programme contains a novel material testing procedure, the so-called Small Punch Test (SPT). The SPT technique was developed in the early 1980s for the nuclear industry to determine the actual material properties of the nuclear pressure vessels from a very small amount of material [1]. For evaluation of the measurement results from on-site instrumented hardness test (IH) simplified evaluation method is applied to determine the mechanical properties based on the ABI test. Using manual hardness tester, the load-indentation curve can be registered using only one load cycle. This method that can be used on-site has this advantage.

In this study, three of them are presented and compared to standard size uni-axial tensile test results. Small size tensile test (SST), the SPT and also the IHT are applicable to determine tensile properties. The IH test can only determine the properties of the outer surface, while using SP and SST test more properties can be evaluated.

2 Small Punch Testing

The SPT is a useful technique in residual life assessment thanks to the tests evaluation cost compared to destructive methods and has higher life evaluation accuracy than the NDT techniques [2]. The test which is suitable for identification of unknown materials, examine the material properties in base material, welds, HAZs, coatings. From the test results, the tensile and fracture properties can be determined; creep properties or the behaviour of the metallic material in ductile-to-brittle transition region can be evaluated [3]. The SPT has a disadvantage: the loading makes biaxial stress state in the specimen during the test which causes complication in the determination of the correct material properties.

The specimen geometry in this study is the same as in the most of the international literature. The size of a specimen is 8 mm in diameter and the thickness of

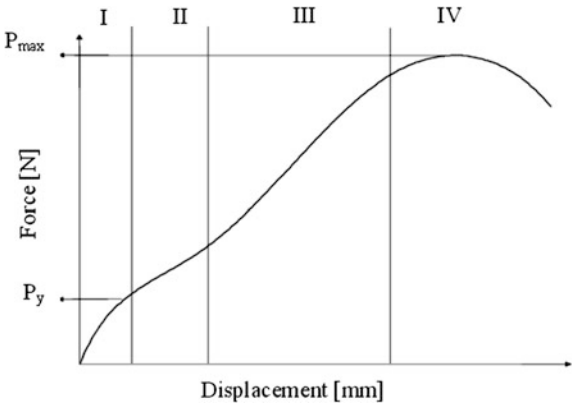

Fig. 2 Typical SP force-displacement curve

the small disc is 0.5 mm. The geometry of the SP specimen is shown in Fig. 2. In the present case, the specimens are made by testing rods. Used specimens can also be the base material of the SP specimens.

The test technique is a simple punching method. The specimen is punched with a rigid ball till the disc is fractured. In this case, the puncher ball is made of WC. The force-displacement curves are registered in every measurement. The SPT was performed according to the guidelines of the Code of Practice [4].

The typical SP force-displacement curves had four distinct regions (see Fig. 3). The first part is the elastic bending, the second is the plastic bending, the third part is the membrane stretching and the last one is the region of plastic instability. The force P_y corresponds to the limit of the elastic region and the beginning of the plastic deformations [8].

Two grades of steels were tested by the SPT. One of them was the type 22K steel which is a steam generator (SG) base material and the other steel grade was X6CrNiTi18-10 which is a so-called model material. The SP specimens were produced in two steps: at first rough manufacturing according to the geometry, then polishing process by sandpaper.

The tests were made by an Instron 8874 servo-hydraulic biaxial tensile tester machine at room temperature. For the Small Punch tests a special clamping device was made. The testing device with the extensometer is show in Fig. 4. Tested specimens are show in the Fig. 5. The displacement was measured with an extensometer and a deflection meter at the same time.

In case of yield stress, evaluation method of the SPT results followed the so-called tangents method [5]. The yield point is the first inflexion point of the curve; it can be determined by the two tangents fit to the elastic region and the elastic-bending region (Fig. 6). The intersection of the tangents gives the value of the yielding point. In each of the SPT curves, this point (P_y) is evaluated and with

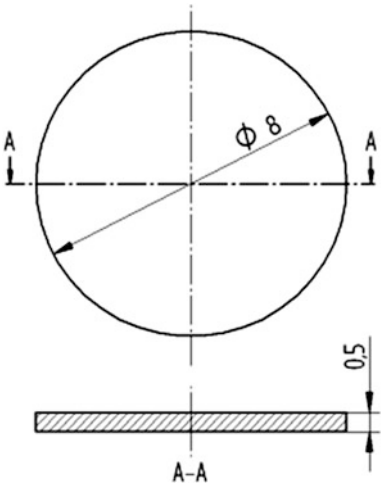

Fig. 3 Geometry of the specimen

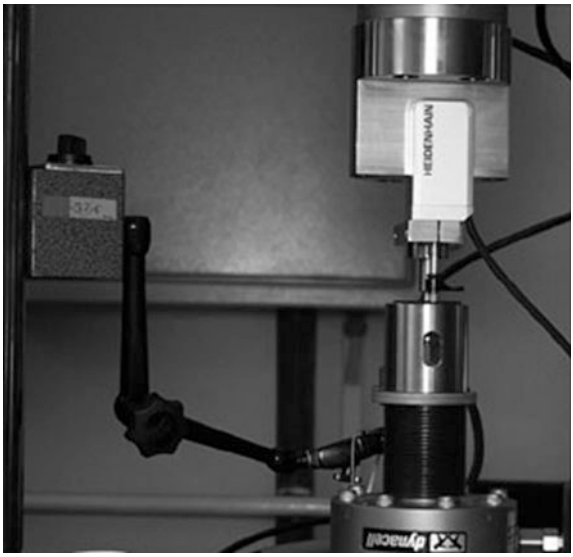

Fig. 4 Testing device

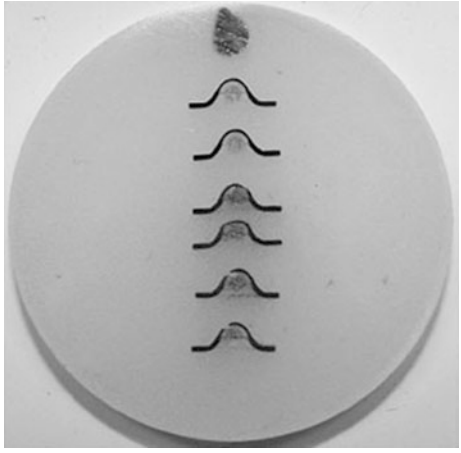

Fig. 5 Specimens after test

Eq. (1), the yield stress is calculated. α is material constant ($\alpha_{22K} = 0.36$, $\alpha_{X6CrNiTi18\text{-}10} = 0.477$) and t is the original thickness of the specimens ($t = 0.5$ mm).

$$\sigma_y = \alpha \cdot \frac{P_y}{t^2} \tag{1}$$

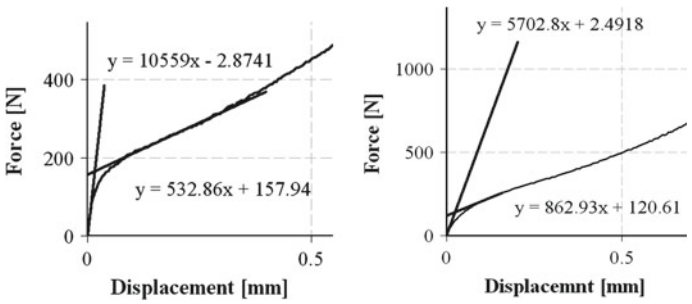

22K X6CrNiTi 10-18

Fig. 6 Determination of the P_y yield load from SP curves with two-tangents method

For the determination of the ultimate tensile strength, an empirical equation was used, similar as in [6]. The 1/3 of the $P_{\max}/(d_{\max} \cdot t)$ value gives a good approximation for the tensile test results.

$$\sigma_u = 0.3 \cdot \frac{P_{\max}}{d_{\max} \cdot t} \tag{2}$$

For the determination of the tensile stress, statistical methods were applied. There are several equations in the literature which are appropriate in certain cases, for example the following formula:

$$\frac{\mathrm{F}}{\sigma} = 3.33 \cdot k_{SP} \cdot R^{-0.2} r^{1.2} \cdot h_0, \tag{3}$$

where F is the maximum force during the test, R is the radius of the fixture, r is the radius of the loading ball, h_0 is the original specimen thickness, k_{SP} is a proposed coefficient ($k_{SP} = 1.385$) and σ is the stress.

The comparison of the yield strengths from the Eq. (1) and from tensile tests are presented in Table 1.

The problem with the two tangents method is how the tangent lines fit to the original curve. Taking the average of the measured curve, two-three adjacent points are used. This new curve is much clearer than the measured and it is easier to fit the tangents.

Table 1 Comparison of the measured yield strengths

	Yield strength from SP (MPa)	Yield strength from FEM (MPa)	Yield strength from tensile test (MPa)
22K	244	245	250
X6CrNiTi18-10	270	276	305

3 Parameter Sensitivity Analyses by FEA Simulation

The Parameter sensitivity analyses were made by FE software, MSC.Marc&Mentat. It was applied to simulate the response of the specimen under loading. The SPT can be modelled as a 2D axis-symmetric model, because the specimen, the clamping device, and the load are cylindrical symmetric. The model is shown in Fig. 7. The conjecture is that materials with high strength can cause deformation in the device, so it is modelled by three parts. The upper die has two parts, because there is a large deviation in the results in the case of steels which has got high strength according to the expectation. The upper part of the upper die can move up 0.1 mm during the test by the leverage of the specimen. This movement can compensate the deviation in the elastic-bending zone between the measurement and the FEA results.

The three parts of the device are linked with a spring to each other in the model considering the elasticity of the clamping device. The ball and the disc were inhibited in displacement in the horizontal direction. The puncher is represented by a curve which is on the upper part of the ball. Its position is changing during the test. The ball and the puncher were glued to each other in the contact properties.

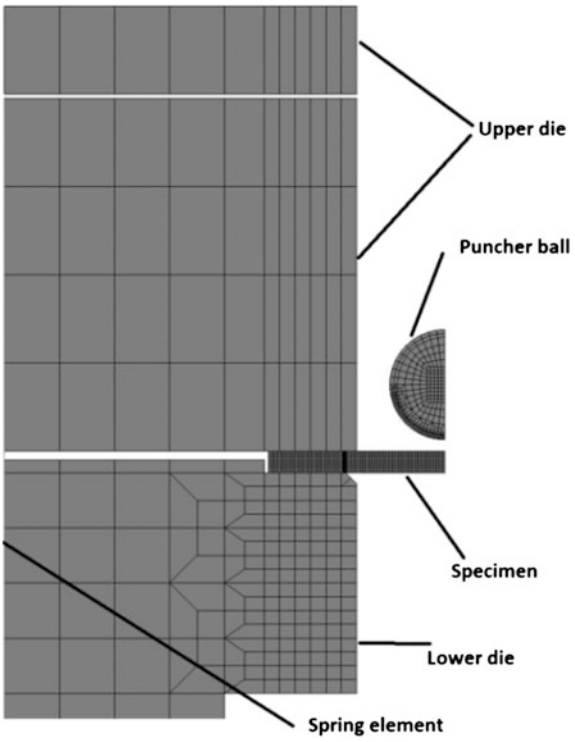

Fig. 7 FE model of the SPT

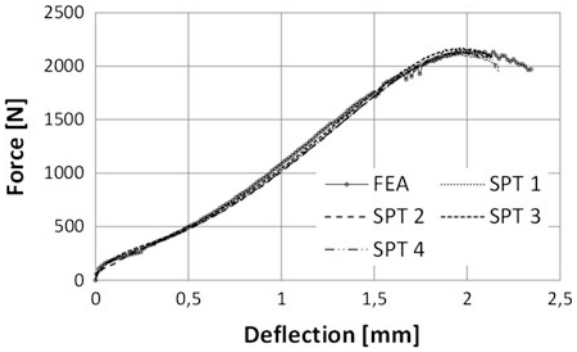

Fig. 8 Comparison of the tests and the FE calculation (X6CrNiTi18-10)

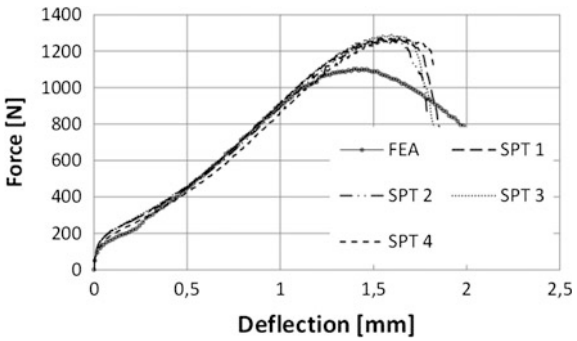

Fig. 9 Comparison of the tests and the FE calculation (22K)

The device, the ball and the SP specimen are modelled as a deformable contact body. The total number of the finite elements in the model is 1213; the specimen has 650 four-node type quadrilateral elements.

The comparison of the test results and FE calculations shows a good agreement. There is a small deviation in the elastic region in case of X6CrNiTi18-10 and a large deviation in the maximum force values in case of 22K. The comparisons are shown in Figs. 8 and 9.

Parameter sensitivity analyses are performed on the X6CrNiTi18-10 type steel. The effect of the friction coefficient and the thickness deviation of the specimen were examined by FE. The numerical study shows that the results are highly depending on these parameters. The effect of the friction coefficient appears in the value of the maximum force. This deviation gives false results on the conversed values of tensile strength (Fig. 10). The higher deviation from the prescribed tolerance (± 0.05 mm) of the thickness causes different curves (Fig. 11); this phenomenon leads to poor results.

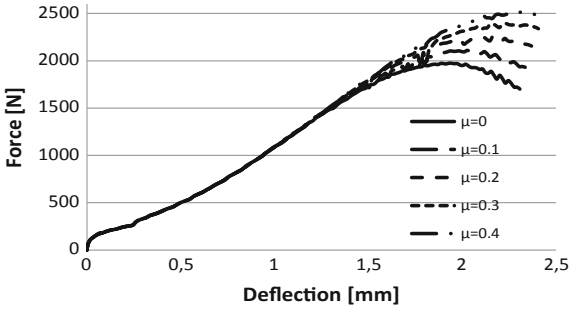

Fig. 10 Effect of the friction coefficient

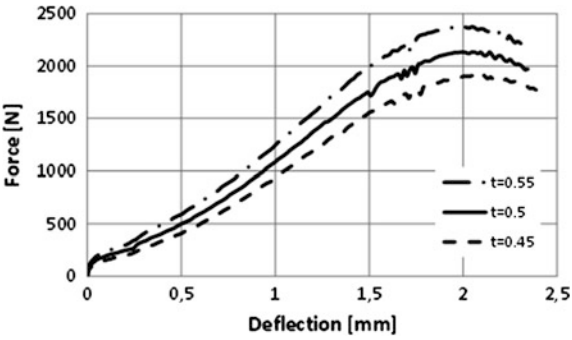

Fig. 11 Effect of the specimen thickness

4 Instrumented Hardness Test

In several cases, hardness measurement is the only accepted non-destructive testing method whose results can be used to assess the actual mechanical properties such as yield stress or tensile strength. Since the scatter of the properties calculated directly from the pure hardness value is usually too large and the number of properties to be assessed is limited, methods have been developed for the evaluation of the mechanical properties from the load–indentation curve using instrumented hardness testing. The most reliable method is the so-called instrumented hardness (IH) test [7]. This method requires quite a complex measurement device (Fig. 12) and application on a real structure can be problematic.

For handling the difficulties in the case of on-site measurements, a simplified measurement procedure has been implemented for manually operated instrumented hardness tester, neglecting the download cycles. The method has been successfully

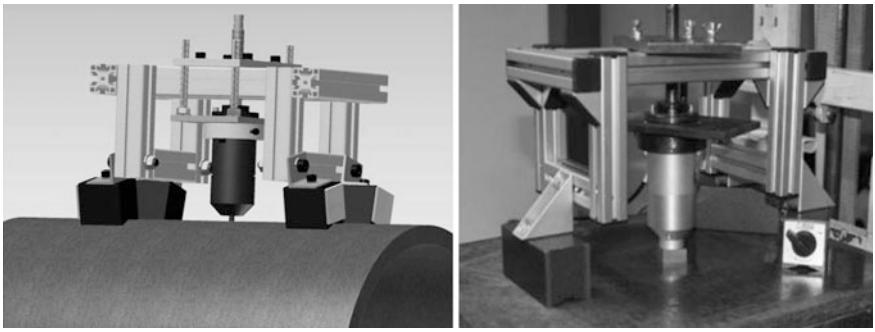

Fig. 12 IH testing machine

tested on different materials of real components at the Mechanical Testing Laboratory of BAY-LOGI. True stress–true strain curves were derived from the indentation curves and the results were validated with tensile tests and with finite element modelling as well.

5 Test Parameters and Evaluation Method

The Mat-Tec Unihard S3 type portable instrumented indentation test machine was used, for which an extra aluminium frame was designed and manufactured, in order to clamp the machine properly on the tested equipment surface (Fig. 1). In the case of carbon steel 4 magnet blocks and in the case of austenitic steel, two fixing belts could be used. The maximum applied indentation load was 500 N. The indenter was tungsten carbide cone with 1 mm tip radius. The load and indentation depth curves were recorded and evaluated.

The IHT method was used [7] to determine the true stress–true plastic strain curve, the yield stress and the ultimate tensile strength of the tested materials. These parameters were also determined with tensile tests carried out at room temperature and were compared to the indentation test results. Using the true stress–true strain curve determined with tensile tests and with the indentation tests, the load–indentation depth curve was also determined using finite element methods in three cases. Some kind of statistical analysis was also carried out to determine the uncertainty of the instrumented hardness measurement with conservative approximation.

Numerous types of steel were tests by IHT. Table 2 contains the results of the tensile tests and IH tests. In case of carbon steel the Lüders strain was considered.

Table 2 Test results

Material	Tensile test				IHT			
	$R_{p0.2}$ (MPa)	R_m (MPa)	K	n	$R_{p0.2}$ (MPa)	R_m (MPa)	K	n
22K	**250** (1.8%)	**436** (2.3%)	**792** (2.5%)	**0.2326** (3.0%)	**282** (4.7%)	**436** (5.3%)	**772** (10.9%)	**0.2317** (17.8%)
S355	**457** (1.8%)	**564** (0.8%)	**906** (0.3%)	**0.1679** (1.6%)	**398** (5.1%)	**601** (5.5%)	**1026** (12.6%)	**0.2082** (23.3%)
20MnMoNi55	**479** (0.3%)	**620** (0.1%)	**1012** (0.0%)	**0.1653** (1.6%)	**433** (3.8%)	**633** (3.2%)	**1000** (6.7%)	**0.1620** (13.0%)
15H2MFA	**498** (0.5%)	**617** (0.2%)	**853** (0.4%)	**0.0988** (1.8%)	**441** (5.1%)	**641** (4.6%)	**1000** (11.3%)	**0.1546** (25.7%)
15H2MFA Q+T to 35 hrs	**777** (0.7%)	**873** (0.4%)	-	-	**652** (3.5%)	**845** (2.4%)	-	-
X6CrNiTi18-10	**305** (0.7%)	**582** (0.1%)	**937** (3.0%)	**0.2619** (4.6%)	**281** (8.2%)	**523** (10.6%)	**948** (21.3%)	**0.2462** (31.6%)
Cladding	**583** (0.1%)	**806** (0.2%)	**1240** (0.2%)	**0.1529** (0.2%)	**513** (7.6%)	**790** (8.4%)	**1258** (18.6%)	**0.1651** (34.7%)
KO3 (*08H18N12T*)	**299** (4.2%)	**536** (1.6%)	**898** (3.5%)	**0.2495** (6.8%)	**274** (4.9%)	**506** (5.9%)	**913** (11.9%)	**0.2442** (19.4%)
KO5 (*08H18N12T*)	**296** (6.8%)	**540** (2.8%)	**907** (4.0%)	**0.2414** (2.1%)	**275** (5.5%)	**510** (6.4%)	**938** (10.8%)	**0.2591** (14.5%)

6 Numerical Results

The results of the finite element method (FEM) simulation show that the indentation curves and the finite element results along the loading part of the curve are in good agreement (Fig. 13). The true stress–true strain curves determined from indentation curves are in good agreement with those determined from tensile tests (Figs. 14, 15 and 16). The yield stress and the ultimate tensile strength calculated with IHT method fits well with the tensile test results. The differences were not more than 3.7 % in the case of yield stress and 4.5 % in the case of ultimate tensile strength for each tested material type.

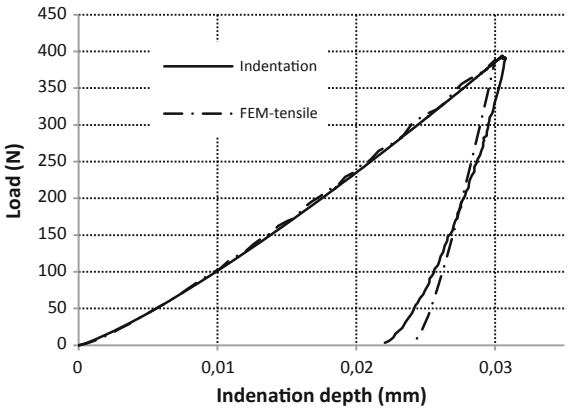

Fig. 13 Comparison of the tested and the simulated IH curves

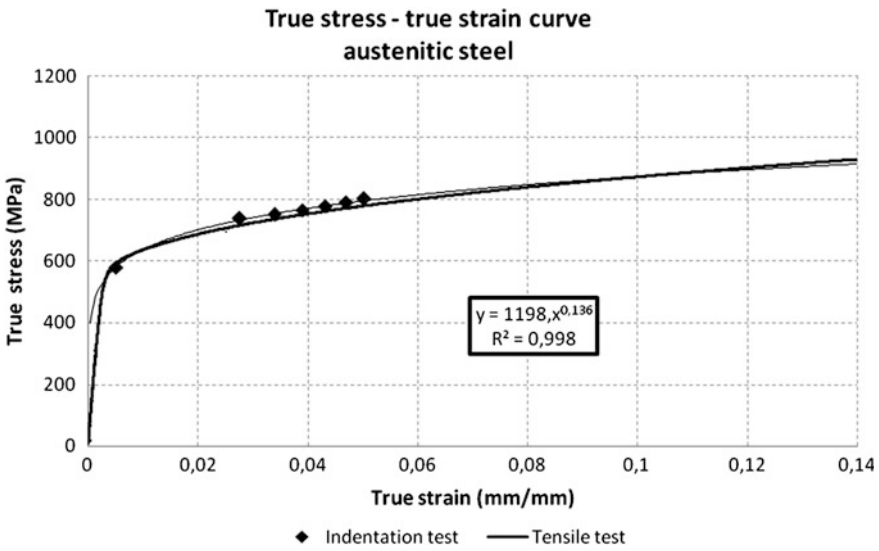

Fig. 14 True stress–true strain curve of austenitic steel

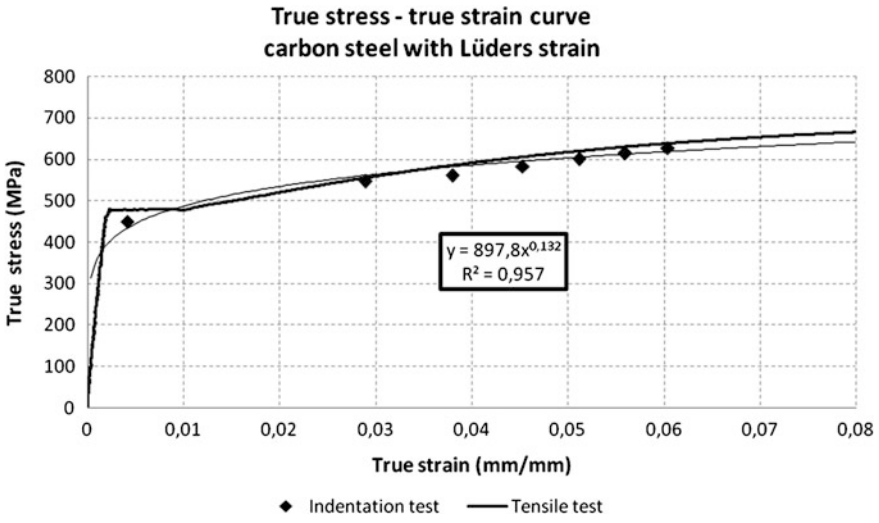

Fig. 15 True stress–true strain curve of carbon steel without Lüders strain

The calculated measurement uncertainties were 5.85 % for yield stress and 7.46 % for the ultimate tensile strength. The measurement uncertainty calculation was based on a conservative method. To determine this with more accuracy, the work be will continued in the future and more extended analysis of the test parameters will be needed. Despite the fact that the curves, the yield stress and the

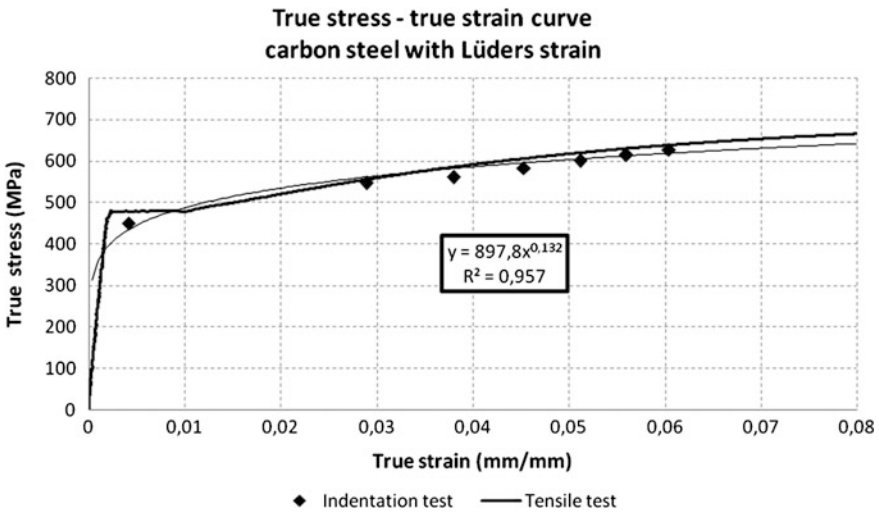

Fig. 16 True stress–true strain curve of carbon steel with Lüders strain

ultimate tensile strength calculated with IHT method fitted well with the tensile test results, the results have some scatter and not always provide accurate data for further assessment.

7 Small Size Tensile Test

It is not possible to sample standard sized specimens from in situ components. Ideally the results of the tensile test are independent of the size of the specimen, but in practice the size of the grains and the test speed are relevant. The speed of the test should be proportional to the size, because at the same testing speed the size is in inverse ratio to the strain. In case of small tensile specimens, the holder can cause additional stresses in the specimen. By finite element analysis, the effect of the holder can be verified and if it is needed the optimisation of the geometry of the holder can be performed.

In this case two types of uniaxial tensile specimens were examined. One of them is a small flat specimen that is easy to manufacture. The specimens should be very accurate regarding their sizes. The surface of the specimens should be very smooth because every little imperfection causes inaccuracy in the results. The temperature of the specimen should be no more than 100 °C under the manufacturing conditions in order to avoid changes in the micro-structure. It is suggested that three pieces of specimens should be tested at every temperature. The developed specimen can be

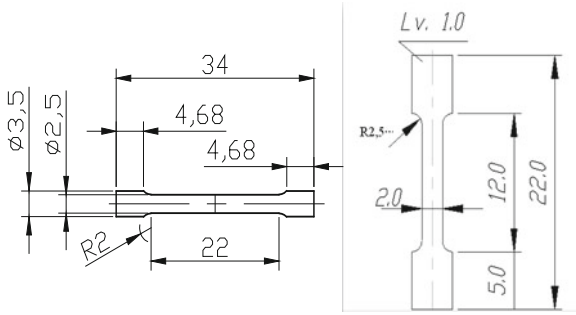

Fig. 17 Sizes of the small flat and cylindrical tensile specimens

tested by most of the tensile testing machines with adjustable loading capability. The geometry of the specimen is shown in Fig. 17.

The other type of tensile specimen is the small cylindrical uniaxial tensile specimen Fig. 17. These types of specimens are not standard sized so the sizing of the specimen depends on the size of the sample, the properties of the testing machine, the strain gauges and the clamping of the specimen.

The test is sensitive to the testing speed so the crosshead-speed should be proportional to the ratio of the diameters.

In case of tensile test specimens, the gauge length of the specimen should be proportionate to the cross-section of the specimen (expedient the standard 5D flat or equivalent specimen application); otherwise the values of the elongation cannot be compared with the measured values of other sizes specimens.

8 Comparison of the Tests

The 22K and the X6CrNiTi18-10 types of steel were compared by four types of material testing technique. The results are quite good (for yield stress and tensile strength), but it needs further research to determine better values from the small specimens and IHT. The comparison of the results is shown in Fig. 18. The sub sized tensile specimens show higher values than the normal size specimen. The values of the SPT and IHT are underestimating the tensile properties in most of cases.

The values determined with different methods show good agreement with the tensile test results. Although the scatter of the material properties determined by SP and IH is larger than which one obtained from the tensile test, these methods can be used for in situ inspection, when basic material properties are unknown and there is no way to cut pieces from the structure for standard size specimens.

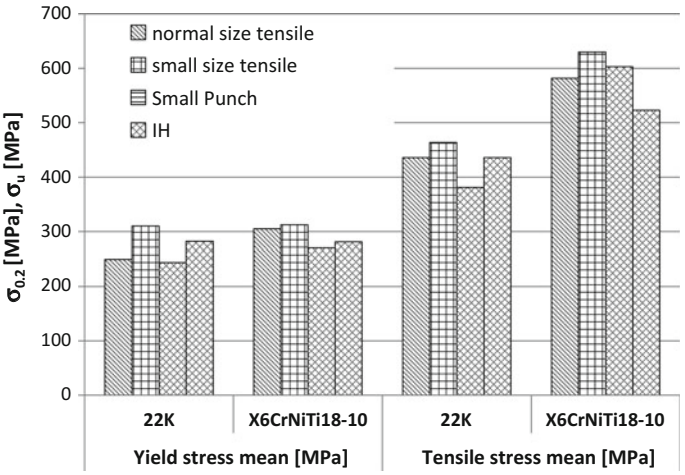

Fig. 18 Comparison of the tests

9 Summary

Analyses of the Instrumented Hardness Test, the Small Punch Test and small size tensile test were performed using experimental tests and finite element simulation. All test techniques are applied for determination of the material properties of aged NPP materials. The IHT test shows some scatter in the results but with some further development it is applicable, when only non-destructive test technique is permitted. The validation of the SPT was also completed and the results from finite element analyses show the measurements are correct. The yield strength determination shows that the equations are good agreement with the results from tensile tests.

The advantages and disadvantages of the small punch specimens are:

- The specimen is very little, so no need for huge amount of material.
- A large number of specimens can be produced from the sample.
- The test can be performed at any temperature.
- It is not a standardised method.
- Biaxial stress arises in the specimen.
- A large number of tests are needed to determine empirical constants.

The advantages and disadvantages of the instrumented hardness test are:

- No specimen needed so no excavation need.
- On-site measurement can be done.
- A large number of tests can be done on a small surface.
- The test can be performed on room temperature.
- Complex measurement device needed.
- Scattering can be relatively high.

The advantages and disadvantages of the small tensile specimens are:

- The flat specimen can be machined from thin surface layers.
- In most cases the direction of the specimen can be longitudinal and transversal too.
- The results of the tests are comparable with the original documentations of the structure.
- Three pieces of specimens are enough for testing.
- The test can be performed at any temperature.
- The test can be performed by any standard testing machine.
- Arbitrary structural material can be tested.
- If the ageing occurs without hardening, specimens should be tested by microstructural methods.

These methods can be used, when some material properties are unknown and there is no way to cut out larger pieces from the structure to determine them with standard size specimens.

References

1. Turba K, Gülçimen B, Li YZ, Blagoeva D, Hähner P, Hurst RC (2011) Introduction of a new notched specimen geometry to determine fracture properties by small punch testing. Eng Fract Mech 78(16):2826–2833
2. Nonaka I, Kanaya A, Komazaki S, Kobayashi K (2010) Standardization of test method for small punch creep testing in Japan. In: Proceedings of 1st international conference "determination of mechanical properties of materials by small punch and other miniature testing techniques", Ostrava, pp 12–18
3. Linse T, Kuna M, Schuhknecht J, Viehrig H-W (2008) Usage of the small-punch-test for the characterisation of reactor vessel steels in the brittle–ductile transition region. Eng Fract Mech 75(11):3520–3533
4. Hurst R, Matocha K (2010) The European Code of Practice for Small Punch testing—where do we go from here? In: Proceedings of 1st international conference "determination of mechanical properties of materials by small punch and other miniature testing techniques", Ostrava, pp 5–11
5. Rodrígez C, Belzunce TE, Penuelas I (2012) The application of the small punch test to the mechanical characterization of different steel grades. In: 2nd International conference on determination of mechanical properties of materials by small punch and other miniature testing techniques, Ostrava, pp 188–195
6. Konopík P, Dzugan J (2010) Small punch test application to fracture toughness determination in the upper shelf region. In: Proceedings of 1st international conference "determination of mechanical properties of materials by small punch and other miniature testing techniques", Ostrava, pp 123–127
7. Haggag FM (1993) In-situ measurements of mechanical properties using novel automated ball indentation system. In: Corwin WR, Haggag FM, Server WL (eds) Small specimen test techniques applied to nuclear reactor vessel thermal annealing and plant life extension, ASTM STP 1204, pp 27–44
8. Klevtsov I, Dedov A (2010) Experience in tensile properties determination by small punch test. In: Proceedings of 1st international conference "determination of mechanical properties of materials by small punch and other miniature testing techniques", Ostrava, pp 128–132

Characterization of Tube Repair Weld in Thermal Power Plant Made of a 12%Cr Tempered Martensite Ferritic Steel

Gordana M. Bakic, Milos B. Djukic, Bratislav Rajicic, Vera Sijacki Zeravcic, Aleksandar Maslarevic, Miladin Radovic, Vesna Maksimovic and Nenad Milosevic

Abstract The heat resistant tempered martensite ferritic steel X20CrMoV121 (DIN) has been extensively used within the last few decades as a material for boiler tubing systems and pipelines in thermal power plants (TPP). Long-term behavior of this steel is vastly researched and very well known, but main disadvantage is its poor weldability. In situ welding of martensitic steels is always challenging task and is usually quite difficult to implement properly in a short time, during forced outages of TPP. In this paper, characterization and mechanical properties of undermatch welded joint made during partial replacement of boiler outlet superheater (SH) in TPP by austenitic filler material, after 10 years of service are presented. Due to "cold" technique of welding, which does not required post weld heat treatment, this procedure were regular and widely used repair welding technique in two TPP (620 MW) units. In the purpose of comparison, two other type of matching welding joints of the same SH were also characterized: shop welded joint made by electrical resistance flash butt welding, as well as field welded joint made by gas tungsten arc welding during assembling of SH, which were both in service approximately 150,000 h.

G.M. Bakic (✉) · M.B. Djukic · B. Rajicic · V. Sijacki Zeravcic · N. Milosevic
Faculty of Mechanical Engineering, University of Belgrade, Kraljice Marije 16, Belgrade 11120, Serbia
e-mail: gbakic@mas.bg.ac.rs

A. Maslarevic
Innovation Center of Faculty of Mechanical Engineering, University of Belgrade, Kraljice Marije 16, Belgrade 11120, Serbia

M. Radovic
Department of Materials Science and Engineering, Texas A&M University, College Station, TX 77843, USA

V. Maksimovic
Department of Materials Sciences, Institute of Nuclear Sciences Vinca, University of Belgrade, P.O. Box 522, Belgrade, Serbia

G. Pluvinage and L. Milovic (eds.), *Fracture at all Scales*,
Lecture Notes in Mechanical Engineering, DOI 10.1007/978-3-319-32634-4_8

1 Introduction

In the past decades, tempered martensite ferritic steels with 9–12 % chromium and containing carbide stabilizing elements have been widely used for components which operate within the creep range in power and industrial processing plants [1–6]. This class of 12Cr steels, X20CrMoV 12.1 (DIN 17175) steel was successfully used for boiler tubing system outlet sections superheaters (SH), headers and main steam pipelines in TPP at service temperatures up to 565 °C.

The mechanical, creep and fracture properties of X20CrMoV 12.1 steel strongly depends on its microstructure, which in turn depends on the chemical composition, thermo-mechanical treatment and welding process used for components assembly [1]. The heat treatment of X20CrMoV 12.1 steel consists of austenitizing (at 1020 up to 1070 °C) and subsequent tempering (at 730–780 °C) both followed by air cooling [7, 8], in order to achieve a long term stability, as well as a good combination of strength, toughness and high temperature creep strength. The typical microstructure of such steel is tempered martensite with fine dispersed carbide phase precipitated along the former austenite grain boundaries and martensitic lath [1]. Basic strengthening mechanisms of X20CrMoV 12.1 steel are done by refined grains due to a formation of tempered martensitic lath structure with high dislocation density, precipitation strengthening by uniformly dispersed carbides, mainly of a $M_{23}C_6$ type rich in Cr and Mo, and also MX particles that containing V, as well as a solid solution strengthening obtained by the high content of Cr and Mo in the matrix [1–5, 7]. Some investigations on X20CrMoV 12.1 steel indicated that the carbides of M_7C_3 and M_2X type are also responsible for the precipitation hardening and high creep strength [9, 10].

Furthermore, during prolonged service at high temperatures different mechanisms are activated in material and as a result, microstructural degradation and decrease in mechanical properties occur [4, 5, 11–17]. However, some of the investigations of X20CrMoV 12.1 steam pipelines indicated that severe softening did not always occurs after long-term service exposure at elevated temperature [8]. Some microstructural investigation during long-term aging and creep using interrupted creep tests [18, 19] shows that coarsening of subgrain size, loss of the correlation between carbides and subgrain boundaries and an increase of the number of low-angle subgrain boundaries occurred after long-term service. Also, a direct interaction of carbides with dislocation processes at subgrain boundaries was detected using transmission electron microscope [20, 21]. It was shown that the creep strength of tempered martensitic steels strongly relies on $M_{23}C_6$ carbides, that can change their chemical composition [18, 22] during aging and they also undergo coarsening trough Ostwald ripening [18, 22–24]. Also, Laves phase particles has been reported after creep exposure [3, 8, 18, 22, 25–27] in a specific condition and also observed in the immediate vicinity of $M_{23}C_6$ carbides [4, 22, 28]. Finally, creep rupture in tempered martensitic steels is usually controlled by cavity nucleation and growth [3] originating mainly on different inclusions particles [2, 4, 29].

In the case of welded joints of X20CrMoV121 steel, several additional aspects must be taken into consideration. Tempered martensite ferritic steels with relatively high-carbon content and generally difficult weldability have to be properly heat treated in order to provide adequate quality and service life [1, 5, 30–32]. Generally, the martensitic heat resistant steels harden during the heat treatment. However, the low-carbon martensitic steels can be still welded without special precautions. If the content of carbon exceeds 0.15 %, as in the case of X20CrMoV121 steel with carbon content of approximately 0.2 %, the heat treatment before and after welding is required to avoid hardening of the material, as well as mandatory undercooling immediately after welding in order to complete martensitic transformation [5]. During welding the initial microstructure is partly changed due to the thermal cycle of welding and the heat-affected zone (HAZ) generally is less resistant to creep damage in comparison to the base material, especially in an intercritical zone [3].

Having in mind the large number of SH welded joints, located in the boiler of TPP, it is necessary to emphasize the great importance of deterioration of welded joint properties and their evaluation during long-term service in order to provide the sufficient data for residual life estimation of such components [4, 5, 12–14, 33–42]. SH consist of parallel-mounted steel tubes, butt welded and bent, with different outside diameters. During service, it is common to expect outages of some tubes and therefore the main purpose of repair welding during power plant maintenance is to quickly restore serviceability of an original part [32]. Repair welding should be performed at minimal costs and quickly during plant outage [12, 37]. For hard-enable steels, during repair procedure pre and post-welding heat treatments with slow cooling are needed and do not always represent the best solution from the efficiency point of view, especially during very short outages.

In two 620 MW lignite-fired TPP units the long period that was required for repair welding of SH tubes made of martensitic X20CrMoV121 steel was a serious maintenance task and challenge [5, 12]. The solution was found in “cold” welding that involves repair welding by high Ni containing filler material (70Ni20Cr alloy). This technique has many advantages such as short welding time and a relatively easy welding process without post weld heat treatment (PWHT). However, “cold” repair welding is mostly considered to be only a temporarily solution for damage repair and most of those welds were replaced during next TPP overhaul, but for purpose of investigation some of them were maintained in service for more than 10 years [5].

In this paper, the summary of characterization of base and filler material of undermatch repair welding joint in the final SH after 10 years of service is presented. In the purpose of comparison, two other type of matching weld joints of the same SH were also characterized: (a) shop welded joint made by electrical resistance flash butt welding process (FBW) and (b) field welded joint made by gas tungsten arc welding process (GTAW) during assembling of SH, which were both in service approximately 150,000 h.

2 Background and Experimental Procedure Details

Superheaters (SH) located in boilers of TTP are exposed to severe operating conditions which are usually accompanied by simultaneous activity of multiple damage mechanisms of material which can considerably reduce their designed service life. The most important damage mechanisms are long-term creep and oxidation. Particularly endangered and exposed to the most severe operating conditions are final SH that provide fresh steam of the highest parameters.

During long-term service of SH, microstructural degradation and creep damage typically occurred simultaneously and also a drop in the mechanical properties of material. These processes can lead to premature damage of SH tubes and forced outages of TPP. In order to avoid and prevent forced outages during plant service, it is necessary to implement monitoring of boiler heating surfaces and to assess the degree of exhaustion of the material, particularly after approximately half of the design service life spent in exploitation. The most common methods that are used are sampling and different types of non destructive testing.

The final SH in a 620 MW lignite-fired TPP unit was made of X20CrMoV121 steel. The SH consists of tubes (outer diameter: 38 mm) with different wall thicknesses in the different sections, Table 1.

The inlet sections of the final SH (Sects. 1 and 2) were made of tubes with wall thickness of 4 and 4.5 mm, while operating temperatures and pressure are: (t_{steam} = 485 °C, p_{steam} = 190.8 bar and t_{gas} = 900 °C). However, the outlet tubes of SH (Sects. 3 and 4) have a greater wall thickness: 5 and 5.6 mm, since the operating parameters are much higher in this sections (t_{steam} = 540 °C, p_{steam} = 186 bar and t_{gas} = 900 °C).

The number of boiler outages due to the damages of SH tubes was not large during service. In order to monitor the condition of final superheaters and to form a data base about the state of the material in two identical TPP units (620 MW each), the practice of periodic testing of tube samples was introduced after 80,000 h of service. In addition to material data obtained during regular annual overhauls of TPP, also data about the damage mechanisms obtained during failure analyses, which were carried out before the start of the systematic monitoring of material state were used.

After reaching approximately 150,000 h of service, the first signs of serious degree of material aging and the appearance of creep damage in localized zones of welded joints were observed, Fig. 1. It is important to note that the boiler tubes shop welds were made by FBW welding process, which is typical for the time when these TPP units were built, while field welds were made by GTAW process.

Table 1 The tube dimensions in different sections of the final SH (X20CrMoV121 steel)

SH No. 4	Tube dimensions (mm)	Length (m)
Section 1 (inlet)	Ø38 × 4	21.7
Section 2	Ø38 × 4.5	8.3
Section 3	Ø38 × 5	6.2
Section 4 (outlet)	Ø38 × 5.6	11.5

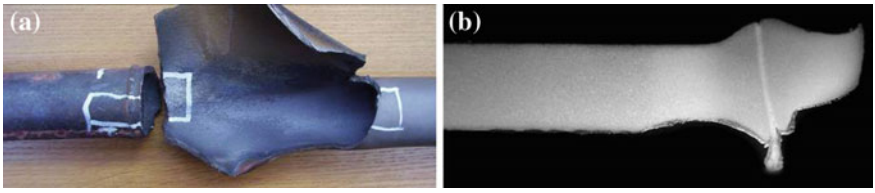

Fig. 1 Fracture features of SH tube welded joint: **a** macro view, **b** cross section; photos courtesy by Welding Institute Ltd., Serbia

The regular repair procedure for X20CrMoV121 steel includes pre and post weld heat treatments and required a lot of time which was not acceptable in many cases. The solution was found in "cold" welding that involves repair welding by austenitic filer material with high contents of nickel and chromium, such as FOX NIBAS 70/20, Böhler—70Ni20Cr alloy due to its preferable mechanical properties [5].

Testing of three samples of SH tube butt welded joints was done, Table 2. One of the SH repair undermatching welds was sampled (sample 1) to study the mechanical and structural properties of the base material and austenitic filler material (70Ni20Cr alloy) after 60,000 h of service [36]. In the purpose of comparison, two other type of matching weld joints of the same SH were also characterized: (a) shop welded joint made by FBW process (sample 2) and (b) field welded joint made by GTAW process during assembling of SH (sample 3), which were both in service approximately 150,000 h.

Several experimental techniques have been used in order to characterize microstructural and mechanical properties of the welded joints after prolonged service. The following experimental techniques were used during experimental research: visual testing and dimensional measurement, hardness measurement, tensile testing, microstructural characterization by optical microscopy and scanning electron microscopy (SEM), as well as chemical composition analysis of metal by quantometer and qualitative analysis of tube scale by X-ray diffraction (XRD) analysis.

Visual testing and macrographic examination of outer and inner surfaces of SH tubes in the vicinity of welded joints were done in order to detect deposits and oxide scales.

Tube samples dimensional measurements: tube outer diameter, tube wall thickness, outer surface deposit thickness and weld reinforcement measurement were done using a mechanical external measuring gauge, Kroeplin D1R10.

Table 2 SH welded joint samples characteristics

Sample	Type of joint	Welding process	Filler material	Tube dimension (mm)	Service time (h)
1	Repair weld	"Cold"	70Ni20Cr alloy	Ø38 × 4/Ø38 × 4.5	60,000
2	Shop weld	FBW	–	Ø38 × 4/Ø38 × 4.5	150,000
3	Field weld	GTAW	Matching	Ø38 × 4/Ø38 × 4.5	150,000

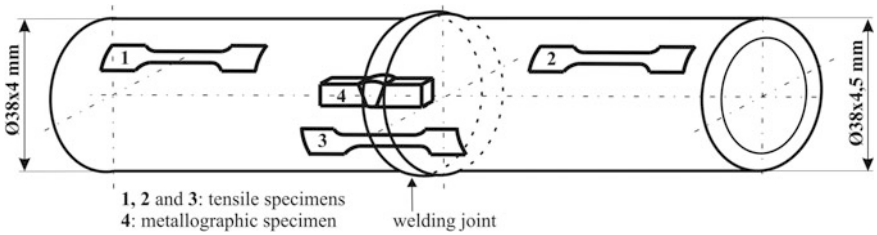

Fig. 2 The position of tensile and metallographic specimens on SH tube samples 1–3

For the hardness measurement (Vickers hardness HV30) of material metallographic specimens and a stable Vickers hardness device, type HPO 250 VEB-WPM Leipzig, were used.

Tensile testing of specimens was carried out on a mechanical tensile machine AVK, type 10t at ambient (20 °C) temperature, according to EN 10002-1. Testing was performed on the total of nine specimens cut out from SH tube samples No. 1–3 (Table 2) with weld joint, Fig. 2.

For all tube samples (1–3), Table 2, tensile test were performed on specimens cut out from the base materials (specimen 1 and 2) and also specimens that contain a weld joint (specimen 3) as shown in Fig. 2.

The microstructural characterization by optical microscopy at different magnifications was carried out on specimens cut out from tube samples 1–3 in the area of tube butt weld joints, using an optical microscope Carl Ziess Axiovert 25 equipped with a Panasonic WV-CD50 digital camera. Exact location of specimen is shown in Fig. 2 (specimen 4). All specimens were polished and etched in 10 ml HNO_3 + 30 ml HCl and 5 g $FeCl_2$ + 50 ml HCl + 100 ml H_2O solutions. Inner surface oxide scale thickness measurement was also done by optical microscopy.

Specimens for SEM examination of the microstructure were prepared in the standard way, by cutting, grinding, polishing, etching and vapor deposition of gold. A metallographic examination was carried out on SEM unit, type JEOL JSM-6460LV at different magnifications.

Analysis of the chemical composition of material was performed by mass spectroscopy using an ARL 31000 quantometer. The chemical composition (qualitative and quantitative XRD diffraction analysis) of SH boiler tube scale deposits—powders on the tube inner surfaces was performed using a Siemens D500 PC diffractometer, CuKα radiation (λ = 1.54056 Å), in the 2θ range 10–70° with a step of 0.02°. Identification of phases was carried out using DIFFRACTplus software package and joint committe on powder diffraction standards (JCPDS) database for XRD peak identification.

3 Results and Discussion

3.1 Visual Testing and Tube Dimensional Measurements

The outer surface of sample 1 was exposed to the combustion product and thus covered with a thick gas side deposit, Fig. 3. The deposit is strongly adhered to the metal surface and thickness varies along the tube, with maximum thickness up to 15 mm.

Visual inspection of sample 1 ("cold" process) indicates on an area with excessive weld reinforcement (height: 1.5–3.5 mm) and also an area with an incomplete root fusion and penetration (depth: 1.5 mm). The thick magnetite layer can be observed on the inner surface of the tube, Fig. 3.

The sample 2 (FBW process) has the similar thick oxide layer on tube inner surface, but outer surface without deposit suggests that this particular tube was shielded by some other parts and thus not exposed to intensive erosion or gas side deposit formation during service. Oxide scale is detected on the tube inner surface which is covered by a very fine steam side deposit, Fig. 3.

The sample 3 (GTAW process) is also exposed to gas side deposition and has excessive weld reinforcement up to 1.2 mm. Inner side has fine deposit on the top of the oxide scale. Both sample 2 and 3 are without visible corrosion damage, Fig. 3.

The results of tube dimensional measurements for samples 1–3 are summarized in Table 3. Tube wall thinning is detected for all three samples most probable due to oxidation process. Excessive gas side deposit detected in samples 1 and 3, results in a little bit larger tube outer diameters, measured after deposit removal.

In order to determine the scale uniformity oxide scale thicknesses on the tube inner surface are measured for all three samples in the base metal area at 30

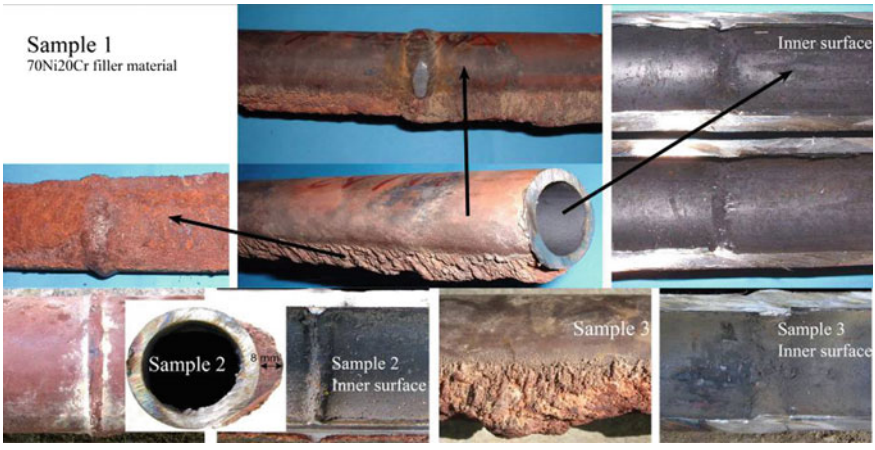

Fig. 3 Macro photographs of SH tube samples 1–3

Table 3 Dimensional measurements for SH tube samples 1–3

Sample	Tube outer diameter (mm)	Tube wall thickness (mm)	Outer surface deposit thickness (mm)	Inner oxide scale thickness (mm)	Weld reinforcement (mm)
1	38.2–38.4	3.95–4.15/4.2–4.7	up to 12	0.14–0.18	1.5–3.5
2	37.9–38.2	4.0–4.1/4.5–4.6	up to 8	0.10–0.20	0.45
3	38.1–38.2	3.8–3.9/4.4–4.7	up to 15	0.06–0.12	0.7–1.2

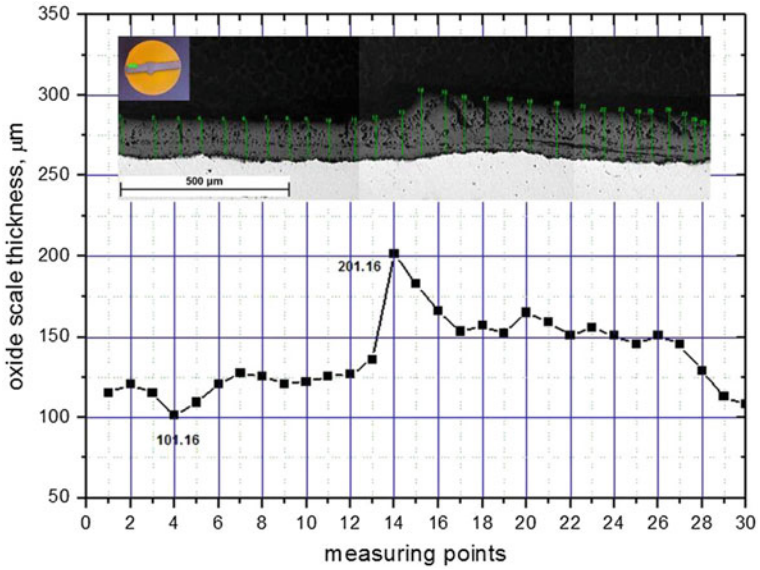

Fig. 4 Distribution of oxide scales thickness on inner side of SH tube sample 2

positions and obtained results with minimum and maximum values for sample 2 are shown in Fig. 4.

Oxide scales thickness are relatively uniform on all 3 samples, except in the area of defective weld root of sample 1 with an excessive root penetration, where the oxides formed thicker layer downstream of the welded joint, a local flow disrupter, due to a locally different steam flow conditions [35].

3.2 Chemical Analysis

Chemical composition of base metal of sample 1 and 2 (BM1, BM2), as well as the standard data for X20CrMoV121 steel (DIN–17175/79) [43] and an austenitic filer material—70Ni20Cr alloy (FOX NIBAS 70/20, Böhler) are shown in Table 4.

Table 4 Chemical composition, wt %

Sample	C	Si	S	P	Mn	Ni	Cr	Mo	V
1-BM1	0.19	0.42	0.01	0.02	0.47	0.73	9.25	1.17	0.26
1-BM2	0.20	0.35	0.006	0.018	0.45	0.46	11.3	1.10	0.30
2-BM1	0.21	0.33	0.01	0.02	0.42	0.68	10.1	0.95	0.33
2-BM2	0.21	0.26	0.006	0.019	0.51	0.443	12.24	1.01	0.32
3-BM1	0.23	0.27	0.005	0.023	0.52	0.46	12.30	1.04	0.32
3-BM2	0.21	0.38	0.001	0.018	0.57	0.584	11.99	0.97	0.27
X20CrMoV121 (DIN 17175)	0.17–0.23	≤0.50	max 0.03	max 0.03	≤1.00	0.30–0.80	10.0–12.5	0.80–1.20	0.25–0.35
FOX NIBAS 70/20—Böhler[a]	0.025	0.4	–	–	5.0	≥67.0	19.0	≤1.2	–

[a] Rest: Nb 2.2; Fe 3.0; Co ≤ 0.08; Ti^{+}

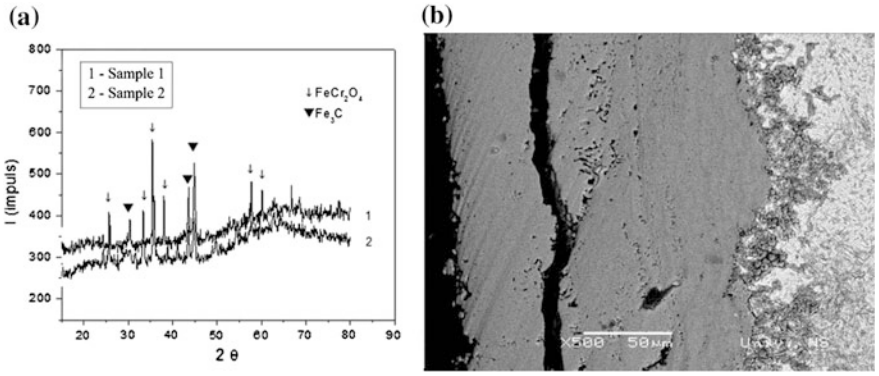

Fig. 5 Tubes inner side oxide scale: **a** XRD analysis, **b** SEM backscattering image

The chemical composition of the BM is within the standard range, except for sample 1-BM1 that contains less Cr. The results of qualitative and quantitative analyses of tubes inner side oxide scale of sample 1 and 2 indicates on the presence of iron (Fe) and oxygen (O), mainly in the form of complex oxide $(Cr, Fe)_3O_4$, while iron carbide Fe_3C was also detected, Fig. 4a. The detected carbide phase is most probable residual from oxidation process that attack only matrix and not carbide phase, Fig. 5b.

3.3 Mechanical Properties

The average hardness values of the base metals and weld joints for all three samples (1–3) are shown in Fig. 6. In the case of sample 3, GTAW joint with a matching filler material the hardness of the weld metal and the HAZ are almost equal and

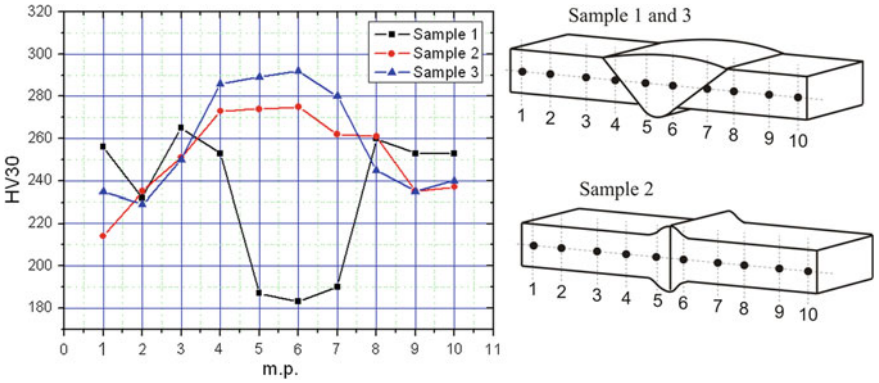

Fig. 6 Sample 1–3: hardness measurements results and measurement positions

both are higher in comparison with the base metal. The similar results is obtained for sample 2 (FBW), but an absence of filler material and generally lower heat input during this welding process, results in a smaller differences in hardness. The variation of hardness along the cross-section of the weld joints correspond to the different area within weld joint and type of joint (for base metal the required value of hardness, according to VGB-R501H Norm [44] is 215–265HV). However, somewhat lower hardness values were measured on sample 2 in weld HAZ most probably due to prolonged service at the elevated temperature.

The measured hardness of the weld metal of sample 1 is significantly lower then martensitic base material due to the presence of different filler material—70Ni20Cr alloy, as expected.

The results of tensile tests (yield strength—*YS*, ultimate tensile strength—UTS and percent elongation A%) are summarized in Table 5. The position of tensile specimens on SH tube samples 1–3 is shown in Fig. 2. For all samples, tensile test of both base metals (BM1 and BM2)—X20CrMoV121 steel and weld metal (WM) were conducted. In the case of sample 2 and 3, tensile specimens that containing WM (specimen 3 as shown in Fig. 2) failed in the area of the base metal

Table 5 Tensile properties

Sample	BM–X20CrMoV121 steel			WM and fracture location
	YS (MPa)	UTS (MPa)	A (%)	UTS (MPa)
1-BM1	590	750	21.3	594 (WM—70Ni20Cr)
1-BM2	645	820	23.2	
2-BM1	601	752	21.3	680 (BM1)
2-BM2	626	806	22.3	
3-BM1	498	689	27.0	650 (BM1)
3-BM2	533	674	26.0	
X20CrMoV121 (DIN)	490	690–840	min 17	–

with a lower thickness. In the case of Sample 1, the tensile strength of the austenitic filler material was found to be lower than that the specified by manufacturer (FOX NIBAS 70/20 Böhler) which could be attributed to welding defects such as incomplete root penetration, as well as long term exposure to the elevated temperatures.

Also, it should be noted that both BM of sample 3 (3-BM1 and 3-BM2) have a little bit lower tensile strength which could be considered as a first sign of aging effect.

3.4 Microstructural Characterization

3.4.1 SH Tube Sample 1—"Cold" Process

Optical micrographs of the different areas of the welding joint with 70Ni20Cr filer material (70/20WM), SH tube sample 1, are shown in Fig. 7. The original SH tube that had been in service 150,000 h is marked BM1, while the tube that had been replaced (service: 60,000 h) is marked BM2. It is obvious from Fig. 7a that root has an incomplete root fusion and penetration.

The microstructure of BM1 and BM2 consist of fine-grained and coarse-grained tempered martensite. The microstructural evidence of the long term exposure to the elevated temperature, such as martensite decomposition and presence of small amount of ferrite with carbides, can be observed. In addition, inhomogeneous distribution of carbide phase, along with a huge number of fragmented oxides and MnS inclusions (length: 6–76 μm) are observed. The large number of inclusions is also visible in BM2, Fig. 7f. The defects such as subsurface micro cracks are visible in BM1, Fig. 7e. Macro cracks that were formed during service are also present in the WM, Fig. 7a.

In the vicinity of the WM, a large number of cavities are present in BM1, indicating creep damage of class 3a or 4 according to VGB-TW 507 standard classification [44], Fig. 7b, c. Cavities are visible in the vicinity of both inner and outer surfaces, Fig. 7c, e. However, the coalescence of the cavities is more pronounced in the subsurface area of the tube outer surface where they forming micro cracks, as shown in Fig. 7e, as well as in the vicinity of the corrosion pits, Fig. 7c. The creep cavities nucleation were additionally promoted due to the presence of microstructural defects such as oxides and MnS inclusions, Fig. 7b, and also by inadequate weld joint geometry-counter defects which also contributes to the increased local stress.

Damage caused by high temperature corrosion in the wide area of BM on the tube outer surface, Fig. 8a, and oxidation on the inner surface of SH tube sample 1 are also observed. Some of corrosion pits are filled with the oxide and their depth are in the range: 0.15–0.20 mm, while the width of the corrosion pits usually do not exceeds 0.25 mm.

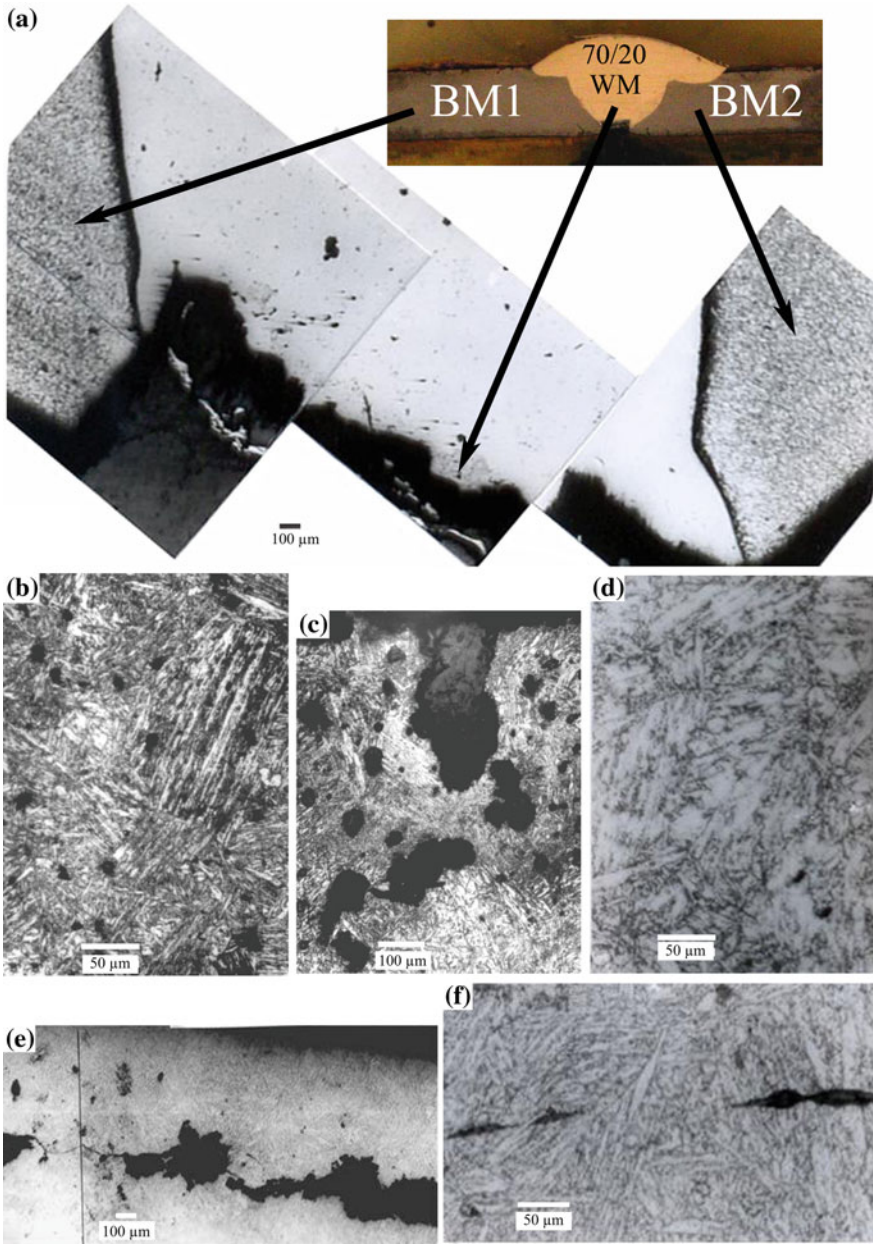

Fig. 7 Optical micrographs of SH tube sample 1—70Ni20Cr filler material: **a** WM, BM1 and BM2, **b** BM1, **c** BM1-cavities, **d** BM2, **e** BM1 outer surface and **f** BM2 middle of cross section. Adapted from [5]

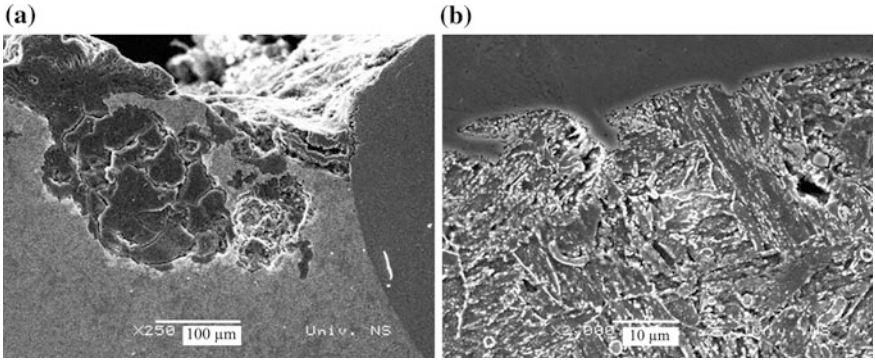

Fig. 8 SH tube sample 1, SEM: **a** BM1, **b** interface WM–BM1

The contact zone between WM and BM contains a large quantity of carbide phase (with of the zone: 0.1–0.3 mm), Fig. 7a. In close vicinity of fusion line, much coarser needle like carbide phase could be observed, Fig. 8b. The areas rich in Cr carbide phase is followed by areas of carbon depletion as shown in Fig. 7a. that are result of a long term service at elevated temperatures due to intensive diffusion processes.

Since heterogeneous welding joints contain materials differ in the composition (the filler material contains much more Cr than the martensitic base material), diffusion processes occur in the weld and surrounding HAZ at high service temperatures. At these temperatures, Cr diffusion leads to the formation of the carbone reach diffusion layer.

The carbon reach zones were observed in both base materials, but this process was more pronounced in the BM1, because of already aged microstructure before repair welding (during previous service) and more intensive degradation processes governed by diffusion.

3.4.2 SH Tube Sample 2—FBW Process

FBW welding process of steam boiler tubes lead to undesirable weld joint shape on inner surface of the tube from the flow point of view as could be seen in SH tube sample 2, Figs. 9a, c and 3. The compact layer of oxides on tube inner side was formed during the long term service at elevated temperature, Fig. 9a, c and d, in all zones exposed to oxidation environment leading to continuous thinning of tube metal, Table 3 and Fig. 4.

The microstructure of SH tube sample 2 is tempered martensite, Fig. 9. Generally, the morphology of the tempered martensite depends on the maximum temperature to which it was exposed material during welding. The coarse grained zone was detected in the vicinity of fusion/welding line, Fig. 9b, followed by fine grain zone and soft annealing zone of HAZ as shown in Fig. 9f.

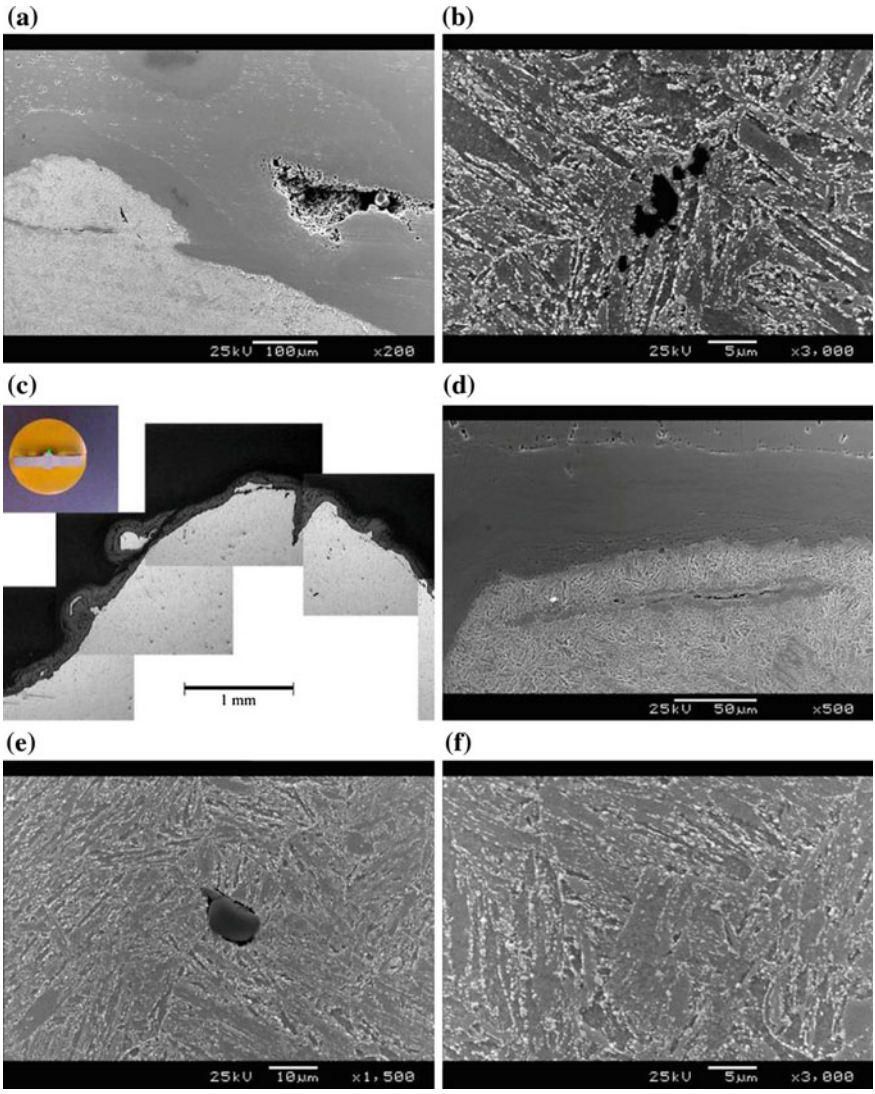

Fig. 9 SH tube sample 2 (FBW process), SEM: **a** oxide scale on inner surface of weld tip, **b** fusion/welding line, **c** inner surface of weld tip, **d** detail from **c**, **e** BM1, **f** HAZ—soft annealing zone

In weld fusion line imperfections like inclusions and cavities could be observed, Fig. 9b. The origin of these imperfections is in FBW process, during which a high current density is applied, leading to heating and a softening of the zones at tube ends, and after flashing final weld is formed by applied force, squeezing out melted material and eliminating oxides and contaminants. In this case some of the imperfections were not eliminated during welding process.

There is not significant microstructural evidence of the long-term exposure to the elevated temperature except in soft annealing zone of HAZ where slight degree of martensitic phase degradation was observed, with wider martensitic laths and carbide phase precipitated on the laths boundaries, Fig. 9f, as well as on former austenite grain boundaries. Boiler service history clearly indicates that damages in the HAZ soft annealing zone of shop welded joints of final SH was one of the most preferable location for repeated boiler tube failures. Also slightly lower hardness values in HAZ of SH tube sample 2 are in accordance with observed microstructural characteristics, Fig. 6.

3.4.3 SH Tube Sample 3—GTAW Process

The microstructure of SH tube sample 3 (GTAW process), Fig. 10c, with the matching filler material is tempered martensite, Fig. 10a, b. In weld metal large area of δ-ferrite was observed in vicinity of BM2, Fig. 10d. The appearance of δ-ferrite in martensitic welded joint is common in the case of high heat input during welding [45], which was confirmed by a higher hardness values in WM, Fig. 6. To achieve full martensite transformation after welding, weld should be cooled to the temperature in the range: 100–120 °C with minimum holding time 1 h. After welding, the stress relieving of welded joints is required [42]. In this case morphology of the tempered martensite also depends on the maximum temperature to which material was exposed during welding, Fig. 10a, b.

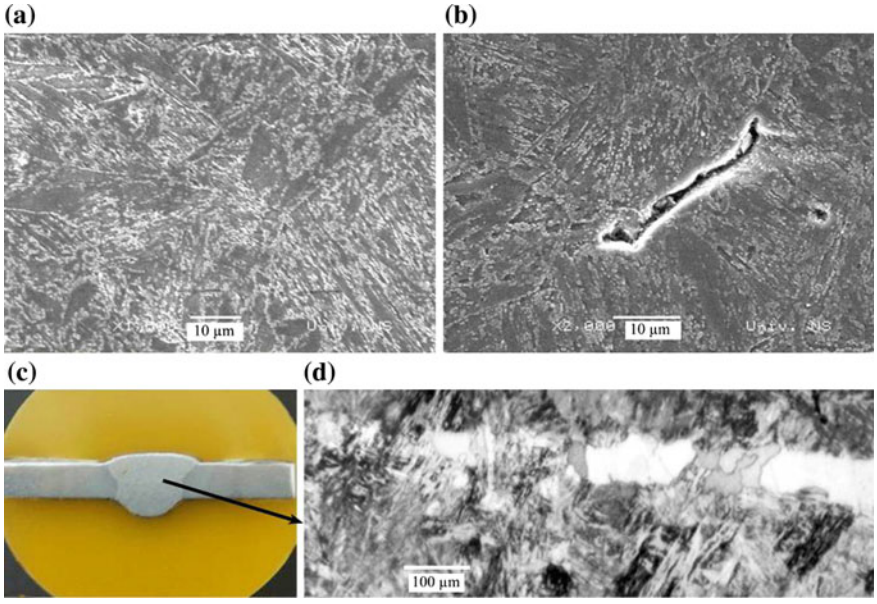

Fig. 10 SH tube sample 3 (GTAW process): **a** SEM, BM1; **b** SEM, HAZ-BM2, inclusion; **c** macroview sample 3, **d** optical microscopy: WM near BM2

The compact oxide layer that was formed during the long-term service at elevated temperatures can be seen on the inner surface of the tube, Fig. 3. The diffusion of the Cr resulted in the formation of Cr-rich oxide layer on the inner surface of the tube. The very low degree of the martensitic decomposition can be observed in both BM and WM due to the aging, Fig. 10a, b, but in the vicinity of complex oxide type inclusion complete decohesion of inclusions with the matrix could be observed, Fig. 10b.

4 Conclusions

The welding of a 12%Cr tempered martensite ferritic steel, such as X20CrMoV121 steel, that is characterized with a poor weldability required careful application of proper pre and post weld heat treatment procedure in order to achieve the high quality welded joint. Such procedure required a lot of time which was not acceptable in the case of frequent forced outages of TPP when the full heat treatment of the repaired weld joints it is not always feasible to perform. The solution was found in "cold" weld process that involves repair welding of SH tubing system using an austenitic filer material with high contents of nickel and chromium, (70Ni20Cr-alloy) due to its preferable mechanical properties. The application of an austenitic filler material for repair welding of boiler tubes has many advantages such as: short welding time, no need of specific atmosphere, relatively easy welding process and tough and ductile welding joints. However, the main disadvantage of this repair welding technique is inhomogeneous characteristics of welding joint with shorter service life in a creep regime in comparison with similar metal martensitic welds. These disadvantages are particularly pronounced in the case of when the repaired welded joint is exposed to the long-time service at elevated temperature. Thus, the repair welding of the martensitic steels with an austenitic filler materials can be used only as a temporarily solution in order to avoid a time consuming full welding cycle. Usually, these types of repaired welds are recommended for a short term service and replacement during TPP overhauls. Results presented in this paper, clearly indicate that despite mentioned restriction regarding usage of an austenitic filler material for repair welding of boiler tubes, these welds could have decent and reliable service time. Service time depends on the quality of repair welding process.

References

1. Gandy D (2006) X20 CrMoV12-1 steel handbook. EPRI, Palo Alto, CA. 1012740
2. Van Zul FH et al (2005) Life assessment and creep damage monitoring of high temperature power components in South Africa's power plant. In: Abstracts of the 1st ECCC creep conference, DEStech Publications, London, 12–14 Sept 2005

3. Eggeler G (1989) The effect of long-term creep on particle coarsening in tempered martensite ferritic steels. Acta Metall 37:3225–3234
4. Bakic G, Sijacki Zeravcic V, Djukic MB et al (2014) Material characterization of the main steam gate valve made of X20CrMoV 12.1 steel after long term service. Proced Mater Sci 3:1512–1517. doi:10.1016/j.mspro.2014.06.244
5. Bakic G, Sijacki Zeravcic V, Djukic M et al (2014) Characterisation of undermatch welded joint of X20CrMoV121 steel after prolonged service. Struct Integr Life 14:133–140
6. Milovic LJ, Vuherer T, Blacic I (2013) Microstructures and mechanical properties of creep resistant steel for application at elevated temperatures. Mater Des 46:660–667. doi:10.1016/j.matdes.2012.10.057
7. Zielińska-Lipiec A, Kozieł T, Czyrska-Filemonowicz A (2010) Quantitative characterisation of the microstructure high chromium steel with boron for advanced steam power plants. J Achiev Mater Manuf Eng 43:200–204
8. Maile K (2007) Evaluation of microstructural parameters in 9–12 % Cr-steels. Int J Press Vessels Pip 84:62–68. doi:10.1016/j.ijpvp.2006.09.012
9. Straub S, Blum W, Röttger D et al (1997) Microstructural stability of the martensitic steel X20CrMoV12-1 after 130000 h of service at 530 °C. Steel Res 68:368–373
10. Zhen-Fel H, Zhen-Guo Y (2003) Identification of the precipitates by TEM and EDS in X20CrMoV12.1 after long-term service at elevated temperature. J Mater Eng Perform 12:106–111. doi:10.1361/105994903770343556
11. Bakic G (2012) Model for remaining life assessment of thermal power plant components. Dissertation, University of Belgrade
12. Sijacki Zeravcic V, Bakic G, Djukic M et al (2010) Contemporary maintenance management of power plant life exhaustion components. Tech Technol Educ Manag 5:431–436
13. Bakic GM, Sijacki Zeravcic VM, Djukic MB et al (2011) Thermal history and stress state of a fresh steam-pipeline influencing its remaining service life. Therm Sci 15:691–704. doi:10.2298/TSCI110509050B
14. Bakic GM, Sijacki Zeravcic VM, Djukic MB et al (2014) Remaining life assessment of a high pressure turbine casing in creep and low cycle service regime. Therm Sci 17:S127–S138. doi:10.2298/TSCI121219179B
15. Djukic MB, Sijacki Zeravcic V, Bakic GM et al (2015) Hydrogen damage of steel: a case study and hydrogen embrittlement model. Eng Fail Anal 58:485–498. doi:10.1016/j.engfailanal.2015.05.017
16. Sijacki Zeravcic V, Bakic G, Djukic M et al (2008) Failures at elevated temperatures. In: Sedmak S, Radakovic Z (eds) The challenge of materials and weldments, structural integrity and life assessment. Monograph from 9th international fracture mechanics school. Society for Structural Integrity and Life, Faculty of Technology and Metallurgy, University of Belgrade, Gosa, Serbia, pp 183–202
17. Sijacki Zeravcic V, Bakic G, Djukic M et al (2004) Malfunctioning during service life. In: Sedmak S, Radakovic Z (eds) From fracture mechanics to structural integrity assessment. Monograph from 8th international fracture mechanics summer school—IFMASS8. Society for Structural Integrity and Life, Faculty of Technology and Metallurgy, University of Belgrade, pp 193–208
18. Aghajani A, Somsen Ch, Eggeler G (2009) On the effect of long-term creep on the microstructure of a 12 % chromium tempered martensite ferritic steel. Acta Mater 57:5093–5106. doi:10.1016/j.actamat.2009.07.010
19. Aghajani A, Richter F, Somsen C et al (2009) On the formation and growth of Mo-rich Laves phase particles during long-term creep of a 12 % chromium tempered martensite ferritic steel. Scripta Mater 61:1068–1071. doi:10.1016/j.scriptamat.2009.08.031
20. Kostka A, Tak K-G, Hellmig RJ et al (2007) On the contribution of carbides and micrograin boundaries to the creep strength of tempered martensite ferritic steels. Acta Mater 55:539–550. doi:10.1016/j.actamat.2006.08.046

21. Pesicka J, Aghajani A, Somsen Ch et al (2010) How dislocation substructures evolve during long-term creep of a 12 % Cr tempered martensitic ferritic steel. Scripta Mater 62:353–356. doi:10.1016/j.scriptamat.2009.10.037
22. Isik MI, Kostka A, Eggeler G (2014) On the nucleation of Laves phase particles during high-temperature exposure and creep of tempered martensite ferritic steels. Acta Mater 81:230–240. doi:10.1016/j.actamat.2014.08.008
23. Liu F, Fors DHR, Golpayegani A et al (2012) Effect of boron on carbide coarsening at 873 K (600 ˚C) in 9 to 12 pct chromium steels. Metall Mater Trans A 43:4053–4062. doi:10.1007/s11661-012-1205-6
24. Rojas D, Garcia J, Prat O et al (2011) Effect of processing parameters on the evolution of dislocation density and sub-grain size of a 12 % Cr heat resistant steel during creep at 650 ˚C. Mater Sci Eng A 528:1372–1381. doi:10.1016/j.msea.2010.10.028
25. Yamamoto K, Kimura Y, Mishima Y (2003) Effect of matrix substructures on precipitation of the Laves phase in Fe–Cr–Nb–Ni system. ISIJ Int 43:1253–1259. doi:10.2355/isijinternational.43.1253
26. Kipelova A, Belyakov Kaibyshev R (2012) Laves phase evolution in a modified P911 heat resistant steel during creep at 923 K. Mater Sci Eng A 532:71–77. doi:10.1016/j.msea.2011.10.064
27. Hald J (2008) Microstructure and long-term creep properties of 9–12 % Cr steel. Int J Press Vessels Pip 85:30–37. doi:10.1016/j.ijpvp.2007.06.010
28. Isik MI, Kostka A, Yardley VA (2015) The nucleation of Mo-rich Laves phase particles adjacent to $M_{23}C_6$ micrograin boundary carbides in 12 % Cr tempered martensite ferritic steels. Acta Mater 90:94–104. doi:10.1016/j.actamat.2015.01.027
29. Wu R, Sandström R (1995) Creep cavity nucleation and growth in 12Cr–Mo–V steel. Mater Sci Technol 11:579–588. doi:10.1179/mst.1995.11.6.579
30. Tian ZL, Coussement C, Witte MD et al (1991) Creep behaviour of 12Cr–Mo–V steel weldments. Int J Press Vessels Pip 46:339–348. doi:10.1016/0308-0161(91)90077-F
31. Fournier B, Sauzay M et al (2005) Experimentally based modelling of cyclically induced softening in a martensitic steel at high temperature. In: Abstracts of ECCC creep conference, London, 12–14 Sept 2005
32. Béres L, Balogh A, Irmer W et al (2003) Behavior of welded joints of creep-resistant steels at service temperature. Weld Res 82:330S–336S
33. Mladenovic SM, Sijacki Zeravcic VM, Bakic GM et al (2014) Numerical analysis of thermal stresses in welded joint made of steels X20 and X22. Therm Sci 18:S121–S126. doi:10.2298/TSCI131211178M
34. Vasovic I, Maksimovic S, Maksimovic K et al (2014) Determination of stress intensity factors in low pressure turbine rotor discs. Math Probl Eng 2014. article ID 304638. doi:10.1155/2014/304638
35. Djukic M, Sijacki Zeravcic V, Bakic G et al (2006) Weld geometry defect influence on boiler tube structural integrity. In: IIW international congress “welding and joining technologies for a sustainable development and environment”, the 1st south-east European welding congress, proceedings of the 2006 IIW international congress, vol 3, Timisoara, 24–26 May. The International Institute of Welding (IIW), pp 169–179
36. Sijacki Zeravcic V, Bakic G et al (2004) International report. 12-03-12.04/2004 Study of remaining life of boiler tubing system, Unit 1, TPP “Nikola Tesla”, Faculty of Mechanical Engineering, Belgrade, p 283
37. Sijacki Zeravcic V, Bakic G et al (2002) RCM in power plant practice illustrated on observation of material aging and defining of component life exhaustion. In: Abstracts of the international conference POWER-GEN Middle East 2002, Abu Dhabi, UAE, 21–23 Oct 2002
38. Bakic G, Sijacki Zeravcic V, Djukic M et al (2007) Probability of failure of thermal power plant boiler tubing system due to corrosion. FME Trans 35:47–54
39. Burzic Z, Gaco DZ, Islamovic F et al (2013) The effect of a variable loading on integrity of a welded joint of high alloy-steel X20. Metalurgija 52:181–184

40. Mitrovic R, Momcilovic D, Eric O et al (2012) Study on impact properties of creep-resistant steel thermally simulated heat affected zone. Therm Sci 16:513–525. doi:10.2298/TSCI111006142M
41. Bakic G, Sijacki Zeravcic V, Radovic M et al (2005) Estimation of the failure time for low-carbon CrMoV steels in creep condition using modified kinetic theory based on microstructural parameters. In: Abstract of the 1st ECCC creep conference, London, 12–14 Sept 2005
42. DIN 17175:1979 standard (1979) Seamless tubes of heat-resistant steels—technical conditions of delivery
43. VGB-R501H Norm (2002) Production and construction supervision of high power steam boilers
44. VGB-TW 507:1992 standard (1992) Guideline for the assessment of microstructure and damage development of creep exposed materials for pipes and boiler components
45. Hrivnák I (1992) Theory of weldability of metals and alloys. Elsevier, Amsterdam

Modelling Crack Propagation and Arrest in Gas Pipes Using CTOA Criterion

M. Ben Amara, Guy Pluvinage, J. Capelle and Z. Azari

Abstract In this paper, the resistance to ductile crack extension is discussed in terms of Charpy or DWTT energy, R curve and CTOA. Methods used in numerical simulations of ductile crack extension are presented including the cohesive zone model, a critical damage with the Gurson–Tvergaard–Needleman model, critical damage given by SRDD model or a critical crack opening angle (CTOA). Selection of CTOA is based on the reduced number of parameters and the low sensitivity to pipe geometry. Numerical simulations of crack propagation and arrest based on CTOA, use the node release technique, which is described. Results on a pipe made in steel API L X65 are presented. The influence of geometrical and material parameters on crack arrest and velocity using this technique are presented. Finally, an arrest pressure equation similar to the BTCM's equation but including critical CTOA is introduced. For the same decompression wave pressure, the crack propagation velocity is inversely proportional to the resistance to crack extension of the material, which is the dominant parameter. The crack velocity versus decompression is expressed by a $CTOA_c$ function of resistance to crack extension.

Keywords Service life · Power plants · Micro-alloyed steel

1 Introduction

In several spectacular brittle fractures in 1950s and 1960s in gas pipelines, crack running for several kilometres until arrest occurred at a valve site or upon reaching a heavier wall pipe. These long crack propagations are explained by the fact that crack velocity in a pipe made in a brittle material is faster than the decompression wave velocity of the gas. Therefore the crack tip is always submitted to the service

M. Ben Amara (✉) · J. Capelle · Z. Azari
LaBPS – ENIM, 1 route d'Ars Laquenexy, CS 65820, 57078 Metz, France
e-mail: mohamed.ben.amara.enim@gmail.com

G. Pluvinage
FM.C, 57530 Silly Sur-Nied, France

G. Pluvinage and L. Milovic (eds.), *Fracture at all Scales*,
Lecture Notes in Mechanical Engineering, DOI 10.1007/978-3-319-32634-4_9

hoop stress. Research on prevention of such a kind of fracture in gas pipelines is, at this time, focused on the brittle-ductile transition behaviour of pipe steel. Eiber [8] found that the Charpy test tends to give an assessment about unsafe situations.

In the late 1960s, progress in steel pipe manufacturing led to pipelines also failing by ductile fracture. For these steels, the crack velocity is much slower than for brittle fracture. A significant plasticity near the crack tip, bulging and opening of the pipe reduces crack velocity. The ductile character can be easily seen of the fracture surface where the typical cups and cones fractographic aspect is easily recognisable. Therefore the gas decompression wave could interact with the crack tip. After fracture initiation, the pipe is fully open and there will always be some length of pipe ruptured before the decompression that causes the hoop stress to fall below the arrest level.

This occurs on a distance considerably less than for brittle fracture. One of the objectives of the pipe design is to reduce the crack arrest length in order to repair within a reasonable cost. To solve this problem, developing relationships are required between the decompression behaviour, arrest stress level, and fracture velocity.

The basic idea is to compare fracture resistance and driving force during crack extension. Immediately, when a trough crack appears at the surface of the wall of the pipeline, the gas tends to escape through the opening plug created. This leads to a sudden decompression and creation of two opposite decompression waves running at a speed of the order of 300 m/s along the main direction of the pipe. These waves play the major role on the dynamics of pipe fracture. If the decompression wave celerity is less than the crack propagation speed, the crack tip is constantly loaded at initial pressure, inducing stationary crack propagation. On the contrary, the crack is progressively less unloaded until arrest (Fig. 1).

Fig. 1 Burst test of a pipe made in X52 pipe steel

This approach is the basis of the Two-Curves Method (TCM), which involves the comparison of two curves: the gas decompression pressure versus its velocity and the fracture resistance versus crack velocity. Several two-curve models have been introduced successively: the Batelle Two Curves method BTCM [13], the High Strength Line Pipe (HLP) [17] and the HLP-Sumitomo [11] methods. In practice, the TCM approach consists of comparing the curves of the driving and resistance forces. The relative positions of the two curves determine the potential for sustained fracture propagation or its arrest. If the two curves intersect, the fracture velocity is equal to the decompression wave speed and crack propagation will continue indefinitely at a constant speed. Non-intersection means that the decompression wave overruns the fracture propagation for all pressure levels and crack arrest occurs. All TCM models are based on the assumption that the decompression wave speed is uncoupled from the fracture velocity.

Decompression pressure wave velocity is obtained by numerical models such as the Finite Difference Method (FDM) and the Method of Characteristics (MOC), or experimental methods as shock tubes. Generally one assumes a one-dimensional flux along the pipe axis and isentropic behaviour. In BTCM, HLP and HLP-Sumitomo, the decompression pressure wave velocity is modelled by adopting these assumptions and using the equation of state of Benedict–Webb–Rubin–Starling (BWRS) with adjustable constants to estimate the thermodynamic parameters during the isentropic decompression. The relative pressure at crack tip is given by:

$$\frac{p_d}{p_0} = \left(\frac{V_d}{6V_a} + 0.83\right)^7 \tag{1}$$

where p_0 is the initial pressure, p_d the decompression wave pressure, V_d the decompression wave celerity and V_a the gas acoustic celerity.

The major difference between the 3 TCM leads to the definition of the resistance to crack extension. In the initial BTCM model, the fracture resistance to crack extension R_f is given by the Charpy Energy C_V. The BTCM is limited to low pressure pipes made in steel with low yield stress. In order to overcome these limitations, HLP has proposed to use as fracture resistance to crack extension the drop weight test tearing energy (DWTT). Later HLP-Sumitomo proposed for high strength steel to correct DWTT energy by pipe diameter and thickness. In this paper, we propose to extend the two curves method concept by using crack tip opening angle (CTOA) as a measure of fracture resistance and using a simplified gas depressurisation model, where gas pressure is a function of time and distance from the crack tip. We first discuss the different approach to define the fracture resistance to crack extension and justify the choice of CTOA by the fact that this parameter is directly connected with crack extension and does not take into account fracture resistance to crack initiation.

We discuss also the different method to modelling numerically crack extension; R-curve, cohesive zone model (CZM), Gurson–Tvergaard–Needleman model (GTN), the strain rate dependent damage model (SRDD) and CTOA model. We

justify our choice of the CTOA model by the reducing the number of parameters, leading to less dependency on pipe geometry and reduced computing time. Examples of prediction of arrest pressure and length are given in the case of a pipe of 355 mm diameter and 19 mm wall thickness, made in pipe steel API5L X 65. The influence of geometrical and material parameters on crack arrest and crack velocity is finally discussed.

2 The Resistance to Crack Extension

As a crack grows, the driving force for further crack growth will change. A plot of the crack driving force expressed in terms of stress intensity factor (SIF), J integral (J) or crack-tip opening displacement (CTOD) against crack extension is known as an R-curve. R-curves may be used to analyse the potential for crack-growth initiation and extension. Generally, materials display either a flat R curve or a rising R curve. For a flat R curve, material resistance is constant with respect to crack extension. Nonlinear behaviour, like ductile fracture, can result in a rising R curve as the plastic zone at crack tip increases in size with extension.

Conditions of stable crack growth require that the rate of change of the crack driving force with increasing crack length Δa be smaller than the increase of crack growth resistance expressed in terms of crack opening displacement δ:

$$\frac{d\delta}{da} \leq \frac{d\delta_R}{da} \tag{2}$$

One example of a J-R curve obtained on a pipe steel SA333 Gr6 with a yield stress, σ_y = 288 MPa and ultimate tensile stress σ_u 420 MPa is given in Fig. 2 [3] Test specimens consist of straight pipes with a throughwall circumferential crack in the middle of its length.

In standard methods for determining crack extension in pipes such as the BTCM [13], HLP [17], and HLP-Sumitomo [11], fracture resistance to crack extension R_f is described as the specific fracture energy i.e. energy per fracture surface. R_f obtained either from the Charpy-V energy C_v ($R_f = C_v/A$) or either from DWTT energy U_{DWTT} ($R_f = U_{DWTT}/A$) from standard or embrittled specimens. A is the fracture surface.

The specific fracture energy obtained from Charpy specimens consists of two parts: energy for crack initiation and energy for crack extension. The ratio of energy for crack extension to total energy decreases when the yield stress of the material decreases. Examination of an instrumented Charpy test on X65 pipe steel indicates the difficulty of using Charpy energy as fracture resistance to ductile crack extension. For API 5LX65 at 20 °C, the ratio of energy for fracture initiation U_i to energy for fracture C_v is 21.3 %. A comparison with the X52 pipe steel is made in Table 1, and indicates that this ratio decreases when the yield stress increases.

In the HLP method [17], the pre-crack DWTT absorbed energy has been proposed as a better indicator to express resistance to fracture propagation, as a similar

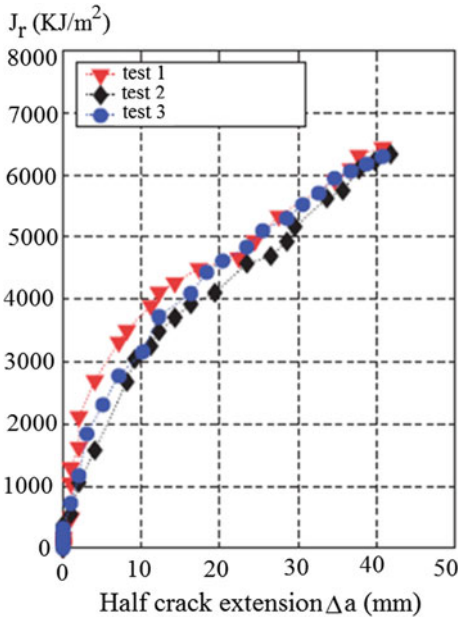

Fig. 2 J-R curve obtained on a pipe steel SA333 Gr6 [3]

Table 1 Ratio of energy for fracture initiation to total energy for fracture for X52 and X65 pipe steel in the Charpy test

	Yield stress	U_i/C_v (%)
X65	465	21.3
X52	436	26.54

fracture surface to the running ductile fracture. For API 5LX65 at 20 °C, the ratio of energy for fracture initiation to energy for fracture is 32.4 %. The value of this ratio is higher than that obtained from the Charpy test and does not follow the argument in favour of DWTT energy used as fracture resistance for a running crack.

To overcome the difficulty in using a fracture resistance parameter including the energy for fracture initiation, Demofonti et al. [6] proposed a method of subtracting energy for fracture initiation U_i by finding the difference between the fracture energies of two similar DWTT specimens, but with different initial notch depths of a_1 = 10 mm and a_2 = 38 mm respectively.

Here the concept of Crack Tip Opening Angle (CTOA) [1] is used to simulate stable crack growth by the finite element method. The CTOA Ψ is defined as the angle between the crack faces of a growing crack. Crack-growth dependence of this angle was expected, and a constant value was used for all of the stages of growth. The value at the first increment of crack growth is called ψ_0 (Fig. 3) and ψ_c is called critical crack tip opening angle ($CTOA_c$) with $\psi_c < \psi_0$.

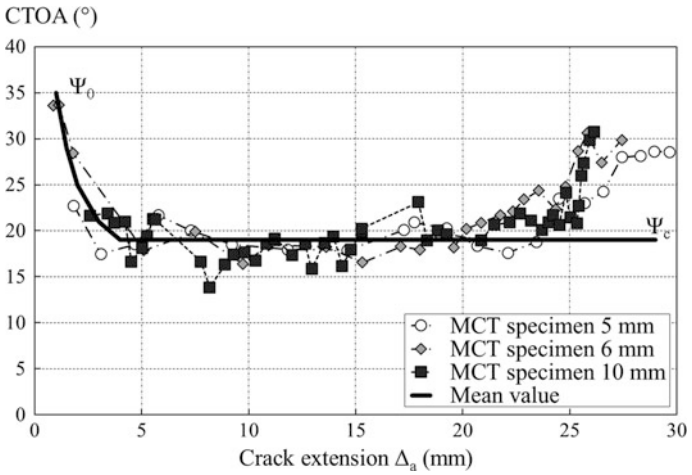

Fig. 3 Evolution of CTOA during crack extension

Since the 1990s, the use of this criterion has been extended to numerical simulations by the finite element method (FEM) of the crack extension.

Nowadays, $CTOA_c$ is used to predict crack length and pressure at arrest of a ductile running crack and particularly in gas pipes [2]. A correlation between Charpy-V energy K_{CV} and CTOA has been proposed in Cen [4], where CTOA is in degrees and K_{CV} in Joules.

$$\Psi_c = 0.05K_{CV} \tag{3}$$

Fracture resistance to crack extension R_f refers strictly to crack propagation. Therefore the use of the fracture test including energy for fracture initiation is doubtful. This is the case for R_f defined from Charpy or DWTT energies; however, they are popular and are used in standards for pipe design. A parameter defined from the R curve like CTOA is therefore preferable.

3 Numerical Simulation of Crack Extension in Pipes

Modelling ductile crack propagation by numerical methods generally uses the node release technique. This technique allows a crack extension over a length equal to the mesh size. Crack extension occurs when energetic, damage or geometric conditions occurs at crack tip. The criteria generally used for that are: a dissipative energy with the cohesive zone model (CZM) [16], a critical damage with the Gurson–Tvergaard–Needleman model (GTN) [16] critical damage given by SRDD model [15] or a critical crack opening angle ($CTOA_c$) [2]. Results are generally sensitive to mesh size.

3.1 Cohesive Zone Model

Using the CZM model, fracture extension is regarded as a gradual phenomenon in which the separation of the crack takes place across an extended crack tip or cohesive zone. The fracture resistance is simulated by cohesive tractions. As the surfaces separate, the opening stress first increases until a maximum σ_{max} is reached and then subsequently decreases to zero, which results in complete separation. The variation in traction in relation to displacement is plotted on a curve called the traction-displacement curve. The area under this curve is equal to the energy needed for separation Γ_c.

The specific work of fracture w_f, according to Cotterell et al. [5], can then be deduced.

$$w_f = \frac{d\Gamma_c}{Bda} = \int_0^{\Delta} \left(\sigma_{max} \frac{d\delta}{da} \right) dx \tag{4}$$

where B is the plate thickness, σ_{max} the cohesive stress, δ is the crack opening displacement. The cohesive distance Δ is chosen as a characteristic distance independent of the mesh element size and can be obtained by a calibration procedure.

For an API 5L X 65 steel pipe, Scheider et al. [16] proposed the values of σ_{max} and Γ_c given in Table 2.

Simulations of ductile cracking with the CZM are generally performed using a coarser mesh, and this reduces the number of elements. The model is sensitive to the shape of the traction-displacement curve. This is a strong limitation of the validity of the method.

3.2 Gurson–Tvergaard–Needleman Model

The Gurson–Tvergaard–Needleman (GTN) model consists of 4 elements: the GTN yield locus, the plastic flow rule, the hardening equation and the damage evolution law. The GTN damage model considers that the yield locus Φ is affected by porosities that are created during the ductile fracture process. It is a function of hydrostatic pressure σ_h and the effective porosity f*.

$$\Phi = \left(\frac{\sigma_{eq}}{R_c} \right) + 2q_1 f^* * cosh\left[-q_2 . \left(\frac{3\sigma_h}{2R_c} \right) \right] - \left(1 + q_3 f^{*2} \right) \tag{5}$$

Table 2 Values of the parameters σ_{max} and Γ_0 of the cohesive zone model for API 5L X 65

CZM parameters	σ_{max} (MPa)	Γ_c (N/mm)
API 5L X 65	1375	900

q_1, q_2 and q_3 are the parameters of the GTN model. The plastic flow rule obeys the normality principle:

$$\epsilon_p = \eta \frac{\partial \Phi}{\partial \sigma}$$

$$\eta \begin{cases} = 0 & if\, \Phi < 0 \\ > 0 & if\, \Phi = 0 \end{cases} \tag{6}$$

where ε_p is the plastic strain and η the plastic multiplier. The equation for the hardening parameter $\bar{\sigma}$ is given by:

$$\bar{\sigma} = \sigma(\varepsilon) \tag{7}$$

Initially a volume fraction of inclusion f_0 in the material is considered. These inclusions are considered as voids. During the ductile fracture process, the size of voids increases and coalescence appears for the strain ε_N with a volume fraction f_N. These larger pores increase more rapidly and crack initiation occurs for the volume fraction f_i. Final fracture occurs for the volume fraction f_c (Fig. 4):

$$\begin{aligned} f^* &= f \, for f \leq f_i \\ f^* &= f_i + \frac{\bar{f}_c - f_i}{f_c - f_i} . (f - f_i) \end{aligned} \tag{8}$$

After coalescence, the volume fraction is submitted to a linear acceleration governed by the parameter $\bar{f}_c$.

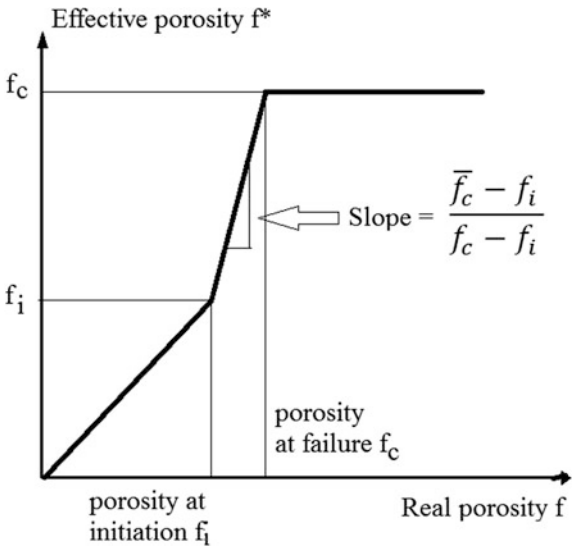

Fig. 4 Evolution of effective porosity* with the volume fraction f

Table 3 Values of GTN constants for API 5L X65 pipe steel [16]

q_1	q_2	q_3	ε_N	f_0	f_N	f_i	f_c	l_y
1.5	1.0	4.0	0.3	1.5.10–4	5.10–4	0.02	0.04	0.25

$$\bar{f}_c = \left(q_3 + \sqrt{q_1^2 - q_3}\right)/q_3 \tag{9}$$

The evolution equation of the effective porosity or damage in the absence of void nucleation is given by:

$$\begin{aligned} \dot{f} &= 3(1-f)\varepsilon_{p,h} \\ \varepsilon_{p,h} &\equiv \frac{1}{3} tr\varepsilon_p \end{aligned} \tag{10}$$

The GTN model needs eight constants. Values of these constants for API 5L X65 pipe steel are given in Table 3 and extracted from Scheider et al. [16].

The great number of parameters and the difficulty of identifying them are the major handicaps of this method, which requires tensile tests and observation with a scanning electron microscope. In [10], simulation of crack extension using the GTN model is relatively simple, requiring no advanced meshing techniques. The element layer with a width equal to the parameter l_y was defined along the crack propagation path. The initiation and dynamic crack propagation are triggered once the critical crack length l_y is reached. The crack propagation distance is limited to five times the outer diameter. The disadvantage of using local damage models for large-scale simulations is important. Due to this fine mesh resolution, the number of elements in the pipe model exceeds 10^6, resulting in the enormous CPU time.

3.3 Strain Rate Dependent Damage Model (SRDD)

The strain rate dependent damage model (SRDD) is a damage model used for prediction of crack propagation and arrest in gas transmission pipelines [15]. The tuned SRDD model was successfully applied by Oikonomidis et al. [15] to simulate an axial crack propagation and arrest in X100 natural gas pipelines (Fig. 5).

The model consists of three parts: the first part is the elasto-plastic response of an undamaged material, the second part is the damage initiation criterion and the third is the energy for crack extension per unit surface area R_f. In the SRDD model, damage initiates when the following condition is fulfilled:

$$\int \frac{d\varepsilon_{eq}}{\varepsilon_{eq,i}\left(\beta, \dot{\varepsilon_{eq}}\right)} = 1 \tag{11}$$

where ε_{eq} is the equivalent plastic strain, $\dot{\varepsilon_{eq}}$ the equivalent plastic strain rate, $\varepsilon_{eq,i}$ the equivalent plastic strain at damage initiation and β the stress triaxiality.

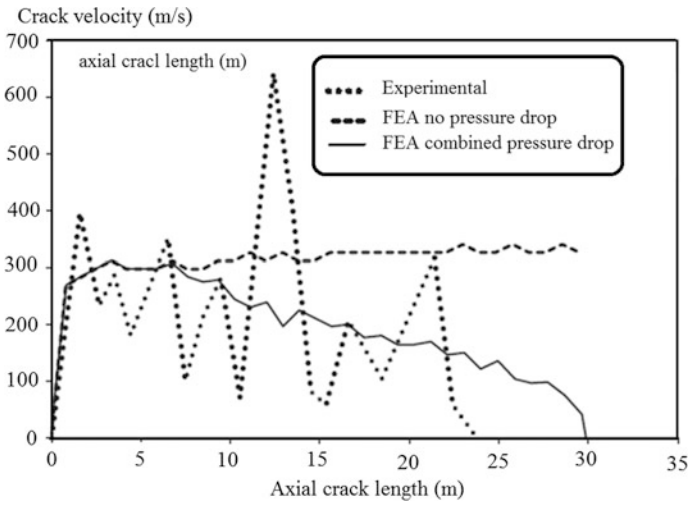

Fig. 5 Simulation of crack velocity with crack length with and without combined pressure drop using the SRDD model [15]

The resistance to crack extension is given by:

$$R_f = \int_{u_{eq,i}}^{u_{eq,c}} \sigma du_{eq} \tag{12}$$

where u_{eq} is the equivalent plastic strain at fracture, $u_{eq,i}$ is the equivalent plastic displacement at damage initiation and $u_{eq,c}$ is equivalent plastic displacement at fracture. R_f is considered to be a material property.

To avoid mesh dependence, a characteristic length parameter is introduced and stress-displacement relationship is used instead of the stress-strain. The element is considered failed when its plastic work exceeds the R_f multiplied by the element area.

4 CTOA Model

Crack extension is modelled by the finite element method using the CTOA criterion coupled with the node release technique. The node release technique algorithm has been presented in an earlier study [8]. It is based on the assumption that cracks grow step-by-step and each step has the length of one mesh element. Triggering of crack extension at each step is given by a CTOA-based criterion.

Boundary conditions were imposed on the pipe, in order to make the simulation as real as possible. They consisted of imposing symmetry along the crack plane and constraining the closed part of the crack with fixed nodes in the circumferential

Table 4 Different methods of modelling crack extension

	CZM	Gurson	SRDD	CTOAc
Number of parameters	2	8	3	1
Advantages	Simple model; ability to model branching crack	Linked to the micro-mechanisms; Constraint effect taken into account	Directly linked to resistance to crack extension	Directly linked to crack extension
Disadvantages	Needs predefined crack path	Non-standard calibration; Mesh-dependence; Long computational time	Resistance to crack extension sensitive to gauge length	Large scatter of CTOA values

direction. These fixed nodes were then removed by the nodal release user subroutine to provoke crack extension.

Acting tractions on uncoupling nodes at the crack faces are reduced as the crack opens. This event occurs when CTOA reaches its critical value and then the representative node of the crack tip is released and the new position of the crack is deduced. This algorithm requires several time increments and a fine mesh (i.e. element size under 1.5 mm) around the crack tip for accurate evaluation of the CTOA. In this approach, the evolution of the crack strictly depends on the mesh element size around the crack tip, since it governs the amount of the crack advance. Moreover, the advancing process is not really continuous since a proper iteration scheme is necessary to evaluate the dynamic crack growth accurately during the integration time.

Table 4 gives a summary of different methods of modelling crack extension showing the number of parameters, advantages, and disadvantages. CTOA is an eligible one-parameter fracture resistance for ductile crack extension.

5 Numerical Simulation of Crack Propagation and Arrest Based on CTOA

Conditions for crack propagation or arrest are given by a coupled fluid-structure problem. Crack propagation speed is controlled by pressure distribution on the opening pipe. If the decompression wave is faster than the propagating crack fracture, the pressure at crack tip will decrease, and the crack will arrest.

In terms of a limit state design, the arrest pressure can be predicted by solving the Eq. (13) between the fracture resistance and component stress, which depend on the pipeline dimensions, internal pressure and material strength. This material resistance is balanced with a component stressing that is determined involving specific pipe dimensions, decompression pressure p_d and material strength. The arrest pressure can be predicted by solving the equation between the stress state at crack tip:

$$\langle \sigma_{ij}(p_d) \rangle = \langle \sigma_{ij,c}(p_{ar}) \rangle \tag{13}$$

In principle, to solve the gas depressurisation problem, one has to solve a coupled gas-solid thermomechanical problem. There are specialised codes developed for this purpose, e.g. GASDECOM [9].

Generally simplified gas depressurisation models have been proposed in literature, which only predict gas pressure as a function of time and distance from the crack tip. These models are based on the isentropic expansion of ideal gas, where a pipe is considered a large pressure vessel with constant volume. These assumptions are justified by the fact that crack propagation cannot outrun the decompression wave. This means that the crack tip is always present in pipe section affected by the decompression process. Gas pressure ahead of the crack depends only on time. This simplification is justified by the fact that the crack propagation speed is at most 200–300 m/s, which is lower than the wave speed in the pressurized gas, estimated at about 400 m/s. This means that the crack cannot outrun the pressure drop wave, and the crack tip will always be in a segment of the pipe with falling pressure. The drop pressure ahead of the running crack tip is given as:

$$p_d(t) = p_0.\exp(kt) \tag{14}$$

k is a constant expressed as:

$$k = -\frac{A}{V_0}\sqrt{\frac{RT}{W_g}} \tag{15}$$

where A is the cross-sectional area of the pipe, V_0 is the initial volume, R is the universal gas constant, T is the average temperature of the gas and W_g is the molecular weight of the gas, k = −7.5 [9]. Instantaneous internal pipe pressure was imposed along a certain distance behind the crack-tip node (Fig. 6). This distance was given by the cohesive zone model of Dugdale–Barenblatt [14]. The distance is $2b = 3\sqrt{R.t}$, where R and t are outer radius and wall thickness, respectively.

Pressure drop behind the crack tip is expressed only as a function of distance. For distances exceeding 1.75 pipe diameters behind the crack tip, the pressure is considered zero. It is also possible to assume a linear pressure drop behind the running crack tip [15]:

$$p_b(z) = p_0\left(1 - \frac{z}{1.75D}\right) \tag{16}$$

where $p_b(z,t)$ is the gas pressure behind the crack tip, which is a function of the distance z, and of time t and p_0 is the initial gas pressure prior to the appearance of the through thickness crack.

The use of CTOA to model the ductile crack propagation of thin structures has been validated by several authors [6, 7]. To simulate crack propagation, the CTOA

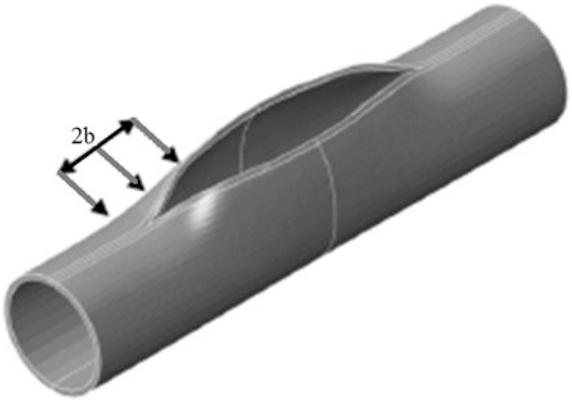

Fig. 6 Zone length where gas pressure is imposed on coupled nodes

fracture criterion is introduced in a numerical model using the node release technique. Condition of node release is given by the following equation:

$$\mathrm{CTOA}\ (p_{ar}) = \mathrm{CTOA_c} \tag{17}$$

where CTOA is the crack tip opening angle induced by the current pressure, p_{ar} the arrest pressure and $\mathrm{CTOA_c}$ the fracture resistance.

The node release technique is based on the assumption that the crack growth is described by uncoupling nodes at the crack faces, whose acting tractions are reduced as far as the crack opens. When the CTOA reaches its critical value ($\Psi = \Psi_c$), the representative node of the crack tip is released and a new position of the crack is deduced. Each propagation step corresponds to the size of a mesh element (see Fig. 7). In this method, crack evolution depends on the size of mesh elements around the crack tip, since it governs the amount of the crack advance. Moreover, the advancing process is not really continuous, since a proper iteration

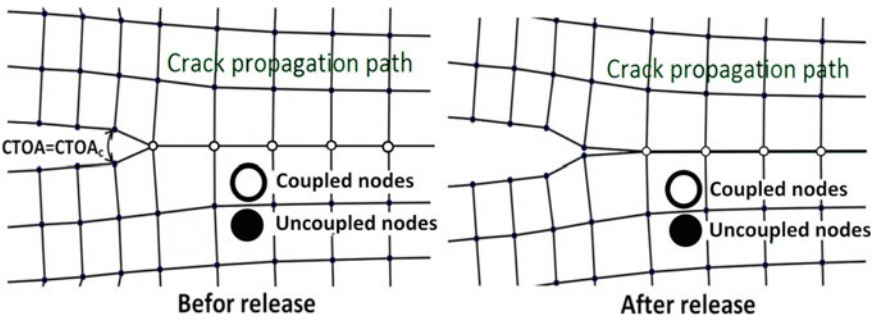

Fig. 7 Crack propagation according to the node release technique and the CTOA criterion, mode I and 2D

scheme is necessary to evaluate the dynamic crack growth during the integration time accurately.

The method requires an a priori knowledge of the crack propagation path. The simulation is performed on a pipe with an outer diameter of 355 mm, wall thickness of 19 mm, and length of 6 m. The studied pipe is made of API 5L X65 steel with a critical CTOA value of 20°.

The computing phase begins by generating a 3D finite element implicit dynamic analysis. Because of the symmetry of the crack planes, only a quarter of the pipeline was analysed. A combined 3D-shell mesh was used to reduce the computing time. A total of 50,976 eight-node hexahedral elements were generated along the crack path and combined with 6000 shell elements.

Crack arrest in gas pipelines was performed with the release user subroutine, in conjunction with the FEM ABAQUS code. The computing phase begins by generating a 3D finite element implicit dynamic analysis. Because of the symmetry of the crack planes, only a quarter of the pipeline was analysed.

Crack extension from an initial crack-like defect is computed using the described model. Running crack propagation along the tube consists of two stages: a boost phase, where the crack reaches its full velocity in a few milliseconds, followed by a steady stage at constant speed. The absence of a deceleration phase is explained by the absence of a pressure drop.

The crack velocity increases with the initial pressure. Ten simulations were performed at different levels of pressure in the range of 28–60 MPa (Fig. 8).

The results indicate that the stationary crack velocity V_c [m/s] increases with initial pressure p_0 [MPa] according to:

$$V_c = 284.2 * \left(\frac{p_d}{25.8} - 1\right)^{0.193} \tag{18}$$

p_0 has been replaced by decompression pressure because if $V_c > V_d$ $p_0 = p_d$.

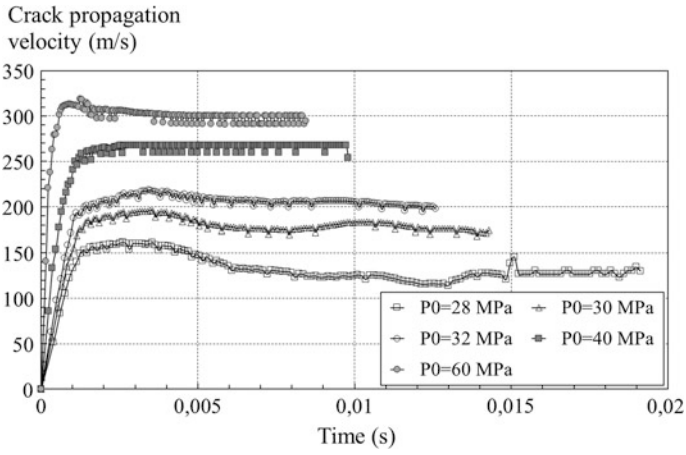

Fig. 8 Crack velocity pipe versus time for different initial pressure in API 5L X65, diameter 355 mm and thickness 19 mm

Qualitatively, this equation is consistent with the experimental results reported by Battelle, HLP, and many other authors [11, 13, 17]. Crack extension at arrest is obtained from the graph of crack velocity versus half the crack extension, to take into account the symmetry of the problem. For the aforementioned conditions of geometry, material, and initial pressure, the numerical simulation gives a crack extension of 42 m, which is of the same order of magnitude as those obtained experimentally.

6 Influence of Geometrical and Material Parameters on Crack Arrest and Velocity

Prediction of crack arrest and crack velocity after fracture initiation in a pipe submitted to internal pressure is modelled here using critical CTOA as a parameter representative of the fracture resistance to crack extension R_f. This parameter is sensitive to geometry in general and to diameter and thickness for pipe particularly. It is also sensitive to material through its flow stress σ_0.

The influence of these different parameters on CTOA has been described by Demofonti et al. [7] and is given by the general form:

$$CTOA = C\left(\frac{\sigma_h}{E}\right)^m \left(\frac{\sigma_h}{\sigma_0}\right)^n \left(\frac{D}{t}\right)^q \tag{19}$$

where m, n, and q are dimensionless constants and C is expressed in degrees; σ_h is the hoop stress (MPa), σ_0 is the flow stress (MPa), D is the diameter (mm), and t is thickness (mm). The following values can be used for methane: C = 106, m = 0.753, n = 0 and q = 0.65. Influence of the quantities $\sqrt{Dt}$ on initial pressure p_0 is introduced by through the Folias factor [13]:

$$p_0 = \sigma_h \frac{2t}{D} = \frac{\sigma_0}{M_F} \cdot \frac{2t}{D} \tag{20}$$

where M_F is the Folias correction factor:

$$M_F = \left[1 + 1.255 \cdot \left(\frac{a}{\sqrt{Dt/2}}\right)^2 - 0.0135 \cdot \left(\frac{a}{\sqrt{Dt/2}}\right)^4\right]^{1/2} \tag{21}$$

6.1 Influence of Thickness

Arrest pressure and crack velocity have been computed using the aforementioned node release technique with four different pipe wall thicknesses [5, 10, 15, 19.05 mm]. In each case, the pipe has a diameter of 355 mm and is made of steel API 5L X65 with a yield stress equal to 465 MPa. Results are reported in Figs. 9 and 10.

Figure 10 shows a linear evolution between arrest pressure and wall thickness. On Fig. 11, the ratio of decompression wave and arrest pressure is plotted versus the crack velocity for the four studied wall thicknesses. The velocity obeys the general law:

$$V_c = H.\left(\frac{p_d}{p_a} - 1\right)^{\beta} \tag{22}$$

where H is a material constant that depends on initial pressure, flow stress and resistance to crack extension of the material, β another constant. There is no influence of wall thickness for values above 10 mm. Higher velocities for low values of the wall thickness may be the result of a mesh problem without certainty. However a wall thickness of 5 mm for a pipe of 355 mm of diameter is not realistic and generally wall thickness for a gas pipe is over 8 mm.

Five simulations to study the influence of the diameter on crack velocity and arrest pressure have been performed. The pipe thickness has been chosen as 19.05 mm and pipe diameter as 0.304, 0.355, 0.393, 0.61 and 0.91 m. The evolutions of arrest pressure and crack velocity pressure have been plotted versus the pipe diameter (Figs. 11, 12). We notice that the arrest pressure is a decreasing function of the diameter of the pipeline. We also highlight a minor effect of the pipe diameter on crack velocity.

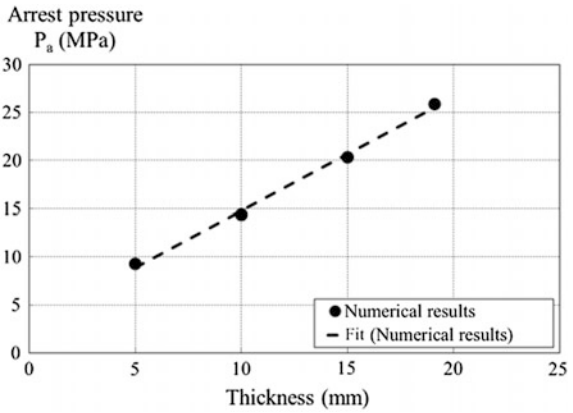

Fig. 9 Influence of pipe wall thickness on arrest pressure, pipe diameter 355 mm, steel API 5L X65, yield stress 465 MPa

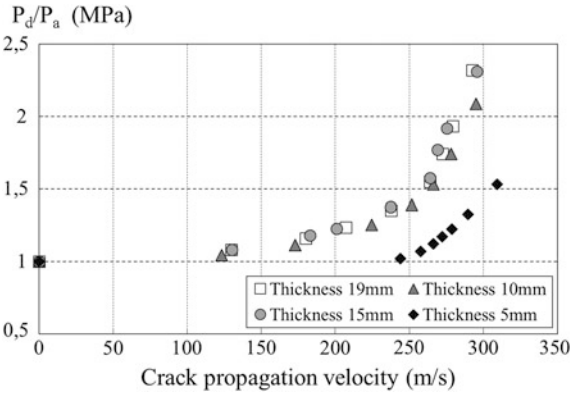

Fig. 10 Influence of pipe wall thickness on crack velocity, pipe diameter 355 mm, steel API 5L X65, yield stress 465 MPa

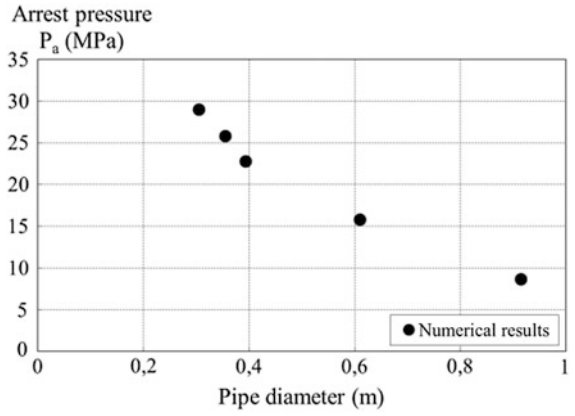

Fig. 11 Influence of pipe diameter on arrest pressure, pipe thickness 19 mm, steel API 5L X65, yield stress 465 MPa

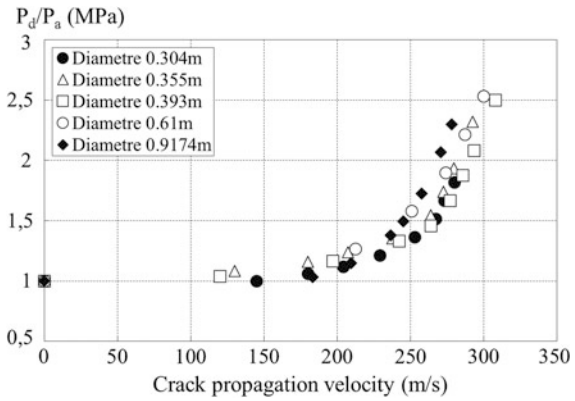

Fig. 12 Influence of pipe diameter on crack velocity, pipe thickness 19 mm, steel API 5L X65, yield stress 465 MPa

6.2 Influence of Yield Stress

We performed several simulations of pipe bursting and modified the yield stress in the interval 320–735 MPa keeping the other parameters identical, i.e., the geometry of the pipe, the strain hardening and the mesh size. A linear function between the arrest pressure and the yield stress is observed (Fig. 13). In Fig. 14, we notice an increase of the crack velocity with increasing yield strength. These results are consistent with the fact that the increases of the yield stress result in a decrease in toughness and therefore the resistance to crack extension.

6.3 Influence of CTOA

Influence of the resistance to crack extension has been studied, over 40 simulations keeping all the parameters of the numerical model identical. Only the value of $CTOA_c$ was modified in the range 5°–20°. Simulations of static and dynamic type

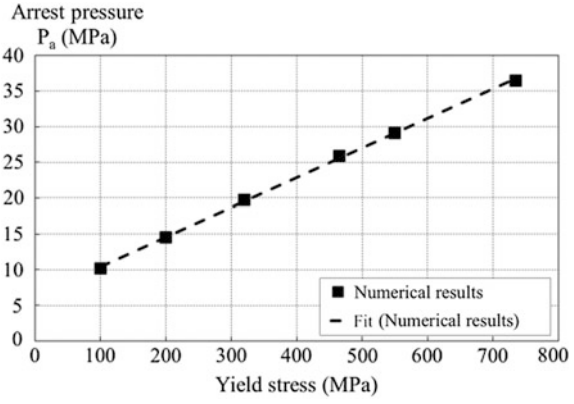

Fig. 13 Influence of yield stress on arrest pressure, pipe thickness 19 mm pipe diameter 355 mm, steel API 5L X6.5

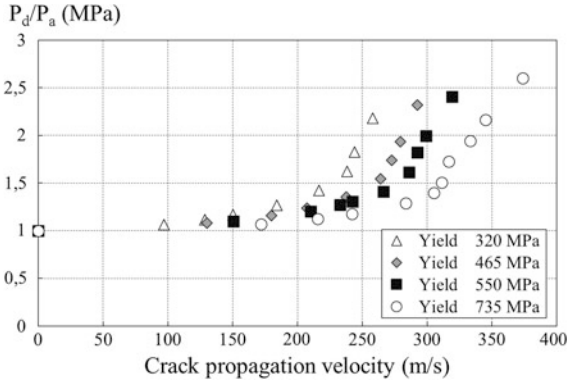

Fig. 14 Influence of yield stress on crack velocity, pipe thickness 19 mm pipe diameter 355 mm, steel API 5L X65

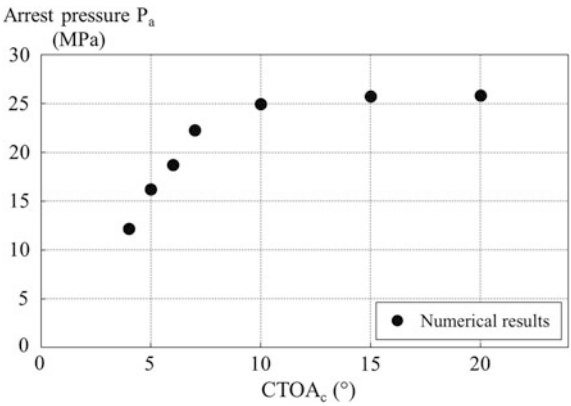

Fig. 15 Influence of CTOA on arrest pressure pipe thickness 19 mm pipe diameter 355 mm, steel API 5L X65

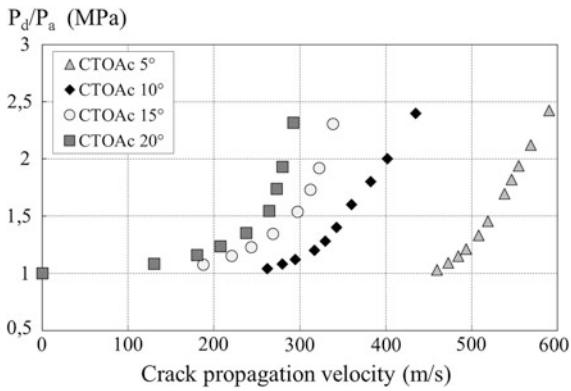

Fig. 16 Influence of CTOA on crack velocity pipe thickness 19 mm pipe diameter 355 mm, steel API 5L X65

provide the evolution of the arrest pressure and crack velocity versus the resistance to crack extension, expressed in terms of $CTOA_c$ (Figs. 15, 16).

The arrest pressure increases relatively linearly versus resistance to crack extension until a value of $CTOA_c$ equal to 10°. After asymptotically, the arrest pressure stabilises to a value of arrest pressure that depends on initial pressure, geometry of the pipe and material flow stress.

For the same decompression wave pressure, the crack propagation velocity is inversely proportional to the resistance to crack extension of the material, which is the dominant parameter.

7 Two Curves Method Based on CROA

During the crack-propagation process, the gas escapes through the opening created in the wall of the pipe by the crack. Indeed, a decompression wave begins to propagate through the pipe at a speed of the order of 300–400 m/s. A number of

models have been developed for predicting the gas decompression wave speed. Many of these assume a one-dimensional (along the pipe axis) and isentropic flow and use the Finite Difference Method (FDM) or the Method of Characteristics (MOC).

BTCM is a model that assumes a one-dimensional, frictionless, isentropic, and homogeneous fluid and uses the Benedict–Webb–Rubin–Starling equation of state with modified constants to estimate the thermodynamic parameters during the isentropic decompression.

According to this one-dimensional flow model analysis and experimental results obtained from shock tube tests, the decompression pressure at the crack tip p_d is given by Eq. 1.

It was proven by Battelle [13] that the ratio between the gas decompression wave and crack-propagation speed has a major role in the dynamics of crack growth. Indeed, if the crack propagates faster than the decompression wave, the crack tip is always loaded by the initial pressure p_0. Otherwise, the crack tip is progressively less and less loaded, up to crack arrest.

7.1 Crack Velocity Versus Decompression Pressure

The crack velocity versus decompression is expressed by the general following equation, which can be found in different TCMs as BTCM [13] HLP [17] and HLP-Sumitomo [11] methods:

$$V_c = \alpha . \frac{\sigma_0}{\sqrt{R_f}} . \left(\frac{p_d}{p_a} - 1 \right)^{\beta} \tag{23}$$

where α, β parameters are pipe geometry dependants. σ_o is the flow stress and R_f is the resistance to crack extension expressed in terms of CTOA.

Crack velocity and arrest pressure were computed for a pipe made in steel API 5L X65 with a diameter of 355 mm and a thickness of 19 mm. Initial pressure, p_o varies from 28–60 MPa. Results are reported in a graph of $p_d/p_a = f\left(V_c\sqrt{CTOA}_c/\sigma_0\right)$ similar to the original HLP formula and in a graph $p_d/p_a = f\left(V_c\sqrt{CTOA}_c/\sqrt{\sigma_0}\right)$: see Fig. 17. It appears that the second approach leads to a better correlation coefficient and data are fitted by Eq. (25).

$$V_c = 6.78 \frac{\sqrt{\sigma_0}}{\sqrt{CTOA_c}} \left(\frac{p_d}{p_a} - 1 \right)^{0.162} \tag{24}$$

The square root of the flow stress instead the flow stress itself operates in this equation.

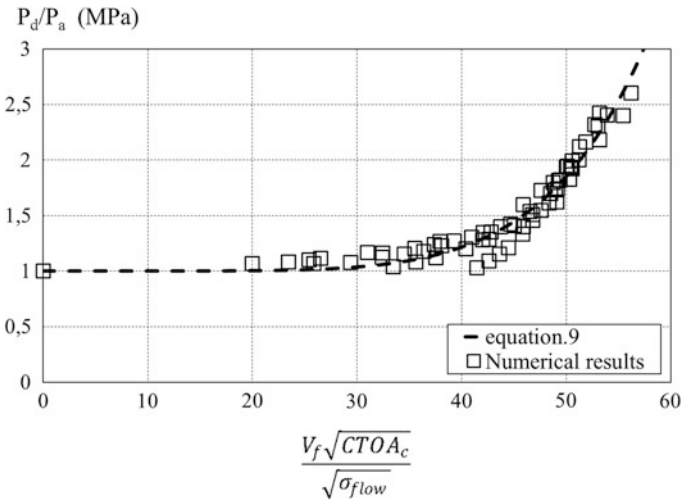

Fig. 17 Evolution of the ratio p_d/p_a versus the parameter $\left(V_c\sqrt{CTOA}_c/\sqrt{\sigma_0}\right)$

7.2 Arrest Pressure Equation

The arrest pressure is expressed by the following general equation, according to the BTCM [13], HLP [17] and HLP-Sumitomo [11] methods.

$$p_a = A.\frac{t}{D}.\sigma_0.cos^{-1}exp\left(\frac{-.\pi E.R_f}{24\sigma_0^2\sqrt{Dt/2}}\right) \tag{25}$$

A is a parameter that depends of the ratio diameter-thickness D/t. The arrest pressure is a linear function of the flow stress, which is confirmed by the numerical results. In the BTCM, the flow stress is defined as:

$$\sigma_0 = \sigma_y + 69MPa \tag{26}$$

Pipe made in API 5L X65 steel, pipe diameter 355 mm, thickness 19 mm.
To take into account the strain hardening, the following definition is used:

$$\sigma_0 = \left(\sigma_y + \sigma_u\right)/2 \tag{27}$$

The arrest stress is defined as:

$$\sigma_a = \frac{p_a D}{2t} \tag{28}$$

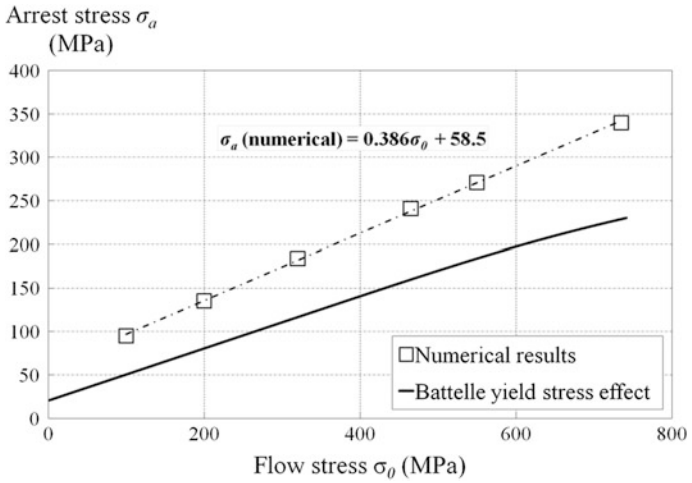

Fig. 18 Numerical simulation of arrest pressure versus flow stress using CTOA as resistance to crack extension

In Fig. 18, the arrest stress has been plotted versus yield stress. Numerical simulations confirm the linear dependence of the arrest stress with the flow stress.

Several burst tests carried out at Batelle have been reported by Kiefner et al. [12]. They concern ductile fracture initiation, propagation and arrest in cylindrical vessels that range from 168–1219 mm and made in steel with yield stress in the range 151–765 MPa. For these tests, the ratio of arrest stress and flow stress is plotted versus the parameter $\frac{.\pi E.CTOA_c}{24\sigma_0^2\sqrt{Dt/2}}$.

The arrest pressure curve separates the arrest zone with data as a triangle to crack extension zone with data as square. The flow stress according to Eq. (28) is equal to 511 MPa and the ratio D/t = 18.7. The best fit confirms the ($\cos^{-1}$exp) dependence of the arrest pressure with the parameter $\frac{\pi E.CTOA_c}{24\sigma_0^2\sqrt{Dt/2}}$ with the following equation, similar to the BTCM's equation (Fig. 19) with Ω and μ as another constants (Ω = 1.39, μ = 115 * 10^3)

$$p_a = \Omega.\frac{t}{D}.\sigma_0.cos^{-1}exp\left(\frac{-\mu.\pi E.CTOA_c}{24\sigma_0^2\sqrt{Dt/2}}\right) \tag{29}$$

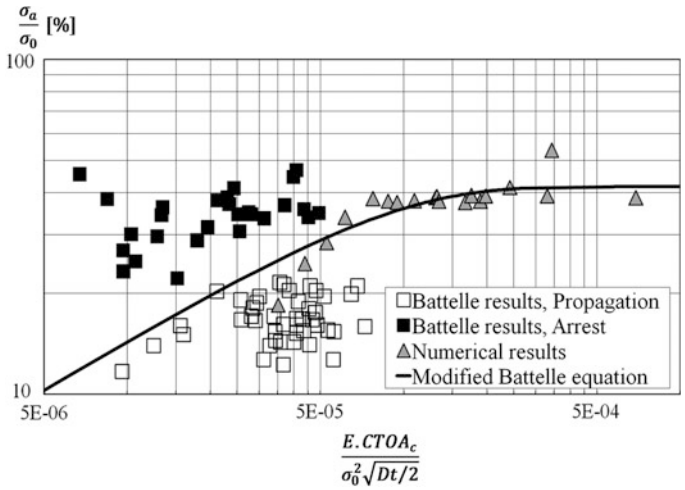

Fig. 19 Dependence of the arrest pressure with the parameter $\frac{E.CTOA_c}{\sigma_0^2\sqrt{Dt/2}}$

8 Conclusion

Fracture resistance to crack extension R_f refers strictly to crack propagation. Therefore the use of fracture tests including energy for fracture initiation (Charpy or DWTT tests) is doubtful. A parameter defined from the R curve like CTOA is therefore preferable. Numerical simulation of crack extension in pipes can be made using the cohesive zone model, a critical damage with the Gurson–Tvergaard–Needleman model, critical damage given by SRDD model or a critical crack opening angle. The use of CTOA to model the ductile crack propagation of thin structures is justified by the fact that it is a one-parameter criterion and results are not very sensitive to pipe geometry. To simulate crack propagation, the CTOA fracture criterion is introduced in a numerical model using the node release technique. Results of numerical modelling indicate that there is no influence of wall thickness for values above 10 mm and a minor effect of the pipe diameter on crack velocity. Crack velocity increases with increasing yield strength, and the arrest pressure stabilises to a value that depends on initial pressure, geometry of the pipe, and material flow stress.

For the same decompression wave pressure, the crack propagation velocity is inversely proportional to the resistance to crack extension of the material, which is the dominant parameter. The crack velocity versus decompression is expressed by a $CTOA_c$ function versus the parameter $\frac{\pi E.CTOA_c}{24\sigma_0^2\sqrt{Dt/2}}$.

References

1. Andersson H (1973) A finite element representation of stable crack growth. J Mech Phys Solids 21:337–356
2. Ben Amara M, Capelle J, Azari Z, Pluvinage G (2015) Prediction of arrest pressure in pipe based on CTOA. J Pipe Eng 14(4)
3. Chapuliotb S, Marieb S, Kayserb I (2006) Derivation of J-resistance curve for through wall cracked pipes from crack mouth opening displacement. Int J Press Vessels Pip 83:686–699
4. Cen C (2013) Characterization and calculation of fracture toughness for high grade pipes. PhD thesis, University of Alberta
5. Cotterell B, Reddel JK (1977) The essential work of plane stress fracture". Int J Fract 13:267–277
6. Demofonti G, Buzzichelli G, Venzi S, Kanninen M (1995) Step by step procedure for the two specimen CTOA test. In: Denys R (ed) Pipeline technology, vol II. Elsevier, Amsterdam
7. Demofonti G, Mannucci G, Hillenbrand HG, Harris D (2004) Evaluation of X100 steel pipes for high pressure gas transportation pipelines by full scale tests. In: International pipeline conference, Calgary, Canada
8. Eiber RJ (1969) "Fracture propagation". Paper I. In: Proceedings of the 4th symposium on line pipe research. AGA catalogue no. L30075
9. Eiber R, Bubenik T, Maxey W (1993) GASDECOM, computer code for the calculation of gas decompression speed that is included in fracture control technology for natural gas pipelines. NG-18 Report 208, American Gas Association Catalog
10. Gullerud AS, Dodds RH, Hampton RW, Dawicke DS (1999) Three-dimensional modeling of ductile crack growth in thin sheet metals: computational aspects and validation. Eng Fract Mech 63(4):347–374
11. Higuchi R, Makino H, Takeuchi I (2009) New concept and test method on running ductile fracturearrest for high pressure gas pipeline. In: 24th world gas conference, WGC 2009, vol 4. International Gas Union, Buenos Aires, Argentina pp 2730–2737
12. Kiefner JF, Eiber RJ, Duffy AR (1972) Ductile fracture initiation, propagation and arrest in cylindrical vessels. ASTM STP 514:70–81
13. Maxey WA (1974) 5th symposium on line pipe research, PRCI Catalog No. L30174, Paper J, p 16
14. Maxey WA (1981) Dynamic crack propagation in line pipe. In: Sih GC, Mirabile M (eds) Analytical and experimental, fracture mechanics, Sijthoff and Noordhoff, pp 109–123
15. Oikonomidis F, Shterenlikht A, Truman CE (2013) Prediction of crack propagation and arrest in X100 natural gas transmission pipelines with the strain rate dependent damage model. Part 1: a novel specimen for the measurement of high strain rate fracture properties and validation of the SRDD model parameters. Int J Press Vessels Pip 105:60–68
16. Scheider I, Schödel M, Brocks W, Schönfeld W (2006) "Crack propagation analyses with CTOA and cohesive model": comparison and experimental validation. Eng Fract Mech 73 (2):252–263
17. Sugie E, Matsuoka M, Akiyama H, Mimura T, Kawaguchi Y (1982) A study of shear crack-propagation in gas-pressurized pipelines. J Press Vessels Technol ASME 104(4):338–343

Experimental Determination of Chloride Penetration in Concrete with Real Cracks

C. Sosdean, D. Gubencu, G. De Schutter and L. Marsavina

Abstract It is well known that the presence of cracks in reinforced concrete structures in aggressive environments accelerates rebar corrosion. The influence of real cracks in concrete structures on the penetration of chlorides and the resulting service life is being investigated in this study. Investigations were carried on at the Magnel Laboratory for Concrete Research of Ghent University, Belgium within a bilateral agreement with University Politehnica Timisoara, Romania. Non-steady state migration tests were realized according to NT BUILD 492, using an electrical field and real cracks in order to determine the chloride profile. Samples with different crack patterns, obtained by drilling from a reinforced concrete slab exposed to a simulated accidental failure of the central support and subsequent vertical loading until collapse, were used in the study in order to provide a more realistic image of the geometry of the cracks. The crack widths were measured using an optical microscope. The chloride penetration depth was measured with a colorimetric method on each specimen and the non-steady state diffusion coefficients were determined. For evaluating the parameters which have the most influence on chloride migration on the samples used in this experiment, a two-level factorial experiment was designed and carried out in the early stage. Afterwards, using a higher number of samples, the influence of the existence of cracks and also the influence of crack widths on chloride penetration was studied by means of other statistical procedures: comparison of two means, one-way ANOVA. The results obtained provide a better understanding of the diffusion process when dealing with concrete structures with real crack.

C. Sosdean (✉) · D. Gubencu · L. Marsavina
Department Strength of Materials, University of Timisoara,
Blvd. M. Viteazu, No. 1, 300222 Timisoara, Romania
e-mail: corina.sosdean@yahoo.com

G. De Schutter
Magnel Laboratory for Concrete Research, Department of Structural Engineering,
Ghent University, Technologiepark-Zwijnaarde 904, B-9052 Ghent, Belgium

G. Pluvinage and L. Milovic (eds.), *Fracture at all Scales*,
Lecture Notes in Mechanical Engineering, DOI 10.1007/978-3-319-32634-4_10

1 Introduction

Even though significant studies were performed in the last years in order to predict durability of concrete structures, chloride induced corrosion in reinforced concrete structures remains one of the major challenges. Due to the fact that most reinforced concrete structures are cracked either due to extreme loading, aggressive environment or poor workmanship during execution, it is very important to have a better understanding of chloride diffusivity in cracked concrete.

Researchers used a variety of programs to create cracks in undamaged concrete. Based on the crack preparation method, the reported experimental studies can be divided into two groups: destructive methods and non-destructive methods. The methods from the first category adopt different mechanical loading techniques to prepare cracks, such as: wedge splitting test [21], three or four-point bending test [27], Brazillian splitting test [2] and expansive core method [9]. Non-destructive methods used to generate cracks in concrete include studies based on the positioning and removal of thin copper sheets before final setting of concrete [3, 13] or inducing a crack by saw-cutting concrete cylinders longitudinally [19].

Real cracks in concrete have a complex 3D geometry and their influence on transport and degradation mechanisms is not straightforward, therefore very limited investigation of the influence of chloride diffusion on samples with real cracks has been conducted [22].

Due to the fact that it is difficult to evaluate the crack effect on the chloride diffusion characteristics, many applications using probabilistic approaches have been generally limited to the sound concrete without considering crack effect. Still, some researchers developed parametric studies of service life in cracked concrete, in order to determine the time to durability failure (time to corrosion). Kwon et al. [10] considered the cover depth and time-exposure parameter as design factors with varying values. Full parametric studies of the influence of crack width, roughness and the interval of drying-wetting cycles on the chloride profiles at cracked zone were developed by Ye et al. [26].

In present work, a study on the influence of cracks and crack widths in reinforced concrete structures with real cracks subjected to chloride ingress is presented.

Even though the behaviour of many natural phenomena was described by means of mathematical and statistical models, when referring to civil engineering and especially for the analysis of chloride penetration, few experimental data can be found in literature [12, 15].

2 Experimental Program

2.1 Details of Specimen

In this research four kinds of samples have been used: samples without cracks and without rebars (S) (a); samples with cracks and without rebars (SC) (b); samples without cracks and with rebars (SR) (c) and samples with cracks and with rebars (SCR) (d), as it can be observed in Fig. 1, where a representative sample from each group is presented.

In order to obtain samples with real cracks, cylinders with 100 mm diameter and 50 mm thickness were drilled from a RC slab of 140 mm thickness and 1800 mm wide with the total length of 14.30 m. This slab was exposed to failure of the central support and subsequent vertical loading which generated cracking and finally its collapse. As noticed, the cracks go all the way to the specimens and that is why the crack depth is not being considered in this research.

A concrete class C30/37 with a maximum size of 14 mm of the coarse aggregate was used in order to manufacture the slab. The test set-up and the results for the experimental large-scale test are described in detail in [6, 8].

For the investigation of the influence of different parameters on chloride diffusion, in this study, concrete samples with or without rebars, having different crack widths were used.

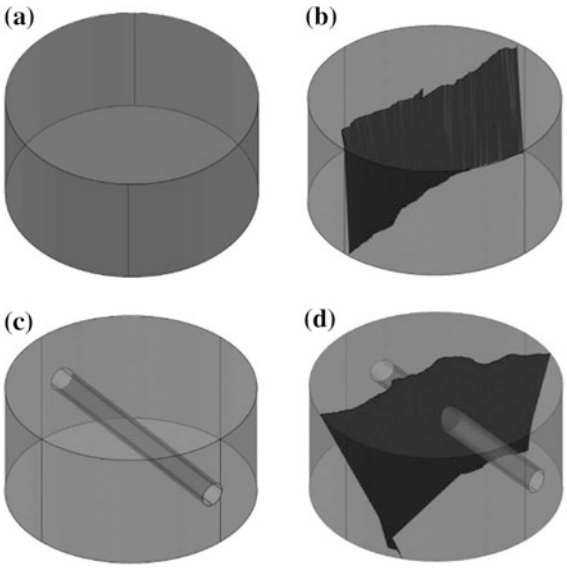

Fig. 1 Drilled sample categories [22]. **a** Sample type S, **b** sample type SC, **c** sample type SR, **d** sample type SCR

2.2 Testing Method

A non-steady state migration test was performed on the obtained concrete samples, according to NT BUILD 492 [16]. Before testing, the samples were placed in a vacuum container for vacuum treatment for 3 h to a pressure in the range of 10–50 mbar; afterwards with the vacuum pump still running, the container was filled with saturated $Ca(OH)_2$ solution so as to immerse all specimens which was maintained for a further hour before allowing air to re-enter the container. The specimens were kept in the solution for 18 ± 2 h.

Afterwards, the samples were placed in the reservoir and an external electrical potential of 30 and 35 V was applied on the samples for 24 h, forcing the chloride ions from the 10 % NaCl solution to migrate into the specimens.

2.3 Penetration Depth

After the test, the samples were split and sprayed with 0.01 N $AgNO_3$ solution and by using the colorimetric method [17] the chloride penetration profile was determined. The mean penetration profiles were determined after cutting the sample perpendicular to the crack path and by measuring the chloride front on each of them. It must be mentioned that samples type S were split in two, while samples type SR, SC and SCR were cut in 6 parts each perpendicular to the crack. A schematic representation of the procedure is presented in Fig. 2 for sample type SC.

For samples type SC and SCR, the average chloride depth (x_d) and the chloride depth near the crack (x_c) were determined. For sample type S, only x_d was determined, while for sample type SR both x_d and x_c were determined. A schematic representation of the chloride depths measurement in the middle of the sample is presented in Fig. 3.

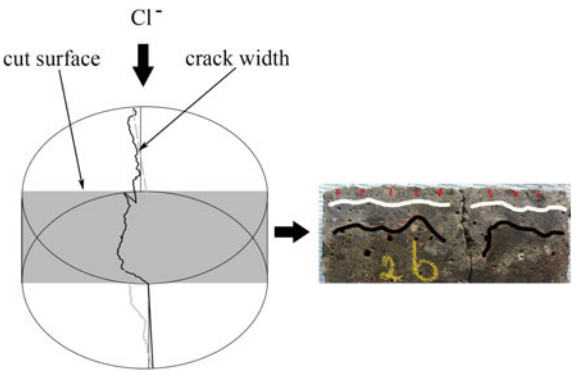

Fig. 2 Sample preparation for measuring the chloride front [22]

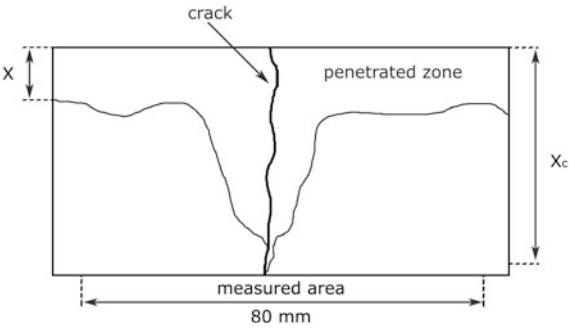

Fig. 3 Chloride front measurement in the middle of the sample

Based on the chloride penetration depth the chloride migration coefficient (D_{nssm}) can be calculated according to Eq. 1:

$$D_{nssm} = \frac{RT}{z \cdot FE} \cdot \frac{x_d - \alpha\sqrt{x_d}}{t} \tag{1}$$

where

$$E = \frac{U - 2}{L}$$

$$\alpha = 2\sqrt{\frac{RT}{zFE} \cdot erf^{-1}\left(1 - \frac{2c_d}{c_0}\right)} \tag{2}$$

C_d chloride concentration at which the color changes (=0.07 N)
C_0 chloride concentration in the cathodic solution (=2 N)
erf^{-1} inverse of error function
F Faraday constant (=9.648 × 10^4 J/(V Mol))
L thickness of the specimens (m)
R gas constant (=8.314 J/(K Mol))
x_d chloride penetration depth (m)
t test duration (sec)
T average value of the initial and final temperatures in the anolyte solution (K)
U applied voltage (V)
z absolute value of ionic valence (=1 for chloride)

Figure 4 shows the combined effect of crack width and rebar position on the diffusion coefficient. It can be easily seen that the migration coefficient increases with the existence of cracks; when increasing the crack width from 0 (Sample S) to 0.2 mm (Sample SC), the migration coefficient increases from 5.96 × 10^{-12} to 8.87 × 10^{-12} m^2/s. Also it can be observed that the existence of rebars "blocks" chloride diffusion, the migration coefficient decreases to 8.41 × 10^{-12} m^2/s. It seems that a lower value of 7.91 × 10–12 m^2/s is registered for the sample containing both rebars and cracks.

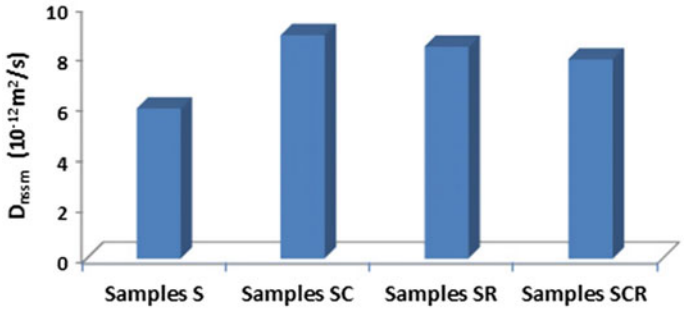

Fig. 4 Comparison of diffusion coefficient according to sample type [22]

It is important to mention that the values of the diffusion coefficient used in this study are mean values.

3 Experimental Investigations and Discussions on Chloride Diffusivity in Non-steady State Migration Test

3.1 Early Stage: Experimental Modeling by Factorial Experiment

The experimental data was analyzed using [24] software. In the first step of the experimental program, a limited number of samples were available. Moreover, certain parameters related to the crack pattern and the spatial orientation of the rebars couldn't be adjusted at rigorous set levels, but were randomly obtained. This is a consequence of the fact that the crack geometries were not induced artificially and are in fact real cracks obtained as a result of the collapsing of a real-scale slab.

Through the above presented results (Fig. 4), it can be observed that the presence of both cracks and rebars has an important influence on chloride ingress in cracked samples.

For the parametric study of chloride diffusion a two-level factorial experiment without randomization was designed and carried out in order to determine which of the following parameters: existence of cracks (Crack width l) and existence of rebars (Rebar no), used in the experimental program, has the most important influence on chloride ingress in cracked samples subjected to non-steady state migration test. This type of experiment was considered to be the most appropriate in this stage of the research, due to the fact that with a minimum number of runs (available samples) an exploratory mathematical model of high precision can be obtained.

The values of the considered parameters, both coded and physical, for each sample together with measured values of the objective function—chloride penetration depth (x_d)—are presented in Table 1.

Table 1 Experimental matrix [22]

Run no.	Levels of the influence factors				Measured values
	$x_1 \equiv$ crack width_l		$x_2 \equiv$ rebar No	RN	$y \equiv x_d$
	Coded	(mm)	Coded	–	(mm)
1	−1	0	−1	0	17.33
2	1	0.2	−1	0	22.48
3	−1	0	1	1	21.21
4	1	0.2	1	1	19.2

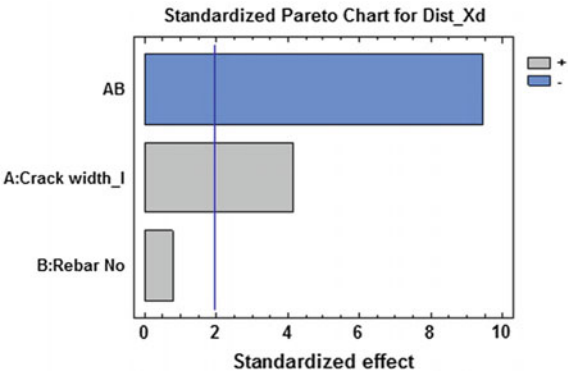

Fig. 5 Standardized Pareto chart

A standardized Pareto chart is presented in Fig. 5, which allows the hierarchy of both main effects and interaction effect on the response function.

As it can be observed, the interaction effect of crack width and rebar existence on chloride ingress is the most significant, followed by the existence of cracks. The effect of the rebar presence is not statistically significant on the chloride penetration depth x_d, having a magnitude comparable with the experimental error determined by performing 3 replicas in one experimental point. A possible explanation could be the fact that chlorides penetrate along the crack relatively fast up to the top of the crack (crack tip) [18], but their further propagation is being "blocked" by the existence of rebars. According to [25], when a crack in concrete intersects the steel reinforcing bar, it allows easy ingress of chloride ions, oxygen and water to the steel surface, which results in a faster initiation of corrosion.

The Eq. (3) of the fitted model is presented for coded values of the considered factors:

$$x_d = 20.055 + 0.785\mathrm{l} + 0.15\mathrm{RN} - 1.79\mathrm{l}\,\mathrm{RN} \tag{3}$$

Due to the fact that it is not possible to validate the model based on the different values of crack widths and, in addition, the experimental error was determined only for one experimental point located at the boundary of the multifactorial space, the practical applicability of the presented model could be limited.

Moreover, it is possible that different parameters, such as: crack existence, rebar presence, different crack widths, might influence chloride penetration in concrete

and, consequently, have a significant importance in the determination of the migration coefficient. Therefore, a statistical analysis of the chloride penetration data was performed, using different methods: the comparison of means, the comparison of standard deviation and the analysis of variance (ANOVA). It must be noted that the results presented in this statistical analysis were previously presented as part of the research conducted in [23].

3.2 *Influence of the Existence of Cracks by Two Samples Comparison*

In order to determine whether the existence of cracks has a significant influence on the chloride penetration depth, the comparison of means method was used by comparing the means of the different test series using t-tests with a significance level of 0.05.

It must be mentioned that in order to obtain an accurate result, a sufficient number of replicas is needed for each of the performed tests. As mentioned earlier, considering the fact that the crack geometries are in fact real cracks, the number of equal replicas for each test is almost impossible. Still, based on the existent information, the statistical analysis was realized in order to investigate the possible influence of the existence of cracks on chloride ingress.

Two-sample comparison tests based on the comparison of two means and the comparison of standard deviation methods were realized in order to determine the possible influence of the existence of cracks. These comparisons were made for different considered cases using the values of x_c (chloride penetration depth near the crack) which was considered to be the most relevant when determining the influence of the existence of cracks on chloride penetration.

The two samples of data considered in this case are the values of x_c obtained for reference samples and for samples with cracks having the top surface exposed. These values are presented in Table 2. It is important to mention that in the case of

Table 2 Penetration depth for samples with cracks

Sample	Chloride penetration		Sample	Chloride penetration	
	x_d (mm)	x_c (mm)		x_d (mm)	x_c (mm)
J	23.1	28.4	7	28.1	37.0
K	28.0	36.8	13	25.9	30.9
L	22.3	27.7	16	24.0	31.3
M	23.9	26.4	25	21.1	31.9
N	20.1	20.6	A2	23.7	26.5/27.2
4	22.4	26.8	B2	25.2	34.8
6	15.2	28.4	–	–	–

Table 3 Penetration depth for reference samples type S

Chloride penetration		Chloride penetration	
	x_d (mm)		x_d (mm)
Ref IV a	21.4	Ref IV b	15.7
Ref V	24.2	Ref VII	17.6
Ref VI	26.3	Ref VIII	18.7

Table 4 Summary statistics: depth x_c by sample type

	Sample type = R	Sample type = S
Count	9	13
Average	20.8222	29.8077
Standard deviation	3.56783	4.63797
Coeff. of variation	17.1347 %	15.5596 %
Minimum	15.7	20.6
Maximum	26.3	37.0
Range	10.6	16.4
Stnd. skewness	0.191175	−0.0674505
Stnd. kurtosis	−0.742232	0.0187035

reference samples, considering they have no cracks, the value of x_d (average chloride penetration depth) was used (Table 3).

Sample 1, representing reference samples type S and SR, consists in 9 values ranging from 15.7 to 26.3 while sample 2, representing samples with cracks type SC and SCR, consists in 13 values ranging from 20.6 to 37.0. These two samples of data are compared by means of various statistics and graphs and by running several tests in order to determine whether there are statistically significant differences between the two samples.

The sample characteristics are further presented in Table 4. The standardized skewness and standardized kurtosis can be used to determine whether the samples come from normal distributions. Values of these statistics outside the range of −2 to +2 indicate significant departures from normality. In this case, both standardized skewness and standardized kurtosis are within the range expected.

A t-test is run to compare the means of the two samples and it also constructs confidence intervals for each mean and also for the difference between the means. The test is used to investigate the null hypothesis about the difference between the means of the populations from which the two samples come. Considering that in the present test $t = -4.88436$ and $P = 0.0000897041$, meaning $P < 0.05$ the null hypothesis is rejected in favor of the alternative. It means there is a statistically significant difference between the means of the two samples at the 95 % confidence level.

The previously presented results assume that the variances of the two samples are equal. These assumptions are made based on the results of an F-test to compare the standard deviations presented in Table 5.

An F-test is run to compare the variances of the two samples and it also constructs confidence intervals for each standard deviation and for the ratio of the

Table 5 Comparison of standard deviations: depth x_c by sample type for top surface exposed

	Sample type = R	Sample type = S
Standard deviation	3.56783	4.63797
Variance	12.7294	21.5108
Df	8	12

variances. The test is used to investigate the null hypothesis about the standard deviations of the populations from which the two samples come. Considering that in this test F = 0.591771 and $P = 0.464524$, meaning $P > 0.05$ and the ratio of the standard deviation equals 0.591771, the null hypothesis cannot be rejected. As a result there is not a statistically significant difference between the standard deviations of the two samples at the 95 % confidence level.

The conclusion of this two-sample comparison test is that there is a statistically significant difference between the x_c values of the compared two samples, meaning that, at 95 % confidence level, the chloride penetration depth is influenced by the existence of cracks.

3.3 *Influence of Crack Widths by One-Way ANOVA*

For determining the influence of different crack widths, on the chloride penetration depth, respectively on the diffusion coefficient, one-way ANOVA analysis were performed with a level of significance of 0.05.

One-way ANOVA tests were performed in order to determine the possible influence of the crack width on D_c (diffusion coefficient measured near the crack). This procedure performs a one-way analysis of variance for diffusion coefficient D_c considering the average crack width presented in Table 6.

Various tests and graphs are constructed to compare the mean values of D_c for the considered 16 cores type SC and SCR with 4 different levels of crack width. The result characteristics of the one-way ANOVA are further presented in Table 7. The ANOVA table decomposes the variance of D_c into two components: a between-group component, which measures the variability amongst D_c determined

Table 6 Crack widths in samples

Sample	Crack opening (μm)			Sample	Crack opening (μm)		
	Top	Bottom	Average		Top	Bottom	Average
J	187	442	314	7	169	68	119
K	190	396	293	13	164	131	148
L	269	359	314	16	130	108	119
M	211	389	300	25	141	66	104
N	338	232	285	A2	173	148	161
4	143	79	111	B2	93	155	124
6	154	160	157	–	–	–	–

Table 7 Summary statistics: diffusion

Source	Sum of squares	Df	Mean square	F-ratio	*P*-value
Between groups	51.4673	3	MS_{level} = 17.1558	5.28	0.0149
Within groups (error)	39.0063	12	MS_E = 3.25052		
Total (corr.)	90.4736	15			

Table 8 Table of means for Dc by crack width with 95 % LSD intervals

Stnd. error					
Level	Count	Mean	(pooled s)	Lower limit	Upper limit
0	3	8.38333	1.04092	6.77964	9.98703
0.1	5	13.47	0.80629	12.2278	14.7122
0.15	3	12.7167	1.04092	11.113	14.3204
0.3	5	11.994	0.80629	10.7518	13.2362
Total	16	11.9137			

for samples with different crack width and a within-group component, which measures the variability amongst D_c determined for samples with the same crack width. The F ratio, which in this case F = 5.27785, is a ratio of the between-group mean square (MS_{level}) to the within-group estimate (MS_E). Since the calculated probability, $P = 0.0149$, computed for the determined F and for the considered degrees of freedom (Df) is less than the pre-chosen significance level 0.05 ($P < 0.05$) there is a statistically significant difference between the mean D_c from one level of crack width to another at the 95 % confidence level [14].

The table of means for D_c by crack width is further presented in Table 8. Also, the table shows the standard error of each mean which is a measure of its sampling variability. The standard error is formed by dividing the pooled standard deviation by the square root of the number of observations at each level. The table also displays an interval around each mean. The intervals are based on Fisher's least significant difference (LSD) procedure and are constructed in such a way that if two means are the same, the intervals will overlap 95 % of the time. This does not imply that every mean is significantly different from every other mean.

To determine which means are significantly different from which others the Multiple Range Test is carried on. Table 9 presents which means are significantly different from which others by using a multiple comparison procedure.

The bottom half of the output shows the estimated difference between each pair of means. An asterisk has been placed next to 3 pairs, indicating that these pairs show statistically significant differences at the 95 % confidence level.

Figure 6 presents the interval plots at 95 % confidence of diffusion coefficient D_c for each crack width. It can be observed that there is a statistical significant difference between the values obtained for the reference samples and the values obtained for samples with cracks, but no statistical significant difference is between the different considered widths.

Table 9 Multiple range tests results for 95 % LSD-Dc by crack width

Level	Count	Mean	Homogeneous groups
0	3	8.38333	X
0.3	5	11.994	X
0.15	3	12.7167	X
0.1	5	13.47	X

Contrast	Sig.	Difference	±Limits
0–0.1	*	−5.08667	2.86878
0–0.15	*	−4.33333	3.20739
0–0.3	*	−3.61067	2.86878
0.1–0.15		0.753333	2.86878
0.1–0.3		1.476	2.48443
0.15–0.3		0.722667	2.86878

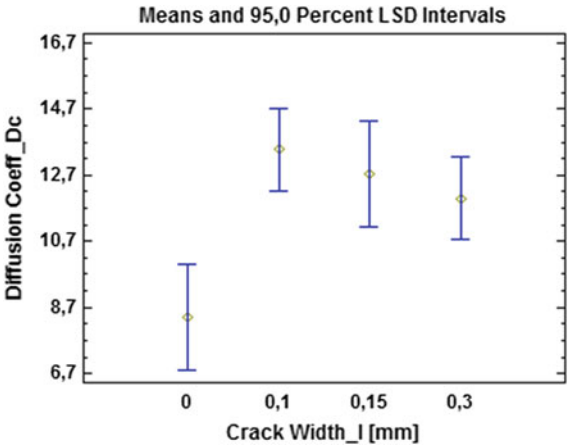

Fig. 6 Interval plot (95 % confidence) of D_c for crack width [22]

4 Conclusions

The effects hierarchy and the experimental model achieved in the early stage of investigation show that even if the presence of cracks led to the enlargement of the chloride penetration depth, it seems that the combined effect of both crack width and rebar existence determine the decrease of this objective function. In that case, the rebar presence obstructs the diffusion process and makes it more difficult.

The possible influence of the presence of cracks was further investigated, by the comparison of means method at a 95 % confidence interval, in order to eliminate its influence. The chloride penetration depth near the crack (x_c) is influenced by the existence of cracks when having the top surface exposed and taking into consideration all sample types (S—samples without cracks and rebars, SC—samples with cracks and without rebars, SR—samples without cracks and with rebars and SCR—samples with cracks and rebars).

Next, the possible influence of the crack widths on the available samples was investigated by performing a one-way ANOVA test at a 95 % confidence interval and considering the average crack width, as previously presented in Table 6, respectively the values of D_c (migration coefficient near the crack) computed considering the average crack widths of: 0.1; 0.15 and 0.3. It seems there is no statistical significant difference between the values of D_c for the considered crack widths.

It is generally recognized that the existence of cracks provide fast transport routes for chloride. However, crack width can be considered to be one of the most controverted parameters that can influence chloride ingress.

Even though there are different codes prescribing an allowable crack width ranging from 0.05 to 0.3 mm [1, 4, 5], the influence of crack width on concrete properties is still under debate. Gérard and Marchand [7] show that the steady state migration coefficients of concrete with different crack widths are one order of magnitude higher than for uncracked concrete. While some researchers [11] suggest the dependence between chloride profiles and crack width, Rodriguez and Hooton [20] suggests that chloride diffusion in concrete is independent of the crack width since cracks act as free concrete surfaces and greatly promote chloride ingress and Marsavina et al. [13] concludes that the influence of crack on chloride penetration is still not clear and requires further research.

Acknowledgments This work was done in the framework of Bilateral Scientific Agreement between Ghent University, Belgium and Politehnica University of Timisoara, Romania. Also, the financial support by the Special Research Fund (BOF) of Ghent University is gratefully acknowledged.

References

1. ACI Committee 224 (1999) Control of cracking in concrete structures (ACI 224R-90), ACI manual of concrete practice, part 3, ACI
2. Aldea CM et al (1999) Effect of cracking on water and chloride permeability of concrete. J Mater Civ Eng ASCE 11(3):181–187
3. Audenaert K et al (2009) Influence of cracks on the service life of concrete structures in a marine environment. Key Eng Mater 339:153–160
4. British Standards Institution (1997) BS 8110: part 1. BSI, London
5. British Standards Institution (1992) ENV 1991-1-1. BSI, London
6. Caspeele R et al (2013) Structural reliability of concrete slabs considering tensile membrane action. In: Safety, reliability and risk analysis: beyond the horizon, proceedings, pp 2713–2720
7. Gérard B, Marchand J (2000) Influence of cracking on the diffusion properties of cement-based materials: part I: influence of continuous cracks on the steady-state regime. Cem Concr Res 30(1):37–43
8. Gouverneur D et al (2013) Experimental investigation of the load–displacement behavior under catenary action in a restrained reinforced concrete slab strip. Eng Struct 49:1007–1016
9. Ismail M et al (2004) Effect of crack opening on the local diffusion of chloride in inert materials. Cem Concr Res 34(4):711–716

10. Kwon SJ et al (2009) Service life prediction of concrete wharves with early-aged crack: probabilistic approach for chloride diffusion. Struct Saf 31:75–83
11. Li CQ (2001) Initiation of chloride-induced reinforcement corrosion in concrete structural members—experimentation. ACI Struct J 98(4):502–510
12. Maes M, De Belie N (2013) Resistance of cracked concrete to chloride attack. In: 3rd international conference on sustainable construction materials and technologies. Kyoto Research Park, pp 1–10
13. Marsavina L et al (2009) Experimental and numerical determination of the chloride penetration in cracked concrete. Constr Build Mater 23(1):264–274
14. Montgomery DC, Runger GC (2010) Applied statistics and probability for engineers. Wiley, Hoboken
15. Nieves-Mendoza D, Gaona-Tiburcio C, Hervert-Zamora HL, Almeraya-Calderón F (2012) Statistical analysis of factors influencing corrosion in concrete structures. Int J Electrochem Sci 7:5495–5509
16. NT BUILD 492 (1999) Concrete, mortar and cement-based repair materials: chloride migration coefficient from non-steady-state migration experiments. NORDTEST
17. Otsuki N et al (1992) Evaluation of $AgNO_3$ solution spray method for measurement of chloride penetration into hardened cementations matrix materials. ACI Mater J 89(6):587–592
18. Ožbolt J, Balabanic G, Periškić, Kušter M (2010) Modelling the effect of damage on transport processes in concrete. Constr Build Mater 24(9):1638–1648
19. Pour-Ghaz M et al (2009) Numerical and experimental assessment of unsaturated fluid transport in saw-cut (Notched) concrete elements. ACI Special Publication SP266-06, vol 266, pp 73–86
20. Rodriguez OG, Hooton RD (2003) Influence of cracks on chloride ingress into concrete. ACI Mater J 100(2):102–126
21. Schlangen E et al (2007) Measurement of chloride ingress in cracked concrete. In: Audenaert K, Marsavina L, De Schutter G (eds) International RILEM workshop on transport mechanisms in cracked concrete. Acco, Leuven, pp 19–25
22. Sosdean C et al (2014) Influence of real cracks on chloride diffusion. In: Kytyr D (ed) YSESM proceedings of XIIIth youth symposium on experimental solid mechanics. CTUP, CZ, pp 16–120
23. Sosdean C (2015) Experimental and numerical investigations of the influence of cracks on mass diffusion in mortar and concrete (PhD thesis), Politehnica University of Timisoara, Timisoara, Romania
24. Statgraphics (1997). Statgraphics plus, version 3.0
25. Subramaniam KV, Bi M (2010) Investigation of steel corrosion in cracked concrete: evaluation of macrocell and microcell rates using Tafel polarization response. Corros Sci 52:2725–2735
26. Ye H et al (2012) Model of chloride penetration into cracked concrete subject to drying–wetting cycles. Constr Build Mater 36:259–269
27. Ye H et al (2013) Influence of cracking on chloride diffusivity and moisture influential depth in concrete subjected to simulated environmental conditions. Constr Build Mater 47:66–79

Cleavage Fracture in Continuously Cooled V-Microalloyed Medium Carbon Steel

D. Glišić, N. Radović, D.J. Drobnjak and A. Fadel

Abstract Medium carbon V-microalloyed steel continuously cooled from the austenitization temperature at still air, with predominantly acicular ferrite structure, has been investigated by means of four-point bending of notched Griffiths–Owens's type specimens at liquid nitrogen temperature. Local fracture stress and plastic strain were determined by using finite element analysis and fracture surface examination using scanning electron microscope. It was revealed that cleavage fracture initiation, which takes place close to the notch root in the narrow zone of high plastic strains, is not related to any broken coarse second phase particles. It was assumed that microcracks nucleate by strain induced fracture of pearlite nodules. Two effective surface energy values of 24 and 42 J/m^2 were estimated according to the Griffith's equation, indicating the influence of crystallographic orientation between neighboring grains at the origin of fracture. Lower value was attributed to fracture of coarse ferrite–pearlite units with similar crystallographic orientation and higher value to fracture propagation through fine acicular ferrite matrix.

Keywords Micro-alloyed steel · Cleavage stress · Surface energy

1 Introduction

Microalloyed medium carbon forging steels are designed in attempt to attain required strength of forged parts by direct cooling from the hot working temperature, thus eliminating expensive procedure of quenching and tempering. Microalloying elements increase strength of the steels through grain refinement and

D. Glišić (✉) · N. Radović · D.J. Drobnjak
Faculty of Technology and Metallurgy, University of Belgrade, Karnegijeva 4,
11120 Belgrade, Serbia
e-mail: gile@tmf.bg.ac.rs

A. Fadel
Al Zawiya University, Zawiya, Libya

G. Pluvinage and L. Milovic (eds.), *Fracture at all Scales*,
Lecture Notes in Mechanical Engineering, DOI 10.1007/978-3-319-32634-4_11

precipitation of fine carbo-nitride particles. Although satisfactory strength level and fatigue properties are achieved, toughness of the continuously cooled microalloyed forging steels is much lower compared to that of quenched and tempered steels. An improvement of the toughness is observed in microalloyed steels with acicular ferrite present as dominant in the structure [20, 22]. It is believed that fine randomly oriented interlocking ferrite plates and laths provide additional barriers for cleavage crack propagation [22, 24].

Cleavage fracture of continuously cooled medium carbon microalloyed steels has been studied prevalently for ferrite–pearlite and bainite structures, while the steels with predominantly acicular ferrite structure received relatively limited attention [11, 16].

The aim of present work is to assess cleavage fracture mechanism in continuously cooled medium carbon V-microalloyed steel with predominantly acicular ferrite structure.

2 Material and Experiment

Samples of commercial V-microalloyed medium carbon hot-rolled steel rods 19 mm in diameter, with chemical composition given in Table 1, have been heat-treated with intention to obtain acicular ferrite in the structure by cooling at still air directly from the austenitization temperature. In order to eliminate as-received microstructure specimens were initially homogenized at 1250 °C for 4 h in argon protective atmosphere followed by oil quenching. Specimens were then austenitized at 1250 °C for 30 min in argon atmosphere and cooled at still air.

The cleavage fracture strength was measured via four-point bending (4 PB) testing at constant crosshead speed of 0.1 mm/min in liquid nitrogen (−196 °C) using Griffiths–Owens's specimen (12.7 × 12.7 × 75 mm with 45° notch 4.23 mm deep and with radius of 0.250 mm) [18].

Fracture surface was analyzed by scanning electron microscope (SEM) equipped with energy dispersive X-ray spectrometer (EDS). The cleavage initiation sites were identified by tracing chevron stripes at lower magnifications and river pattern lines at higher magnifications back to the cleavage origin. Cleavage origin distance from the notch root and cleavage facets sizes were measured from the SEM micrographs.

Stresses and strains ahead of the notch root of the four-point bending specimen were calculated by finite element analysis (FEA) using ABAQUS code. The specimen was modeled in two dimensions with quadratic eight-node plane strain elements (CPEG8). Material's elastic properties were represented by Young's modulus of 200 GPa, Poisson's ratio of 0.28 [18]. Plastic response was modeled by experimentally determined true stress–strain curve. True stress–strain curve were obtained by polynomial regression of experimental data obtained by uniaxial tensile test at liquid nitrogen temperature. Tensile testing was performed at constant crosshead speed of 0.1 mm/min, which corresponds to that of four-point bending. Specimens 6 mm in diameter and with 30 mm gauge length were used [17].

Table 1 Chemical composition of the tested steel (in wt.%)

C	Si	Mn	P	S	Cr	Ni	Mo	V	Ti	Al	Nb	N
0.256	0.416	1.451	0.0113	0.0112	0.201	0.149	0.023	0.099	0.002	0.038	0.002	0.0229

3 Results and Discussion

Typical microstructure of the steel is shown in Fig. 1. Grain boundary ferrite idiomorphs (GBF) form continuous network along previous austenite grain boundaries. Some alotriomorphs could be observed, sometimes with Widmanstätten saw-teeth (WST) ferrite plates that have nucleated on them (Fig. 1a). Most of the grain interiors are occupied by acicular ferrite (AF) typically bordered by pearlite nodules (P) and grain boundary idiomorphs (GBI) (Fig. 1b).

During cooling from austenitization temperature, proeutectoid ferrite is formed along austenite grain boundaries. Due to low solubility in ferrite, carbon diffuses into neighboring austenite. This local enrichment on carbon increases the stability of present austenite until Ar_1 temperature is reached when diffusional transformation to pearlite occurred. At lower temperatures, when diffusion becomes sluggish, remained austenite transforms by bainitic mechanism. Since grain boundaries are already occupied by ferrite grains, grain boundary nucleation of bainitic sheaves is precluded, and therefore intragranular nucleation of acicular ferrite takes place. Intragranular nucleation of acicular ferrite is promoted by second phase particles, which act as a ferrite nucleation sites. Among them, most potent for acicular ferrite nucleation are vanadium-carbonitride particles [14, 20], which could be expected in the present case, considering chemical composition of the steel.

Fracture surfaces of all tested four-point bending samples, shown in Fig. 2a–d, exhibit typical transgranular brittle fracture. Fracture surface is characterized by mixture of small irregular cleavage facets that surround coarse, usually elongated facets. Chevron lines clearly point to the zone of cleavage initiation, which is for all specimens placed near the notch root. Fine river lines are clearly visible on coarse facets, but on small facets seem to be finer and somewhat difficult to trace toward the cleavage origin.

Moreover, twisted or greatly tilted cleavage planes of small facets indicate high crystallographic misorientation. Such frequent change of crack propagation

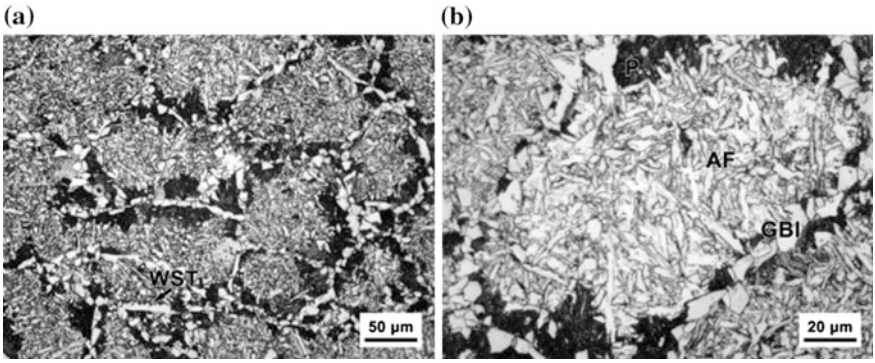

Fig. 1 Microstructure of the tested steel; *WST* Widmanstätten saw-teeth ferrite, *P* pearlite, *GBI* grain boundary idiomorphs, *AF* acicular ferrite

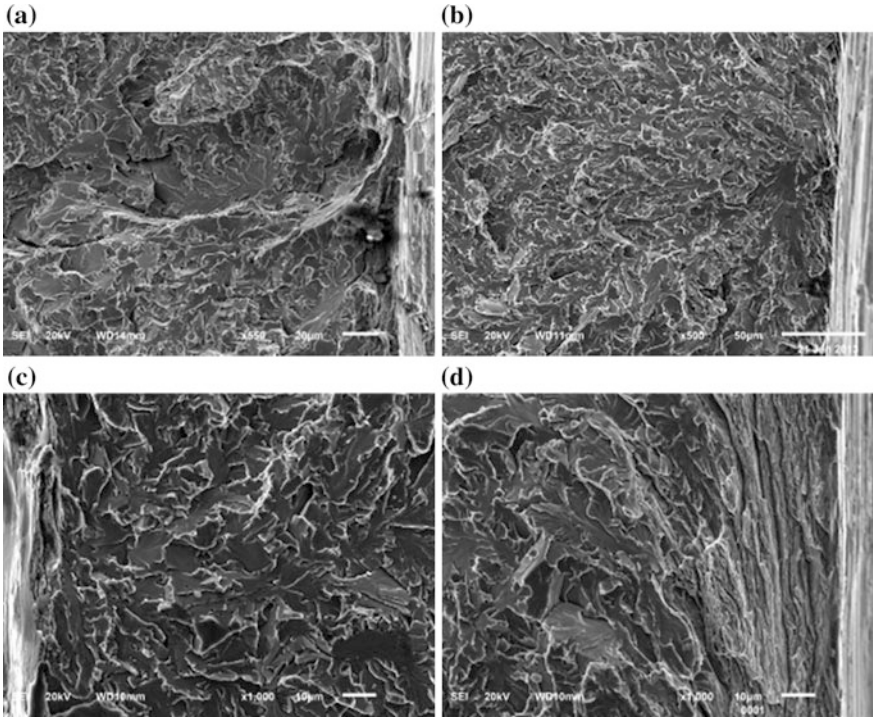

Fig. 2 Fracture surfaces near the fracture initiation site

direction and elevation clearly reflects underlying fine interlocked structure of acicular ferrite. Consequently, many local crack branches and deep side microcracks could be observed.

Small facets connected by uninterrupted surface traces, tilted at low angles, could be ascribed to cleaved sheaves of acicular ferrite laths or plates with low crystallographic misorientation. It had been established that acicular ferrite formed at lower temperature range, around 400–450 °C, consists of sheaves of nearly parallel laths and plates with similar crystallographic orientation [8, 19]. Acicular ferrite formed in higher temperature range is characterized by higher density of fine ferrite laths or plates with high crystallographic misorientation [8, 12, 19]. It is assumed that continuously cooled acicular ferrite would consist of mixture of both types. Although some of the coarse laths observable in micrograph in Fig. 1b could be recognized as a sheaf of nearly parallel acicular ferrite laths/plates, it is not actually possible to distinguish different types of acicular ferrite at light microscopy level. As it had been established, only high angle boundaries, with misorientation angle higher than 15°, could be an effective barrier to cleavage crack propagation and morphological size does not correspond to "effective" or crystallographic packet size [8, 26].

Coarse elongated facets correspond to some large microconstituent or a group of grains with similar crystallographic orientation. In medium carbon steels such large grains belong to ferrite–pearlite aggregates with the same crystallographic orientation, which is easily trespassed by propagating crack [25].

As could be observed from the SEM micrographs in Fig. 2a–d, cleavage origin is located almost at the notch root. Distances of the initiation site from the notch root, X_0, summarized in Table 2 among other measured values, range from only 14 to 56 μm. Second phase particles have not been found at the origin. Similar case of the cleavage initiation at the notch root of a microalloyed medium carbon steel with acicular ferrite structure had been reported earlier [9]. Cleavage fracture of medium carbon microalloyed steels with ferritic–pearlitic, bainitic or martensitic structure is usually related to the fracture of coarse second phase particles. In most cases of the microalloyed steels, broken TiN or complex (Ti,V)(C,N) particles were responsible for cleavage initiation, but also fractured or delaminated MnS inclusion, other complex particles or fractured coarse carbides in the zone of high stress intensification [2–4, 13, 27].

Stress and strain distribution along the distance from the notch root, calculated by FEM analysis, is shown in Fig. 3. Cleavage initiation is located in the narrow zone of high plastic strains (shaded area in the graph), where maximum principal stress is relatively low. The values of the principal plastic strain at the location of cleavage origin, ε_{pc}, range from 0.19 to 0.35, while local fracture stress, σ_F^*, does not exceed 1672 MPa. Considering that stresses for fracture of particles in microalloyed medium carbon steels with various microstructures is approximately 2500 MPa [10, 23], it is clear that cleavage initiation by this mechanism could not be expected near the notch root. Fracture of coarse particles should be expected around 400–600 μm away from the notch, where peak values of principal stress, σ_{1max}, reach between 2360 and 2589 MPa (Fig. 3 and Table 1).

Plastic strains in this zone are considerably lower implying that critical flaw had been formed under the influence of high plastic strains near notch root. Critical value of plastic strain had been proposed earlier by Chen et al. [5, 6]. They

Table 2 Values measured in the four-point bending test at −196 °C and calculated values of local fracture stress and plastic strain at the origin of fracture

F_{max} (N)	σ_F (MPa)	σ_F/σ_Y (MPa)	σ_{1max} (MPa)	X_0 (μm)	σ_F^* (MPa)	ε_{pc}	$D_{max} \times D_{min}$ (μm)	D_{eff} (μm)	γ
28,521.6	1192.7	1.54	2524.7	32	1556.1	0.26	36.8 × 15.5	24.5	87.0
				53	1671.5	0.22	12.8 × 17.3	11.9	48.7
30,318.1	1267.8	1.64	2588.6	19	1484.3	0.35	23.7 × 9.8	15.6	50.3
				19	1484.3	0.35	21.0 × 11.3	16.7	53.9
				28	1545.1	0.33	29.3 × 24.1	28.5	99.9
25,084.6	1049.0	1.35	2360.0	15	1433.2	0.20	41.0 × 8.1	14.0	42.1
				14	1430.5	0.20	8.6 × 6.8	8.3	24.8
27,561.2	1152.5	1.49	2474.2	56	1669.4	0.19	34.7 × 8.2	14.0	57.4
				54	1662.4	0.19	10.7 × 3.7	6.0	24.4

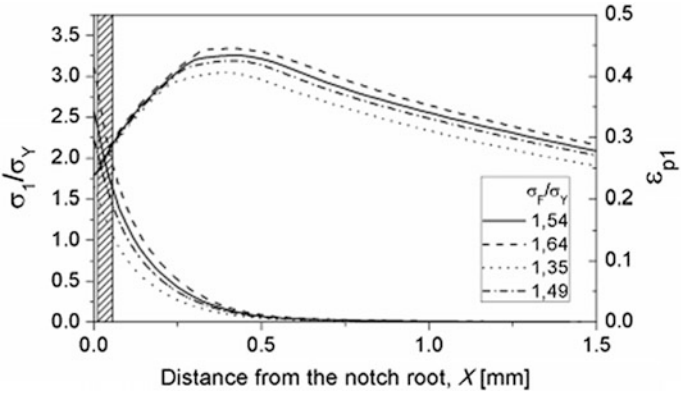

Fig. 3 Distribution of the maximum principal stress and plastic strain along the distance from the notch root for all samples

suggested that critical strain must be attained for microcrack nucleation, critical stress triaxiality to prevent crack from blunting at stress level to provide further crack propagation [6]. Nevertheless, it remains unclear why particles remain inactive in a presence of acicular ferrite structure. Aside the fact that present steel contains negligible amount of titanium added, other aforementioned coarse particles or inclusions could be the candidate for cleavage nucleation. An example of broken particle at the fracture surface, which is not the origin of the fracture, is shown in Fig. 4. Elongated cylindrical form of the particle is typical for the MnS modified by calcium addition. It is apparently surrounded by a cluster of small facets, likely related to the acicular ferrite plates/laths, while the main crack path emanating from the coarse facets at the cleavage origin traverse them. Large facet probably belongs to ferrite–pearlite grains with same crystallographic orientation that was easily surpassed by advancing cleavage crack.

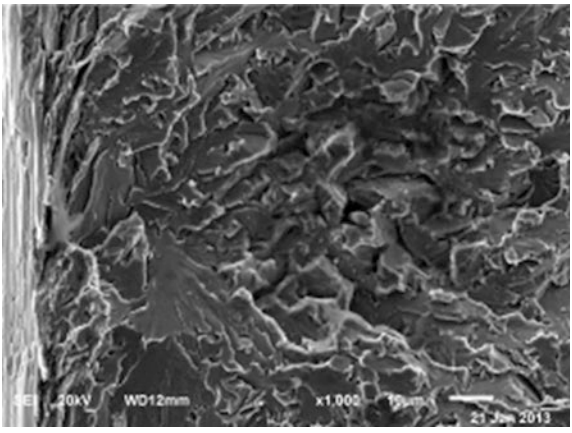

Fig. 4 An example of broken inclusion (in the *middle*), not related to the fracture initiation site (to the *left*)

Two mechanisms of strain induced critical microcrack formation should be taken into account. According to the model proposed by Smith, grain boundary carbide fractures under the influence of stress field ahead of the dislocation pile-ups [28]. However, it had been established that Smith's mechanism is not applicable in the case of fine pearlite [21]. Based on the investigations of cleavage fracture in fully pearlitic steels, authors proposed that critical flaw is created by accumulation of damage within the pearlite colonies under the influence of plastic strain. Having in mind the presence of grain boundary ferrite and neighboring pearlite with similar crystallographic orientation in the microstructure of the steel investigated (Fig. 1) it seems that the latter mechanism is more applicable. Strain induced fracture of coarse ferrite–pearlite unit could create a critical flaw that would propagate further through the matrix at relatively low stress. As it was established, microcracks formed within ferrite or pearlite propagates through low angle boundaries of ferrite–pearlite units with same crystallographic orientation uninterruptedly [15, 25].

Since there were no particles at the cleavage origin, it was difficult to distinguish first cleavage facet. Therefore, two or three facets were measured, assuming they correspond to the initial microcrack. Maximum and minimum ferret diameters of the first facets measured are presented in Table 2, alongside with the effective crack diameter, D_{eff}, calculated using following equation [1, 9]:

$$D_{eff} = \frac{D_{\min}}{\phi^2}\frac{\pi^2}{4} \tag{1}$$

$$\phi = \frac{3\pi}{8} + \frac{\pi}{8}\left(\frac{D_{\min}}{D_{\max}}\right) \tag{2}$$

By considering determined values of local fracture stress, σ_F*, and values of effective diameter of the first cleavage facet, D_{eff}, effective surface energy, γ, can be calculated from Griffith's equation for penny-shaped microcrack [7, 9]:

$$\sigma_F^* = \sqrt{\frac{\pi \cdot E \cdot \gamma}{(1-\nu^2)\cdot D_{eff}}} \tag{3}$$

Calculated values of the effective surface energy, γ, are listed in Table 1, along with corresponding local fracture stresses and first facet diameters. The values of effective surface energy are in the range of 24–100 J/m^2.

Local fracture stress is plotted against reciprocal value of square root of the effective diameter in Fig. 5. The lower bounds of the effective surface energies represented by the straight lines below two groups of points that correspond to coarse and fine facets, may be considered as an upper limit value, because it is higher or equal to the "real" value for given microstructure of the steel examined.

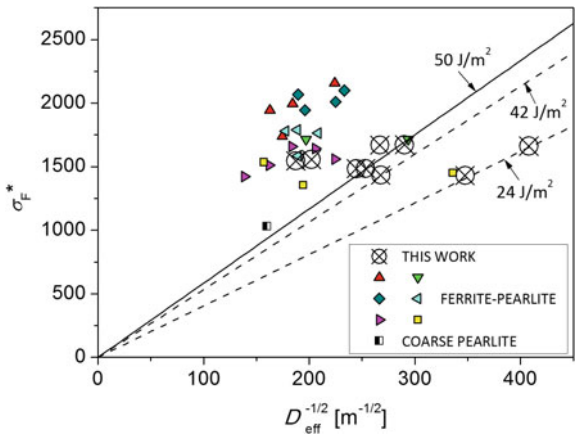

Fig. 5 Values of the local critical fracture stress plotted against first cleavage facet's effective diameter and comparison with the values from literature [25, 27]

Method used here had been adopted from the Linaza, Echeverria and coworkers, who have calculated values of approx. 50 J/m^2 for ferrite–pearlite microalloyed medium carbon steels [25, 27]. Values from this work are plotted in Fig. 5 for the purpose of comparison. The first group of points from this work is somewhat lower. Unusually low values of the second group of points in present work are higher than values reported for fracture initiation on broken TiN particles, approx. 7 J/m^2 [25]. Cleavage initiation by fracture of the coarse second phase particles in present case could be considered as competing mechanism that has not been operative, or has been precluded by other process of initial microcrack nucleation. Therefore, it could be concluded that observed facets with small diameters, corresponding to lower values of effective surface energy, are related to fractured pearlite nodules. These pearlite nodules are between proeutectoid ferrite grains, along previous austenite grain boundaries, and acicular ferrite in the previous austenite grain interiors.

Relatively large initial microcracks formed in the zone of high plastic deformation near the notch root, require comparatively small stresses to propagate, in accordance to Griffith's equation. Initial microcrack easily propagates through the matrix regardless of its size. However, two values of effective fracture energies from the graph in Fig. 5, of 24 and 42 J/m^2, imply the effect of the underlying microstructure on initial microcrack propagation. The values of effective surface energy calculated here are comparable to the values determined in previous investigations found in literature for microalloyed medium carbon steels [25, 27]. It could be assumed that large initial microcrack is necessary to propagate through the matrix consisting of fine acicular ferrite laths/plates. Conversely, initial microcrack easily propagates when it encounters another pearlite nodule or ferrite grain with small crystallographic misorientation, rendering lower bound values of effective surface energy.

4 Conclusion

1. Cleavage fracture of the prevalently acicular ferrite steel, with ferrite and pearlite along previous austenite grain boundaries, was initiated by strain induced fracture of pearlite nodules and uninterrupted propagation through bordering ferrite grain or pearlite nodule with similar crystallographic orientation.
2. Effective surface energies of 24 and 42 J/m^2 were calculated using Griffith's–Owen approach. The latter value is in agreement with previously reported, although somewhat lower. Dual values of the effective surface energy were ascribed to differences in continuously cooled microstructure.
3. Although strain induced microcracks propagate at low stresses near the notch, local fracture stress and effective surface energy depend on propagation stage of the cleavage process and is affected by the microstructure surrounding initial microcrack. Propagation of the small facets, approximately 6–8 μm in diameter, is related to propagation through the matrix with small crystallographic misorientation. Inversely, larger initial microcracks are surrounded by finer grains that are related to the acicular ferrite structure.

References

1. Alexander DJ, Bernstein IM (1989) Cleavage fracture in pearlitic eutectoid steel. Metall Trans A 20:2321–2335
2. Balart MJ, Davis CL, Strangwood M (2004) Observations of cleavage initiation at (Ti, V)(C, N) particles of heterogeneous composition in microalloyed steels. Scr Mater 50:371–375
3. Balart MJ, Davis CL, Strangwood M (2000) Cleavage initiation in Ti–V–N and V–N microalloyed ferritic–pearlitic forging steels. Mater Sci Eng A 284:1–13
4. Balart MJ, Davis CL, Strangwood M, Knott JF (2005) Cleavage initiation in Ti–V–N and V–N microalloyed forging steels. Mater Sci Forum 500:729–736
5. Chen JH, Wang GZ, Wang Q (2002) Change of critical events of cleavage fracture with variation of microscopic features of low-alloy steels. Metall Mater Trans 33A:3393–3402
6. Chen JH, Wang Q, Wang GZ, Li Z (2003) Fracture behavior at crack tip—a new framework for cleavage mechanism of steel. Acta Mater 51:1841–1855
7. Curry DA, Knott JF (1978) Effect of microstructure on cleavage fracture stress in steel. Metal Sci 12:511–514
8. Diáz-Fuentes M, Iza-Mendia A, Gutiérrez I (2003) Analysis of different acicular ferrite microstructures in low-carbon steels by electron backscattered diffraction. Study of their toughness behavior. Metall Mater Trans A 34:2505–2516
9. Echeverria A, Rodriguez-Ibabe JM (2003) The role of grain size in brittle particle induced fracture of steels. Mater Sci Eng A A346:149–158
10. Echeverria A, Rodriguez-Ibabe JM (2004) Cleavage micromechanisms on microalloyed steels. Evolution with temperature of some critical parameters. Scr Mater 50:307–312
11. Fadel A, Glišić D, Radović N, Drobnjak DJ (2012) Influence of Cr, Mn and Mo addition on structure and properties of V microalloyed medium carbon steels. J Mater Sci Technol 28:1053–1058
12. Fadel A, Glišić D, Radović N, Drobnjak DJ (2013) Intragranular ferrite morphologies in medium carbon vanadium-microalloyed steel. J Min Metall Sect B Metall 49:237–244

13. Fairchild DP, Howden DG, Clark WAT (2000) The mechanism of brittle fracture in a microalloyed steel, part I: inclusion-induced cleavage. Metall Mater Trans A 31A:641–652
14. Garcia-Mateo C, Capdevila C, Caballero FG, De Andrés CG (2008) Influence of V precipitates on acicular ferrite transformation part 1: the role of nitrogen. ISIJ Int 48:1270–1275
15. Ghosh A, Ray A, Chakrabarti D, Davis CL (2013) Cleavage initiation in steel: competition between large grains and large particles. Mater Sci Eng A 561:126–135
16. Glišić D, Radović N, Koprivica A, Fadel A, Drobnjak DJ (2010) Influence of reheating temperature and vanadium content on transformation behavior and mechanical properties of medium carbon forging steels. ISIJ Int 50:601–606
17. Glišić D, Fadel A, Radović N, Drobnjak DJ, Zrilić M (2013) Deformation behavior of two continuously cooled vanadium microalloyed steels at liquid nitrogen temperature. Hem Ind 67:981–988
18. Griffiths JR, Owen DR (1971) An elastic–plastic stress analysis for a notched bar in plane strain bending. J Mech Phys Solids 19:419–431
19. Gutiérrez I, Diáz-Fuentes M (2003) Analysis of different acicular ferrite microstructures generated in a medium-carbon molybdenum steel. Mater Sci Eng A 363:316–324
20. Ishikawa F, Takahashi T (1995) The formation of intragranular ferrite plates in medium-carbon steels for hot-forging and its effect on the toughness. ISIJ Int 35:28–33
21. Lewandowski JJ, Thompson AW (1987) Micromechanisms of cleavage fracture in fully pearlitic microstructures. Acta Metall 35:1453–1462
22. Linaza MA, Romero JL, Rodriguez-Ibabe JM, Urcola JJ (1993) Improvement of fracture toughness of forging steels microalloyed with titanium by accelerated cooling after hot working. Scr Metall Mater 29:1217–1222
23. Linaza MA, Romero JL, Rodriguez-Ibabe JM, Urcola JJ (1995) Cleavage fracture of microalloyed forging steels. Scr Metall Mater 32:395–400
24. Linaza MA, Romero JL, San Martín I, Rodriguez-Ibabe JM, Urcola JJ (1996) Improvement of toughness by stopping brittle process nucleated in ceramic particles through thermomechanically optimized microstructures in engineering steels. In: Van Tyne CJ, Krauss G, Matlock DK (eds) Microalloyed bar and forging steels. TMS, Golden, p 311
25. Linaza MA, Rodriguez-Ibabe JM, Urcola JJ (1997) Determination of the energetic parameters controlling cleavage fracture initiation in steels. Fatigue Fract Eng Mater Struct 20:619–632
26. Rancel L, Gómez M, Medina SF, Gutierrez I (2011) Measurement of bainite packet size and its influence on cleavage fracture in a medium carbon bainitic steel. Mater Sci Eng A 530:21–27
27. Rodriguez-Ibabe JM (1998) The role of microstructure in toughness behaviour of microalloyed steels. Mater Sci Forum 284–286:51–62
28. Smith E (1968) Cleavage fracture in mild steel. Int J Fract Mech 4:131–145

Experimental Determination of Mixed-Mode Fracture Toughness for Rigid Polyurethane Foams

E. Linul and L. Marsavina

Abstract Cellular materials represent a new class of materials and main parameters that characterize the cellular structure are relative density, cells shapes (open or closed cells), wall thickness and cell diameter/length. Polyurethane foams crush in compression and have a brittle fracture in tension, so their failure could be evaluated based on Linear Elastic Fracture Mechanics. Fracture toughness in mixed mode loading is of particular interest because foam cracking weakens the structure's capacity for carrying loads. The mixed mode fracture of three closed-cell rigid PUR foams with densities: 100, 145 and 300 kg/m^3 were experimentally investigated. Fracture tests were performed with a loading speed of 2 mm/min at room temperature, using both Asymmetric Semi-Circular Bend (ASCB) specimens and Single Edge Cracked (SEC) specimen and a mixed mode loading device. In this respect a numerical determination of Stress Intensity Factor (SIF) solutions for ASCB specimen were performed using Abaqus software. The advantages of these specimens are the simple geometry and the ability to produce full range of mixed modes, from pure mode I to pure mode II, only by changing the support span or loading direction. Fracture criteria based on the cellular topology and tensile strength of the solid material is assessed. It was found that the density of foams is the most important parameter influencing the fracture toughness. The crack propagation angles and the crack path were also determined experimentally and numerically. The foams cells morphology and pore distribution were studied before testing through scanning electron microscopy.

E. Linul (✉) · L. Marsavina
Department of Mechanics and Strength of Materials,
Politehnica University of Timisoara, 1 Mihai Viteazu Avenue,
300 222 Timisoara, Romania
e-mail: emanoil.linul@upt.ro

G. Pluvinage and L. Milovic (eds.), *Fracture at all Scales*,
Lecture Notes in Mechanical Engineering, DOI 10.1007/978-3-319-32634-4_12

1 Introduction

Cellular materials, such as rigid PUR foams are made up of an interconnected network of solid struts or plates which form the edges and faces of cells [10, 14, 33]. The main mechanical properties of rigid polyurethane (PUR) foams are influenced: by the properties of solid material of which the foam is made (polymers, metals, ceramics); by the typical topology (connectivity) and shape of the cell edges and faces (open cells, closed cells, open and closed cells) and by the most important feature: the relative density ρ^*/ρ_s (cell edge length and cell wall thickness) [26]. The mechanical strength of PUR foams is remarkable because high compressive and shear strengths allow low-density insulating cores to be faced with relatively thin steel or aluminium, providing relative good stiffness and strength. This unique combination of properties (lightweight, high porosity, high insulation and good energy absorption capacity) allows PUR foams to be used in many applications [19, 28]. With its excellent strength-to-weight ratio, insulation properties, durability and versatility, polyurethane are frequently used in building and construction applications (walls and roofs, entry doors and garage doors, floors) and appliances (refrigerator and freezer thermal insulation systems). In addition, PUR foam insulates boats from noise and extreme temperatures, provides abrasion and tear resistance, and increases load-bearing capacity all while adding minimal weight. Polyurethane foams also enables manufacturers to provide drivers and passengers significantly more automobile "mileage" by reducing weight and increasing fuel economy, comfort, corrosion resistance, insulation and sound absorption. Foam materials crush in compression [17], but show a brittle fracture in tension [20, 35]. Sandwich structures [5, 15] with foam cores are usually loaded in bending and crack in the foam core can initiate in mode I, mode II or mixed mode (see Fig. 1).

The knowledge of the fracture properties of sandwich foam core becomes an important requirement for the design of such composite structures. Up to now most results are related to fracture toughness in mode I [6, 8, 13, 16, 34, 29] and only several theoretical and experimental methods have been suggested by researchers for exploring mixed mode (MM) brittle fracture of rigid foams [1, 18, 25]. Hallsträm and Grenestedt [11] investigated MM fracture of cracks and wedge shaped notches in expanded polyvinyl chloride (PVC) foams. Different types of

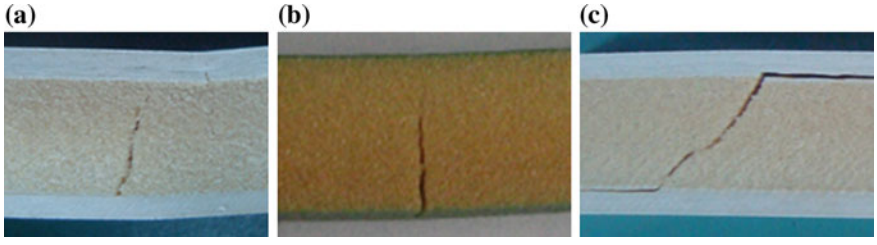

Fig. 1 Shear failure of sandwich foam core: core shear (**a**), core shear after face tensile failure (**b**), core shear after face-core debonding (**c**)

specimens made of Divinycell H100 were investigated and the non singular T-stress was considered in formulation of fracture criteria. Three different densities of PVC foams were investigated by Noury et al. [27] using a compact tension (CT) specimen with Arcan fixtures to produce MM conditions. A correlation between static and dynamic fracture toughness of PUR foams were proposed in Marsavina et al. [21]. The authors have found that for all foam densities, the dynamic fracture toughness values are higher than the static ones. Some refinements on fracture toughness of PUR foams were investigated by Marsavina et al. [22] together with a study on size effect, loading speed and loading directions. Also, they proposed some correlations for density, cell orientation and MM loading. The ASCB specimens were adopted by Marsavina et al. [23] to determine the fracture toughness for three different densities of PUR foams under mixed-mode loading. Recently, the shear elastic (shear modulus) and mechanical (shear strength) properties of polyurethane foams were investigated in Marsavina et al. [24] on three different types of specimens. The authors propose a micromechanical model to estimate fracture toughness based on the tensile strength of the solid material and the topology of the cellular structure.

Present study assessed the fracture of rigid PUR foam materials under MM loading (from pure mode I to pure mode II), using both Asymmetric Semi-Circular Bend (ASCB) specimens and Single Edge Crack (SEC) specimens and relates the fracture criteria based on the cellular topology and tensile strength of the solid material. A numerical determination of stress intensity factor (SIFs) solutions was performed. Finally, the crack propagation angles and the crack path were also determined experimentally and numerically.

2 Experimental Procedure

The experimental procedure for determining the fracture properties of investigated cellular materials under MM loading includes: a presentation of used materials and methods; a statistical analysis of pore distribution; followed by a presentation of experimental program according to current standards.

2.1 Materials and Methods

Experimental investigations were carried out on three different types of closed-cell rigid PUR foams, manufactured by NECUMER GmbH, Germany. The densities of these foams are 100 (Necuron 100), 145 (Necuron 160) and 300 kg/m^3 (Necuron 301). The geometrical parameters and loading conditions of used specimens are presented in Fig. 2.

The ASCB specimen (Fig. 2a) was used to perform mode I, mode II and MM fracture toughness tests [4]. This ASCB specimen with radius R, which contains an

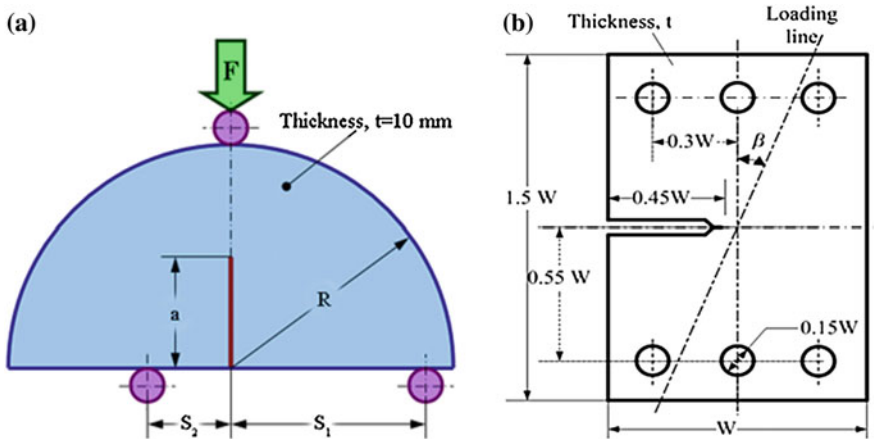

Fig. 2 Geometrical parameters of specimens used for fracture toughness and MM loading tests: **a** ASCB specimen; **b** SEC specimen

edge crack of length a oriented normal to the specimen edge, loaded with a Three Point Bend (3 PB) fixture, was proved to give a wide range of mixed modes (MMs) from pure mode I ($S_1 = S_2$) to pure mode II ($S_1 \neq S_2$), only by changing the position of one support. The considered geometry of the specimen has: R = 40 mm, a = 20 mm, t = 10 mm, S_1 = 30 mm for symmetric loading and mode I fracture toughness determination, S_2 = 2.66 mm for mode II fracture toughness determination, respectively S_2 = 4, 6, 8 and 12 mm for different MMs.

Also, the SEC specimen (Fig. 2b) with Arcan grips can produce from pure mode I to pure mode II only by changing the loading angle, β [24]. The dimensions of the SEC specimens were: width, W = 75 mm; thickness, t = 8 mm; crack length, a = 33.75 mm and the loading angle was β = 0° for pure mode I of loading, β = 90° for pure mode II of loading, respectively β = 30°, 45° and 60° for different MMs.

The main mechanical properties of the investigated foams are presented in Table 1 [18, 36].

Table 1 Main properties of the investigated PUR foams

Mechanical property (MPa)	Density (kg/m^3)		
	100	145	300
Young's modulus	30.18	66.89	281.39
Compressive modulus	10.38	62.95	208.22
Flexural modulus	25.73	36.83	164.17
Tensile strength	1.16	1.87	3.86
Compressive yield strength	0.75	2.09	4.95
Flexural strength	1.81	2.54	7.49

2.2 Micromechanical Analysis

The microstructures of the investigated rigid PUR foams at 500X magnification were obtained through scanning electron microscopy (SEM) using QUANTA™ FEG 250 and are shown in Fig. 3. Based on the microstructure analysis the cell length and the cell wall thickness were determined using SigmaScanPro software. The results of the statistical analysis of the foams microstructure show a closed-cell configuration with approximately uniform distribution of pores with a spherical shape and are shown also in Fig. 3. For pore concentration investigation we used a reference surface with the area of 1.9072 mm^2 (1.28 mm × 1.49 mm) at a magnitude of 200X. In order to obtain a better correlation of results were used the same geometrical parameters and magnitude for all densities.

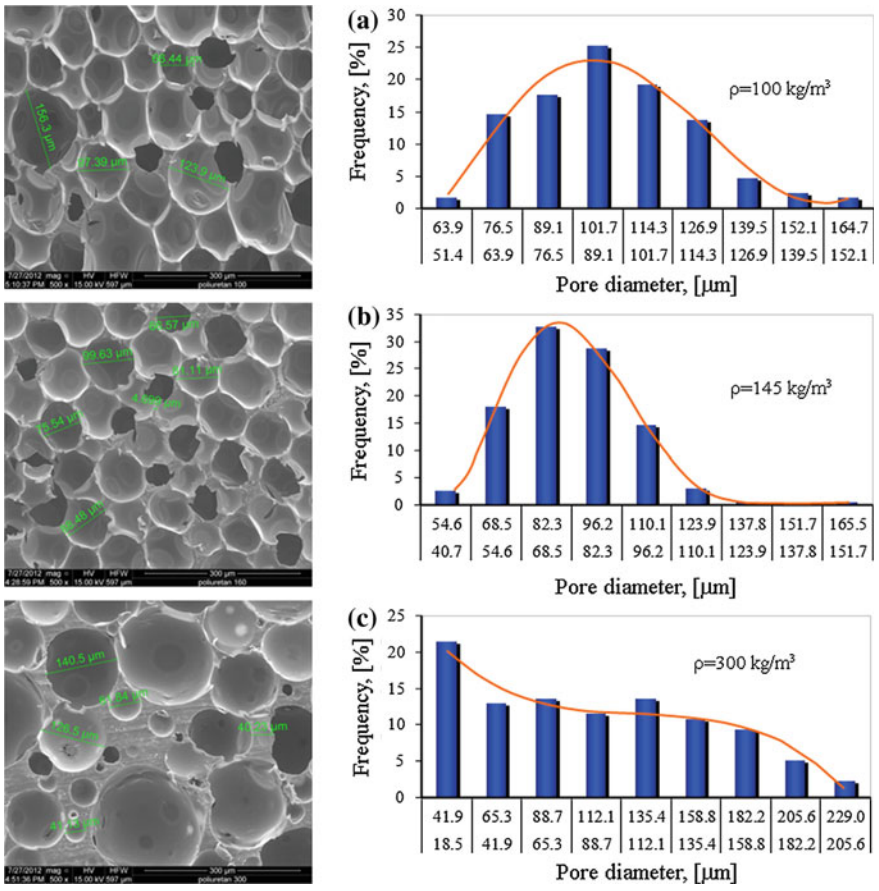

Fig. 3 SEM microstructures and pore distribution for investigated PUR foams

Table 2 Statistical analysis of the foam microstructure

Cellular structure property	Density (kg/m^3)		
	100	145	300
Cell length in plane (μm)	104.5 ± 9.4	83.8 ± 9.6	68.5 ± 33.9
Cell length out of plane (μm)	120.2 ± 14.5	88.1 ± 11.2	67.8 ± 32.1
Cell wall thickness (μm)	2.9–5.8	5.1–13.1	3.8–21.8
Density (kg/m^3)	100.35 ± 0.25	145.53 ± 0.22	300.28 ± 1.38

Statistical analysis of the microstructure provide the mean values with standard deviation of cell size and cell thickness of used foams on the rise direction (named "in plane") and flow direction (named "out of plane"), see Table 2.

The density of the foams was determined according with ASTM D [2], using cubic specimens of 15 × 15 × 15 mm, an electronic balance Sartorius LA230S for weighting and a digital caliper Mytotoyo Digimatic for dimension measurement. The determined mean values of density are also presented in Table 2 and are in agreement with the manufacturer data.

2.3 Experimental Setup

All experimental tests were performed on a 5 kN Zwick/Roell 005 testing machine at room temperature in displacement control, with a loading speed of 2 mm/min. At least four valid tests were carried on for each set of test conditions according with ASTM D [3]. The MM conditions were produced only by changing the position of one support (for ASCB) and by changing the loading angle β (for SEC). Considering this aspect the MM loading device is shown in Fig. 4 only for SEC specimens.

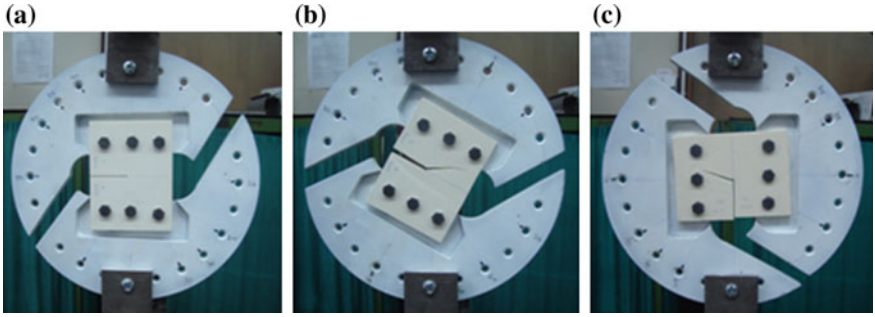

Fig. 4 SEC cracked foam specimens in loading grips: **a** mode I, **b** mixed mode, **c** mode II

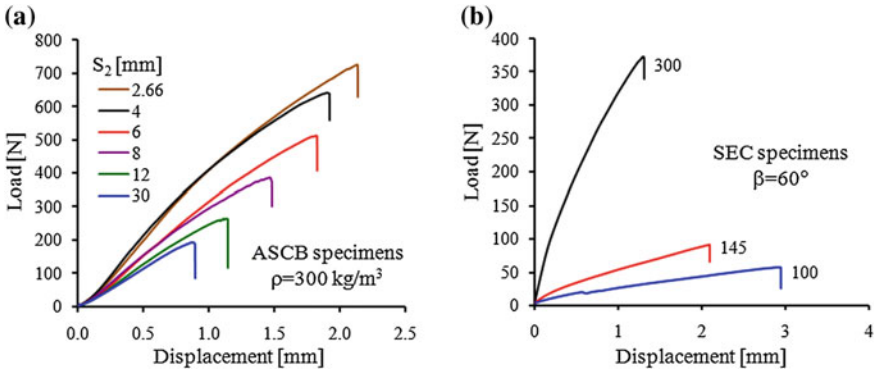

Fig. 5 Mixed-mode load-displacement curves for ASCB (**a**) and SEC (**b**) specimens

Typical load-displacement curves are shown in Fig. 5: (a) the effect of applied MM on ASCB specimens for the foam with 300 kg/m^3 density, and (b) the influence of density on SEC specimens loaded in MM ($\beta = 60°$).

For all specimens a linear diagram was obtained with an abrupt drop of load to zero after reaching the maximum load. Brittle fracture was observed and the linear-elastic behavior was confirmed during the tests when no cushioning and plastic deformations remain after tests. Due to brittle behavior the maximum load from load-displacement curves was used in the calculation of fracture toughness.

3 Fracture Toughness/Crack Path Investigation

3.1 Numerical Solutions for SIFs

Figure 6 shows a typical mesh pattern generated for simulating the ASCB and SEC specimens (quadratic elements (CPS8) were used). The loading conditions were considered: R = 40 mm, t = 10 mm, P = 100 N and crack length of 20 mm. S_1 was set at a fixed value of 30 mm and S_2 varied from zero to 30 mm to obtain a wide range of MMs. Using a polynomial interpolation the pure mode II exact position of support S_2 was determined at distance S_2 = 2.66 mm from the symmetry line of the semi-circle.

The elastic material properties of PUR foam as E = 40 MPa and $\nu = 0.284$ were also considered in the FE model. A J-integral based method built in Abaqus was used for obtaining the stress intensity factors directly from software. For the ASCB specimen the stress intensity factors K_I and K_{II} are functions of the crack length a, the radius R and the locations of loading supports (S_1 and S_2) [4]. The stress intensity factors K_I and K_{II} can be written as:

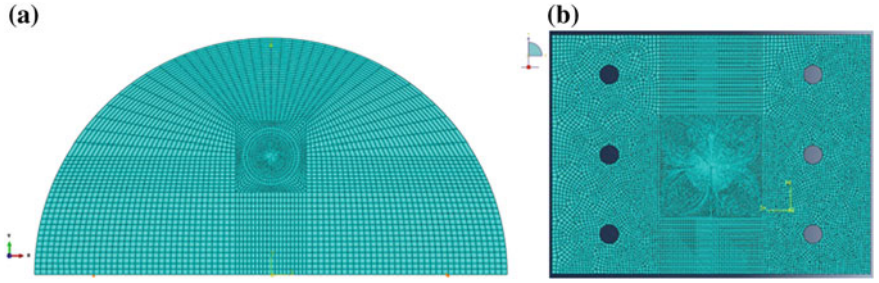

Fig. 6 Typical mesh pattern generated for simulating the ASCB (**a**) and SEC (**b**) specimens

$$K_I = \frac{F_{max}}{2Rt}\sqrt{\pi a}Y_I\left(\frac{a}{R};\frac{S_1}{R};\frac{S_2}{R}\right) \text{ and } K_{II} = \frac{F_{max}}{2Rt}\sqrt{\pi a}Y_{II}\left(\frac{a}{R};\frac{S_1}{R};\frac{S_2}{R}\right) \quad (1)$$

where F_{max} represents the maximum load from the load-displacement recordings, Y_I and Y_{II} are the geometry factors corresponding to mode I and mode II. For the case of $a/R = 0.5$ and $S_1/R = 0.75$, the geometry factors Y_I and Y_{II} were determined through a linear elastic finite element analysis using ABAQUS. Figure 7 shows the von Mises stress contour plot for different mode mixities: (a) pure mode I ($K_{II} = 0$); (b) pure mode II ($K_I = 0$); (c) MM loading with $K_I = K_{II}$.

$$\begin{aligned} Y_{II} &= 6.24\left(\frac{S_2}{R}\right)^3 - 15.07\left(\frac{S_2}{R}\right)^2 + 17.23\left(\frac{S_2}{R}\right) - 1.06 \\ Y_{II} &= 1.9\left(\frac{S_2}{R}\right)^5 - 7.3\left(\frac{S_2}{R}\right)^4 + 5.04\left(\frac{S_2}{R}\right)^3 + 2.8\left(\frac{S_2}{R}\right)^2 - 5.06\left(\frac{S_2}{R}\right) + 1.98 \end{aligned} \quad (2)$$

It can be easily seen that in pure mode I and pure mode II loading on ASCB specimens, the stress contour is symmetric relative to the crack plane, while in MM conditions, the contour plot is asymmetric with respect to the crack plane.

Stress Intensity Factors (SIFs) solutions for SEC specimens were obtained according with Richard [30]:

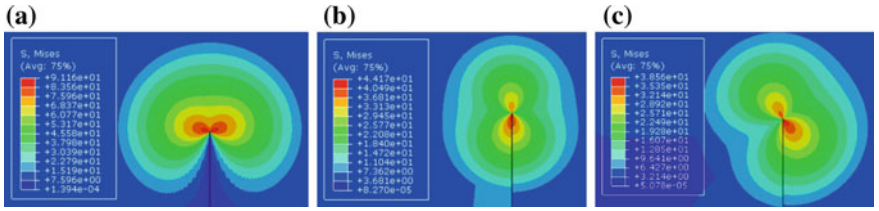

Fig. 7 The von Mises stress contours plot in front of the crack tip

Table 3 Fracture toughness results for investigated rigid PUR foams

Specimens	Fracture toughness (MPa·m$^{0.5}$)	Necuron		
		100	160	301
ASCB	K_{IC}	0.087 ± 0.003	0.131 ± 0.003	0.372 ± 0.014
	K_{IIC}	0.050 ± 0.002	0.079 ± 0.004	0.374 ± 0.013
SEC	K_{IC}	0.132 ± 0.003	0.140 ± 0.003	0.421 ± 0.014
	K_{IIC}	0.069 ± 0.002	0.095 ± 0.004	0.319 ± 0.013

$$K_I = \frac{F_{max}}{Wt}\sqrt{\pi a} f_I\left(\beta;\frac{a}{W}\right) \text{ and } K_{II} = \frac{F_{max}}{Wt}\sqrt{\pi a} f_{II}\left(\beta;\frac{a}{W}\right) \tag{3}$$

where non-dimensional stress intensity factors (f_I, f_{II}) are obtained with:

$$f_I = \sqrt{\frac{0.26 + 2.65[a/(W-a)]}{1 + 0.55[a/(W-a)] - 0.88[a/(W-a)]^2}}$$
$$f_{II} = \sqrt{\frac{-0.23 + 1.40[a/(W-a)]}{1 - 0.67[a/(W-a)] + 2.08[a/(W-a)]^2}} \tag{4}$$

The obtained values of mode I and mode II fracture toughness are presented in Table 3 for both ASCB and SEC loading configuration together with standard deviation. It could be observed that higher values of fracture toughness K_{IC} and K_{IIC} were obtained on SEC specimens than those obtained on ASCB specimens.

3.2 *Fracture Toughness and Crack Path on ASCB Specimens*

Figure 8 presents the mean values of the ratio between K_{II}/K_{IC} versus K_I/K_{IC}, together with the fracture curves predicted by the four considered fracture criteria:

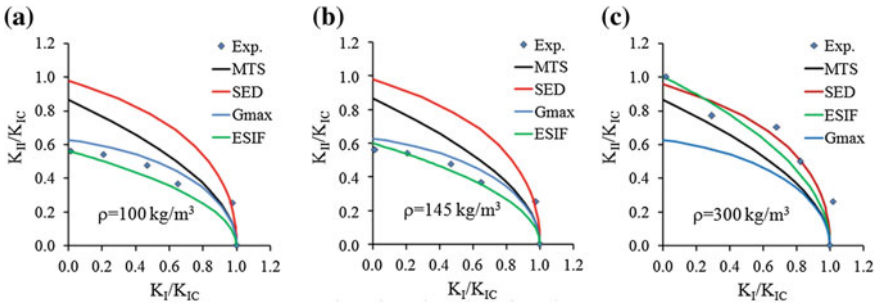

Fig. 8 MM fracture toughness results of PUR foams together with theoretical fracture criteria

(i) Maximum Circumferential Tensile Stress (MTS) of Erdogan and Sih [9], (ii) Minimum Strain Energy Density (SED) of Sih [32], (iii) Maximum Energy Release Rate Criterion (Gmax) of Hussain et al. [12] and (iv) Equivalent Stress Intensity Factor (ESIF) of Richard [30] and Richard et al. [31].

ESIF appears to predict better the MM fracture of polyurethane foams, this being probably due to the fact that takes into account the ratio between mode I and mode II fracture toughness K_{IC}/K_{IIC}. However, for the low density foams the Gmax criterion can be also considered, while for high density (300 kg/m^3 density) the SED criterion provides a good prediction of fracture.

Figure 9 presents the variation of fracture toughness values with relative density for ASCB specimens loaded in mode I and mode II. Based on the experimental data, a polynomial correlation is proposed which could be useful for estimation of fracture toughness if relative density values are available (in the considered relative density range 0.085–0.256).

$$\begin{aligned} K_{IC} &= 3.950(\rho^*/\rho_s)^2 + 0.317(\rho^*/\rho_s) + 0.031 \\ K_{IIC} &= 38.464(\rho^*/\rho_s)^2 - 0.992(\rho^*/\rho_s) + 0.072 \end{aligned} \tag{5}$$

with a coefficient of determination $R^2 = 1$.

The correlations given by Eqs. (5) are very important in practical applications because the 3 PB tests made on ASCB specimens are carried difficult than SENB ones. In this respect, through Eqs. (5) can be estimated the K_{IC} and K_{IIC} values according to the relative density which is obtained relatively easily. Also, from Fig. 9 and Table 3 it can be easily seen that on ASCB specimens the mode II fracture toughness is lower than the mode I fracture toughness for low density foams (100 and 145 kg/m^3) and almost equal for 300 kg/m^3 density. Also, it could

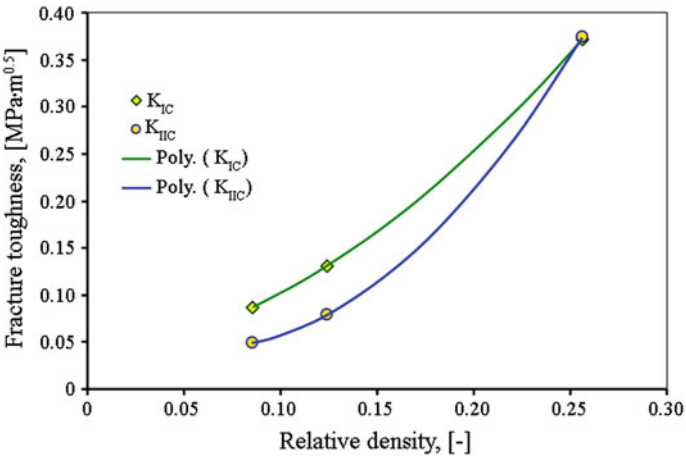

Fig. 9 Mode I and mode II fracture toughness variation with relative density

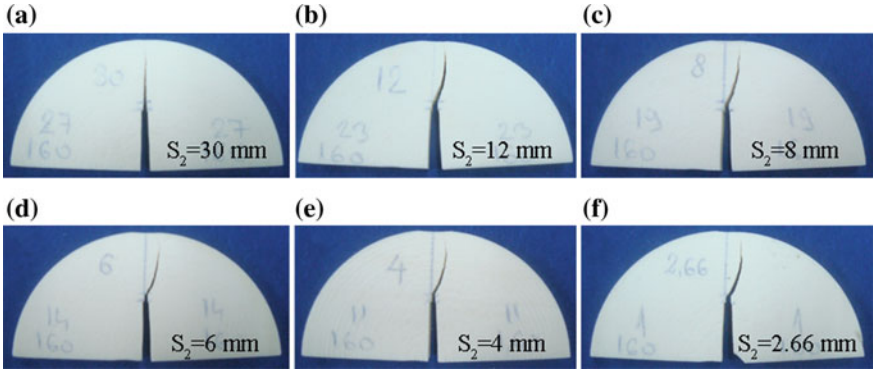

Fig. 10 Crack paths for different positions of S2 support

be observed that both mode I and mode II fracture toughness increases with increasing of density.

The obtained crack paths for six different support position S_2 [mode I (a), predominantly mode I (b, c), predominantly mode II (d, e) and mode II (f)] are shown in Fig. 10. Excepting mode I case, when the crack propagates like a straight line, all other cases show curvilinear crack paths.

Figure 11 presents the experimental (Fig. 11a) and FEA (Fig. 11b) crack path, respectively a comparison (Fig. 11c) between experimental and FEA crack path for support position S_2 = 8 mm. In this case the investigated foam shows 145 kg/m^3 density and a good correlation was obtained. In this respect the experimental crack path were measured with SigmaScanPro, while FEA crack path were obtained with Franc 2D software.

The mean values of the experimental crack initiation angle θ_C measured on the specimens and the maximum loads values obtained from experimental tests as a function of support position S_2 are listed in Table 4.

As it can be observed from Table 4 the crack initiation angle θ_C decreases with increasing of S_2 support position from a value of 68.13° for pure mode II

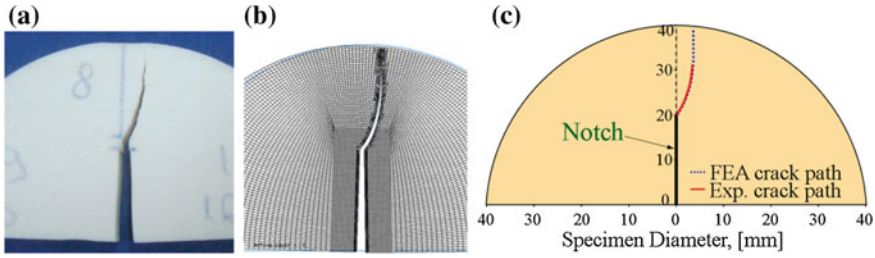

Fig. 11 Crack paths for support positions S_2 = 8 mm: experimental (**a**), FEA (**b**), experimental-FEA comparison (**c**)

Table 4 Maximum load and crack propagation angle results depending on support position

Support position (mm)		Crack initiation angle, θc (°)			Maximum load, F_{max} (N)		
S_1	S_2	100	145	300	100	145	300
30	2.66	56.47	57.07	68.13	103.00	154.00	712.33
30	4	52.76	44.58	50.29	101	151.25	662.00
30	6	46.48	41.34	43.89	98.20	149.33	645.00
30	8	39.99	38.54	35.12	95.6	145.00	535.50
30	12	30.15	27.29	26.91	88.55	133.50	397.25
30	30	0	0	0	44.53	67.80	190.00

(S_1 = 30 mm and S_2 = 2.66 mm) to a value of 0° for pure mode I (S_1 = S_2 = 30 mm).

3.3 *Fracture Toughness and Crack Path on SEC Specimens*

Figure 12 presents the mean values of the ratio between K_{II}/K_{IC} versus K_I/K_{IC}, together with the fracture curves predicted by the considered criteria (MTS, SED, Gmax and ESIF).

As it can be observed in Fig. 12 both ESIF and Gmax criteria appears to predict better the MM fracture of rigid PUR foams. The predictions based on classical fracture criteria (MTS and SED) for MM are moderate for this class of cellular materials [22]. Also, the mode I fracture toughness values on SEC specimens are higher than those obtained for mode II of loading and both mode I and mode II fracture toughness increases with increasing of density.

Chen et al. [7] proposed a relationship to relate the MM fracture to the tensile strength of the solid material σ_{fs} and the dimensions of the cellular structure (cell length, l and cell thickness, h):

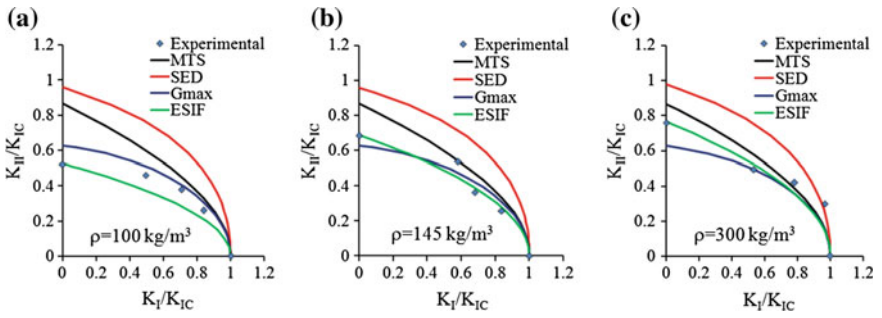

Fig. 12 MM fracture toughness results of PUR foams together with theoretical fracture criteria

$$K_{IC} = C_I \frac{\sigma_{fs} h}{\sqrt{l}} \text{ and } K_{IIC} = C_{II} \frac{\sigma_{fs} h}{\sqrt{l}} \quad (6)$$

where C_I, C_{II} are coefficients depending on the topology of the cellular structure.

Figure 13 presents the fracture toughness locus for the investigated PUR foams having three different densities.

Straight lines were considered to predict the fracture envelope, which means that MM fracture toughness can be easily determined from mode I and mode II fracture toughness and mode mixity of applied load. The fracture envelope is plotted taking into account the tensile strength of the PUR material (σ_{fs} = 130 MPa) and the cellular topology (l and h). The obtained crack paths of SEC specimens for five different loading angles (from pure mode I to pure mode II) are shown in Fig. 14.

Figure 15 presents the mean values and standard deviation of the crack propagation angle θc measured on the specimens versus the loading angle together with the theoretical criteria for three different densities. Crack propagation angle was measured on each fractured specimen. The mean values of maximum load and crack initiation angle depending on loading angle are presented in Table 5.

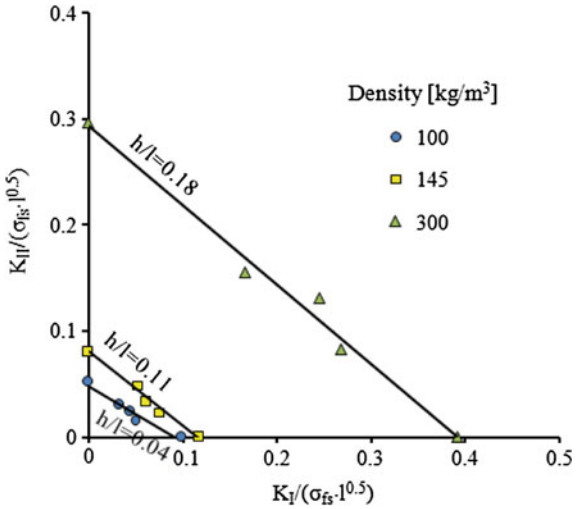

Fig. 13 SEC mixed mode fracture toughness results of PUR foams taking into account the cellular topology (l and h)

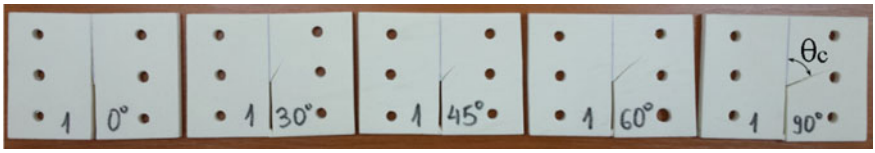

Fig. 14 Crack propagation angle measured on the specimens

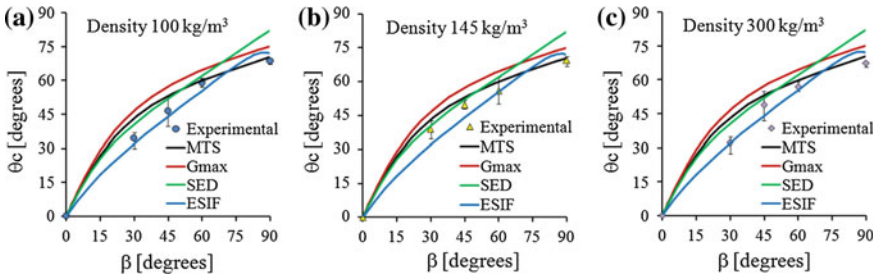

Fig. 15 Crack propagation angle versus loading angle and theoretical criteria

Table 5 Maximum load and crack propagation angle results depending on loading angle

Loading angle, β (°)	Crack initiation angle, θc (°)			Maximum load, F_{max} (N)		
	100	145	300	100	145	300
0	0	0	0	52.65	64.06	217.57
30	34.31	38.94	32.08	60.09	75.99	266.98
45	46.53	49.57	48.76	63.47	80.57	287.56
60	58.94	55.86	56.85	75.47	95.34	373.53
90	68.78	69.68	67.45	96.89	138.47	481.14

As was expected the crack initiation angle increases with increasing the loading angle. The maximum values of crack propagation angle were obtained for pure mode II having values from 67° to 70°.

4 Conclusion

This work presents the mode I, mode II and MM fracture toughness results of three different types of rigid PUR foams using ASCB and SEC specimens. The crack propagation angles and the crack path were also determined experimentally and numerically. The following conclusions can be drawn:

- The results of the statistical analysis of the foams microstructure show a closed-cell configuration with approximately uniform distribution of pores with a spherical shape.
- Pore diameters versus frequency of pores histogram provides the estimation of the mean diameter of cells and the wall thickness on two directions.
- Using a polynomial interpolation the pure mode II exact position of support S_2 was determined at distance S_2 = 2.66 mm from the symmetry line of the ASCB specimen.
- The von Mises stress contours plot in the region of the crack tip show that in pure mode I and pure mode II loading, the stress contour is symmetric relative to

the crack plane, while in MM conditions, the contour plot is asymmetric with respect to the crack plane.

- It was also determined experimentally and numerically the crack propagation angle and the crack path on the fractured specimens. A good correlation was obtained between experimental and FEA crack path.
- Based on the experimental data, a polynomial correlation is proposed which could be useful for estimation of mode I and mode II fracture toughness if relative density values of foams are available (in the considered relative density range 0.085–0.256), with a coefficient of determination $R^2 = 1$, see Eq. (5).
- Was found that the mode II fracture toughness values are lower than the mode I fracture toughness results for low density foams (100 and 145 kg/m^3) and almost equal for 300 kg/m^3 density.
- It was observed that both mode I and mode II fracture toughness is strongly dependent on foam density and increases with increasing of density.
- Experimental results show that the ESIF criterion of Richard [30] predicts better the fracture toughness under MM conditions of rigid PUR foams.
- The fracture of polyurethane foams is brittle, as no plastic deformations remains after the test and no cushioning occurs during tests, see Fig. 5.

Acknowledgments This work was partially supported by the strategic grant POSDRU/159/1.5/S/137070 (2014) of the Ministry of National Education, Romania, co-financed by the European Social Fund—Investing in People, within the Sectoral Operational Programme Human Resources Development 2007–2013.

Experimental tests were performed in the framework of the CNCS-UEFISCDI Grant PN-II-ID-PCE-2011-3-0456, Contract Number 172/2011.

References

1. Apostol DA, Constantinescu DM, Marsavina L, Linul E (2015) Mixed-mode testing for an asymmetric four-point bending configuration of polyurethane foams. Appl Mech Mater 760:239–244
2. ASTM D 1622-08 Standard test method for apparent density of rigid cellular plastics
3. ASTM D 5045-99 Standard test methods for plane-strain fracture toughness and strain energy release rate of plastic materials
4. Ayatollahi MR, Aliha MRM, Aghafi H (2011) An improved semi-circular bend specimen for investigating mixed mode brittle fracture. Eng Fract Mech 78:110–123
5. Birsan M, Sadowski T, Marsavina L, Linul E, Pietras D (2013) Mechanical behavior of sandwich composite beams made of foams and functionally graded materials. Int J Solids Struct 50:519–530
6. Burman M (1998) Fatigue crack initiation and propagation in sandwich structures, Report No. 98-29, Stockholm
7. Chen JY, Huang Y, Ortiz M (1998) Fracture analysis of cellular materials: a strain gradient model. J Mech Phys Solids 46(5):789–828
8. Danielsson M (1996) Toughened rigid foam core material for use in sandwich construction. Cell Polym 15:417–435

9. Erdogan F, Sih GC (1963) On the crack extension in plates under plane loading and transverse shear. J Basic Eng 85:519–525
10. Gibson LJ, Ashby MF (1997) Cellular solids, structure and properties, 2nd edn. Cambridge University Press, Cambridge
11. Hallstrom S, Grenestedt JL (1997) Mixed mode fracture of cracks and wedge shaped notches in expanded PVC foam. Int J Fract 88:343–358
12. Hussain MA, Pu SL, Underwood J (1974) Strain energy release rate for a crack under combined mode I and mode II. In: Paris PC, Irwin GR (eds) Fracture analysis. ASTM STP560, Philadelphia, pp 2–28
13. Kabir ME, Saha MC, Jeelani S (2006) Tensile and fracture behavior of polymer foams. Mater Sci Eng A Struct 429:225–235
14. Linul E, Marsavina L (2011) Prediction of fracture toughness for open cell polyurethane foams by finite element micromechanical analysis. Iran Polym J 20(9):736–746
15. Linul E, Marsavina L (2015) Assesment of sandwich beams with rigid polyurethane foam core using failure-mode maps. Proc Rom Acad A 16(4):522–530
16. Linul E, Marsavina L, Sadowski T, Kneć M (2012) Size Effect on fracture toughness of rigid polyurethane foams. Solid State Phenom 188:205–210
17. Linul E, Voiconi T, Marsavina L, Sadowski T (2013) Study of factors influencing the mechanical properties of polyurethane foams under dynamic compression. J Phys Conf 451:1–6
18. Linul E, Voiconi T, Marsavina L (2014) Determination of mixed mode fracture toughness of PUR foams. Struct Integr Life 14(2):87–92
19. Linul E, Serban DA, Voiconi T, Marsavina L, Sadowski T (2014) Energy-absorption and efficiency diagrams of rigid PUR foams. Key Eng Mater 601:246–249
20. Marsavina L, Linul E (2010) Fracture toughness of polyurethane foams. Experiments versus micromechanical models. In: Proceedings of ECF18, Dresden
21. Marsavina L, Linul E, Voiconi T, Sadowski T (2013) A comparison between dynamic and static fracture toughness of polyurethane foams. Polym Test 32:673–680
22. Marsavina L, Constantinescu DM, Linul E, Apostol DA, Voiconi T, Sadowski T (2014) Refinements on fracture toughness of PUR foams. Eng Fract Mech 129:54–66
23. Marsavina L, Constantinescu DM, Linul E, Voiconi T, Apostol DA, Sadowski T (2014) Evaluation of mixed mode fracture for PUR foams. Proc Mater Sci 3:1342–1352
24. Marsavina L, Constantinescu DM, Linul E, Voiconi T, Apostol DA (2015) Shear and mode II fracture of PUR foams. Eng Fail Anal 58:465–476
25. Marsavina L, Linul E, Voiconi T, Constantinescu DM, Apostol DA (2015) On the crack path under mixed mode loading on PUR foams. Fract Struct Integr 34:444–453
26. Mills NJ (2007) Polymer foams handbook: engineering and biomechanics applications and design guide. Elsevier, Amsterdam
27. Noury PM, Shenoi RA, Sinclair I (1998) On mixed-mode fracture of PVC foam. Int J Fract 92:131–151
28. Negru R, Marsavina L, Voiconi T, Linul E, Filipescu H, Belciu G (2015) Application of TCD for brittle fracture of notched PUR materials. Theor Appl Fract Mech 80:87–95
29. Poapongsakorn P, Carlsson LA (2013) Fracture toughness of closed-cell PVC foams: effects of loading configuration and cell size. Compos Struct 102:1–8
30. Richard HA (1985) Bruchvorhersagen bei uberlagreter normal- und schubbeanspruchung von rissen. VDI, Düsseldorf
31. Richard HA, Fulland M, Sander M (2005) Theoretical crack path prediction. Fatigue Fract Eng Mater Struct 28:3–12
32. Sih GC (1974) Strain-energy-density factor applied to mixed mode crack problems. Int J Fract 10:305–321

33. Şerban D, Linul E, Voiconi T, Marsavina L, Modler N (2015) Numerical evaluation of two-dimensional micromechanical structures of anisotropic cellular materials: case study for polyurethane rigid foams. Iran Polym J 24:515–529
34. Viana GM, Carlsson LA (2002) Mechanical properties and fracture characterization of cross-linked PVC foams. J Sandw Struct Mater 4:91–113
35. Voiconi T, Negru R, Linul E, Marsavina L, Filipescu H (2014) The notch effect on fracture of polyurethane materials. Fract Struct Integr 30:101–108
36. Voiconi T, Linul E, Marsavina L, Sadowski T, Knec M (2014) Determination of flexural properties of rigid PUR foams using digital image correlation. Solid State Phenom 216:116–121

Fatigue Damage Assessment of Bolted Joint Under Different Preload Forces and Variable Amplitude Eccentric Forces for High Reliability

Stipica Novoselac, Dražan Kozak, Todor Ergić and Darko Damjanović

Abstract Fatigue damage assessments of M10 bolted joint, made of 42CrMo4 heat treatable steel and strength class 10.9, were carried out for different preload forces and variable amplitude eccentric forces for high reliability. Assessments were done with preload forces of 50, 70 and 90 % of force at bolt yield point and without preload force. The nominal approaches from Eurocode standard and VDI 2230 guidelines are mostly used for fatigue assessment. These nominal approaches cannot consider and describe in detail the local stress state at the thread root, which on bolt M10 have a radius of 217 μm. Threaded joints have several peculiarities that complicate the fatigue damage assessments. Range of dispersion was used to describe material cyclic scatter band with Gaussian normal distribution in logarithmic scales. Range of dispersion for notched structure of 42CrMo4 steel was taken from measurements. In order to take multiaxial stress field in thread root with high notch effect, multiaxial fatigue stress criterion based on a critical plane theory was applied for fatigue damage assessment. Critical plane approach is used for estimation of the fatigue damage and fatigue fracture plane position. Decrease of fatigue strength beyond the *S-N* curve knee point at 2×10^6 cycles was considered for the damage calculation. The main difficulties encountered in threaded joint fatigue damage assessment are due to the uncertainties and therefore, statistics and probability were applied. Assessments were carried out for 50, 97.5, 99, 99.9, 99.99, 99.999, 99.9999, 99.99999 and 99.999999 % survival probability.

Keywords Fatigue damage · Threaded joints · Survival probability

S. Novoselac (✉) · D. Kozak · T. Ergić · D. Damjanović
Mechanical Engineering Faculty in Slavonski Brod,
Josip Juraj Strossmayer University of Osijek, Osijek, Croatia
e-mail: stipica.novoselac@gmail.com

G. Pluvinage and L. Milovic (eds.), *Fracture at all Scales*,
Lecture Notes in Mechanical Engineering, DOI 10.1007/978-3-319-32634-4_13

1 Introduction

The high strength bolted joints are often used in a variety of industry. However, bolted joints can be damaged due to the fatigue or hydrogen embrittlement (HE). Fatigue assessment of bolted joints are in fatigue problem areas and requires research [1, 2]. The problem of determination of threaded joints fatigue strength and damage has been investigated for many years. Fatigue limit affected by the stress gradients, size effect and surface quality for high reliability in industry are also in the problem areas. Offshore and subsea applications, where bolted joints are the critical points, can be found on wellheads, xmas trees, drilling risers, structural connections, flanges, and similar [3–5]. Drill pipe threaded connections are susceptible to fatigue damage because of high stress concentration due to the geometry and high mean stress induced by preload [4]. Fatigue life prediction using the Dang Van criterion for threaded joints was proposed on a drill string joint used in the oil and gas industry [6]. The drill string is a threaded assembly of tubes with a length of several kilometers, diameter of ≈10–30 cm, and the roots radius of some millimeters [7]. For the oil and gas industry, Hill [7] reported that 65 % of the drill string failures are related to fatigue problems. Fatigue of this problem is relevant [8, 9]. Therefore, high integrity of bolted joints are required. Although some recent works have investigated the fatigue of notched specimens [10–12], the complete problem of the fatigue assessment procedure has not yet been solved. A similar work has also been presented in [13] with bolt fatigue lifetime evaluation using Dang Van criterion. Investigations of the stress-gradient effect on fatigue have been performed using the Dang Van criterion [14, 15]. Development of deep water reservoirs with higher water depths, higher pressure and higher temperature requires higher safety and reliability of structures [3]. It is well known that high strength steels are prone to HE and their resistance decreases with the strength increase. The resistance is generally expressed in terms of hardness limit above which the material is not recommended for use in the specific environment (e.g., sea water) or HE threshold stress intensity factors. Steels with yield strength below 800 MPa are generally resistant to HE [16, 17]. Design of bolted joints for offshore industry are governed by ASME Code: ASME B16.5 [18] and API Standards: API 6A: Specifications for Wellhead and Christmas Tree Equipment [19]. The Health and Safety Executive from UK stated that the main cause of structural damage for installation in the North Sea is fatigue with 25 %, whereas only 6 % damage is due to corrosion [20]. Besides structures in oil and gas industry, automotive industry also has problems with bolted joints fatigue failures [21], biomechanics with fatigue of pedicle screws used for the spinal implants [22, 23], and dental implants [24, 25].

In order to assess the fatigue life of threaded joints on the basis of the nominal stresses, nominal approaches from standards Eurocode 3 [26] and VDI 2230 guidelines [27] are mainly used for fatigue assessment. However, bolted joints have a complex geometry with blunt notches and nonlinear contact interactions. The assessment methods based on nominal stresses cannot consider and describe in detail the local stress-strain state at the thread root. When assessment is done

according to nominal approaches, without accurate thread notch dimensions, the definition of nominal stress is simple at first glance. For the bolted joint, it is average stress in bolt cross-section calculated with simple engineering expressions or by FE analysis on ideally cylindrical bolt joint, usually without nonlinear contacts. At a closer look, the problems emerge due to many details and influence factors which are not taken into account. Even normal and fine threads are not different, so by engineering judgements distinction must be done. Variations within the thread details in dimensions and tolerances for thread roots and flanks, fatigue influence factors, preload forces, and accurate stress distribution inside bolt continuum are not covered. The consequence is that this reduction in details gives rise to the scatter of the fatigue assessments results, because even a change from normal to fine threaded joint can increase stress concentrations due to the smaller thread root radius. Investigation regarding the local strain approach was published [28].

Until recently, bolting technicians did not need to have the same competence standards as welders. However, in 2013 two standards were published highlighting the requirements for bolted joints. ASME updated the 2010 PCC-1 "Guidelines for Pressure Boundary Bolted Flange Joint Assembly" with an appendix defining the requirements for training and qualification of technicians working in the field of bolted joints. The European Committee for Standardization (CEN) re-published EN1591 Part 4 "Flanges and their Joints—Part 4: Qualification of personnel competency in assembly of the bolted connections of critical service pressurized systems". Consequence of joint loosening result with fluid leakage and/or structure failure. Too low preload forces on dental implants can, for example, create micro gap formation between dental implant and abutment screw which may foster bacterial invasion of the screw joint interface [29].

Load distribution and stresses in threaded joints have been widely investigated [30–34]. All results show that load is not uniformly distributed along the threads and that the first engaged thread is subjected to highest load. As observed by Croccolo et al. [35], it is difficult to find in published investigations systematic and effective experiments concerning fatigue tests performed on screws or bolts. It is even more difficult to find investigations that take into account the tightened members [36].

Recent review by Patterson [37] evaluated the different methods for bolt fatigue life prediction. Even if the loading in the threaded joint is uniaxial, multiaxial (triaxial) stress state exists at the thread roots. Fatigue of the bolted joints requires multiaxial fatigue criterion [15]. The damage evaluation without stress triaxiality consideration results with unrealistic fracture [38].

The state-of-the-art overview shows that the majority of approaches which estimate multiaxial fatigue behaviour in high-cycle fatigue (HCF) regime is either stress or energy quantities based on the critical plane approach [15, 38–44]. Critical plane approach takes as a starting point that the fatigue damage reaches its maximum value on the plane of maximum shear stress amplitude τ_A [45–49], and it is based on the hypothesis that stage I is the most critical stage in forming fatigue cracks. Furthermore, multiaxial fatigue strength is estimated with the stress perpendicular to the critical plane. The maximum normal stress (σ_{nmax}) relative to the

plane with maximum shear stress amplitude (τ_A) is used to evaluate the detrimental effect of non-zero mean normal stress [45–49]. Therefore, according to the critical plane approach theory, fatigue damage depends on both τ_A and σ_{nmax}. Forsyth [50] defined fatigue crack growth as a two stage process, where stage I corresponds to Mode II crack growth (caused by shear component) and stage II corresponds to Mode I crack growth (induced by normal components). This justified the use of both shear and normal components in fatigue parameter definition [51]. Fatigue strength depends not only on the value of the elastic stress but also on their spatial distribution because fatigue at a point is a nonlocal phenomenon [52]. Detailed investigation of stress gradients influence on bolted joint fatigue behavior was recently published [53].

The aim of this study was the fatigue damage assessment of M10 bolted joint, made of 42CrMo4 heat treatable steel, strength class 10.9, with different preload forces and variable amplitude eccentric forces for high reliability up to survival probability of $P_S = 99.999999$ %. Range of dispersion was used to describe material cyclic scatter band with Gaussian normal distribution in logarithmic scales. This study takes into account elastic support from tightened steel members. Due to the high stress concentrations in thread roots, complex nonlinear contact interactions, complex loading combinations, and cyclic material nonlinearity, the stress gradient and critical plane approach based on stresses with multiaxial failure criterion was used for fatigue assessment. Decrease of fatigue strength beyond the *S-N* curve knee point at 2×10^6 cycles was considered for the damage calculation according to the modified Palmgren-Miner linear damage accumulation hypothesis. Assessments were carried out for 50, 97.5, 99, 99.9, 99.99, 99.999, 99.9999, 99.99999 and 99.999999 % survival probability.

2 Modeling

Very detailed FE analyses were conducted to obtain the realistic stress distributions in the thread roots. FE model consists of: bolt, nut, and two plates, as shown in Fig. 1. Mesh was created with solid hexahedral elements (Abaqus C3D8 element) with 108,332 nodes and 95,652 elements. Thread profile was defined as axi-symmetric because it has been found that helical effect does not influence the load distribution [54]. Nonlinear contacts were modeled with sliding surface contact. Contact surfaces are shown in Fig. 2a, b. Average finite element size in thread root is ≈30 μm. From the experience can be suggested that average element size in thread root shall be in interval from 10 to 15 % of the thread root radius. In total four element layers were created in depth with this size to accomplish a certain ratio. This ratio can be suggested as approximately 0.1–0.15 % of bolt diameter (or any other threaded structure, for instance like drill pipe). In this case, result is ≈0.125 mm, as shown in Fig. 2c. The coefficient of friction was set to $\mu = 0.1$. According to VDI 2230 Guidelines [27], for material combination steel–steel in dry state, $\mu = 0.1$–0.23. Furthermore, according to VDI 2230 Guidelines, in the case of

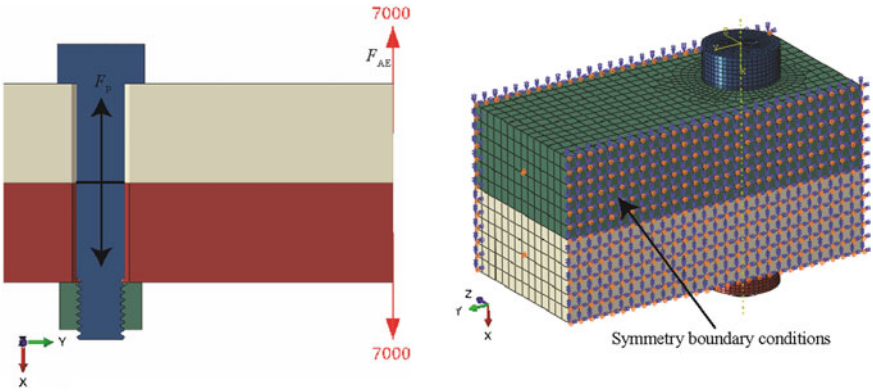

Fig. 1 FE model of the bolted joint

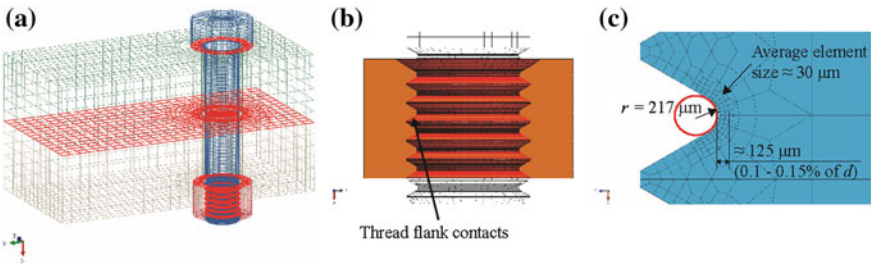

Fig. 2 **a** Contact surfaces, **b** detailed view of thread flank contacts and **c** view on mesh of thread root detail

uncertainty about friction in the thread flanks and under the bolt head and nut, the lowest possible coefficient of friction must be selected. Preload scatter will be minimized if lubricants are used on thread contact surfaces. The bolted joint consist of M10 bolt, strength class 10.9 with metric standard thread (pitch according to DIN 13-1 and -28, stress cross section and cross section at minor diameter according to DIN 13-28, and minimum yield point according to DIN EN ISO 898-1). Kinematic couplings were created in the middle of each plate for applying the eccentric forces and to hold the model. Boundary conditions were defined around the plates with symmetry constraints in XY plane and displacements in YZ direction on the kinematic couplings were prevented to establish model without rigid body motion. During the in-service life of any bolted or threaded joint, first load is due to the tightening. Bolt preload forces (F_p) were defined according to force at yield point ($F_{0.2}$) for M10 bolt, strength class 10.9, with value of $F_{0.2}$ = 55,000 N [27]. Applied preload forces were defined as 50, 70, 90, and 0 % of $F_{0.2}$, and these forces define the models as 1, 2, 3, and 4, respectively. Abaqus command, "Bolt Preload" was used for application of the force on surface in middle of the bolt shank. In this case, there is only one bolt, but when there is more bolts, it is generally

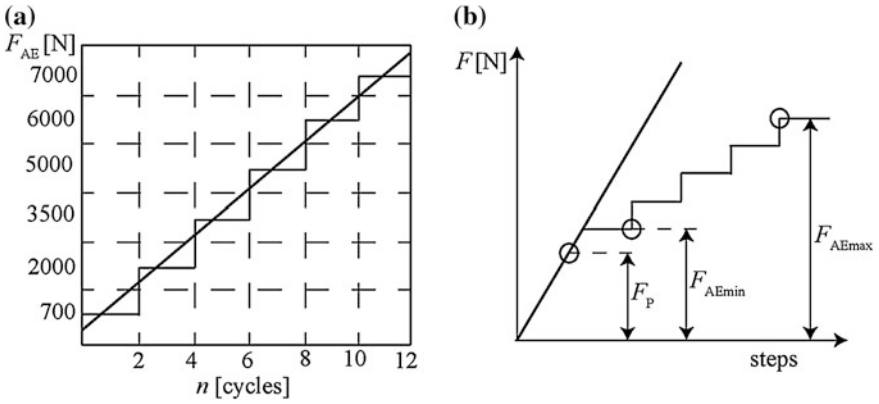

Fig. 3 **a** Loadings on bolted joint and **b** cumulative spectrum distribution of variable amplitudes

recommended to simultaneously introduce the tensioning of all bolts in-service, for instance in flange applications. In the case when only half of the bolts were tensioned simultaneously, elastic interactions between bolts occur which result with small difference of preload forces in bolts, which can be only visible with ultrasonic or strain gauges measurements of the tension in the bolts. After constant bolt preload force, further steps consist of additional eccentric forces with variable amplitudes, as shown in Fig. 3a. If only a proportion (normally 90 %) of the minimum yield point $R_{p0,2min}$ of the bolt standardized according to DIN EN ISO 898-1 or DIN EN ISO 3506-1 may be utilized for the equivalent stress $\sigma_{eqv,Pall}$ then, with the utilization factor ν equivalent stress due to the assembly preload force is:

$$\sigma_{eqv,Pall} = \nu \cdot R_{p0,2min} \tag{1}$$

where ν is utilization factor of the yield point stress (limit of full plastification of the cross section) during tightening.

Allowable assembly stress can be calculated according to the following equation:

$$\sigma_{Pall} = \frac{\nu \cdot R_{p0,2min}}{\sqrt{1 + 3\left[\frac{3}{2} \cdot \frac{d_2}{d_0}\left(\frac{P}{\pi \cdot d_2} + 1,155 \cdot \mu_{Tmin}\right)\right]^2}} \tag{2}$$

where d_2 is pitch diameter of the bolt thread, d_0 is diameter at the relevant smallest cross section of the bolt, P is pitch, and μ_{Tmin} is minimal value of thread friction coefficient.

The allowable assembly preload force (F_{Pall}) may additionally be taken as 90 % of the standardized minimum yield point ($R_{p0,2min}$) according to the standard DIN EN ISO 898-1. The values from standard have been calculated without taking into account dimensional and geometrical tolerances.

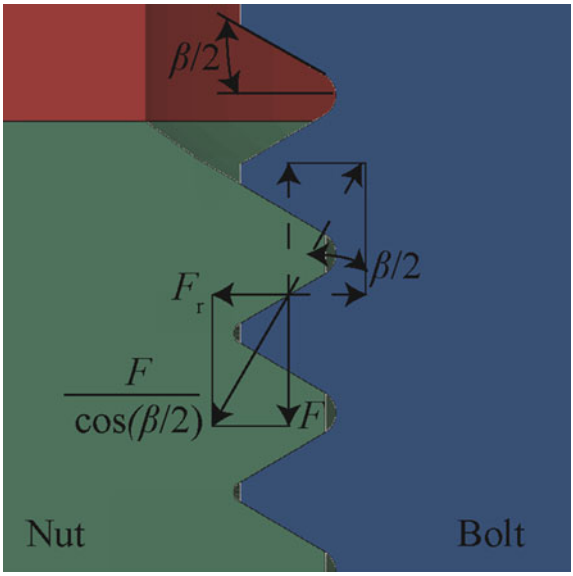

Fig. 4 Force components on thread flank

Cyclic eccentric tensile forces with variable amplitudes (F_{AE}) were defined at the 40 mm distance from bolt axis. Cumulative spectrum distribution of variable amplitudes is shown in Fig. 3b. This type of block-program investigation is Lo-Hi (Low–High) sequence [55].

Normal (F) and radial (F_r) force components on thread flank are shown in Fig. 4.

Equivalent stress in bolts are usually calculated according to the VDI 2230 with following equation:

$$\sigma_{eqv} = \sqrt{\sigma_{max}^2 + 3 \cdot (k_\tau \cdot \tau_t)^2} \tag{3}$$

where σ_{max} is maximal tensile stress, $\sigma_{max} = F_{Smax}/A_0$, where $A_0 = A_S$. A_S is the bolt stress section. τ_t is the maximal shear stress. k_τ is a reduction coefficient for shear stress during the life. Usually, $k_\tau = 0.5$ [27].

Numerical analyses were done on FEM model in Abaqus 6.12 (Simulia, Providence, RI, USA). The stress tensors with influence factors and nonlinear cyclic material properties were further calculated in the FemFat 4.8 (ECS, Steyr, Austria) software.

3 42CrMo4 Heat Treatable Steel Properties

For bolt strength grade 10.9, frequently used material is 42CrMo4 [56]. Alloy steels, mainly 42CrMo4, 40NiCrMo6, and 34CrNiMo6 remains the most common material for subsea fasteners [3].

Table 1 Monotonic and cyclic properties for 42CrMo4 steel

Property	Value
Modulus of elasticity, E [MPa]	210,000
Poisson coefficient, v [–]	0.3
Tensile strength, R_m [MPa]	1100
Yield strength, $R_{0.2}$ [MPa]	900
Cyclic coefficient of hardening, K' [MPa]	1771
Cyclic exponent of hardening, n' [–]	0.15
Elongation at fracture, A [%]	11

Material monotonic and cyclic properties are shown in Table 1. According to DIN EN 10 083-1 this material is in the class of heat treatable steel [57]. Cyclic stress–-strain hysteresis loop behaviour was defined with cyclic coefficient of hardening $K' = 1.61\ R_m$ and cyclic exponent of hardening $n' = 0.15$ [55, 58].

Smooth circular specimen diameter for basic material cyclic properties is 7.5 mm. The *S-N* curve for alternating tension/compression loading (stress ratio $R = -1$) and relative stress gradient ($\chi' = 0$) with survival probability defined at 50 % is shown in Fig. 5a. The fatigue limit for $R = -1$ have a knee-point in the *S-N* curve at 2×10^6 cycles with the slope of $k = 12$. Alternating fatigue strength under tension/compression ($R = -1$) is $\sigma_{D,tc} = 495$ MPa [57]. Due to the issues of uncertainty, in this investigation material cyclic properties uncertainties in *S-N* curve were considered and reliability was taken into account. The concept of fatigue reliability is illustrated schematically in Fig. 5a. Equation of *S-N* curve (for $R = \text{const.}$):

$$\sigma_A = \sigma_D \left(\frac{N_D}{N} \right)^{1/k} \tag{4}$$

$$k = \tan \alpha = \frac{\Delta(\log N)}{\Delta(\log \sigma_A)} = \frac{\log(N_1/N_2)}{\log(\sigma_{A1}/\sigma_{A2})} \tag{5}$$

Mean stress influence is taken into account by means of Haigh diagram, which is generated by polygonal lines. Fatigue strength is decreased for tensile mean stress and increased for compressive mean stress. Therefore, Haigh diagram is unsymmetric, as shown in Fig. 5b. Mean stress rearrangement is done according to Neuber-hyperbola with FemFat PLAST.

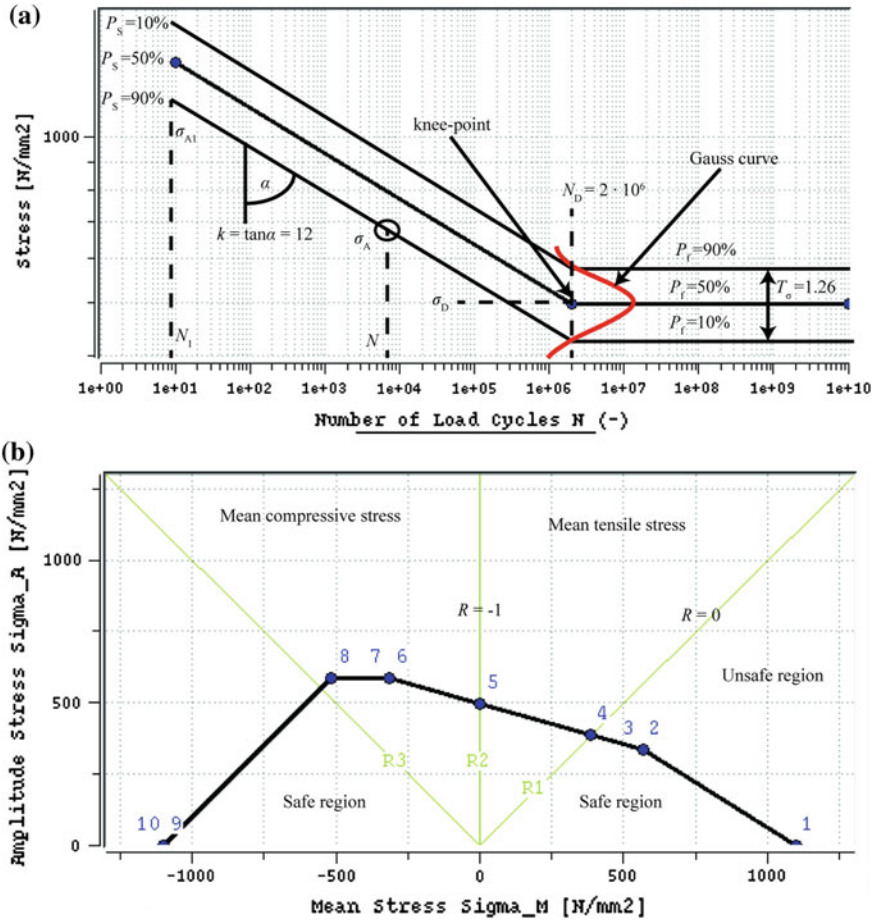

Fig. 5 42CrMo4 steel. **a** *S-N* curve and **b** Haigh diagram

4 Fatigue Damage Calculation

The calculation of local *S-N* curve and Haigh diagram starts from the known basic smooth specimen data, as was explained in previous chapter. At each node the particular local *S-N* curve and Haigh diagram is calculated from the specimen cyclic fatigue properties, influence factors, and stress conditions. The definition of the *S-N* curve model in the double logarithmic system is that the linear damage accumulation is done with the amplitude stress tensor of the particular hysteresis. Other influences like stress distribution, notch effects, diameter, mean stress, mean stress rearrangement due to local plastification, surface roughness and statistics (range of dispersion and survival probability) are taken into account at a locally modified *S-N* curve and Haigh diagram to obtain correct endurance fatigue limit at critical areas.

Transfer of the results from specimens to components are one of the main challenges for fatigue assessment [59]. The main purpose of the equivalent stress calculation algorithm is reduction of the multiaxial (triaxial) stress state in the thread roots to the equivalent uniaxial state with a criterion of multiaxial fatigue failure, suitable for a given ductile material. After that, the calculated equivalent stress history is processed in order to make assessment of the fatigue life. Loading history is analyzed in the time domain with the numerical algorithm of Rainflow cycle counting. The critical plane position is determined with damage accumulation method [58, 60–65]. Fatigue fracture plane is defined by its orthogonal vector according to following equation:

$$\vec{\eta} = \hat{l}_1\vec{i} + \hat{m}_1\vec{j} + \hat{n}_1\vec{k} \tag{6}$$

where $\vec{i}$, $\vec{j}$, and $\vec{k}$ are unit normal vectors of critical cutting plane along the axes x, y, and z, respectively. Furthermore, $\hat{l}_1$, $\hat{m}_1$, and $\hat{n}_1$ are direction cosines of the principal stresses referred to a coordinate system (x, y, z). The normal stress at every time point σ_η (t) acting on this fatigue fracture plane is given by [66, 67]:

$$\begin{aligned}\sigma_\eta(t) = {} & \hat{l}_1^2\sigma_{xx}(t) + \hat{m}_1^2\sigma_{yy}(t) + \hat{n}_1^2\sigma_{zz}(t) + 2\hat{l}_1\hat{m}_1\tau_{xy}(t) \\ & + 2\hat{l}_1\hat{n}_1\tau_{xz}(t) + 2m_1\hat{n}_1\tau_{yz}(t)\end{aligned} \tag{7}$$

For each cutting plane, which is defined by its orthogonal vector $\vec{\eta}$, Eq. (6), the orthogonal and the shear stress components are determined separately for the mean stress and the stress amplitude tensor. Therefore, the stress components normal to the cutting plane are stress amplitudes and mean stress at every time point.

Equivalent stress algorithm used for the fatigue damage was scaled normal stress in critical plane. This algorithm solves the problem of identifying closed stress cycles for complex random loads with spatial stress states and rotary normal stresses. This algorithm is recommended for ductile materials [58]. This algorithm takes into account the damaging effect of shear. Damage equivalent scaling of the normal stress in material planes is in dependence on the stress state (tension/compression, shear, hydrostatic stress state, and its combinations). A variable, $V(t_i)$ is introduced to characterize the stress state at each time step t_i. First step in stress algorithm is calculation of principal normal stress $\sigma_1 > \sigma_2 > \sigma_3$ at every time point. Furthermore, variable $V(t_i)$ represent the ratio between the minimum and maximum principal normal stress in time and is calculated according to the following equations:

$$V(t_i) = \sigma_3/\sigma_1 \quad \text{for} \quad |\sigma_1| > |\sigma_3| \tag{8}$$

$$V(t_i) = \sigma_1/\sigma_3 \quad \text{for} \quad |\sigma_3| > |\sigma_1| \tag{9}$$

Ratio V can be between −1 and 1. Certain ratios represent three different stress states:

- $V(t_i) = -1$ for dominant shear load,
- $V(t_i) = 0$ for dominant tension/compression load,
- $V(t_i) = 1$ for hydrostatic stress state.

Mohr's circle of stress states for torsion, uniaxial tension, and hydrostatic loading are shown in Fig. 6, respectively.

Moreover, the stress tensor in time is scaled as a function of $V(t_i)$. The scaling factor is calculated according to the:

$$f(t_i) = 1 + (1-k) \cdot V(t_i) \tag{10}$$

where k is a material ductility factor, which can be calculated according to the following equation:

$$k = \frac{\sigma_D}{\tau_D} \tag{11}$$

where σ_D and τ_D are alternating and shear fatigue limit, respectively. With this approach, stress is not modified for tension/compression. For dominant shear it is scaled up by the factor k, in order to model the damaging effect of shear [67]. For the hydrostatic stress state, $f(t_i)$ is linearly extrapolated. Therefore, magnitude of hydrostatic stress is scaled down which correlates with distortion energy criterion. This algorithm can be used to solve the biaxial and triaxial stress states [67]. With the critical cutting plane method, the normal stress in the cutting planes is scaled with $f(t_i)$ for each time point.

The damage accumulation method includes accumulation of fatigue damage on all critical planes. Furthermore, the plane of the maximum damage degree is selected as the most critical. Multiaxial interaction between stress amplitude tensors and mean stress tensors was solved with critical plane approach in combination with the Haigh diagram. If in the cumulative loading spectrum with variable amplitude of a bolted structure local stress values are in the elasto-plastic area of

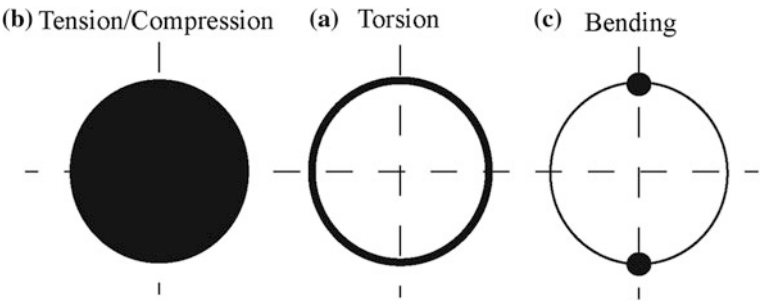

Fig. 6 Mohr's circle of stress for: **a** torsion, **b** uniaxial tension and **c** hydrostatic loading

material, than mean stress tensors are rearranged by the means of Neuber-hyperbola rule in the cycle stabilised stress-strain curve. Haigh diagram was used to define the most critical cutting plane angle and the damaging factor for each node. Cutting plane was defined at every 10°. The relative stress gradient (χ') influences the local *S-N* curve (both slope k and endurance cycle limit N_D), and fatigue strength limit σ_D. Mean stress and surface roughness influences also the local *S-N* curve, and fatigue strength σ_D, whereas influence factors like size and statistics influence only fatigue strength σ_D.

The modified Palmgren-Miner linear damage accumulation (or sometimes called Haibach) hypothesis was used for the evaluation of fatigue life. The fatigue damage accumulation is calculated from Eq. (12):

$$D = \sum_{i=1}^{n} \frac{n_i}{N_i} \tag{12}$$

where n_i is the number of applied certain stress amplitudes and N_i is the number of cycles to failure at that certain stress.

The drop of fatigue strength in the high-cycle range is considered using *S-N* curve for the damage calculation with fictitious slopes beyond the knee point of $k' = 2k - 1$ or $2k - 2$ (according to Haibach [55]) depending on material condition (wrought, cast or welded). In engineering standards the knee point of the *S-N* curve is defined as the transition to infinite life. Recent experimental results up to giga-cycles shows that there is a further decline of the *S-N* curve beyond the knee point at higher cycles. The fatigue strength decline of ≈10 % per decade was usually assumed. The *S-N* curve is generally limited to 10^6, 2×10^6, 5×10^6, 10^7 cycles or some other value depending on the standard or structure [68]. Beyond knee point, it is considered that the fatigue life is infinite. In principle, the fatigue limit is given for a particular number of cycles to failure. Fatigue limit is given by the average alternating stress σ_D and the probability of fracture is given by the standard deviation of the scatter (s). There is no knee point between 10^6 and 10^9 cycles for the Cr-Mo steel as the fatigue limit σ_D decreases by 60 MPa [68]. Various standards and regulations point out [26, 57, 69] that the fatigue limit does not exist in the case of jointed components such as press-fits or bolted joints because of fretting, high temperatures, and/or corrosion [70].

From the resulting equivalent stress history, a Rainflow cycle counting is applied to identify closed cycles in the stress-strain-path. This basically means that the resultant loading is saved in a square 64 × 64 amplitude/mean stress matrix. Rainflow counting method has been shown to be superior method compared with peak, range and range-pair method [71]. Rainflow cycle counting method was first proposed by Endo in 1971 [72]. The counting method is described in an ASTM standard [73].

The multiaxial fatigue criteria is based on the fatigue crack initiation stage and the fatigue crack growth stage is not included. The bolt thread surface roughness was defined as $R_z = 2.5$ µm. Influence of size was also taken into account in accordance with FKM-Guidelines [57] with the bolt diameter of 10 mm. It has been found that the fatigue life reduces as the bolt nominal size increases [56].

Instead of the standard deviation s common in statistics, fatigue testing and analysis usually use the range of dispersion. The range of dispersion for cyclic material properties is defined as the ratio of the bolt fatigue strength at 10 % survival probability to fatigue strength at 90 % survival probability P_S.

$$T_S = 1 : \frac{\sigma_D(P_s = 10\,\%)}{\sigma_D(P_s = 90\,\%)} \tag{13}$$

The following simple relationship exists between cycle range of dispersion T_N and T_S, where k is included as the slope of the S-N curve:

$$T_N = T_S^k \tag{14}$$

For example, a value of $T_S = 1.5$ (after Radaj) may be specified for analyzing a welded joint in structural steel.

In statistics, a Gaussian distribution is described by the mean value and the standard deviation. The statistics applied regarding distribution type is the Gaussian Log-Normal distribution for the calculation of statistics influencing variables, both for range of dispersion and survival probability. The characteristic parameters of the scatter band are the standard deviations s_σ and s_N relating to σ_A and N, respectively and alternatively, they are related to the T_S and T_N. The logarithmic standard deviation s and the T_S are related by the equation:

$$s_\sigma = \left(\frac{1}{2 \cdot 1.28}\right) \cdot \log\left(\frac{1}{T_S}\right) \tag{15}$$

$$s_N = \left(\frac{1}{2 \cdot 1.28}\right) \cdot \log\left(\frac{1}{T_N}\right) \tag{16}$$

Range of dispersion for notched structure of 42CrMo4 quenched and tempered steel was taken from measurements [74]. From measurements of 300 smooth specimens ($K_t = 1$) made of 42CrMo4 steel at $R = -1$ and $R = 0$, it was obtained that $T_S = 1.12$. However, from measurements of 372 notched specimens (with maximal $K_t = 5.2$) made of 42CrMo4 quenched and tempered steel at $R = -1$ and $R = 0$, it was obtained that $T_S = 1.26$. For 18 specimens under alternating bending with $K_t = 1.6$ and 25 specimens under alternating torsion with $K_t = 1.35$, obtained range of dispersion was again $T_S = 1.26$. From these measurements, it is obvious that stress concentration lead to higher range of dispersion. This value is additionally also recommended for steel in [67]. Therefore, range of dispersion was set as $T_S = 1.26$. It is interesting to compare range of dispersion distribution under normal stresses for stress relieved welded joints of $T_S = 1.55$ for $R = 0.4$, $T_S = 1.42$ for $R = 0$, and $T_S = 1.44$ for $R = -1$ [75]. From results published in [76] for welded joints of high-strength steels under axial and bending constant amplitude loadings, obtained range of dispersion was $T_S = 1.50$. For laser beam welded thin-sheet steels

and aluminium alloys (t = 1–2 mm), results were T_S = 1.30 and T_S = 1.36, respectively, after Eibl et al. [77, 78].

The fatigue strength of a bolted joint depend on notch effect which contains both stress concentration and strength reduction by notches. High stress gradients resulting from the stress concentrations in thread roots by bending of the bolt and thread flanks cause the material surface be supported with micro support effect, which result with higher surface fatigue strength [53]. Gradient support effect is determined with the relative stress gradient (χ'). Furthermore, support effects was evaluated with the FemFat method [58]. According to this method, the ratio of cyclic tensile/compressive strength to the bending fatigue strength can be used to calculate the support factor n:

$$n = f_{GR,af} = 1 + \frac{\left(\sigma_{A,b}/\sigma_{A,tsc}\right) - 1}{(2/b)^{v}} \cdot \chi'^{v} \tag{17}$$

where $\sigma_{A,b}$ is the material alternating stress limit for bending and $\sigma_{A,tsc}$ the material alternating stress limit for tension/compression. The material parameter v takes into consideration the nonproportional increase in the support effect with regard to the relative stress gradient. For steel, v = 0.3 [58]. Specimen thickness is b. Factor $f_{GR,af}$ is the stress gradient factor influencing the fatigue limit. The influence of the χ' on the slope $k_{C,GR}$ of the local component S-N curve is calculated with the following equations:

$$f_{GR,sf} = 1 + \frac{1.8 \cdot \chi'^{1.2}}{f_{GR,af}} \cdot \chi'^{v} \tag{18}$$

$$k_{C,GR} = \frac{(k_M - IFK2)}{f_{GR,sf}^{IFK3}} + IFK2 \tag{19}$$

where $f_{GR,sf}$ is the stress gradient influence factor affecting the slope of the local component S-N curve, $k_{C,GR}$ is the slope of the local component S-N curve as a result from the gradient influence, k_M is the slope of the material S-N curve at $R = -1$, $IFK2$ is the slope exponent of the specimen fracture S-N curve, $IFK3$ is the material class dependent exponent (for the steel, $IFK2$ = 3 and $IFK3$ = 2 [58]).

5 Results

The fatigue damage assessments are carried out for following survival probabilities P_S: 50, 97.5, 99, 99.9, 99.99, 99.999, 99.9999, 99.99999 and 99.999999 % for four numerical models. Stress distributions for model 1 are shown in Fig. 7. Detailed views on threaded region with section cut in xy plane clearly shows Max principal, Min principal, shear τ_{xy}, and Tresca stress distribution after tightening with 50 % of

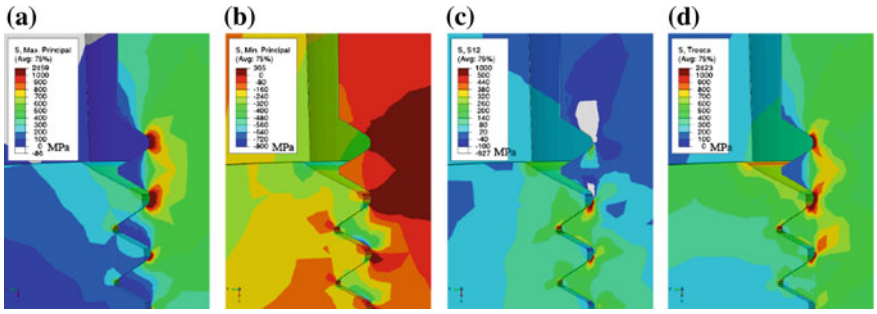

Fig. 7 Stress distribution in bolted joint under the maximal tensile eccentric force for **a** Max principal, **b** Min principal, **c** shear τ_{xy}, and **d** Tresca stress

$F_{0.2}$ and variable amplitude loadings. Stresses are shown for step with maximal eccentric tensile forces. Deformation scale in figures was set to 10.

Maximal values of all shown stresses are on the first engaged thread root. High stress values are present in the model due to the liner-elastic material definition, which lead to the usage of Neuber-hyperbola for achieving realistic elasto-plastic behaviour.

The fatigue damage distribution in the thread roots reveals that first three thread roots have highest damage, whereas first engaged thread have maximal damage, as can be observed from Fig. 8a, b. The results are shown for model 2 (with 70 % of $F_{0.2}$) for P_S = 99.9999 %. Furthermore, stress amplitudes are shown in Fig. 8c, d. The results show that maximal stress amplitude of σ_A = 93 MPa was obtained at first engaged thread root.

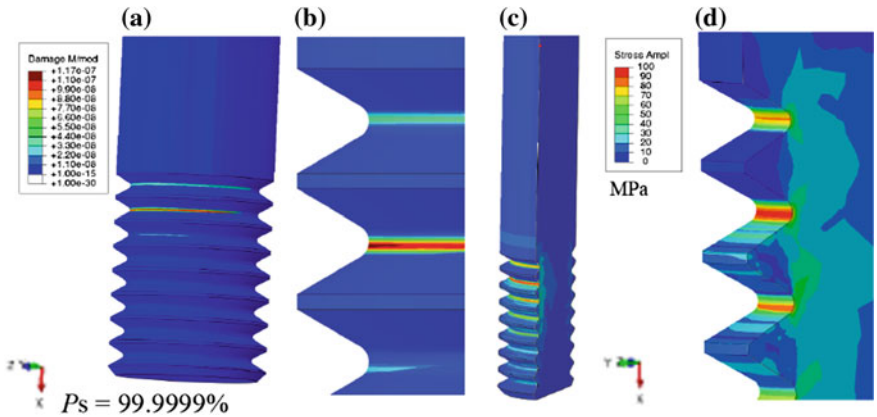

Fig. 8 Fatigue damage of model 2 (with 70 % of $F_{0.2}$) for P_S = 99.9999 %. **a** Distribution on bolt, **b** distribution in first three thread roots, **c** stress amplitudes distribution and **d** stress amplitudes distribution in first three thread roots

It is a well known fact that, at thread roots, very high stress concentrations occur and under preload force significant mean stresses are introduced in roots. These high mean stresses are introduced in thread roots due to preload force and together with the stress amplitudes under dynamic loadings govern the fatigue performance.

The fatigue damage assessments for all four models and for all survival probabilities are shown in following tables. Tables show fatigue damage and fatigue limit for model 1 (with 50 % of $F_{0.2}$), model 2 (with 70 % of $F_{0.2}$), model 3 (with 90 % of $F_{0.2}$), and model 4 (with 0 % of $F_{0.2}$), respectively. The results are shown for most critical node in first engaged thread root where highest damage was obtained. Model 1 have a highest damage of D = 2.53E−06 and fatigue limit of σ_D = 179 MPa for P_S = 99.999999 %. Further increase of bolt preload force F_P lead to lower fatigue damage. For instance, model 3 have a highest damage of D = 100.97E−09. However, with increase of F_P, fatigue limit is decreased. On the other hand, with increase of F_P, maximal stress amplitude decrease. For instance, model 1 with 50 % of $F_{0.2}$, which result with F_P = 27,500 N, has a σ_A = 232 MPa, whereas model 3 with F_P = 49,500 N result with σ_A = 58 MPa. Present results shows that the model 4 (without preload force) have highest fatigue damage. Maximal damages are in all cases always for P_S = 99.999999 %, as expected. One of the main and biggest challenges for fatigue assessment is how to transfer the results from specimens to components [59]. In this particular case of threaded joint, problem is how to transfer the results from smooth circular specimen to threaded region. Specimen have alternating fatigue limit of $\sigma_{D,tc}$ = 495 MPa for tension/compression (R = −1), for alternating bending is $\sigma_{D,b}$ = 525 MPa, and for alternating shear τ_D = 285 MPa [57]. It is evident that calculated fatigue limit strongly depends on preload force. Fatigue limit is highest for F_P = 0 N with value of σ_D = 480 MPa. Lowest fatigue limit was calculated for F_P = 49,500 N with value of σ_D = 193 MPa. It is interesting to observe decrease of fatigue limit from P_S = 50 to 99.999999 %. Decrease of 76 MPa was calculated for F_P = 49,500 N, whereas 191 MPa for F_P = 0 N. The diagram of Fig. 9 makes it evident that σ_D have a significant decrease for lower failure probabilities. From this diagram, it can be easily seen that curves have a shape of Gaussian distribution (Tables 2, 3, 4, 5).

The unit vectors of critical cutting plane for crack initiation are shown in Fig. 10a–c. The unit normal vectors of critical cutting plane $\vec{i}$, $\vec{j}$, and $\vec{k}$ are related to the axes x, y, and z, respectively. As can be seen from these figures, unit normal vector $\vec{i}$ = 0.9848, $\vec{j}$ = 0.1736, whereas $\vec{k}$ = 0. These unit normal vectors are shown for the most critical node in first engaged thread root.

The *S-N* curve at thread root has a modification from basic material in slope from k = 12 at $N_D = 2 \times 10^6$ cycles to k = 3.1 at $N_D = 4.06 \times 10^5$ cycles. The thread root transition in slope is from k = 3.1 to k' = 5.2 at $N_D = 4.06 \times 10^5$ cycles for cumulative damage calculation, as shown in Fig. 11. R1 position indicates the thread root, F1 indicates right thread flank position which is on tensile side, whereas F2 indicates the left thread flank which is on compression side due to the contact with nut thread flank. As can be seen in Fig. 11 for F1 and F2, local *S-N* curve slopes are k = 5.2 and k = 4, respectively. However, at bolt shank *S-N* curve has a

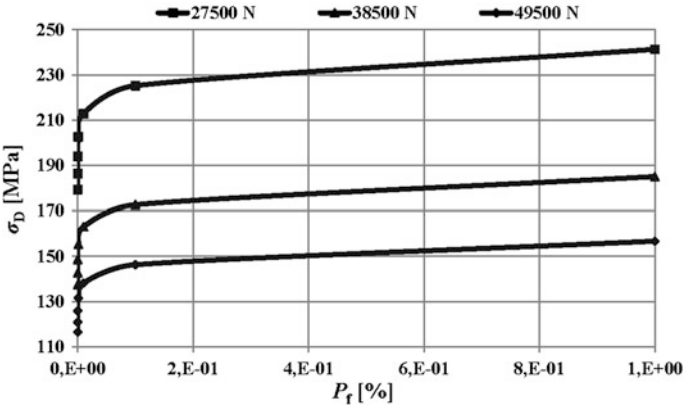

Fig. 9 Fatigue strength in dependence of failure probability P_f for models with 50, 70 and 90 % of $F_{0.2}$

Table 2 Model 1 fatigue damage and fatigue strength in dependence of survival probability

P_S (%)	D (–)	σ_D (MPa)
50	312.16E−09	298
97.5	779.38E−09	249
99	924.72E−09	241
99.9	1.25E−06	225
99.99	1.49E−06	213
99.999	1.73E−06	203
99.9999	1.98E−06	194
99.99999	2.25E−06	186
99.999999	2.53E−06	179

Table 3 Model 2 fatigue damage and fatigue strength in dependence of survival probability

P_S (%)	D (–)	σ_D (MPa)
50	12.76E−09	228
97.5	31.79E−09	191
99	37.7E−09	185
99.9	53.8E−09	173
99.99	72.11E−09	163
99.999	92.97E−09	155
99.9999	116.72E−09	149
99.99999	143.66E−09	143
99.999999	174.51E−09	138

transition in slope from $k = 9.4$ to $k' = 17.8$ at $N_D = 1.76 \times 10^6$ cycles, as shown in Fig. 12. Steeper slopes at thread roots are caused with the high stress gradients and mean stress, whereas at bolt shank the stress gradients are very small which result

Table 4 Model 3 fatigue damage and fatigue strength in dependence of survival probability

P_S (%)	D (–)	σ_D (MPa)
50	7.41E−09	193
97.5	18.43E−09	162
99	21.86E−09	157
99.9	31.18E−09	146
99.99	41.77E−09	138
99.999	53.84E−09	132
99.9999	67.57E−09	126
99.99999	83.14E−09	121
99.999999	100.97E−09	117

Table 5 Model 4 fatigue damage and fatigue strength in dependence of survival probability

P_S (%)	D (–)	σ_D (MPa)
50	14.29E−06	480
97.5	24.45E−06	402
99	27.03E−06	389
99.9	33.33E−06	363
99.99	39.6E−06	343
99.999	45.99E−06	327
99.9999	52.59E−06	313
99.99999	59.43E−06	300
99.999999	66.64E−06	289

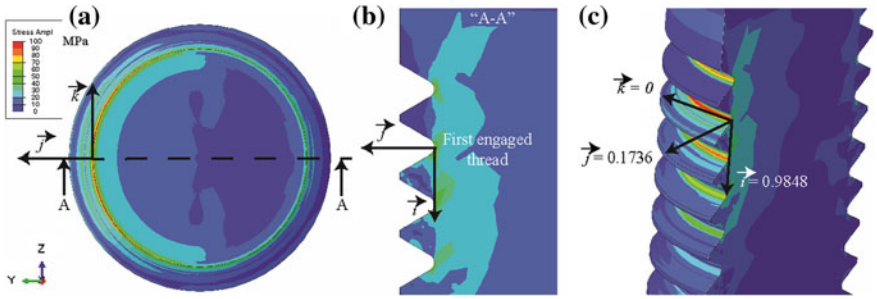

Fig. 10 Unit normal vectors of critical cutting plane for crack initiation **a** top view of first engaged thread root, **b** and **c** section view

with shallower slope. The slope at bolt shank is shallower due to the influence from mean stresses only.

The stress gradient influence on slope of the local *S-N* curve ($f_{GR,sf}$) and mean stress influence ($f_{\sigma M,sf}$) were evaluated to investigate the dominant influence on *S-N* curve slope at first engaged thread root. The results are shown in Table 6. Influence of stress gradients on *S-N* curve slope has a slightly decreased for higher

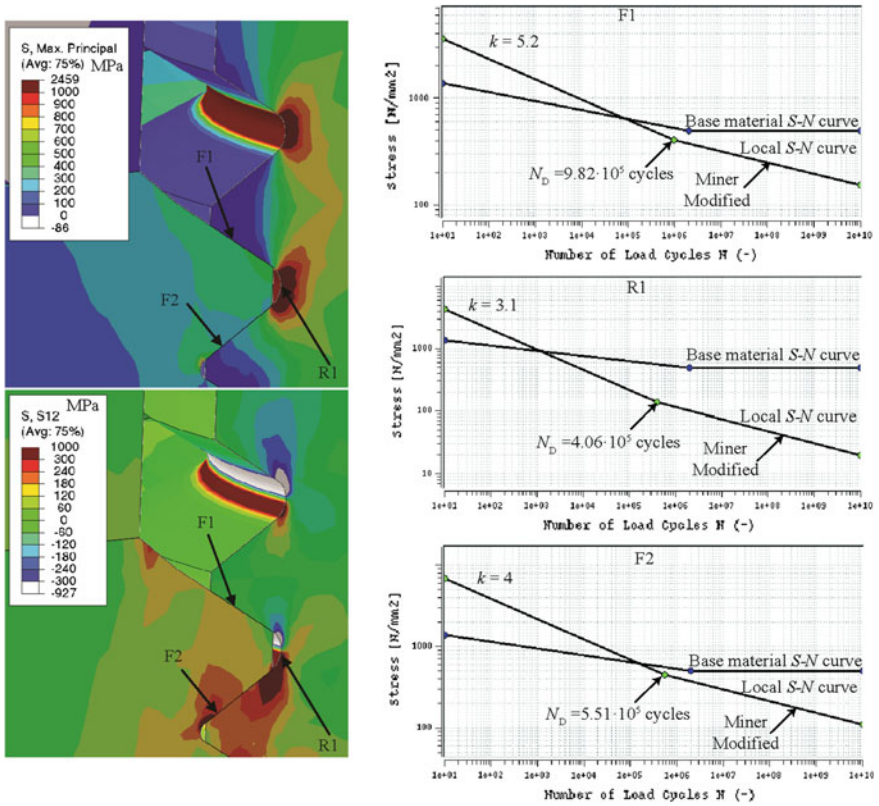

Fig. 11 Local *S-N* curves for thread root and thread flanks

preloads. From $f_{GR,sf}$ = 22.4 at preload force of F_P = 27,500 N, to $f_{GR,sf}$ = 21.1 at preload force of F_P = 49,500 N. However, on the other hand, the mean stress influence on local *S-N* curve slope has increased due to the higher preload forces. From $f_{\sigma M,sf}$ = 1.8 at F_P = 27,500 N, to $f_{\sigma M,sf}$ = 3.4 at F_P = 49,500 N.

Influence of stress gradients (χ) on *S-N* curve slope at first engaged thread root is shown in Table 7. With χ influence slope is k = 3.1, whereas without χ influence slope is k = 11.1 for first three models with preload forces. The model 4 with χ influence result with slope of k = 3, whereas without χ influence k = 11. The *S-N* curve slope for bolt shank is k = 9.4 and k = 10.9 without stress gradient influence.

As can be seen from results, with increase of survival probability the fatigue strength is significantly decreased, especially for very high reliability. One of the most important influence on fatigue damage of bolted joint is stress gradient which lead to much steeper local *S-N* curves.

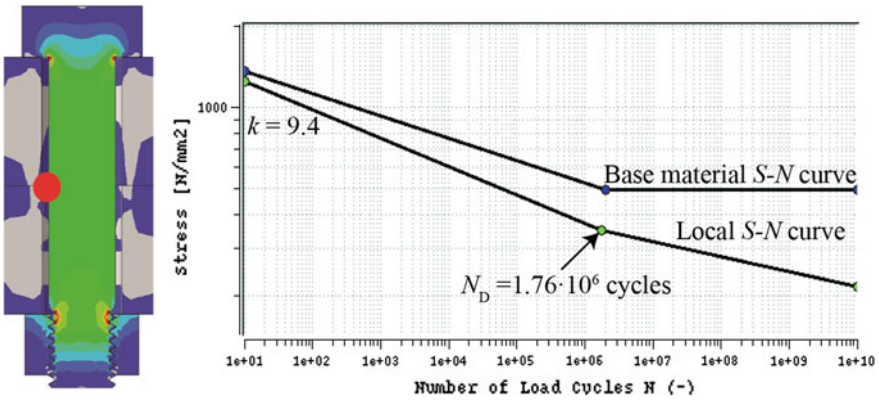

Fig. 12 Local *S-N* curve for bolt shank

Table 6 Stress gradient ($f_{GR,sf}$) and mean stress ($f_{\sigma M,sf}$) influence on local *S-N* curve slope at first engaged thread root

F_P (N)	$f_{GR,sf}$	$f_{\sigma M,sf}$
27,500	22.4	1.8
38,500	21.8	2.7
49,500	21.1	3.4
0	22.8	1.0

Table 7 Influence of stress gradients on *S-N* curve slope at first engaged thread root

F_P (N)	k (–) with χ influence	k (–) without χ influence
27,500	3.1	11.1
38,500	3.1	11.1
49,500	3.1	11.1
0	3.0	11

6 Discussion

These results, based on FE and fatigue damage analyses with stress based critical plane approach, have shown that the most critical fatigue point is at the first engaged thread root, which matches results from the literature [8, 21, 79–84].

Furthermore, the results are in accordance with experimental results for the *S-N* curve slope and knee point. This investigation shows that on the most critical thread root position, obtained slope is $k = 3.1$ and number of cycles with $N_D = 4.06 \times 10^5$. A comprehensive literature overview for steels according to Hück et al. [85], shows the average decrease in the slope of $k = 12.5$ for $K_t = 1$ on $k = 4$ for $K_t = 8$. The number of cycles in the knee point of the *S-N* curve was shifted from $N_D = 2 \times 10^6$ to $N_D = 4 \times 10^5$ for $k = 3$. Mostly for steel smooth specimen $k \approx 15$, whereas for structure with notches $k \approx 5$ and in the case that sharp notch is present, $k \approx 3$ [57]. For welded joints in general, $k = 3$–4. In the case

when nominal stress method is used with normal stress, slope is $k = 3.0$. Slopes of the $k = 3$ are according to the IIW recommendations [86].

As valid for the welded joints regarding the *S-N* curve slope k, the similar can be applied for the bolted or threaded joints in general. However, according to the Sonsino [87], the slope depends on the loading mode (axial, bending, torsion, stress ratio), geometry, stiffness, stress concentration and, in consequence, on the ratio between crack propagation and total life. The slope beyond the knee point result from linear regression analyses and curve fitting. Moreover, in the case of welded joints, knee point additionally depends on the magnitude of the residual stresses [88, 89]. In general, with an increase of the notch sharpness, the slope k become steeper and the number of cycles at the fatigue limit N_D decreases in *S-N* curve.

Generally speaking, fatigue assessment is usually done with nominal stress approach from Eurocode 3 [26] or VDI 2230 [27]. Eurocode 3 provides a unique (rough) limit of stress amplitude at 2×10^6 cycles equal to $\sigma_A = 25$ MPa. VDI 2230 apply to steel bolts (threads with 60° flank angle), strength classes 8.8–12.9, and is recommended for bolt diameters smaller than 40 mm. The load can consists of a static and/or dynamic axial loads, whereas bending moments and transverse loads may occur. VDI 2230 recommend for the most critical joints to verify calculation results with experimental or numerical investigations. In the case of Eurocode 3, the relevant *S-N* curve detail category 50 is not verified for bolt diameters larger than 36 mm [90].

The fatigue strength for bolted joints is more conservative in EC3 than in VDI 2230 [90]. According to the VDI 2230, if numbers of alternating cycles are $N_D = 2 \times 10^6$, then for the stress amplitude of the thread fatigue limit, which was rolled before heat treatment or rolled after heat treatment can be calculated with the following equations, respectively.

$$\sigma_{ASV} = 0,85 \cdot (150/d + 45) \tag{20}$$

$$\sigma_{ASG} = (2 - F_{Sm}/F_{0,2min}) \cdot \sigma_{ASV} \tag{21}$$

where d is the diameter of the bolt, F_{Sm} is the average bolt load, and $F_{0,2min}$ is the bolt load at the minimum yield point. The values for the fatigue limit are related to the stress cross section A_S according to the DIN 969 and ISO 3800, of high-strength bolts according to DIN EN ISO 898-1 with standard threads 6g/6H. Only Eq. (21) for fatigue limit of thread which was rolled after heat treatment is preload dependent.

Moreover, bolted joints can be assessed with DNV-RP-C203 [91]. According to DNV-RP-C203, connections where the pretensioned bolts are subjected to dynamic axial forces should be designed with respect to fatigue, taking into account the stress range in the bolts. Accordingly, fatigue assessment in the HCF region is for bolts and threaded rods in tension as well as bolts in single or double shear. DNV-RP-C203 detail category for cold rolled threads with no following heat treatment is F1, whereas for cut threads detail category is W3. F1 and W3 corresponds to the notation of 63 and 36, respectively in Eurocode 3 and IIW. It can be

seen that cut threads corresponds to the worst case of welded joint. According to DNV-RP-C203, stress response from wave action shows typically 5×10^6 cycles.

Additionally, unfired pressure vessels standard BS EN 13445-3:2009 [92] include bolted joints fatigue assessment. Fatigue limit can be calculated as $\Delta\sigma_D/R_m = 0.0522$ at 2×10^6 cycles and is used for any thread form (machined, ground or rolled) for failure probability of $P_f = 0.1$ %.

Besides previously mentioned engineering fields of general application, high pressure equipment and offshore structures, safe design of bolted joints is additionally very important in transportation and hoisting equipment where special safety regulations must be fulfilled. For instance, according to the safety standards of the Nuclear Safety Standards Commission (KTA) for the design of lifting equipment in nuclear power plants [93], the stress analysis shall be performed with respect to the VDI 2230 guidelines for bolted joints where the yield stress during tightening is limited to 70 % and safety factor of 2.0 against the stress amplitude of the endurance shall be satisfied.

Fatigue of threaded joints is different from general structural fatigue problems because of the various influence factors and in-service conditions in variety of industrial applications. Fatigue assessment of the bolted joints is a typical fatigue problem with the multitude of parameters and influence factors which have an influence on the bolted joints fatigue strength. Fatigue damage results from the combined effect of a large number of influence factors. Nominal approaches does not take into account complex thread geometry with blunt notches, nonlinear contact interactions, and cannot consider local stress-strain state at the thread root which result without accurate thread notch effect. For the nominal approach, stress is really simple because it is just the average stress in bolt cross-section on ideally cylindrical bolt joint. To consider and describe local stress-strain state in thread root with realistic notch effect, stress gradients, remarkable mean stress introduced during tightening, stress amplitudes, and damage accumulation can only be estimated by the local method. Nevertheless, fatigue assessment is a complex task due to the significant number of uncertainties that are inherent to the fatigue phenomenon [94–96]. Threaded joints have several peculiarities that complicate the fatigue damage assessments. This statement, however, holds true at least as far as an attempt is made to take all the details and influence factors into account for fatigue assessment. The number of influencing parameters is large, but can be summarized for local approach. The main difficulties encountered in threaded joint fatigue damage assessment are due to the uncertainties in accurately defining the following:

1. material monotonic/cyclic properties, local *S-N* curve, and Haigh diagram,
2. production aspects (surface quality, residual stresses, hardness, etc.),
3. thread profile geometry and tolerances,
4. uncertainties regarding the coefficient of friction,
5. uncertainties in the scatter of preload force and dynamic loads spectra,
6. uncertainties in Palmgren-Miner damage summation rule, and
7. in environment influences.

Mechanical properties can be quite different throughout the threaded joint due to production and surface treatments. The thread profile geometry within appropriate tolerance class may vary in reality since many dimensional parameters exist (pitch, major and minor diameter, height of thread profile, root radius, etc., and their relationship).

These all parameters are usually very small and include complex thread details like thread root radius with blunt notches and thread flanks which on the other hand have nonlinear contact interactions. Thread blunt notches with small root radius and application of the coarse or fine threads which have different root radius results with different fatigue response. Thread flank contact surfaces experiences slippage and they are subjected to contact forces due to pressure and friction which result in thread bending. This in turn result with high stress concentrations and stress gradients in thread roots. Only the local approach has a potential with sensitivity analysis to improve fatigue behaviour of the particular structure. Nominal approach without detailed geometry of thread roots and influence factors cannot give the answers related to that details where fatigue cracks initiate. Furthermore, high strength steels provide higher fatigue strength, but they are significantly more notch sensitive. In this case, thread notches are more detrimental than in low strength steels. Scatter of preload force depends on tightening approach which in some cases have a high scatter (e.g., tightening with impact wrench or impact wrench with momentum control up to ± 60 %, torque-controlled tightening up to ± 43 %, yield-controlled tightening up to ± 17 %, elongation-controlled tightening with ultrasound ± 10 %). Hydraulic tensioners have significantly lower scatter which is usually from ± 5 % up to ± 10 %. Hydraulic tensioners are commercially available for a variety of engineering application like wind turbines, pump heads, engine cylinder heads, foundation bolt connections, etc. In addition, special application like subsea tensioners are also available. Highest accuracy of ± 1 % can be achieved with the usage of the strain gauges. Special nuts were also developed, like for instance, a hydraulic nut which is an internally threaded annular jack. These all uncertainties are directly related to the threaded joint reliability and safety. Threaded joint integrity is the key basis of safe and leak-free operations and tightening is one of the key factors related to the bolted joint integrity. For many applications, stress history due to dynamic loadings can only be made with approximate estimations. For some fields of application, standardised load histories are given by a regulation or code. For instance, WASH for offshore structures (structural members of oil platforms), WISPER for wind turbines, WAWESTA for drive train components, Gaussian load distributions with narrow-band, medium-band, and wide-band random sequence, and many others. Statistical data for fatigue and cyclic properties mostly coming from laboratory experimental investigations, not from real in-service conditions. This is very important for environment conditions. These all peculiarities change over the time. The first microcrack growth is a surface phenomenon where a various number of influences are present. Surface roughness, surface treatments and layers are of particular significance and influence on crack initiation phase since fatigue cracks initiate on surface. These surface conditions have no particular influence on crack growth

because crack growth is a matter of material bulk properties [97]. According to Schijve [97], material and surface finish effects on scatter/range of dispersion is similar on specimen and real structures. The failure initiated always at the surface (also at very high number of cycles), which is caused by the high stress concentration in the thread root. The crack initiation site for the smooth specimens at higher number of cycles (approximately $N > 7 \times 10^6$) was always below the surface in a distance between several 10 μm–1 mm [80]. The number of influence factors significantly increase when approach is switched from the nominal to the local approach. This in turn require excessive detail modeling and knowledge of a variety of influence factors.

The fatigue damage D theoretically equals 1.0 at fatigue failure. However, in reality and engineering practice due to the uncertainties related to the proportional and non-proportional loadings, stress multiaxility, fabrication, and other errors, the value of D is usually <1. About 90 % of all experimental results are below 1 [98]. According to the FKM-Guidelines [57], critical damage sum for non-welded steel component is $D_M = 0.3$.

The discussion above shows that generally, the standard nominal approach can be used as a first guideline for dimensioning, from which further design improvement based on local approaches may originate. The potential of the local approach lies in the fact that only local approach takes into account the influence factors and detailed geometry which have a decisive influence on the fatigue behaviour and lifetime.

The safety margin and the influence of each influence factor on structural reliability are significantly valuable knowledge for the structural integrity. The expensive interventions and the demand for higher safety and environment protection increased the need for higher reliability of bolted joints [3].

Determination of the fatigue limit of threads is relevant for considering the risk of fatigue crack initiation in structures in-service, especially for large structures with complex loading which must accomplish high reliability of structural integrity.

If regular in-service monitoring is not specified, the survival probability must be high [86]. High uncertainties are associated with the fatigue damage assessment. These high uncertainties associated with fatigue damage imply that in-service inspection for fatigue cracks will be required during life depending on consequence of a fatigue failure and estimated fatigue damage/life. Certain reliability depend on the consequence and nature of failure. Uncertainty modelling for target reliability level in offshore is according to [99], with value of failure probability $P_f = 10^{-6}$ for serious consequence when class of failure have no warning before the occurence of failure.

According to the DNV-RP-C-203 [91]: if the consequence of a fatigue crack is substantial the accumulated probability of a fatigue failure should be $<10^{-4}$ and an inspection would be required after 2 years. After a first inspection the time interval to the next inspection can be estimated based on fracture mechanics and probabilistic analysis taking the uncertainty in the inspection method into account.

According to the DNV-OS-C101 [100], design fatigue factors (DFF) shall be applied to reduce of fatigue failure probability (P_f). This factors are dependent on the significance of the structural components with respect to structural integrity and availability for inspection and repair. DFF has a maximum value of 3 for the non-accessible areas, areas not planned to be accessible for inspection and repair during operation. For instance, welds beneath positions 150 m below water level and splash zone should be assumed inaccessible for in-service inspection. Units intended to follow normal inspection schedule according to class requirements, i.e., the 5-yearly inspection interval in sheltered waters or drydock, may apply a Design Fatigue Factor (DFF) of 1. According to the DNV-OS-C101, the *S-N* curves shall be based on a survival probability of $P_S = 97.6$ %, corresponding to the mean minus-two-standard-deviation curves of relevant experimental data. The IIW-Recommendations [86] require the prerequisites for allowable stress ranges for welded joints must be derived for $P_s = 97.7$ %. The allowable equivalent stress ranges for $P_s = 97.7$ % were derived based on Gaussian log-normal distribution with a scatter of $T_S = 1.50$ for welded joints. Therefore, fatigue strength properties are usually given with ± 1 up to three standard deviations. From engineering standards the accepted survival probability or failure probability depends on the consequences of failure with target reliability levels.

These values of fatigue limits in thread roots also need to be determined based on the experiments. However, experiments are extremely hard to apply on thread roots due to very small dimensions. For instance, thread root radius on used bolt M10 with normal threads is only $r = 0.217$ mm. Therefore, from authors knowledge, all experiments on bolted joints were done with nominal approach, with stresses on bolt stress cross section.

It is the authors opinion that threaded joints have a large number of significant influence factors and peculiarities affecting the fatigue behaviour and fatigue damage, and trying to predict damage with high accuracy on single numerical model is a quite hard. Moreover, in service is always present the lack of information. But, this study shows how tightening forces and survival probability influence the fatigue damage, which give a useful information for engineering practice. The target of fatigue damage analysis should be to insure that the probability of fatigue failure and consequences of this failure be in the safety range for risk and economical significance.

Furthermore, it is authors opinion that with acceptance of all uncertainities related to the fatigue, statistics and probability should be applied for threaded joint integrity. Concentration on influence factors which have highest influence and are decisive is the most important basis for the reliable application of local approach.

Conclusively, fatigue damage and structural integrity of bolted joints can be determined only with certain probability of survival or failure. Due to the significant survival probability influence on fatigue damage results, in-service inspection for fatigue cracks will be required during life depending on consequence of a fatigue failure and estimated fatigue damage, because connection between assessment of fatigue damage and in-service inspection is a mandatory.

7 Conclusions

The most important conclusion to be drawn here is that the fatigue damage and fatigue limit for specific number of cycles can be determined only with certain probability of survival or failure. Nevertheless, under the parameters of FE and fatigue damage analyses with influence factors, statistics, and probability of this study, the following conclusions were drawn concerning the fatigue in dependence of survival probability:

- Increase of bolt preload force up to 90 % of $F_{0.2}$ results with lower fatigue damage, whereas fatigue limit decreases. On the other hand, with increase of preload force, maximal stress amplitude decreases. It has a beneficial effect on fatigue damage. Model without preload force has the highest fatigue damage, whereas model with 90 % of $F_{0.2}$ has a minimal fatigue damage.
- Fatigue strength has a significant decrease for lower failure probabilities and therefore, statistics and probability have a very significant influence on fatigue damage and fatigue strength.
- Steeper slopes at thread root with $k = 3.1$ are caused with the high stress gradients and mean stresses, whereas at bolt shank the stress gradients are very small which results with shallower slope of $k = 9.4$. Thread flanks on compressive side have slope of $k = 4$, whereas on tensile side slope is $k = 5.2$. In general, with an increase of the notch sharpness, the slope k become steeper and the number of cycles at the fatigue limit N_D decreases in S-N curve.
- Nominal approach can be used as a first guideline for dimensioning, from which further design improvement based on local approaches may originate. The number of influence factors significantly increases when approach is switched from the nominal to the local approach.

Determined fatigue damage and/or fatigue life should form the basis for efficient and safe in-service inspection time intervals as well as inspection during the manufacturing.

References

1. Schijve J (2003) Fatigue of structures and materials in the 20th century and the state of the art. Int J Fatigue 25:679–702
2. Schijve J (2014) The significance of fatigue crack initiation for predictions of the fatigue limit of specimens and structures. Int J Fatigue 61:39–45
3. Esaklul KA, Ahmed TM (2009) Prevention of failures of high strength fasteners in use in offshore and subsea applications. Eng Fail Anal 16:1195–1202
4. Sungkon H (2003) Fatigue analysis of drillstring threaded connections. In: Proceedings of the thirteenth international offshore and polar engineering conference Honolulu, Hawaii, USA, May 25–30, pp 202–208
5. Shahani AR, Sharifi SMH (2009) Contact stress analysis and calculation of stress concentration factors at the tool joint of a drill pipe. Mater Des 30:3615–3621

6. Ferjani M, Averbuch D, Constantinescu A (2011) A computational approach for the fatigue design of threaded connections. Int J Fatigue 33:610–623
7. Hill TH (1992) A unified approach to drillstem failure prevention. SPE Drill Eng 7:254–260
8. Tafreshi A, Dover WD (1993) Stress analysis of drillstring threaded connections using the finite element method. Int J Fatigue 15:429–438
9. Bertini L, Beghini M, Santus C, Baryshnikov A (2008) Resonant test rigs for fatigue full scale testing of oil drill string connections. Int J Fatigue 30:978–988
10. Ciavarella M, Meneghetti G (2004) On fatigue limit in the presence of notches: classical vs. recent unified formulations. Int J Fatigue 26:289–298
11. Susmel L, Taylor D (2003) Two methods for predicting the multiaxial fatigue limits of sharp notches. Fatigue Fract Eng Mater Struct 26:821–833
12. Naik RA, Lanning DB, Nicholas T, Kallmeyer AR (2005) A critical plane gradient approach for the prediction of notched HCF life. Int J Fatigue 27:481–492
13. Hofmann F, Bertolino G, Constantinescu A, Ferjani M (2007) A multiscale discussion of fatigue and shakedown for notched structures. Theor Appl Fract Mech 48:140–151
14. Hofmann F, Bertolino G, Constantinescu A, Ferjani M (2009) A discussion at the mesoscopic scale of the stress-gradient effects in high cycle fatigue based on the Dang Van criterion. J Mech Mater Struct 4:293–308
15. Fares Y, Chaussumier M, Daidie A, Guillot J (2006) Determining the life cycle of bolts using a local approach and the Dang Van criterion. Fatigue Fract Eng Mater Struct 29:588–596
16. McEvily AJ (1990) Atlas of stress corrosion and corrosion fatigue curves. ASM International, Materials Park, OH
17. Bickford JH (1990) An introduction to the design and behavior of bolted joints, 2nd edn. Marcel Dekker, New York, NY
18. ASME/ANSI B16, Standards of pipes and fittings
19. API Spec 6A (2004) Specification for wellhead and christmas tree equipment. American Petroleum Institute, Washington, DC
20. Review of Repairs to Offshore Structures and Pipelines,1994. Publication 94/102, Marine Technology Directorate, UK
21. Cho SS, Chang H, Lee KW (2009) Dependence of fatigue limit of high-tension bolts on mean stress and ultimate tensile strength. Int J Automot Technol 10:475–479
22. Johnston TL, Karaikovic EE, Lautenschlager EP, Marcu D (2006) Cervical pedicle screws vs. lateral mass screws: uniplanar fatigue analysis and residual pullout strengths. Spine J 6:667–672
23. Brasiliense LBC, Lazaro BCR, Reyes PM, Newcomb AGUS, Turner JL, Crandall DG, Crawford NR (2013) Characteristics of immediate and fatigue strength of a dual-threaded pedicle screw in cadaveric spines. Spine J 13:947–956
24. Novoselac S, Ergić T, Kozak D, Sertić J, Pacak M (2013) Influence of dental implant screw preload force on high-cycle fatigue. In: Karšaj I, Jarak T, Stubica D (eds) Proceedings of 5th Croatian society of mechanics, Croatia, 6–7 June, pp 137–142 (in Croatian)
25. Novoselac S, Ergić T, Kozak D, Baškarić T (2014) Structural durability of dental implants. In: Jelenić G, Gaćeša M (eds) Proceedings of 6th Croatian society of mechanics, Rijeka, Croatia, 29–30 May, pp 251–256 (in Croatian)
26. Eurocode No. 3 (1993) Design of steel constructions, Part 1. Beuth-Verlag, Berlin
27. Verein Deutscher Ingenieure (2003) VDI 2230 Guidelines
28. Schneider R, Wuttke U, Berger C (2010) Fatigue analysis of threaded connections using the local strain approach. Proc Eng 2:2357–2366
29. Dixon DL, Breeding LC, Sadler JP, McKay ML (1995) Comparison of screw loosening, rotation, and deflection among three implant designs. J Prosthet Dent 74:270–278
30. Patterson EA, Kenny B (1986) A modification to the theory for the load distribution in conventional nuts and bolts. J Strain Anal Eng Des 21:17–23
31. Sopwith DG (1948) The distribution of load in screw threads. Inst Mech Eng Proc 159: 373–383

32. D'Eramo M, Cappa P (1991) An experimental validation of load distribution in screw threads. Exp Mech 31:70–75
33. Kenny B, Patterson E (1985) Load and stress distribution in screw threads. Exp Mech 25:208–213
34. Wang W, Marshek KM (1996) Determination of load distribution in a threaded connector with yielding threads. Mech Mach Theory 31:229–244
35. Croccolo D, Agostinis M, Vincenzi N (2012) A contribution to the selection and calculation of screws in high duty bolted joints. Int J Press Vessels Pip 96–97:38–48
36. Griza S, da Silva MEG, dos Santos SV, Pizzio E, Strohaecker TR (2013) The effect of bolt length in the fatigue strength of M24x3 bolt studs. Eng Fail Anal 34:397–406
37. Patterson EA (1990) A comparative study of methods for estimating bolt fatigue limits. Fatigue Fract Eng Mater Struct 13:59–81
38. Liao R, Sun Y, Liu J, Zhang W (2011) Applicability of damage models for failure analysis of threaded bolts. Eng Fract Mech 78:514–524
39. Susmel L, Tovo R (2011) Estimating fatigue damage under variable amplitude multiaxial fatigue loading. Fatigue Fract Eng Mater Struct 34:1053–1077
40. Łagoda T, Macha E (1994) Estimated and experimental fatigue lives of 30CrNiMo8 steel under in-and out-of-phase combined bending and torsion with variable amplitude. Fatigue Fract Eng Mater Struct 11:1307–1318
41. Morel F (2000) A critical plane approach for life prediction of high cycle fatigue under multiaxial variable amplitude loading. Int J Fatigue 22:101–119
42. Carpinteri A, Spagnoli A, Vantadori S (2003) A multiaxial fatigue criterion for random loading. Fatigue Fract Eng Mater Struct 26:515–522
43. Łagoda T, Ogonowski P (2005) Criteria of multiaxial random fatigue based on stress, strain and energy parameters of damage in the critical plane. Mat-wiss u Werkstofftech 36:429–437
44. Marciniak Z, Rozumek D, Macha E (2008) Fatigue lives of 18G2A and 10HNAP steels under variable amplitude and random non-proportional bending with torsion. Int J Fatigue 30:800–813
45. Matake T (1977) An explanation on fatigue limit under combined stress. Bull JSME 20: 257–263
46. McDiarmid DL (1994) A shear stress based critical-plane criterion of multiaxial fatigue failure for design and life prediction. Fatigue Fract Eng Mater Struct 17:1475–1484
47. Susmel L, Lazzarin P (2002) A bi-parametric modified Wöhler curve for high cycle multiaxial fatigue assessment. Fatigue Fract Eng Mater Struct 25:63–78
48. Susmel L, Petrone N (2003) Multiaxial fatigue life estimations for 6082-T6 cylindrical specimens under in-phase and out-of-phase biaxial loadings. In: Carpinteri A, de Freitas M, Spagnoli A (eds) Biaxial and multiaxial fatigue and fracture. Elsevier and ESIS, Oxford, pp 83–104
49. Lazzarin P, Susmel L (2003) A stress-based method to predict lifetime under multiaxial fatigue loadings. Fatigue Fract Eng Mater Struct 26:1171–1187
50. Forsyth PJE (1961) A two stage process of fatigue crack growth. In: McDowell DL (eds) Proceedings of the crack propagation symposium, Cranfield, pp 76–94
51. Jahed H, Varvani-Farahani A (2006) Upper and lower fatigue life limits model using energy-based fatigue properties. Int J Fatigue 28:467–473
52. Zhang G (2012) Method of effective stress for fatigue: part I—a general theory. Int J Fatigue 37:17–23
53. Novoselac S, Kozak D, Ergić T, Šimić I (2014) Influence of stress gradients on bolted joint fatigue behaviour under different preloads and cyclic loads ratio. Struct Integrity Life 14:3–16
54. Chen JJ, Shih YS (1999) A study of the helical effect on the thread connection by three dimensional finite element analysis. Nucl Eng Des 191:109–116
55. Haibach E (2006) Betriebsfestigkeit: Verfahren und Daten zur Bauteilberechnung, 3rd edn. Springer, Berlin

56. Wiegand H, Kloos KH, Thomala W (2007) Schraubenverbindungen: Grundlagen, Berechnung, Eigenschaften, Handhabung, 5th edn. Springer, Berlin
57. Forschungskuratorium Maschinenbau (FKM) (2003) Analytical strength assessment of components in mechanical engineering, 5th edn. VDMA Verlag GmbH
58. ECS Steyr. FemFat 4.7 (2007) Theory manual. St. Valentin
59. Pyttel B, Schwerdt D, Berger C (2011) Very high cycle fatigue—is there a fatigue limit? Int J Fatigue 33:49–58
60. Karolczuk A, Macha E (2004) Critical and fracture plane orientations under multiaxial cyclic and random loading. Arch Mech Eng 51:415–435
61. Karolczuk A, Macha E (2005) Critical planes in multiaxial fatigue of materials, monograph. Fortschritt-Berichte VDI, Mechanik/Bruchmechanik, reihe 18, nr. 298. Dusseldorf, VDI Verlag, p 204
62. Karolczuk A, Macha E (2005) Critical planes in multiaxial fatigue. Mater Sci Forum 482:109–114
63. Karolczuk A, Macha E (2005) A review of critical plane orientations in multiaxial fatigue failure criteria of metallic materials. Int J Fract 134:267–304
64. Karolczuk A, Macha E (2008) Selection of the critical plane orientation in two parameter multiaxial fatigue failure criterion under combined bending and torsion. Eng Fract Mech 75:389–403
65. Macha E, Niesłony A (2012) Critical plane fatigue life models of materials and structures under multiaxial stationary random loading: the state-of-the-art in Opole Research Centre CESTI and directions of future activities. Int J Fatigue 39:95–102
66. Bedkowski W, Macha E (1987) Maximum normal stress fatigue criterion applied to Random Triaxial Stress State. Theor Appl Fract Mech 7:89–107
67. ECS Steyr. FemFat 4.8 (2007) MAX Manual. St. Valentin
68. Bathias C (1999) There is no infinite fatigue life in metallic materials. Fatigue Fract Eng Mater Struct 22:559–565
69. Eurocode No. 9 (1998) Design of aluminium structures, part 2. Beuth-Verlag, Berlin
70. Sonsino CM (2007) Course of SN-curve especially in the high-cycle fatigue regime with regard to component design and safety. Int J Fatigue 29:2246–2258
71. Dowling N (1972) Fatigue failure predictions for complicated stress–strain histories. J Mater 7:71–78
72. Endo T (1974) Damage evaluation of metals for random or varying loading—three aspects of the rainflow method. Proceedings of the symposium on mechanical behaviour of materials. Society of Materials Science, Japan, pp 372–380
73. Standard Practice for Cycle Counting in Fatigue Analysis (1990) ASTM Standard E 1049-1090. American Society for Testing and Materials
74. Haibach E, Matschke C (1981) Normierte Wöhlerlinien für ungekerbte und gekerbte Formelemente aus Baustahl. Stahl Eisen 101:21–27
75. Amstutz H, Olivier R (2011) Fatigue strength of shear loaded welded joints according to the notch stress concept. Mat-wiss u Werkstofftech 42:254–262
76. Sonsino CM (2009) Effect of residual stresses on the fatigue behaviour of welded joints depending on loading conditions and weld geometry. Int J Fatigue 31:88–101
77. Eibl M, Sonsino CM (2001) Stand der Technik zur Schwingfestigkeitsberechnung von laserstrahl-geschweißten Dünnblechen aus Stahl. Report 668. DVM, Berlin, pp 155–71
78. Eibl M, Sonsino CM, Kaufmann H, Zhang G (2003) Fatigue assessment of laser welded thin sheet aluminium. Int J Fatigue 25:719–731
79. Majzoobi GH, Farrahi GH, Habibi N (2005) Experimental evaluation of the effect of thread pitch on fatigue life of bolts. Int J Fatigue 27:189–196
80. Berger C, Pyttel B, Trossmann T (2006) Very high cycle fatigue tests with smooth and notched specimens and screws made of light metal alloys. Int J Fatigue 28:1640–1646
81. Horn NJ, Stephens RI (2006) Influence of cold rolling threads before or after heat treatment on high strength bolts for different fatigue preload conditions. J ASTM Int 3:95–115

82. Knez M, Glodež S, Kramberger J (2009) Fatigue assessment of piston rod threaded end. Eng Fail Anal 16:1977–1982
83. Macdonald KA, Deans WF (1995) Stress analysis of drillstring threaded connections using the finite element method. Eng Fail Anal 2:1–30
84. Knight MJ, Brennan FP, Dover WD (2003) Effect of residual stress on ACFM crack measurements in drill collar threaded connections. NDT&E Int 37:337–343
85. Hück M, Thrainer L, Schütz W (1981) Berechnung von Wöhler-Linien für Bauteile aus Stahl, Stahlguß und Grauguß, synthetische Wöhler-Linien. VDEh-Bericht ABF 11
86. Hobbacher A (2009) Recommendations for fatigue design of welded joints and components, Doc. IIW-1823-07 (ex-doc. XIII-2151r4-07/XV-1254r4-07), WRC Bulletin 520, Welding Research Council, Inc., New York
87. Sonsino CM (2009) A consideration of allowable equivalent stresses for fatigue design of welded joints according to the notch stress concept with the reference radii r_{ref} = 1.00 and 0.05 mm. Weld World 53:64–75
88. Sonsino CM (1994) Über den Einfluss von Eigenspannungen, Nahtgeometrie und mehrachsigen Spannungszuständen auf die Betriebsfestigkeit geschweißter Konstruktionen aus Baustählen. Mat-wiss u Werkstofftech 25:97–109
89. Ritter W (1994) Kenngrßen der Wöhlerlinien für Schweißverbindungen aus Stählen. Inst. für Stahlbau und Werkstoffmechanik der TU DarmstadtHeft 53, Dissertation TU Darmstadt
90. Schaumann P, Marten F (2009) Fatigue resistance of high strength bolts with large diameters. In: Proceedings of the international symposium for steel structures ISSS, 12.-13.03., Seoul, South Korea, pp 1–8
91. DNV-RP-C203 (2011) Fatigue Design of Offshore Steel Structures. Det Norske Veritas AS
92. BS EN 13445-3:2009 (2009) Unfired pressure vessels. BSI
93. KTA-Geschaeftsstelle c/o BfS, Germany (2014)
94. Svensson T (1997) Prediction uncertainties at variable amplitude fatigue. Int J Fatigue 19:295–302
95. Tovo R (2001) On the fatigue reliability evaluation of structural components under service loading. Int J Fatigue 23:587–598
96. Echard B, Gayton N, Bignonnet A (2013) A reliability analysis method for fatigue design. Int J Fatigue 59:292–300
97. Schijve J (1994) Fatigue predictions and scatter. Fatigue Fract Eng Mater Struct 17:381–396
98. Sonsino CM (2007) Fatigue testing under variable amplitude loading. Int J Fatigue 29:1080–1089
99. DNV (1996) Guideline for offshore structural reliability analysis. Det Norske Veritas, Report no. 95-3204
100. DNV-OS-C101 (2011) Design of offshore steel structures, general (LRFD method). Det Norske Veritas